Sound Propagation in an Urban Environment



David Peter Hewett

St Catherine's College

University of Oxford

A thesis submitted for the degree of

Doctor of Philosophy

Hilary Term 2010

Acknowledgements

Firstly, I would like to thank my supervisors, Professor John Ockendon and Dr David Allwright, for the support, direction and insight they have given me over the past four years.

This work was funded by the Engineering and Physical Sciences Research Council and Dstl under the MOD research programme (contract RD023-2985), and I thank Dr Duncan Williams of Dstl for his involvement in the project.

I also gratefully acknowledge helpful discussions with Prof. C. J. Chapman, Prof. V. P. Smyshlyaev, Prof. R. H. Tew, Prof. J. Woodhouse and Dr W. J. Parnell.

I thank everyone in OCIAM for providing such a stimulating environment in which to work, and for making the last four years so much fun.

Finally, I would like to thank my family, especially my wife, Meghann, for their continued encouragement, patience, and belief in me.

Abstract

This thesis concerns the modelling of sound propagation in an urban environment. For most of the thesis a point source of sound source is assumed, and both 2D and 3D geometries are considered. Buildings are modelled as rigid blocks, with the effects of surface inhomogeneities neglected. In the time-harmonic case, assuming that the wavelength is short compared to typical lengthscales of the domain (street widths and lengths), ray theory is used to derive estimates for the time-averaged acoustic power flows through a network of interconnecting streets in the form of integrals over ray angles. In the impulsive case, the propagation of wave-field singularities in the presence of obstacles is considered, and a general principle concerning the weakening of singularities when they are diffracted by edges and vertices is proposed. The problem of switching on a time-harmonic source is also studied, and an exact solution for the diffraction of a switched on plane wave by a rigid half-line is obtained and analysed. The pulse diffraction theory is then applied in a study of the inverse problem for an impulsive source, where the aim is to locate an unknown source using Time Differences Of Arrival (TDOA) at multiple receivers. By using reflected and diffracted pulse arrivals, the standard free-space TDOA method is extended to urban environments. In particular, approximate source localisation is found to be possible even when the exact building distribution is unknown.

Contents

1 Introduction **1**

1.1 Industrial motivation 1

1.2 Literature review 2

1.2.1 The forward problem in the frequency domain 3

1.2.2 The forward problem in the time domain 5

1.2.3 The inverse problem in the time domain 5

1.3 Structure of the thesis 7

1.4 Statement of originality 11

2 Modelling **12**

2.1 Equations of motion 12

2.1.1 The acoustic approximation 13

2.2 Modelling a source 14

2.3 Time-harmonic sources 15

2.4 Boundary conditions 16

3 Frequency domain analysis **18**

3.1 Introduction 18

3.2 Geometrical acoustics in the frequency domain 19

3.2.1 Geometrical acoustics in free space 19

3.2.2 Geometrical Theory of Diffraction 22

3.3 Review of exact solutions 23

3.3.1 A point source in 2D free space 23

3.3.2 A point source in 3D free space 23

3.3.3 Reflection by a half-plane 23

3.3.4 A point source in a single 2D street 24

3.3.4.1 Modal representation 25

3.3.4.2 Image source representation 27

3.3.4.3 Equivalence of the two representations and ray approximation . . . 29
3.3.5 Diffraction . . . 30
3.3.5.1 The Sommerfeld problem . . . 30
3.3.5.2 A 2D point source . . . 32
3.3.5.3 Diffraction by a wedge in 2D . . . 34
3.3.5.4 Edge diffraction in 3D . . . 34
3.3.5.5 Vertex diffraction in 3D . . . 35
3.4 Acoustic energy . . . 36
3.4.1 Definition of acoustic energy and intensity . . . 37
3.4.2 Time-averaged acoustic energy in the frequency domain . . . 38
3.4.2.1 Acoustic energy associated with a single ray expansion 39
3.4.2.2 Acoustic energy associated with a sum of ray expansions (GTD approximation) . . . 41
3.5 The acoustic power flow in a single 2D street . . . 43
3.5.1 Energy absorption at walls . . . 47
3.5.2 Asymptotic behaviour far from the source . . . 48
3.5.3 Interpretation in terms of ray angles at small absorption ($\alpha \ll 1$) 50
3.6 Energy redistribution at a junction in 2D . . . 51
3.6.1 Energy redistribution at a crossroads . . . 51
3.6.1.1 Neglect of diffraction effects . . . 51
3.6.1.2 Calculation of power flows . . . 57
3.6.2 Range of applicability . . . 60
3.6.3 Interpretation in terms of ray launch angles . . . 60
3.6.4 Probabilistic interpretation . . . 61
3.6.5 Comparison with [26] . . . 62
3.6.6 Other junctions . . . 64
3.7 Multiple junctions in 2D . . . 67
3.7.1 Energy redistribution at a second junction in 2D . . . 67
3.7.2 Validity of integral approximation: expected power flows . . . 70
3.7.3 More than two junctions . . . 77
3.8 A network of streets in 2D . . . 78
3.8.1 Paths of minimal length . . . 78
3.8.2 Network model . . . 83
3.8.2.1 Calculation of net power flows and mean-square pressures . . . 84

3.8.2.2 Exact solution in a regular network 85
3.8.2.3 The case $\beta = 1$ ($\alpha = 0$) 90
3.9 The 3D case 94
3.9.1 Ray approximation in a single street 94
3.9.2 The acoustic power flow in a single street 96
3.9.3 Acoustic power flows in a network of streets 98
3.9.4 Energy redistribution at a crossroads 100
3.9.5 A two-junction environment 102
3.9.6 A regular network of streets 102
3.10 Summary 105

4 Time domain analysis - forward problem 107
4.1 Introduction 107
4.2 Propagation of singularities in solutions of the wave equation 108
4.2.1 Characteristics, wavefronts and rays 108
4.2.2 Singularities 110
4.2.3 Application to the acoustics equations 110
4.2.4 Geometrical acoustics in the time domain and frequency domain 113
4.3 Review of exact solutions 116
4.3.1 Fundamental solutions 116
4.3.2 Reflection by a half-space 117
4.3.3 A point source in a single 2D street 118
4.3.4 Diffraction by a wedge 118
4.3.4.1 Incoming planar step discontinuity at parallel incidence 118
4.3.4.2 Behaviour near diffracted wavefront 122
4.3.4.3 Oblique incidence 123
4.3.4.4 Incident delta-pulse 125
4.3.4.5 A point source in 2D 125
4.3.4.6 A point source in 3D 127
4.3.5 Diffraction by a cone 129
4.4 Pulses with arbitrary time-dependence 134
4.4.1 General principles for diffraction of pulses by edges and vertices 135
4.5 Switching on a time-harmonic source 136
4.5.1 Problem statement 136
4.5.2 A point source in 3D free space 138
4.5.3 A point source in 2D free space 138

4.5.3.1 Behaviour near the leading wavefront 139
4.5.3.2 Convergence to the frequency domain solution 139
4.5.4 A plane wave incident on a rigid half-line in 2D 143
4.5.4.1 Behaviour close to the leading wavefront 144
4.5.4.2 Convergence to the frequency domain solution 145
4.5.4.3 The case $\theta_0 \neq 0$ 155
4.6 Comparison with data from Bourges trials 159
4.6.1 Background 159
4.6.2 Commentary on the data 161
4.6.3 Gaussian model of muzzle blast 164
4.7 Summary 167

5 Source localisation in the time domain 168
5.1 Introduction 168
5.2 TDOA localisation in free space 169
5.2.1 The 2D case with three receivers 170
5.2.2 The 2D case with four receivers 175
5.2.3 The 3D case 178
5.2.4 Measurement errors and least-squares solutions 180
5.3 TDOA localisation in an urban environment: the line-of-sight case . . 186
5.3.1 Image receiver method 187
5.3.1.1 A half space 187
5.3.1.2 A 2D corner 187
5.3.1.3 A single 2D street 190
5.4 The non-line-of-sight case 191
5.4.1 The 2D case - known building distribution 192
5.4.2 The 2D case - unknown building distribution 194
5.4.2.1 Low building density 195
5.4.2.2 A network of narrow streets 196
5.4.2.3 Results of numerical simulation 201
5.4.3 Applicability to the 3D case 203
5.5 Summary 206

6 Conclusions 208
6.1 Summary of results 208
6.2 Future work 210

A Asymptotic analysis of the sums S_1 and S_2 **212**

B Paths through a network of streets **215**

C Evaluation of a useful sum and integral **217**

D A useful integral identity **219**

Bibliography **220**

List of Figures

1.1 Example of the numerical time-reversal method for a two-dimensional urban environment. In (a) a FDTD method is used to solve the forward problem of sound propagation from a source located between the two buildings in the top left corner of the environment. In (b) the time series recorded at the 8 receivers (marked with circles) are retransmitted back into the domain in reverse, using the same FDTD method. The energy is clearly seen to reconverge at the original source location. Plots reprinted with permission from [4]. Copyright 2005, Acoustical Society of America. 6

2.1 3D and 2D models of an urban environment. 16

3.1 Specular reflection law $\theta_r = \theta_i$ in the case of a 2D half-plane 24
3.2 Image sources for a single 2D street 27
3.3 Association between image sources and rays in a single 2D street. . . 30
3.4 The Sommerfeld problem: diffraction of a plane wave by a rigid half-line. The bounding curves of the shaded regions (which represent the shadow boundary regions) are parabolae. 31
3.5 A 2D point source in the presence of a rigid half-line. The bounding curves of the shaded regions are hyperbolae. 33
3.6 (a) The cone of diffracted rays produced by a ray (thick arrow) incident on an edge in 3D (after [48], Figure 1). The semi-angle of the cone is equal to the angle γ_0 between the incident ray and the edge. (b) A ray incident on a vertex gives rise to diffracted rays emanating from the vertex in all directions. 35
3.7 The geometrical interpretation of Θ_n and $\tilde{\Theta}_n$ in a single 2D street. . . 44
3.8 Typical plot of P (solid line) and P_{ray} (dashed line) as a function of the wavenumber k. Here the singularities in P occur at integer multiples of π. 45

3.9 Common junction types 52
3.10 A plane wave incident on the open end of a semi-infinite street. . . . 53
3.11 Schematic showing the shadow boundary regions arising inside the street for the problem considered in Figure 3.10. Only the singly-diffracted fields are considered here - the multiple reflections of these fields give rise to an infinite set of shadow boundary regions in the image plane, associated with the appropriate 'image edges'. Away from these regions ray theory is valid - note that the width of each shadow boundary region has been exaggerated to make the presentation clearer. 53
3.12 Schematic of one of the shadow boundary regions for the problem considered in Figure 3.10. 54
3.13 Junction between two streets - a modal plane wave 'beam' incident on the open end of the right-hand street. 56
3.14 The geometrical interpretation of $\Theta_n(l, w, y_0)$ and $\tilde{\Theta}_n(l, w, y_0)$ - crossroads case. 58
3.15 Comparison of ray tube sum (3.133) (solid line) and the corresponding integral approximation (3.139) (dotted line) for the power flow past a crossroads, plotted against the side street width w. Parameter values are $l = 2$, $y_0 = 0.3$, $\alpha = 0.02$. 60
3.16 The functions F_C and F_T 61
3.17 Energy redistribution at a second crossroads 67
3.18 Determining the ray tubes incident on the first image street cross-section 69
3.19 A portion of the ray tube diagram at a second crossroads 70
3.20 Comparison of (3.166) (solid line) and (3.168) (dotted line) for parameter values $y_0 = 0.4$, $w_1 = 0.8$, $\alpha = 0.02$. 71
3.21 Plot of the error R as a function of λ for parameter values $y_0 = 0.5$, $w_1 = 1$, $w_2 = 1$, $\alpha = 0$. 72
3.22 Plot of the error R as a function of λ for parameter values $y_0 = 0.4$, $w_1 = 0.8$, $w_2 = 1.2$, $\alpha = 0.02$. 73
3.23 Logarithmic plot of $|\langle R \rangle|$ (solid line) and $|R|$ (dashed line) as a function of l_0 for $\lambda = 1$, $\lambda' = \frac{1}{\sqrt{l_0}}$ and parameter values $y_0 = 0.4$, $w_1 = 0.8$, $w_2 = 1$, $\alpha = 0$. 74
3.24 Another two-junction geometry 76
3.25 A three-junction geometry 76
3.26 Contour plots of $\log_{10} P^E_{x,y}$ for different values of β, computed by (3.181) (i.e. using only paths of minimal length). 80

3.27 Contour plots of $\log_{10} P^E_{x,y}$ for different values of β, computed by (3.213) using the exact solution of the network model. 91
3.28 Contour plots of the relative error between the value of $P^E_{x,y}$ computed using paths of minimal length and the exact result computed using the network model. 92
3.29 Contour plots of $\log_{10} W^E_{x,y}$ (defined in (3.214)) for different values of β, computed from solution of network model. Here the street width $w = 1$. 93
3.30 A single street in a 3D urban environment - image source configuration. 94
3.31 The inverse stereographic projection onto the unit sphere centred at the source of the infinite strip C formed by the union of the image street cross-sections forms a segment, bounded by the curves parametrized by $(r, \theta, \phi) = (1, \theta, 0)$ and $(r, \theta, \phi) = (1, \theta, \phi^+(\theta))$ for $-\pi/2 \leq \theta \leq \pi/2$. 98
3.32 A crossroads in 3D. 100
3.33 A plot of the functions E_{2D} (dotted line) and E_{3D} (solid line). 102

4.1 Wavefront diagram for a 2D point source in the presence of a rigid half-plane, showing the incident (red) and reflected (blue) wavefronts. The arrows indicate the direction in which the wavefronts propagate. 117
4.2 Wavefront diagram for diffraction of a plane step discontinuity by a wedge of exterior angle $\beta = 3\pi/2$, showing the incident (red), reflected (blue) and diffracted (green) wavefronts. The arrows indicate the direction in which the wavefronts propagate. 119
4.3 Wavefront diagram for 2D point source in the presence of a wedge of exterior angle $\beta = 3\pi/2$, showing the incident (red), reflected (blue) and diffracted (green) wavefronts. The source location is indicated by the small red circle. 126
4.4 Wavefront diagram for 3D point source in the presence of a wedge of exterior angle $\beta = 3\pi/2$, showing the incident (red), reflected (blue) and diffracted (green) wavefronts. The source location is indicated by the small red sphere. 128
4.5 Wavefront diagram for diffraction of a planar pulse by a polyhedral cone, showing the incident (red), reflected (blue), edge-diffracted (green) and vertex-diffracted (orange) wavefronts. In this example the cone is the region $x > 0$, $y > 0$, $z < 0$ and the pulse is incident from the direction $(-1, -1, 1)$. 130

4.6 Result of FEM solution for diffraction of a planar pulse by a polyhedral cone, with the geometry of Figure 4.5 and an inverse square root singularity on the incident wavefront. The plot shows how the square of Ψ_{diff} varies as a function of ζ in the direction $(-1,-1,1)$, the direction from which the wave was incident. The linear behaviour observed near $\zeta = 1$ confirms our expectation that Ψ_{diff} should have a square-root singularity on the diffracted wavefront. 132
4.7 Wavefront diagrams for diffraction of a planar pulse by a polyhedral cone, showing the incident (red), reflected (blue), singly-edge-diffracted (green), doubly-edge-diffracted (purple) and vertex-diffracted (orange) wavefronts. In this example the cone is the region $x > 0$, $y > 0$, $z < 0$ and the pulse is incident from the direction $(0,1,1)$, with the incident wavefront assumed to reach the vertex $(0,0,0)$ at $t = 0$. 133
4.8 Switching on a time-harmonic point source in 2D free space. Comparison of Φ (solid curves), Φ_{freq} (dashed curves) and the wavefront approximations (4.134) and (4.135) (dotted curves). Parameter values are $\omega = 1$, $c_0 = 1$, $r = 1$, so that the leading wavefront arrives at $t = 1$. 140
4.9 Switching on a time-harmonic source: diffraction of a plane wave by a rigid half-line. The half-line and the incident and diffracted wavefronts have been highlighted. Parameter values are $\theta_0 = 0^+$, $t = 10$, $\omega = 1$, $c_0 = 1$. 146
4.10 Switching on a time-harmonic source: diffraction of a plane wave by an edge. Comparison of Φ (solid curves), Φ_{freq} (dashed curves) and the wavefront approximations (4.171)-(4.174) (dotted curves). Magnified versions of plots (c)-(f) can be found in Figure 4.11. Parameter values are $\theta_0 = 0^+$, $\omega = 1$, $c_0 = 1$, $r = 1$. 147
4.11 Magnified version of Figure 4.10(c)-(f). 148

4.12 Switching on a time-harmonic source: diffraction of a plane wave by an edge. Logarithmic plots of $|\delta_{\mathrm{R}}|$ and $|\delta_{\mathrm{I}}|$ at $t = 10$, with $\theta_0 = 0^+$, $\omega = 1$, $c_0 = 1$. Regions coloured dark red indicate regions in which the relative error is greater than or equal to 1. We remark that the concentric rings observed in the region $r > c_0 t$ in (a) and (b) are due to the zeros of the diffracted component of Φ_{freq}, and do not represent regions of convergence to the frequency domain solution. The magnified plots in (c) and (d) show the behaviour near the point $(-10, 0)$. Near this point the contours of $|\delta_{\mathrm{R}}|$ appear to be ellipsoidal, and the contours of $|\delta_{\mathrm{I}}|$ appear to be horizontal, as is predicted by the analytical results for the regime $\eta \ll \xi \ll 1$. 149

4.13 Illustration of contours of δ_{R}, δ_{I} as predicted by asymptotic analysis. In each plot $\varepsilon = 0.2$. For example, in (a), the plotted curve $\varepsilon = \frac{\sqrt{\eta}}{\xi^{5/2}}$ provides an illustration of a typical contour of δ_{R}, valid in the regime $\xi \gg 1$, $\eta \ll 1$. Other parameter values are $\theta_0 = 0^+$, $t = 10$, $\omega = 1$, $c_0 = 1$. 154

4.14 Switching on a time-harmonic source: diffraction of a plane wave by an edge. Plots of Φ, Φ_{freq}, $|\delta_{\mathrm{R}}|$ and $|\delta_{\mathrm{I}}|$ at $t = 10$, with $\theta_0 = \pi/3$, $\omega = 1$, $c_0 = 1$. 156

4.15 Switching on a time-harmonic source: diffraction of a plane wave by an edge. Plots of Φ, Φ_{freq}, $|\delta_{\mathrm{R}}|$ and $|\delta_{\mathrm{I}}|$ at $t = 10$, with $\theta_0 = 2\pi/3$, $\omega = 1$, $c_0 = 1$. 157

4.16 Schematic (not to scale) showing the geometry of the experimental setup, as viewed from above. The source location is indicated by a cross, and the firing direction by a thick black arrow. The four microphone receivers are indicated by black points. The wall vertices are labelled W_1-W_8. Parameter values are $r_1 = 308.7$m, $r_2 = 307.4$m, $r_4 = 301.7$m, $r_0 = 294.5$m $r = 14.6$m, $\theta_0 = 74°$, $\theta = 262°$. 160

4.17 Typical data from Bourges trials. Event 154, 7.62mm rifle from S2. . 162

4.18 The two pulse arrivals: shockwave and muzzle blast. 163

4.19 Muzzle blast for Event 154, along with the pressure pulse arising from the Gaussian model (4.212). Parameter values are $A = 1100\mathrm{m}^5\mathrm{s}^{-2}$, $\varepsilon = 0.004$s, $t_0 = 3.6087$s, $c_0 = 345.8\mathrm{ms}^{-1}$, $\rho_0 = 1.2\mathrm{kgm}^{-3}$. 165

5.1 Geometry of TDOA localisation in 2D free space with $N = 3$. In (a) the two possible source locations (black crosses) lie on different branches of each of the three hyperbolae, and the correct source location can be determined from the sign of the D_{ij}. In (b) the two possible source locations lie on the same branch of each of the three hyperbolae, and the correct source location cannot be determined from the TDOA data. In both cases the receivers (black points) are at $(0, 0)$, $(1, 0)$ and $(-1, 1)$, and for reference the line (5.14) is drawn in green. 172
5.2 Example of the region (shaded) in which the condition (5.23) fails. Sources located in this region cannot, in general, be recovered uniquely from the TDOA data from the three receivers (points), located at $(0, 0)$, $(1, 0)$ and $(-1, 1)$. The two source location pairs of Figure 5.1 are included for reference (crosses). The checked regions, bounded by the lines (dashed) extending the sides of the triangle formed by the three receivers, is entirely contained within the shaded region. 173
5.3 Four-receiver configurations not satisfying the convex hull condition. . 177
5.4 Example of a four-receiver configuration for which there exist source locations which cannot be recovered from the TDOA data using either the three-receiver or the four-receiver methods. Here the receivers (black points) are at $(0, 0)$, $(1, 0)$, $(-1, 1)$ and $(0.5, 2)$. The shaded regions represent source locations for which the condition (5.23) fails for any choice of three receivers. The curves represent the source locations for which the determinant of the matrix (5.39) vanishes. 178
5.5 TDOA localisation in the presence of measurement errors, $N = 4$. For any choice of three receivers (black points) the three associated hyperbola branches have a point of mutual intersection. However, none of these points coincide with the actual source location (black cross). 181
5.6 TDOA localisation with measurement errors in pulse arrival times; linear minimisation. Plots (a) and (c) correspond to an 'equilateral triangle' four-receiver configuration, and plots (b) and (d) correspond to a 'square' four-receiver configuration. In both configurations the minimum receiver separation is 50m, and the speed of sound $c_0 = 340$m/s. The measurement errors τ_i are taken to be independent and identically distributed Gaussian random variables with zero mean and standard deviation $\sigma = 0.001$s. Localisation errors are averaged over 100 realisations of τ_i. 183

5.7 TDOA localisation with measurement errors in pulse arrival times; nonlinear minimisation. In (a) and (b) the actual source location $\mathbf{x_0}$ was used as the initial guess for the numerical minimisation. In (c) and (d) ${\mathbf{x_0}}^{\text{initial}}$ was taken to be the solution (5.63) of the linear minimisation. Other parameter values are as in Figure 5.6. 185
5.8 Geometry of image receivers for the reflected pulses in a 2D half-plane. 187
5.9 Geometry of image receivers for the reflected pulses in a 2D corner. . 188
5.10 Geometry of image receivers for the reflected pulses in a 2D street. . . 190
5.11 Shortest ray paths from source to receivers in a 2D urban environment. 192
5.12 TDOA localisation in a 2D urban environment, $N = 8$. Plots (a)-(f) show $\log_{10} G(\mathbf{x_0})$ for six different source locations (crosses). The eight receivers are marked with points. 193
5.13 TDOA localisation in a 2D urban environment, $N = 4$. The plot shows $\log_{10} G(\mathbf{x_0})$ for the source location considered in Figure 5.12(a). . . . 194
5.14 TDOA localisation in a 2D urban environment, $N = 8$, using the Euclidean minimisation (5.69). 195
5.15 A network of 2D streets intersecting at right-angled crossroads. 196
5.16 The geometrical structure of H_{ij} in the case $(x_i, y_i) = (0, 0)$ and $(x_j, y_j) = (p, q)$, with $0 < q < p$. Here $l = \frac{1}{2}(p + q - |D_{ij}|)$. 197
5.17 The geometrical structure of H_{ij} when $q = 0$. Here $l = \frac{1}{2}(p - |D_{ij}|)$. . 198
5.18 Regions (I-III) in which a source cannot be located uniquely in the sum-norm approximation. 199
5.19 TDOA localisation in the sum-norm approximation. The TDOA problem for the four-receiver configuration in (a) admits a unique solution for any source location inside the outer rectangle. In contrast, for the four-receiver configuration in (b), source locations inside the inner (shaded) rectangle cannot be recovered uniquely from the TDOA data. In particular, any source location on the diagonal line segment pictured produces the same TDOA data between the 4 receivers. 199
5.20 TDOA localisation in the sum-norm approximation. The two source locations (crosses) produce the same TDOA data at the three receivers (points). The corresponding 'hyperbola' branches B_{ij} are represented by thick lines. 200
5.21 Results of 2D numerical simulation. 202
5.22 Diffracted ray paths in a 3D urban environment. 203

5.23 Illustration of the region (shaded) in which the condition (5.95) holds. The receiver is located at the origin and the (constant) building height, street length and street width are $h = 10$, $l = 9$, $w = 1$, respectively. Both the source and receiver are assumed to be at ground level. The bounding curves of the shaded region are hyperbolae with centre at the receiver. 204

List of Tables

4.1 Switching on a time-harmonic source: diffraction of a plane wave by an edge. Summary of convergence results in the diffracted region $r < c_0 t$ (i.e. $\xi > 0$). 155

4.2 Coordinates of microphone and source locations (in metres), relative to the wall vertex W_1 in Figure 4.16. Here the x- and y-axes run along W_1W_4 and W_1W_2, respectively. 160

5.1 Results of 2D numerical simulation. 202

Chapter 1

Introduction

This thesis concerns the modelling of sound propagation in an urban environment. The motivation is urban source detection and localisation in the defence industry. The main difficulties arising are due to the complexity of the domain, which may contain multiple scatterers (buildings, for example) giving rise to multiple propagation pathways between source and receiver.

In this Introduction we begin by describing the industrial motivation, which was provided by Dstl. We then review the existing literature concerning urban sound propagation and present the outline of the thesis.

1.1 Industrial motivation

Dstl's interest in urban sound propagation primarily concerns the *inverse problem* of source detection and localisation. Here the aim is to estimate, in near real-time, the location of a sound source using measurements from a network of receivers distributed through the propagation domain, which may be either static (e.g. mounted on buildings) or mobile (e.g. mounted on vehicles/personnel).

A prerequisite for a study of the inverse problem is an understanding of the *forward problem* of how the sound from a known source propagates through the environment. The forward problem is also of intrinsic interest to Dstl, because of the desire to minimise the detectability of friendly operations to hostile listeners.

In the applications being considered, the sound field is due to a single point source, which may be either continuous or impulsive in nature. For continuous sources, the

frequency range of interest is up to 1kHz, which corresponds to a spatial wavelength of around 30cm. We remark that this is small compared to typical macro-lengthscales in an urban environment, such as street widths/lengths and building heights.

Dstl are interested in propagation in urban environments containing multiple buildings, over distances of up to 1km. The existence of multiple propagation pathways between source and receiver, combined with the fact that a direct line-of-sight between source and receiver is not generally available, makes the source localisation problem particularly difficult.

Moreover, a detailed model of the propagation domain is not generally available. Basic characteristics such as building dimensions/positions and receiver locations are assumed to be known, but only to a certain degree of accuracy, having been estimated from satellite or UAV (Unmanned Aerial Vehicle) images, for example.

1.2 Literature review

The theoretical modelling of sound propagation in urban environments seems to have begun with the work of Wiener et al. in the 1960s [91]. The original motivation for Wiener's study was to investigate the effectiveness of outdoor communication systems, but the most commonly studied application in the subsequent literature is that of noise reduction (see e.g. [6, 14, 47, 51]), where the objective is to minimise the impact on urban life of intrusive noise sources such as aircraft and road traffic. Interest in the subject from the defence community has arisen only relatively recently, in response to the increasingly urban nature of recent conflicts. Accordingly, the problem has not yet been subject to the same degree of theoretical or experimental effort as have traditionally more defence-related problems such as underwater sound propagation [60].

The main difficulties arising in a mathematical study of urban sound propagation are due to the complexity of the domain. The presence of multiple scatterers such as buildings, vegetation, vehicles, pedestrians and street furniture serves to create an extremely complicated sound field, an exact description of which, either analytical or numerical, is usually impossible. Broadly speaking, the effect of domain complexity may be thought of as occurring on two distinct lengthscales. On the microscale we must consider the effects of wall absorption, scattering by wall inhomogeneities, and by scatterers present in each street. On the macroscale we may view an urban

environment as a network of streets and junctions, through which acoustic energy propagates.

The existing literature mostly concerns the modelling of microscale effects, and is centered around the problem of accurately predicting features of the sound field in a single street. Even in the absence of traffic, pedestrians, vegetation and street furniture this presents a major challenge, because of the absorbent and inhomogeneous nature of building facades [61]. A number of different models have been proposed, and in the following sections we give a brief survey of some of these. The difficulty experienced in trying to obtain reliable predictions of the sound field in a real street has meant that very little theoretical work has been carried out on the macroscale problem [61], and this is the problem we address in this thesis.

1.2.1 The forward problem in the frequency domain

Much of the urban acoustics literature concerns the propagation of sound of a single frequency, which is governed by the Helmholtz equation in the *frequency domain* (see section 2.3). In this section we briefly review the literature concerning the short wavelength regime, where the wavelength is small compared to typical macro-lengthscales such as street widths/lengths and building heights.

Wiener's original study [91] concerns a point source within a single street, which is modelled as a channel between two infinitely long buildings of finite height, with flat, parallel walls, and a perfectly-reflecting ground. The effect of multiple reflections from the walls and ground is dealt with by the insertion of an infinite series of image sources, with diffraction from the tops of the buildings being neglected. The time-averaged acoustic energy density (defined in section 3.4) at the receiver is estimated by summing the free space energy densities due to each image source incoherently (i.e. neglecting interference effects). This approach can be interpreted in terms of energy propagating along straight-line rays emanating from the source, which reflect at the walls according to the *specular* reflection law: 'angle of incidence equals angle of reflection'. Wall absorption is taken into account as follows: the energy propagating along a ray is assumed to decrease at each wall reflection according to a constant multiplicative factor, the *absorption coefficient*, which, for simplicity, is assumed to be constant along the street and independent of the angle of incidence.

This simple model has been the basis of a number of subsequent works by other authors, especially a group working in the 1970s at MIT. Lyon's review paper [61]

provides an overview of some of the problems that were studied in this period (see e.g. [51]), although much of the theoretical work seems to remain unpublished.

Attempts to generalise Wiener's model to include the scattering effect of inhomogeneities in building facades include the work of Davies [27], who modified the reflection law so that, when a ray encounters a wall, a certain proportion of the reflected energy is scattered uniformly in all directions. Davies' model predicts that the non-specular scattering effects are most prominent near to the source, and that at large distances from the source the specularly-reflected field is dominant. However, the parameter regime in which the transition occurs does not seem to be explicitly presented.

Bullen and Fricke [14] propose a different approach, in which the buildings have infinite height and inhomogeneities in building facades are explicitly modelled as small discontinuous changes in the street width. Neglecting wall absorption, the sound field in each region of constant width is assumed to take the form of a modal expansion. In the case where the changes in width are small relative to the average width, an *ad hoc* mode-matching argument leads to a model for acoustic energy propagation along the street, which shows reasonable agreement with the results of a scale model experiment.

Very little theoretical work seems to have been done in urban environments involving multiple streets, although, as Lyon [61] points out, Davies' work on sound propagation along office corridors [26] is of relevance here. The problem considered by Davies concerns a point source in a straight, rectangular corridor, which has a side-branch leading off it (e.g. another corridor, or the entrance to a room), and the aim is to estimate the energy loss to the side branch. Davies' approach is to decompose the sound field in the corridor containing the source into a sum over modal plane waves, and, under the short wavelength assumption, the proportion of energy in each modal plane wave that is lost to the side branch is computed by a geometrical argument, diffraction effects being neglected. Summing over all the propagating modes, Davies obtains an estimate for the proportion of transmitted energy propagating into the side branch, as a function of the ratio of the widths of the two corridors. The estimate is easily generalised to other basic junction types such as crossroads and T-junctions.

Bullen and Fricke [15] have applied a similar approach to estimate the energy loss at a junction between intersecting streets in an urban environment, although they

consider only the simpler case where the energy in the sound field is concentrated in a single mode.

1.2.2 The forward problem in the time domain

The effect of diffuse scattering from building facades on the propagation of sound from non-time-harmonic, and especially impulsive, sources in the time domain has also been considered.

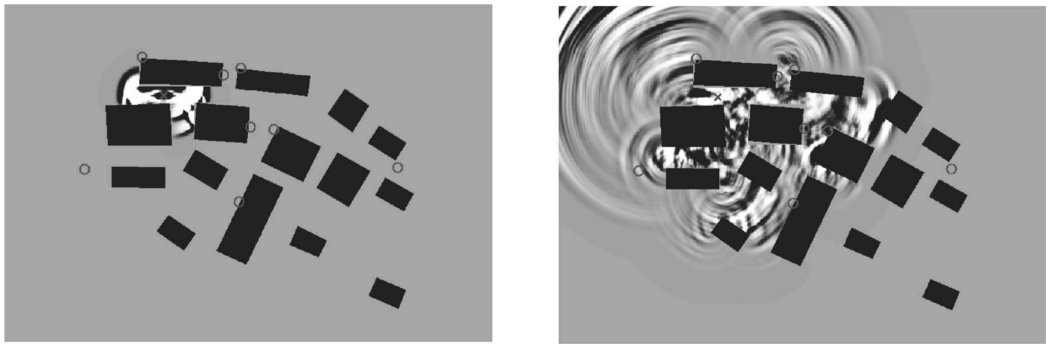
In [73] the acoustic energy density in a single street is assumed to satisfy a diffusion equation, with a diffusion parameter chosen according to the 'level of diffusivity' of the wall reflections. A justification for the diffusion model is presented in a subsequent publication [56], and is based on a statistical-mechanical treatment of the 'sound particle' model, in which small quanta of acoustic energy emitted from the source are assumed to propagate according to the laws of classical particle dynamics. The Lambert law of diffuse reflection is assumed, in which the probability density function for the direction of the reflected particle is proportional to the cosine of the reflection angle, independent of the angle of incidence, although other, more realistic, reflection laws can also be considered (see e.g. [72]).

In [72] numerical experiments based on the sound particle transport theory model in an idealised distribution of buildings (a periodic array of hexagonal buildings) suggest that a diffusion approximation may also be appropriate in the multiple-building case, although experimental validation of this in a real urban environment has not yet been carried out.

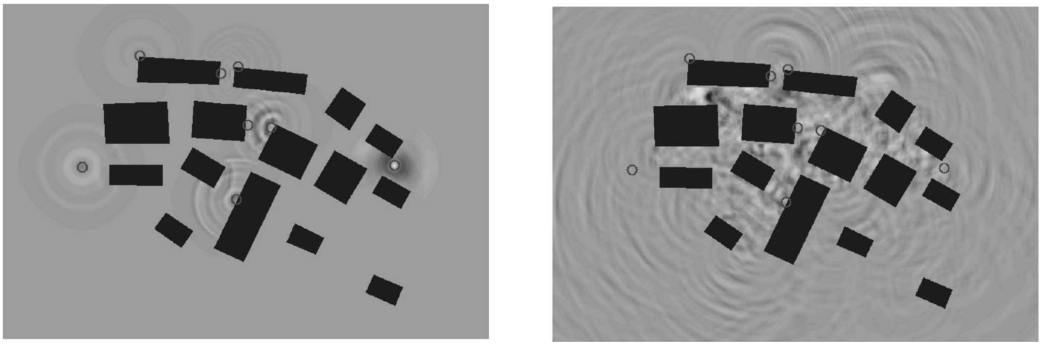
We remark that diffuse reflection laws such as the Lambert law have been implemented in other ways, for example, in the numerical 'radiosity' model developed by Kang [46]. Here the walls of the street are divided into patches, each associated with a 'secondary source', which re-radiates the energy incident on that patch back into the domain according to the Lambert law.

1.2.3 The inverse problem in the time domain

One approach to the inverse problem for an impulsive source is that of time-reversal processing. In [4] Albert, Liu and Moran have applied this technique in a small 2D model of an urban environment comprising fifteen irregularly-positioned buildings.



(a) Forward propagation



(b) Time-reversed propagation

Figure 1.1: Example of the numerical time-reversal method for a two-dimensional urban environment. In (a) a FDTD method is used to solve the forward problem of sound propagation from a source located between the two buildings in the top left corner of the environment. In (b) the time series recorded at the 8 receivers (marked with circles) are retransmitted back into the domain in reverse, using the same FDTD method. The energy is clearly seen to reconverge at the original source location. Plots reprinted with permission from [4]. Copyright 2005, Acoustical Society of America.

The method, which relies on the time-symmetry properties of the wave equation, involves time-reversing the signals received at each of the receiver locations and retransmitting them back into a model of the environment using a numerical finite-difference time domain (FDTD) method. Provided enough receivers are used and they are appropriately positioned (eight receivers were seen to suffice for the particular urban environment under consideration), the acoustic energy is seen to 'reconverge' at the original source location (see Figure 1.1). Encouragingly, it has been shown numerically that the method is stable to small perturbations in the position of the scatterers [59], and as a result, should remain accurate even if the details of the environment are known only approximately. However, the time-reversal method is, at present, very computationally intensive, and the calculation time would need to be decreased by at

least 3 orders of magnitude before it became a feasible technique for real-time source localisation in a 3D urban environment [4].

The approach we adopt in this thesis is that of Time Difference Of Arrival (TDOA) localisation. Rudimentary TDOA methods have been used in military applications for almost a century (see e.g. [41, 42]), and the now-classical free space TDOA method (see e.g. [32, 57]) is widely employed in a number of more recent non-military applications, for example in the context of radio wave propagation in Global Positioning Systems (GPS) and mobile telephone handset localisation (see e.g. [8, 16]). In urban environments, however, the free space method can, in principle, only be applied if there exists a direct line-of-sight (LOS) between the source and each receiver, which will not generally be the case. In spite of this, the method seems to be the basis of a number of commercially-available gunshot-detection systems (see e.g. [1, 78]), although full details of the algorithms used and the observed urban performance are unavailable in the academic literature.

1.3 Structure of the thesis

In Chapter 2 we describe the model of sound propagation that is to be used in this thesis. We briefly review the derivation of the governing equations of linear acoustics, and discuss the insertion of a source term in the wave equation. Our approach in modelling the physical domain is to simplify the microscale features as much as possible, in order to allow a study of the macroscale propagation in domains containing multiple buildings. In particular, we neglect the effect of scattering from inhomogeneities in building facades and assume simple specular reflection (although we will sometimes allow for absorption).

In Chapter 3 we study the frequency domain forward problem, considering in particular the short wavelength regime where the wavelength of the sound is small compared to typical lengthscales of the domain such as street lengths and widths. Our aim is to study the propagation of sound from a point source through a network of interconnecting streets.

We begin this lengthy chapter by reviewing the standard ray approximation and its generalisation to domains involving obstacles using Keller's Geometrical Theory of Diffraction (GTD). We then illustrate the general theory by means of a number of specific domains in which an exact solution of the Helmholtz equation is available.

In the case of a point source in a single 2D street, two equivalent representations of the exact solution are presented, namely a modal summation and an image source representation. The ray approximation is seen to arise naturally from the image source representation.

In principle, GTD can be used to approximate the acoustic pressure in a network of interconnecting streets. However, the highly-oscillatory nature of the pressure field in the short wavelength regime makes its fine details particularly sensitive to perturbations of the domain geometry. Since we wish to consider the case where the geometry is known only approximately, a detailed microscale description of the pressure field in a single realisation of the domain is of little practical relevance. A more robust measure of the strength of the sound field can be obtained by studying the way that the acoustic energy emitted from the source propagates around the domain on the macroscale. Specifically, our strategy is to study the acoustic power flows through the network. For simplicity we initially restrict our attention to 2D geometries.

We first consider the case of a single street. Following the approach taken in [91], the energy contributions along rays are summed incoherently, using an absorption coefficient at the walls. We derive asymptotic approximations to the power flow far from the source which exhibit different qualitative behaviour depending on the size of the absorption coefficient. Since most building materials are relatively good reflectors of sound energy, we focus especially on the small absorption regime, in which the power flow far from the source can be approximated by the integral of a 'power density' over the ray launch angle.

We then consider the case where the street containing the source intersects another street at right angles, and derive similar integral approximations to the power flows out of the exits of the junction, under the assumptions that the source is far from the junction, and that diffraction effects can be neglected. These integral approximations generalise the formulae obtained by Davies [26], who considered only the zero absorption case. The form of the integral approximations suggests a natural generalisation to the calculation of power flows along pathways involving multiple junctions, which has not been previously considered, and on the basis of the results of numerical experiments we claim that the resulting approximations are valid provided that we regard them as expected power flows after averaging over a range of street lengths.

In an infinite network of streets, the total net power flow across a street cross-section can then be computed by summing the power flows along each of the infinitely many propagation pathways between the source and cross-section in question. To avoid having to evaluate this rather formidable summation explicitly, we show how the problem may be reformulated as a system of coupled partial difference equations for the power densities flowing out of the exits of each junction in the network. In a special case we derive an exact solution to this system, which exhibits interesting anisotropic decay with increasing distance from the source.

To end Chapter 3, we discuss how the results obtained in the 2D case might be generalised to a 3D urban environment. The main ways in which the 3D case differs from the 2D case are the higher rate of geometrical spreading, the presence of a ground reflection, and the fact that energy emitted from the source can escape to the atmosphere.

In Chapter 4 we generalise our discussion to the propagation of sound waves with arbitrary time dependence. Even through this generalisation is, in principle, trivial via superposition of frequency domain solutions, it is much easier to give a direct treatment of the propagation of singularities in the wave field, another situation in which the theory of geometrical acoustics applies. We review the standard theory of characteristics, and illustrate it by means of a number of specific examples in which an exact 'pulsed' solution of the wave equation is available. We pay particular attention to diffraction by edges and vertices, a key scattering mechanism in urban environments, and we state and prove a general principle which governs the weakening of singularities when they are diffracted. Via the Fourier transform, this principle is explicitly related to the successive reduction in amplitude of multiply-diffracted time-harmonic waves predicted by GTD.

In section 4.5 we consider the problem of switching on a time-harmonic source, thereby unifying the time domain and frequency domain theories. Specifically, we consider three examples: a point source in an infinite domain in 3D, a point source in an infinite domain in 2D, and the diffraction of a 2D plane wave by a rigid half-line. In each case we derive an exact solution to the time domain problem, and determine the conditions under which this solution is well-approximated by the solution of the corresponding frequency domain problem. We remark that although the case of smooth scatterers and source distributions in 3D has been considered previously (see e.g. [13, 65, 66]), the switched-on edge diffraction problem does not seem to have been studied before.

We end Chapter 4 by commenting on some experimental data collected by Dstl during an investigation into the propagation of sound pulses arising from gunshots. Using a simple Gaussian point source model derived from the exact solutions already presented, we are able to replicate qualitatively a number of features of the data.

In Chapter 5 we study the inverse problem for an impulsive source using the method of TDOA localisation. We begin by reviewing the exact solution of the TDOA problem in 2D and 3D free space, and in both cases determine the minimum number of receivers needed to ensure a unique solution. In practical applications there may be errors in the measurement of pulse arrival times and receiver locations, which, in general, make the TDOA equations inconsistent. We show how, in this case, an estimate of the source location can be obtained by solving the TDOA equations in a least-squares sense.

In urban environments the presence of buildings and other obstacles means that a single pulse emitted at the source may give rise to a series of pulse arrivals at a receiver, corresponding to multiple reflections and diffractions, as discussed in Chapter 4. In principle, the free space TDOA method can still be applied provided there exists a LOS between the source and each receiver, simply by considering only the *first* arrival at each receiver (which must have travelled along this LOS). In fact, in certain domains the arrival times of the subsequent reflected pulses can actually be used to reduce the number of physical receivers needed, and in section 5.3 we present three specific examples of this.

In section 5.4 we consider the more general case in which we cannot assume the existence of a LOS between the source and each receiver. In this case, a naïve application of the free space method (solved in the least-squares sense) may produce erroneous results, especially if the streets are narrow. To deal with this situation we propose an alternative TDOA method which explicitly takes into account the non-line-of-sight (NLOS) propagation by using the arrival times of diffracted pulses. For simplicity, we initially restrict our attention to 2D geometries, illustrating the method using numerical simulations. We also discuss the case where the exact dimensions and positions of buildings are unknown, and show that in certain cases it is still possible to localise the source with reasonable accuracy, using only limited information about the geometry. Finally, we show that our new TDOA method can also be applied in the 3D case provided that the buildings are sufficiently tall.

1.4 Statement of originality

In Chapter 3 the justification of the incoherent summation assumption for the power flow in a single street in section 3.5 is original. The derivation of approximate acoustic power flows out of a single junction using the image source method in section 3.6 is also new, and extends the result of Davies [26] to the case of non-zero wall absorption. The generalisation to multiple junctions and networks of streets in sections 3.7 and 3.8 is entirely original, as is the generalisation to the 3D case in section 3.9.

In Chapter 4 the results of section 4.5 concerning the switching on of time-harmonic sources are original.

In Chapter 5 the generalisation of the TDOA method to domains involving obstacles in sections 5.3 and 5.4 is also original work.

Chapter 2

Modelling

In this chapter we describe the model of sound propagation that is to be used in this thesis. In section 2.1 we briefly review the derivation of the governing equations of linear acoustics from the equations of nonlinear gas dynamics. In section 2.2 we discuss the insertion of a source term in the wave equation. In section 2.3 we recall how time-harmonic sound propagation is governed by the Helmholtz equation in the frequency domain, and in section 2.4 we describe how the physical domain is to be represented.

2.1 Equations of motion

In an non-heat-conducting inviscid compressible fluid with no sources, the velocity $\mathbf{u}$, pressure p, density ρ and temperature T satisfy the equations of conservation of mass

$$\frac{D\rho}{Dt} + \rho \boldsymbol{\nabla} \cdot \mathbf{u} = 0, \tag{2.1}$$

momentum

$$\rho \frac{D\mathbf{u}}{Dt} + \boldsymbol{\nabla} p = \mathbf{0}, \tag{2.2}$$

and energy

$$\rho \mathbf{u} \cdot \frac{D\mathbf{u}}{Dt} + \rho c_v \frac{DT}{Dt} = -\boldsymbol{\nabla} \cdot (p\mathbf{u}). \tag{2.3}$$

Here $\frac{D}{Dt} = \frac{\partial}{\partial t} + \mathbf{u} \cdot \boldsymbol{\nabla}$ is the convective derivative and c_v is the specific heat at constant volume ([70], Chapter 2). Gravitational effects have been omitted since they are negligible for all sound waves in the audible frequency range (see [58], p. 10

or [10], p. 41). The five equations (2.1), (2.2) and (2.3) are supplemented by the equation of state for an ideal gas

$$p = \rho R T, \tag{2.4}$$

where $R = R_u/M$, R_u being the universal gas constant and M the mean molecular weight. This gives a closed system for the six unknowns $\mathbf{u}$, p, ρ and T.

Using (2.4), the energy equation (2.3) can be rewritten as

$$\rho \mathbf{u} \cdot \frac{D\mathbf{u}}{Dt} + \frac{\rho}{\gamma - 1} \frac{D}{Dt}\left(\frac{p}{\rho}\right) = -\boldsymbol{\nabla} \cdot (p\mathbf{u}), \tag{2.5}$$

where $\gamma = 1 + \frac{R}{c_v}$. Use of (2.2) allows further simplification of (2.5) to

$$\frac{DS}{Dt} = 0, \tag{2.6}$$

where the *entropy* $S = S_0 + c_v \log \frac{p}{\rho^\gamma}$, with S_0 a constant. Assuming that the entropy is initially uniform, which will be true, for example, if the medium was initially at rest, then equation (2.6) implies that it remains so for all subsequent time, and the flow is *homentropic*. Integration of (2.6) then gives the constitutive law

$$p = C\rho^\gamma, \tag{2.7}$$

for some constant C.

2.1.1 The acoustic approximation

The acoustic approximation is obtained by linearising equations (2.1), (2.2) and (2.7) under the assumption that the velocity, pressure and density fields can be expressed as small perturbations to a uniform background rest state, i.e.

$$\mathbf{u} = \mathbf{0} + \mathbf{u}', \quad p = p_0 + p', \quad \rho = \rho_0 + \rho', \tag{2.8}$$

where p_0 and ρ_0 are constant, and $\mathbf{u}'$, p' and ρ' are assumed to be small, relative to c_0 (to be defined shortly), p_0 and ρ_0, respectively. The resulting linearised equations are[1]

$$\frac{\partial \rho'}{\partial t} + \rho_0 \boldsymbol{\nabla} \cdot \mathbf{u}' = 0, \tag{2.9}$$

$$\rho_0 \frac{\partial \mathbf{u}'}{\partial t} + \boldsymbol{\nabla} p' = \mathbf{0}, \tag{2.10}$$

$$p' = c_0^2 \rho', \tag{2.11}$$

[1]Although this *ad hoc* approach is completely standard in the acoustics literature, we should, strictly speaking, nondimensionalise appropriately before performing any asymptotic analysis. For a more rigorous derivation see [70], Section 3.1.

where

$$c_0 = \sqrt{\frac{\gamma p_0}{\rho_0}} \tag{2.12}$$

represents the *speed of sound* in the fluid.

Taking the curl of (2.10) reveals that the vorticity $\boldsymbol{\nabla} \wedge \mathbf{u}'$ is conserved in the acoustic approximation. Assuming that the flow is initially irrotational, which will be true, for example, if the medium was originally at rest, it remains so for all subsequent time, and there exists a velocity potential Φ satisfying $\mathbf{u}' = \boldsymbol{\nabla}\Phi$. Equation (2.9) becomes

$$\frac{\partial \rho'}{\partial t} + \rho_0 \nabla^2 \Phi = 0, \tag{2.13}$$

and integration of equation (2.10) leads to the linearised Bernoulli equation

$$\rho_0 \frac{\partial \Phi}{\partial t} + p' = 0, \tag{2.14}$$

after the introduction of an appropriate function of t into the definition of Φ. Eliminating p' and ρ' between (2.13), (2.14) and (2.11), we find that the velocity potential must satisfy the *wave equation*

$$\frac{\partial^2 \Phi}{\partial t^2} - c_0^2 \nabla^2 \Phi = 0. \tag{2.15}$$

2.2 Modelling a source

In the presence of a distribution of acoustic sources we propose to modify equation (2.15) to

$$\frac{\partial^2 \Phi}{\partial t^2} - c_0^2 \nabla^2 \Phi = s, \tag{2.16}$$

for some source function $s = s(\mathbf{x}, t)$, the form of which will depend on nature of the sources in question.

We remark that (2.16) is a rather general model for an acoustic source, since it can represent the effect of a mass, momentum or energy source. Indeed, suppose we modify the original nonlinear governing equations (2.1) - (2.3) to read

$$\frac{D\rho}{Dt} + \rho \boldsymbol{\nabla} \cdot \mathbf{u} = s_{\text{mass}}, \tag{2.17}$$

$$\rho \frac{D\mathbf{u}}{Dt} + \boldsymbol{\nabla} p = \mathbf{s}_{\text{mom}}, \tag{2.18}$$

$$\rho \mathbf{u} \cdot \frac{D\mathbf{u}}{Dt} + \rho c_v \frac{DT}{Dt} + \boldsymbol{\nabla} \cdot (p\mathbf{u}) = s_{\text{energy}}, \tag{2.19}$$

where s_{mass}, $\mathbf{s}_{\text{mom}}$ and s_{energy} represent mass, momentum and energy sources, respectively. Then, linearising (2.17) - (2.19) with respect to the perturbations (2.8), and with

$$s_{\text{mass}} = s'_{\text{mass}}, \qquad \mathbf{s}_{\text{mom}} = \mathbf{s}'_{\text{mom}}, \qquad s_{\text{energy}} = s'_{\text{energy}}, \tag{2.20}$$

also small, gives

$$\frac{\partial \rho'}{\partial t} + \rho_0 \boldsymbol{\nabla} \cdot \mathbf{u}' = s'_{\text{mass}}, \tag{2.21}$$

$$\rho_0 \frac{\partial \mathbf{u}'}{\partial t} + \boldsymbol{\nabla} p' = \mathbf{s}'_{\text{mom}}, \tag{2.22}$$

$$\frac{1}{\gamma - 1}\left(\frac{\partial p'}{\partial t} - \frac{p_0}{\rho_0}\frac{\partial \rho'}{\partial t}\right) + p_0 \boldsymbol{\nabla} \cdot \mathbf{u}' = s'_{\text{energy}}. \tag{2.23}$$

When the momentum source term is irrotational, so that it can be written in the form $\mathbf{s}'_{\text{mom}} = \boldsymbol{\nabla} s'_{\text{mom}}$, a velocity potential Φ can be introduced as before, and we obtain the system

$$\frac{\partial \rho'}{\partial t} + \rho_0 \nabla^2 \Phi = s'_{\text{mass}}, \tag{2.24}$$

$$\rho_0 \frac{\partial \Phi}{\partial t} + p' = s'_{\text{mom}}, \tag{2.25}$$

$$\frac{1}{\gamma - 1}\left(\frac{\partial p'}{\partial t} - \frac{p_0}{\rho_0}\frac{\partial \rho'}{\partial t}\right) + p_0 \nabla^2 \Phi = s'_{\text{energy}}. \tag{2.26}$$

Elimination of p' and ρ' between (2.24)-(2.26) then returns (2.16) with the source function s given by

$$s = \frac{1}{\rho_0}\frac{\partial s'_{\text{mom}}}{\partial t} - \frac{\gamma - 1}{\rho_0} s'_{\text{energy}} - \frac{p_0}{\rho_0^2} s'_{\text{mass}}. \tag{2.27}$$

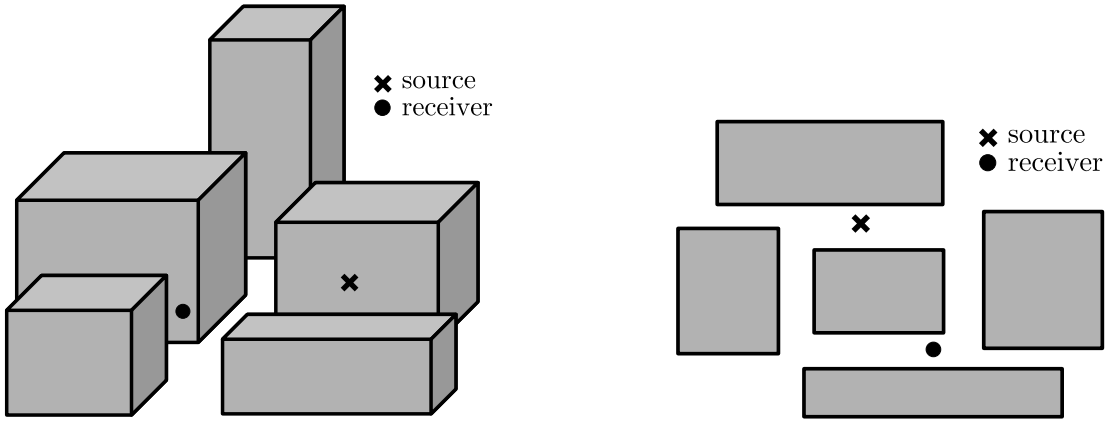
For the majority of this thesis we will assume a point source, with

$$s(\mathbf{x}, t) = \delta(\mathbf{x} - \mathbf{x}_0) g(t), \tag{2.28}$$

for some function $g(t)$.

2.3 Time-harmonic sources

In Chapter 3 we consider the special case where the sound field has harmonic time dependence. In the case of a point source this corresponds to assuming that the



(a) 3D model (b) 2D model

Figure 2.1: 3D and 2D models of an urban environment.

function $g(t)$ in (2.28) has the particular form $g(t) = \mathrm{Re}[Ae^{-i\omega t}]$, where the amplitude A is complex-valued and the frequency ω is real-valued. Substituting the ansatz $\Phi(\mathbf{x}, t) = \mathrm{Re}[-\phi(\mathbf{x})e^{-i\omega t}]$ in (2.16) allows us to suppress the time dependence and study the problem in the so-called *frequency domain*, with $\phi(\mathbf{x})$ satisfying the Helmholtz equation with a point source

$$(\nabla^2 + k^2)\phi(\mathbf{x}) = \frac{A}{c_0^2}\delta(\mathbf{x} - \mathbf{x}_0), \tag{2.29}$$

where the (dimensional) wavenumber $k = \omega/c_0$.

2.4 Boundary conditions

We now describe the domain on which the governing equation (2.16) is to be solved. As was indicated in the Introduction, in order to facilitate study of the global problem we propose to simplify the local model as much as possible. Accordingly, we neglect the scattering effect of surface inhomogeneities and model buildings as homogeneous blocks on a flat plane, representing the ground, as illustrated in Figure 2.1(a). We also consider the analogous problem in 2D, where buildings are represented by polygons rather than polyhedra (see Figure 2.1(b)). Although this 2D model is not directly representative of any real urban environment, the simplification will allow us to develop methods which can then be extended to more realistic 3D geometries.

The rigid boundary condition

$$\frac{\partial \Phi}{\partial \mathbf{n}}(\mathbf{x}) = 0 \tag{2.30}$$

is assumed on the walls, roofs and ground (where applicable), where $\mathbf{n}$ is the outward unit normal vector. The assumption of the boundary condition (2.30) is a reasonable first approximation given that most building materials are very good reflectors of sound energy ([25], p. 708). In reality, however, a small amount of energy will be absorbed at each reflection, and in the frequency domain analysis of Chapter 3 we sometimes adopt a simple absorption coefficient model to take this into account. We postpone further discussion of this model until section 3.4.

In this idealised model, building walls and roofs meet in sharp edges and vertices, and it is well known that these boundary singularities can give rise to issues of nonuniqueness (see e.g. [45], Chapter 9, p. 525 and [34], Chapter 5, p. 110). The physically relevant solution will be that which has the weakest possible singularity at the edge or vertex; this is Van Dyke's principal of minimum singularity[2] (see [88], p. 53), and we assume, without proof, that all of the exact solutions used in this thesis satisfy this principle.

In the frequency domain case, the boundary and edge/vertex conditions must be supplemented by a *radiation condition*, which ensures that the wave field is *outgoing* at infinity. For example, in two dimensional free space the appropriate condition on ϕ is ([82], p. 193)

$$\lim_{r\to\infty} r^{1/2}\left(\frac{\partial\phi}{\partial r} - ik\phi\right) = 0, \tag{2.31}$$

where $r = \sqrt{(x-x_0)^2 + (y-y_0)^2}$. The analogous condition in the three-dimensional case is ([82], p. 189)

$$\lim_{r\to\infty} r\left(\frac{\partial\phi}{\partial r} - ik\phi\right) = 0, \tag{2.32}$$

where $r = \sqrt{(x-x_0)^2 + (y-y_0)^2 + (z-z_0)^2}$.

In a time domain problem for which the source function s vanishes for sufficiently large negative time, the radiation condition is replaced by the assumption that the medium is initially at rest everywhere and at uniform pressure.

[2]Van Dyke's principle is also sometimes referred to as Meixner's principle of absence of sources, or of finiteness of energy - see e.g. [63].

Chapter 3

Frequency domain analysis

3.1 Introduction

In this chapter we study the frequency domain forward problem of the propagation of time-harmonic sound waves through a network of interconnecting streets. In particular we consider the short wavelength regime where the wavelength of the sound is small compared to typical lengthscales of the domain such as street lengths and widths. We restrict our attention almost exclusively to the 2D case, until section 3.9.

In section 3.2 we briefly review the standard ray theory approximation and its generalisation to domains involving obstacles using Keller's Geometrical Theory of Diffraction. In section 3.3 we illustrate this general theory by means of a number of specific domains in which an exact solution of the Helmholtz equation is available. In each case the ray approximation is shown to arise from an asymptotic approximation of the exact solution in the short wavelength regime. In the case of a single 2D street, two equivalent representations of the exact solution are presented, namely a modal decomposition and an image source decomposition. The ray approximation is seen to arise naturally from the image source decomposition.

In section 3.4 we introduce the concept of acoustic energy, intensity and power. Our strategy is to compute acoustic intensities in an urban environment by summing the intensity contributions along rays 'incoherently', i.e. neglecting the effect of interference between ray fields. Two justifications for this approach are given. First, we argue that since the geometry is known only to a certain degree of accuracy, it is reasonable to assume that the phases of the ray fields at any point are independent random variables, so that the expected contribution of the interference effects to the

intensity is zero. Second, we note that even in the fully deterministic case, it is sometimes possible to justify the neglect of interference provided that we perform some sort of spatial averaging over receiver locations. This assertion will be verified in the case of a single 2D street, with the averaging region taken to be a street cross-section (so that we study the power flow down the street). The ray-based model is then extended to account for absorption coefficients that model the effect of energy absorption at the street walls, and, in the case of small absorption, the modified power flow far from the source is shown to be approximated by an integral over a ray-angle-resolved power density.

In section 3.6 the ray model is used to study the power flows out of the exits of a crossroads. In section 3.7 we propose a natural generalisation to domains involving multiple junctions, which we claim is valid provided that the resulting approximations are regarded as power flows averaged over a range of street lengths. In section 3.8 we use these methods to estimate the averaged power flows through a network of 2D streets, and find that the power flows decay exponentially in the number of junctions between source and receiver, except along certain special pathways through the network, along which the decay is algebraic.

In section 3.9 we discuss how the results might be generalised to the 3D case.

3.2 Geometrical acoustics in the frequency domain

In the short wavelength regime, an approximate solution of the Helmholtz equation (2.29) can be obtained by the method of geometrical acoustics, in which the field is represented as a sum of contributions from the geometrical *rays* that exist between source and receiver.

3.2.1 Geometrical acoustics in free space

We first consider the case of propagation in free space. We begin by nondimensionalising (2.29) under the scalings

$$\mathbf{x} = L\hat{\mathbf{x}}, \qquad \phi = \phi_0 \hat{\phi}, \tag{3.1}$$

where L is a characteristic lengthscale over which the waves propagate, $\phi_0 = \frac{A}{c_0^2 L^j}$ and $j = 2, 3$ is the dimension of space. We obtain (after dropping hats)

$$(\nabla^2 + k^2)\phi(\mathbf{x}) = \delta(\mathbf{x} - \mathbf{x}_0), \tag{3.2}$$

where the nondimensional wavenumber $k = \omega L/c_0$. Under the assumption that $k \gg 1$ we make the WKB ansatz (see e.g. [39]) for the field away from the source:

$$\phi(\mathbf{x}) \sim \sum_{n=0}^{\infty} A_n(\mathbf{x})(ik)^{-n} e^{ikU(\mathbf{x})}. \tag{3.3}$$

We then substitute (3.3) in (3.2) and compare powers of k in the resulting expression. The leading order equation reveals that the phase function U must satisfy the eikonal equation

$$|\boldsymbol{\nabla} U|^2 = 1, \tag{3.4}$$

and consideration of the higher order equations reveals that the amplitude functions A_n must satisfy the transport equations

$$2\boldsymbol{\nabla} A_0 \cdot \boldsymbol{\nabla} U + A_0 \nabla^2 U = 0, \tag{3.5}$$

$$2\boldsymbol{\nabla} A_j \cdot \boldsymbol{\nabla} U + A_j \nabla^2 U = -\nabla^2 A_{j-1}, \qquad j > 0. \tag{3.6}$$

The eikonal equation (3.4) is a scalar, first-order, nonlinear PDE, and can be solved using Charpit's method (see [71], p. 360). For ease of presentation we consider the 2D case, but the argument is easily generalised to higher dimensions. Application of the method leads to the equations

$$\frac{dx}{d\tau} = p, \tag{3.7}$$

$$\frac{dy}{d\tau} = q, \tag{3.8}$$

$$\frac{dp}{d\tau} = 0, \tag{3.9}$$

$$\frac{dq}{d\tau} = 0, \tag{3.10}$$

$$\frac{dU}{d\tau} = 1, \tag{3.11}$$

where $(p, q) = \boldsymbol{\nabla} U$, and the parameter τ represents distance along a characteristic. The projections of the characteristics onto physical space are called *rays*, and the curves normal to the rays (i.e. the level curves of U) are called *wavefronts*. We immediately see from (3.7)-(3.10) that the rays are simply straight lines[1]. To solve

[1]This would not be the case if the medium were inhomogeneous.

(3.7)-(3.11) for initial data $U_0(s)$ defined on a curve $(x_0(s), y_0(s))$, we must first determine the value of (p, q) on the curve from the equations

$$p_0(s)^2 + q_0(s)^2 = 1, \tag{3.12}$$

$$\frac{dU_0}{ds} = p_0(s)\frac{dx_0}{ds} q_0(s)\frac{dy_0}{ds}, \tag{3.13}$$

which, in general, provide two possible solutions for (p_0, q_0). For each of these we then obtain the solution

$$x(s, \tau) = p_0(s)\tau + x_0(s), \tag{3.14}$$

$$y(s, \tau) = q_0(s)\tau + y_0(s), \tag{3.15}$$

$$u(s, \tau) = u_0(s) + \tau. \tag{3.16}$$

Having determined the structure of the ray field, we now consider the variation of the leading order amplitude A_0 along each ray. We first note that since $\boldsymbol{\nabla} U = \left(\frac{dx}{d\tau}, \frac{dy}{d\tau}\right)$, we have

$$\boldsymbol{\nabla} A_0 \cdot \boldsymbol{\nabla} U = \frac{dA_0}{d\tau}, \tag{3.17}$$

along a ray. Second, we note that

$$\nabla^2 U = \frac{dp_0}{ds}\frac{\partial s}{\partial x} + \frac{dq_0}{ds}\frac{\partial s}{\partial y}. \tag{3.18}$$

Also, using (3.7)-(3.11), (3.4) and (3.18), it can be shown that the Jacobian determinant

$$J := \left|\frac{\partial(x, y)}{\partial(s, \tau)}\right| \tag{3.19}$$

satisfies

$$\frac{\partial J}{\partial \tau} = \frac{dp_0}{ds}\frac{\partial y}{\partial \tau} - \frac{dq_0}{ds}\frac{\partial x}{\partial \tau} = J\nabla^2 U. \tag{3.20}$$

The transport equation (3.5) then becomes an ODE along the ray, namely

$$2\frac{dA_0}{d\tau} + \frac{1}{J}\frac{dJ}{d\tau}A_0 = 0, \tag{3.21}$$

and integration of (3.21) gives

$$A_0^2(s, \tau) = A_0^2(s, 0)\frac{J(s, 0)}{J(s, \tau)}. \tag{3.22}$$

As we shall see in section 3.4.2, the quantity A_0^2 (or more precisely, $|A_0^2|$) is directly proportional to the time-averaged energy density associated with the propagation. Equation (3.22) implies that this energy density is conserved in ray tubes, which is the *intensity law of geometrical acoustics*. One consequence of (3.22) is that if $J \to 0$ (for example, at a caustic, where neighbouring rays intersect), then the amplitude A_0 becomes infinite (see e.g. [71], p. 371). This is an indication that the WKB ansatz (3.3) is no longer valid, and a different high-frequency approximation must be made in such cases if the correct local behaviour is to be recovered. However, since we will not consider any problems involving caustics in this thesis, we do not pursue this matter here.

3.2.2 Geometrical Theory of Diffraction

In the presence of scattering obstacles the theory must be modified by the inclusion of new families of rays (e.g. reflected, diffracted). For example, a ray incident on a smooth portion of the obstacle boundary at non-grazing incidence gives rise to a reflected ray satisfying the familiar specular reflection law 'angle of incidence equals angle of reflection'. A ray incident on a sharp edge formed where two smooth portions of the boundary meet gives rise to a family of diffracted rays emanating from the edge[2]. Outside the obstacle the resulting ray approximation is no longer of the form (3.3), but rather takes the form of a sum of such expressions, with each term corresponding to a ray (incident, reflected or diffracted) between source and receiver. The correct values of the phase and amplitudes on the reflected or diffracted rays are found by reference to canonical problems for which exact explicit solutions sometimes exist. This is Keller's famous Geometrical Theory of Diffraction (GTD) (see [48]). In the next section we consider some such solutions and determine their respective ray approximations.

[2]We remark that rays incident on smooth scatterers at grazing incidence can give rise to more complicated diffraction phenomena (see e.g. [30, 85]), but in this thesis we consider only diffraction at sharp edges and vertices.

3.3 Review of exact solutions

3.3.1 A point source in 2D free space

The solution of (3.2) in 2D free space satisfying the radiation condition (2.31) is (see e.g. [71], p. 181)

$$\phi(\mathbf{x}) = -\frac{i}{4}H_0^{(1)}(kr), \tag{3.23}$$

where $H_0^{(1)}(z) := J_0(z) + iY_0(z)$ is the zero-order Hankel function of the first kind and $r = \sqrt{(x-x_0)^2 + (y-y_0)^2}$. The ray expansion is found by considering the asymptotic behaviour of (3.23) for $k \gg 1$, namely (see e.g. [2], formula (9.2.7)):

$$\phi \sim -\frac{i}{4}\sqrt{\frac{2}{\pi kr}}\left(1 - \frac{i}{8kr} + ...\right)e^{i(kr-\frac{\pi}{4})}, \tag{3.24}$$

which is clearly of the form (3.3). The expansion (3.24) is valid for $r \gg 1/k$ (the choice of characteristic lengthscale L is arbitrary in this case). The wavefronts in this case are concentric circles centered on the source and the rays are radial lines emanating from the source.

3.3.2 A point source in 3D free space

In 3D free space the solution of (3.2) satisfying the radiation condition (2.32) is

$$\phi(\mathbf{x}) = -\frac{e^{ikr}}{4\pi r}, \tag{3.25}$$

where $r = \sqrt{(x-x_0)^2 + (y-y_0)^2 + (z-z_0)^2}$. Since (3.25) is already of the form (3.3), the ray approximation is exact in this case.

3.3.3 Reflection by a half-plane

We now consider the half-plane $y > 0$ with the rigid boundary condition (2.30) applied on $y = 0$. The solution to (3.2) in this domain can be found by the method of images. We extend the propagation domain to the whole of the plane and insert an image source, identical to the original source, at the point $(x, -y_0)$. Summing the free space fields due to the original and image sources provides a solution of the Helmholtz

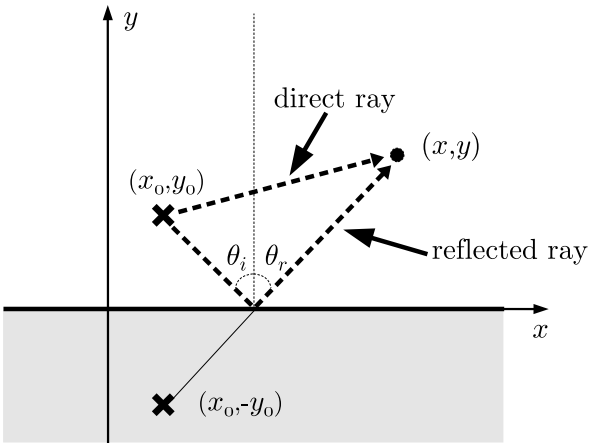


Figure 3.1: Specular reflection law $\theta_r = \theta_i$ in the case of a 2D half-plane

equation which exactly satisfies the boundary condition and is outgoing at infinity, namely

$$\phi(\mathbf{x}) = -\frac{i}{4}\left(H_0^{(1)}(kr) + H_0^{(1)}(kr')\right), \tag{3.26}$$

where $r' = \sqrt{(x-x_0)^2 + (y+y_0)^2}$. The ray approximation of (3.26) is the sum of two ray expansions of the form (3.24). The first is associated with the direct ray from source to receiver, the second with a reflected ray, which satisfies the specular reflection law (see Figure 3.1 for an illustration). The limiting values of the phase and amplitude on the reflected ray as the boundary is approached are equal to those on the incident ray which gives rise to the reflected ray.

3.3.4 A point source in a single 2D street

We now consider the case of a 2D street bounded by infinite parallel rigid walls. As our characteristic lengthscale L we choose the street width, so that without loss of generality the street is parallel to the x-axis and bounded by rigid walls at $y = 0$ and $y = 1$, with the source located at the point $(0, y_0)$, where $0 < y_0 < 1$. This leads to the following problem for ϕ:

$$(\nabla^2 + k^2)\phi(x,y) = \delta(x)\delta(y-y_0), \qquad -\infty < x < \infty,\ 0 < y < 1, \tag{3.27}$$

$$\frac{\partial \phi}{\partial y}(x,y) = 0, \qquad y = 0, 1, \tag{3.28}$$

along with the requirement that ϕ should represent waves which propagate outward at $x = \pm\infty$. The exact solution of this problem can be conveniently represented in two distinct, yet equivalent, closed forms, which we now review.

3.3.4.1 Modal representation

One approach is to view the street as a *waveguide* and use the methods of Fourier analysis to obtain the solution as a sum over waveguide modes[3]. These modes are the separable solutions of the homogeneous Helmholtz equation in $0 < y < 1$ satisfying the boundary condition (3.28), and must therefore be of the form $a(x)\cos m\pi y$, where m is an integer. We then seek a solution of the inhomogeneous equation (3.27) of the form

$$\phi(x,y) = \sum_{m=0}^{\infty} a_m(x)\cos m\pi y. \tag{3.29}$$

To determine the coefficient functions $a_m(x)$ we substitute the ansatz (3.29) into (3.27) (with the summation index in (3.29) replaced by n to avoid confusion). Multiplying both sides by $\cos m\pi y$ and integrating over $y \in (0,1)$, we obtain the following ordinary differential equation satisfied by the function $a_m(x)$

$$\frac{d^2a_m}{dx^2}(x) + (k^2 - (m\pi)^2)a_m(x) = \frac{\cos m\pi y_0}{\sigma_m}\,\delta(x), \qquad -\infty < x < \infty, \tag{3.30}$$

after use of the well-known orthogonality relations

$$\int_0^1 \cos m\pi y \cos n\pi y\, dy = \sigma_m \delta_{mn}, \tag{3.31}$$

where δ_{mn} is the standard Kronecker delta and

$$\sigma_m = \begin{cases} 1, & m = 0 \\ 1/2, & m > 0. \end{cases} \tag{3.32}$$

Assuming that $k \neq m\pi$ we can write the solution of (3.30) in the general form

$$a_m(x) = A_m e^{i\kappa_m x} + B_m e^{-i\kappa_m x}, \tag{3.33}$$

where

$$\kappa_m := \begin{cases} \sqrt{k^2 - (m\pi)^2}, & m^2 < k^2/\pi^2, \\ i\sqrt{(m\pi)^2 - k^2}, & m^2 > k^2/\pi^2 \end{cases} \tag{3.34}$$

(with the positive square root assumed), and A_m and B_m are constants. We note that when $m^2 < k^2/\pi^2$ the exponentials in (3.33) are oscillatory in x, and when $m^2 > k^2/\pi^2$ they are growing or decaying as $|x| \to \infty$. In order for ϕ to represent an outward-propagating wave, the constants A_m and B_m must take different values depending on whether $x > 0$ or $x < 0$. In $x > 0$ we require $B_m = 0$, so that in the case $m^2 < k^2/\pi^2$

[3]This section is based on [45], Section 5.8.

we obtain a wave which is outward-propagating at infinity, corresponding to a so-called *propagating mode*, and in the case $m^2 > k^2/\pi^2$ we obtain exponential decay at infinity rather than exponential growth, corresponding to a so-called *evanescent mode*. In $x < 0$ we must take $A_m = 0$, for the same reasons. Furthermore, to ensure that $a_m(x)$ is continuous across $x = 0$, we choose the value of A_m in $x > 0$ to be equal to the value of B_m in $x < 0$, so that

$$a_m(x) = C_m e^{i\kappa_m |x|}, \tag{3.35}$$

where C_m is a constant which takes the same value in both $x > 0$ and $x < 0$.

The resulting discontinuity in the derivative of (3.35) at $x = 0$ is precisely what will give rise to the delta function we require on the right-hand side of (3.30). The jump condition

$$\lim_{\varepsilon \to 0} \left[\frac{da_m}{dx} \right]_{x=-\varepsilon}^{x=\varepsilon} = \frac{\cos m\pi y_0}{\sigma_m} \tag{3.36}$$

determines the constant C_m as

$$C_m = -\frac{i}{2} \frac{\cos m\pi y_0}{\sigma_m \kappa_m}, \tag{3.37}$$

giving the solution of (3.27) - (3.28) as

$$\phi(x, y) = -\frac{i}{2} \sum_{m=0}^{\infty} \frac{\cos m\pi y_0}{\sigma_m \kappa_m} e^{i\kappa_m |x|} \cos m\pi y. \tag{3.38}$$

Two important remarks must be made about (3.38). First, we note that the ellipticity of the Helmholtz equation (3.27) means that the solution $\phi(x, y)$ must be analytic on $x = 0$, except at the source location $y = y_0$, something that is not at all obvious from the representation (3.38), since each of the terms in the sum is clearly *not* analytic on $x = 0$. We return to this issue in section 3.3.4.3.

Second, a glance at definition (3.34) reveals that the solution (3.38) blows up to infinity as the wavenumber k approaches $m\pi$ for any integer m with $\cos(m\pi y_0) \neq 0$. Integer values of $m = k/\pi$ correspond to resonant modal frequencies of the street width, and values with $\cos(m\pi y_0) \neq 0$ correspond to modes that are actually excited by the source. Near resonance, our assumption that the velocity, pressure and density fluctuations are small becomes invalid, and the linearised model (2.1)-(2.3) breaks down. In order to obtain a valid solution near resonance it is necessary either to work with the original nonlinear equations (2.1) and (2.2), or to introduce some damping into the linear model. However, for simplicity we shall assume that k is sufficiently far away from resonance for our undamped linear model to be valid.

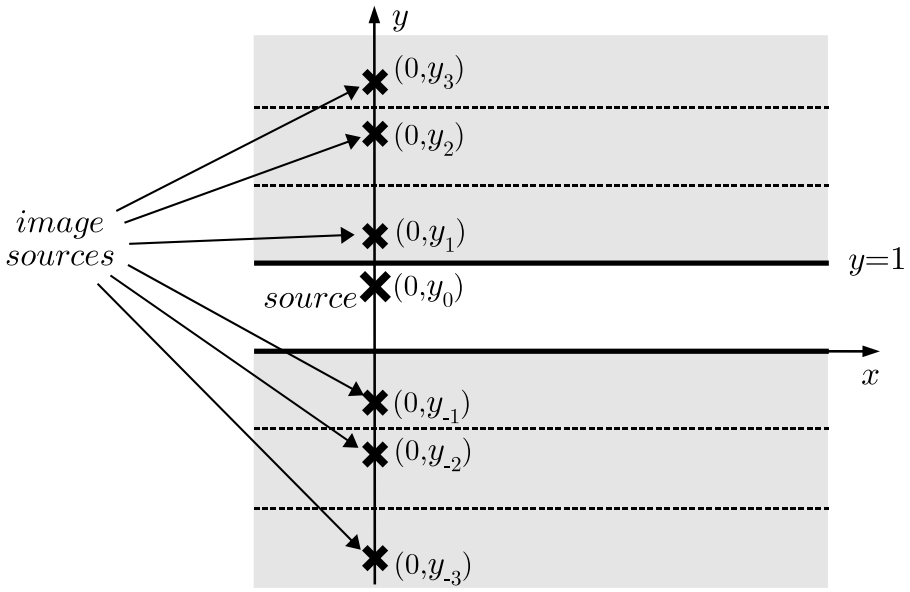


Figure 3.2: Image sources for a single 2D street

3.3.4.2 Image source representation

Another representation of the solution of (3.27) - (3.28) can be constructed by the method of images. We begin by introducing an infinite array of image sources at the points $(0, y_n)$, $n \in \mathbf{Z} \setminus \{0\}$, where, as illustrated in Figure 3.2,

$$y_n = \begin{cases} n + y_0, & n \text{ even}, \ n \neq 0, \\ n + (1 - y_0), & n \text{ odd}. \end{cases} \tag{3.39}$$

A formal solution of (3.27) which exactly satisfies the boundary conditions (3.28) can then be obtained by setting

$$\phi(x, y) = \sum_{n \in \mathbf{Z}} \phi_n(x, y), \tag{3.40}$$

where $\phi_n(x, y)$ is the free space velocity potential associated with each of the image sources. By formula (3.23) we have

$$\phi_n(x, y) = -\frac{i}{4} H_0^{(1)}(k\sqrt{x^2 + (y - y_n)^2}). \tag{3.41}$$

Note that (3.40) automatically represents an outward-propagating wave since each term in the summation is outward-propagating.

To determine the convergence properties of (3.40) we note that by (3.24) the asymptotic behaviour of the summand as $|n| \to \infty$, with x, y, y_0 fixed, is

$$H_0^{(1)}(k\sqrt{x^2+(y-y_n)^2}) \sim \begin{cases} (1-i)\sqrt{\frac{1}{k|n|\pi}}e^{ik(|n|+\mathrm{sgn}(n)(y_0-y)}, & n \text{ even}, \\ (1-i)\sqrt{\frac{1}{k|n|\pi}}e^{ik(|n|+\mathrm{sgn}(n)((1-y_0)-y)}, & n \text{ odd}. \end{cases} \tag{3.42}$$

Convergence of (3.40) is therefore governed by the behaviour of

$$e^{iky_0}\sum_{n=1}^{\infty}\frac{e^{2ikn}}{\sqrt{2n}} + e^{ik(1-y_0)}\sum_{n=1}^{\infty}\frac{e^{ik(2n+1)}}{\sqrt{2n+1}}, \tag{3.43}$$

which, in turn, relies on that of $\sum_{n=1}^{\infty}\frac{e^{2ikn}}{\sqrt{n}}$, and this is the sum we now study. To prove convergence of the partial sum

$$S_N := \sum_{n=1}^{N}\frac{e^{2ikn}}{\sqrt{n}}, \tag{3.44}$$

it is enough to show that S_N forms a Cauchy sequence. We will show by the method of partial summation that this holds provided $k \notin \pi\mathbf{N}$.

The partial summation technique (see e.g. [22], Section 2.43, p. 25) is the summation analogue of integration by parts, and is based on the fact that for any sum $\sum_{n=M+1}^{N} a_n b_n$ the partial summation $B_n = \sum_{r=M+1}^{n} b_r$ satisfies the formula

$$\sum_{n=M+1}^{N} a_n b_n = a_N B_N - \sum_{n=M+1}^{N-1}(a_{n+1}-a_n)B_n. \tag{3.45}$$

With (3.44) in mind we set $a_n = 1/\sqrt{n}$ and $b_n = e^{2ikn}$, and find that B_n can be computed in closed form using the summation formula for a geometric progression, with

$$B_n = \sum_{r=M+1}^{n} e^{2ikr} = \frac{e^{2ik(M+1)} - e^{2ik(n+1)}}{1-e^{2ik}}, \tag{3.46}$$

as long as $k \notin \pi\mathbf{N}$. Formula (3.46) provides the useful bound $|B_n| \leq \frac{2}{|1-e^{2ik}|}$, which holds for all $n \geq M+1$. Formula (3.45) then gives

$$\begin{aligned} |S_N - S_M| &= \left| a_N B_N - \sum_{n=M+1}^{N-1}(a_{n+1}-a_n)B_n \right| \\ &\leq |a_N||B_N| + \sum_{n=M+1}^{N-1}|a_{n+1}-a_n||B_n| \\ &\leq \frac{2}{|1-e^{2ik}|}\left(a_N + \sum_{n=M+1}^{N-1}(a_n - a_{n+1})\right), \end{aligned} \tag{3.47}$$

since the a_n form a positive, monotonically decreasing sequence. The sum in the final line of (3.47) is telescoping, so that

$$\begin{aligned} |S_N - S_M| &\leq \frac{2}{|1 - e^{2ik}|} \left(a_N + a_{M+1} - a_N\right) \\ &= \frac{2}{|1 - e^{2ik}|} \frac{1}{\sqrt{M+1}} \to 0 \text{ as } M \to \infty. \end{aligned} \tag{3.48}$$

We therefore conclude that S_N (and hence (3.40)) is convergent whenever $k \notin \pi\mathbf{N}$. When $k \in \pi\mathbf{N}$ the possibility of resonance is suggested by the fact that, in this case, $S_N = \sum_{n=1}^{N} \frac{1}{\sqrt{n}}$, which is divergent.

3.3.4.3 Equivalence of the two representations and ray approximation

Although we do not include the details here, we remark that the modal decomposition (3.38) and the image source representation (3.40) can be shown to be exactly equivalent via the Poisson summation formula (see e.g. [23], p. 76) and the identities 6.667(3) and 6.667(4) of [37]. The fact that each of the terms in (3.40) is analytic everywhere except at the corresponding image source is certainly in support of the analyticity which we know ϕ must possess (see the discussion after (3.38)). We note, however, that this fact alone cannot, strictly speaking, be used to *prove* analyticity (since a sum of analytic functions is not necessarily analytic).

When $k = O(1)$ the modal representation is clearly the more convenient of the two representations, because the exponential decay of the evanescent modes means that we need only consider the contribution from the first few terms in (3.38). In the short wavelength regime $k \gg 1$, however, the number of terms that need to be included in the modal representation grows like $O(k)$, and the image source representation becomes a more attractive option.

Indeed, the ray approximation is easily found from the image source representation (3.40) and the asymptotic behaviour (3.24), and takes the form of an infinite sum of ray expansions of the form (3.24). As Figure 3.3 illustrates, the contribution of each image source $(0, y_n)$ can be associated with exactly one ray emanating from the physical source, with the launch angle θ_n given by

$$\theta_n(x, y) = \begin{cases} \operatorname{sgn}(n)(-1)^n \arctan\left(\frac{y_n - y}{x}\right), & n \neq 0, \\ -\arctan\left(\frac{y_0 - y}{x}\right), & n = 0. \end{cases} \tag{3.49}$$

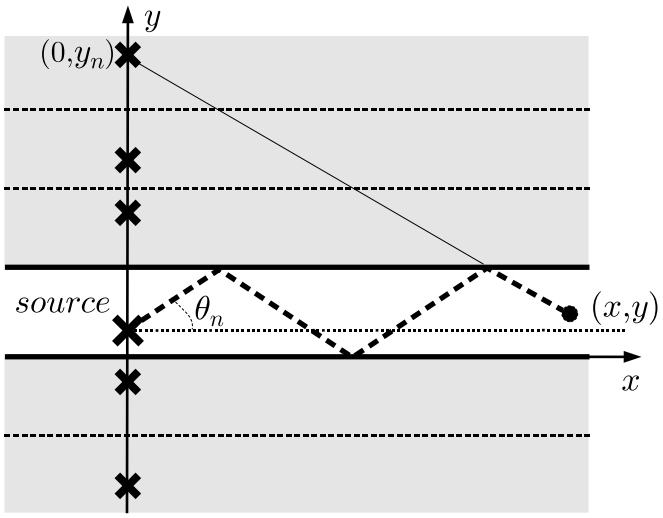


Figure 3.3: Association between image sources and rays in a single 2D street.

3.3.5 Diffraction

3.3.5.1 The Sommerfeld problem

One of the first exact solutions derived in the study of edge diffraction is that of the Sommerfeld problem, where the scatterer is a rigid half-line $y = 0$, $x > 0$. We first consider the classical case, depicted in Figure 3.4, where a plane wave $e^{-ikr\cos(\theta-\theta_0)}$ is incident from the direction $0 < \theta_0 < \pi$, where (r, θ) are the usual polar co-ordinates. The solution to the scattering problem can be found by a number of different methods. Sommerfeld's original approach (see [81], or for an exposition in English see [17]) involves the generalisation of the method of images to a Riemann surface; other authors have obtained the solution by changing variables to a parabolic co-ordinate system (see e.g [54]); others by applying the Wiener-Hopf method (see e.g. [45], Chapter 9, p. 548 or [10], Chapter 11); and yet others by applying the Kontorovich-Lebedev transform (see e.g. [71], p. 192 or [45], Chapter 9, p. 585). All of these approaches lead to the classical result

$$\phi = \frac{e^{ikr-i\pi/4}}{\sqrt{\pi}} \sum_{\pm} F\left(-\sqrt{2kr}\cos\left(\frac{\theta \pm \theta_0}{2}\right)\right), \tag{3.50}$$

where

$$F(\xi) = e^{-i\xi^2} \int_{\xi}^{\infty} e^{is^2}\, ds \tag{3.51}$$

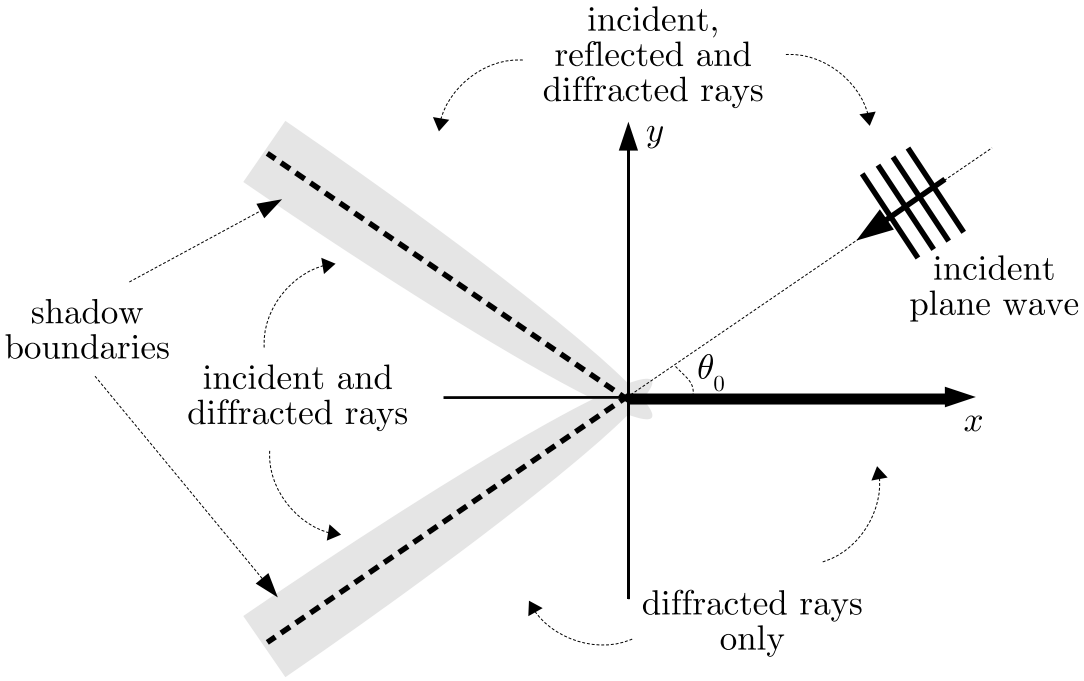


Figure 3.4: The Sommerfeld problem: diffraction of a plane wave by a rigid half-line. The bounding curves of the shaded regions (which represent the shadow boundary regions) are parabolae.

is the Fresnel integral (which must be understood in an improper sense) and $\sum_{\pm}$ indicates that the sum of the + and − terms should be taken.

Noting that

$$F(-\xi) = \sqrt{\pi} e^{i\pi/4} e^{-i\xi^2} - F(\xi) \tag{3.52}$$

for real ξ, the behaviour of $F(\xi)$ for large $|\xi|$ is found by integration by parts to be

$$F(\xi) \sim \begin{cases} \frac{i}{2\xi} + O\left(\frac{1}{|\xi|^3}\right), & \xi > 0, \\ \sqrt{\pi} e^{i\pi/4} e^{-i\xi^2} + \frac{i}{2\xi} + O\left(\frac{1}{|\xi|^3}\right), & \xi < 0. \end{cases} \tag{3.53}$$

The asymptotic behaviour of (3.50) for $kr \gg 1$ is therefore

$$\phi \sim \begin{cases} e^{-ikr\cos(\theta-\theta_0)} + e^{-ikr\cos(\theta+\theta_0)} + D(\theta)\frac{e^{ikr}}{\sqrt{kr}}, & 0 < \theta < \pi - \theta_0, \\ e^{-ikr\cos(\theta-\theta_0)} + D(\theta)\frac{e^{ikr}}{\sqrt{kr}}, & \pi - \theta_0 < \theta < \pi + \theta_0, \\ D(\theta)\frac{e^{ikr}}{\sqrt{kr}}, & \pi + \theta_0 < \theta < 2\pi, \end{cases} \tag{3.54}$$

where

$$D(\theta) = -\frac{e^{i\pi/4}}{2\sqrt{2\pi}} \sum_{\pm} \frac{1}{\cos\left(\frac{\theta \pm \theta_0}{2}\right)}. \tag{3.55}$$

The plane waves $e^{-ikr\cos(\theta-\theta_0)}$ and $e^{-ikr\cos(\theta+\theta_0)}$ represent the incident and reflected ray fields, respectively. The term $D(\theta)\frac{e^{ikr}}{\sqrt{kr}}$ represents the diffracted ray field, and takes the form of a cylindrical wave emanating from the edge with amplitude depending on θ, as described by the *diffraction coefficient* $D(\theta)$. It is easy to see that the approximation (3.54) is not uniform in θ, with the approximation breaking down in the vicinity of the shadow boundaries $\theta = \pi \pm \theta_0$. Indeed, for (3.54) to be a valid asymptotic approximation we require not just that $kr \gg 1$, but that

$$\sqrt{kr}\cos\left(\frac{\theta \pm \theta_0}{2}\right) \gg 1. \tag{3.56}$$

An idea of the regions in which (3.56) fails can be found by considering the curves

$$\sqrt{kr}\cos\left(\frac{\theta \pm \theta_0}{2}\right) = K, \tag{3.57}$$

or

$$kr(1 + \cos(\theta \pm \theta_0)) = 2K^2, \tag{3.58}$$

for some fixed K, which are parabolae with a common focus at the origin and axes $\theta = \pi \pm \theta_0$, respectively (see Figure 3.4). We note that as $kr \to \infty$ the parabolae become vanishingly thin and the ray approximation holds over a greater range of θ. We also remark that away from the shadow boundary regions the diffracted field is $O\left(k^{-1/2}\right)$, and therefore provides a higher order correction to the incident and reflected fields, which are $O(1)$, except in the shadow region $\pi + \theta_0 < \theta < 2\pi$ where it provides the sole contribution to the field.

3.3.5.2 A 2D point source

The exact solution for the case of a 2D point source in the presence of a rigid half line is also well known (see e.g. [17], which is based on Sommerfeld's generalised method of images on a Riemann surface, or [45], p. 557, which uses the Kontorovich-Lebedev transform). We do not quote the exact solution here, but remark that with the source located at the point (r_0, θ_0) in polar coordinates (with $0 < \theta_0 < \pi$), the geometrical structure of the ray field is the same as in the plane wave case, with incident rays present only in $0 < \theta < \pi + \theta_0$ and reflected rays present only in $0 < \theta < \pi - \theta_0$. When both $kr \gg 1$ and $kr_0 \gg 1$ the diffracted ray field is found to be

$$-\frac{ie^{-i\pi/4}}{4}\sqrt{\frac{2}{\pi}}\frac{e^{ikr_0}}{\sqrt{kr_0}}D(\theta)\frac{e^{ikr}}{\sqrt{kr}}, \tag{3.59}$$

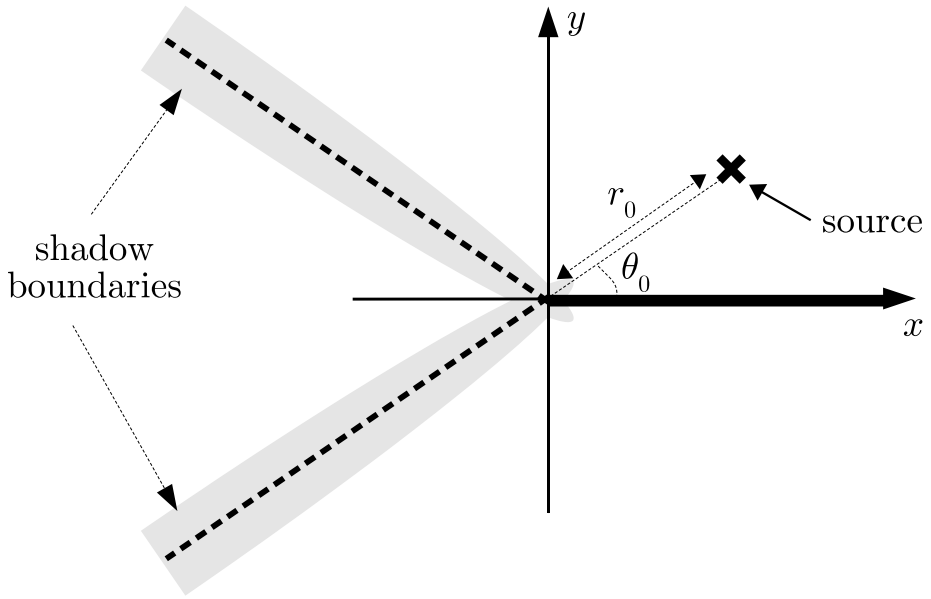


Figure 3.5: A 2D point source in the presence of a rigid half-line. The bounding curves of the shaded regions are hyperbolae.

where $D(\theta)$ is defined as in (3.55). The prefactor in front of $D(\theta)\frac{e^{ikr}}{\sqrt{kr}}$ in (3.59) is the value of the incident field at the edge $r = 0$, and, as in the plane wave case, the diffracted field is a cylindrical wave emanating from the edge with amplitude dictated by the diffraction coefficient $D(\theta)$. The diffracted field is $O(k^{-1})$, with the incident and reflected fields being $O(k^{-1/2})$, so again, the diffracted field is a higher order correction except in the shadow region where no incident or reflected rays exist, and in the shadow boundary regions around $\theta = \pi \pm \theta_0$. Further inspection of the exact solution (see e.g. [45], p. 559) reveals that the validity of the ray approximation relies on the parameters $k(r + r_0 - r_s)$ and $k(r + r_0 - r_i)$ being large, where r_s and r_i are the distances from the receiver to the source and the image point $(r_0, -\theta_0)$, respectively. An idea of the regions in which this condition is violated can be found by considering the curves

$$k(r + r_0 - r_s) = K, \tag{3.60}$$

$$k(r + r_0 - r_i) = K, \tag{3.61}$$

for fixed K, which are hyperbolae with foci at the origin and at the source or image source, and with axes $\theta = \pi \pm \theta_0$, respectively (see Figure 3.5). These hyperbolae are analogous to the parabolae of the plane wave case.

3.3.5.3 Diffraction by a wedge in 2D

Another canonical domain for which an exact solution of the Helmholtz equation is available is the exterior of a rigid 2D wedge, described in polar coordinates (r, θ) by $0 < r < \infty$, $0 < \theta < \beta$, with $\pi < \beta \leq 2\pi$. The Sommerfeld problem is the special case $\beta = 2\pi$. The exact solutions for an incident plane wave or a 2D point source can be found in [18] or [45], p. 585, but we do not quote them here. In both cases the leading order contribution from the diffracted field to the resulting ray approximation is the term

$$\phi_{\text{incident}} D(\theta) \frac{e^{ikr}}{\sqrt{kr}}, \tag{3.62}$$

where ϕ_{incident} is the value of the incident field at the edge $r = 0$, and the diffraction coefficient

$$D(\theta) = \frac{\kappa e^{i\pi/4}}{\sqrt{2\pi}} \sum_{\pm} \frac{\sin \kappa\pi}{\cos \kappa\pi - \cos \kappa \left(\theta \pm \theta_0\right)}, \tag{3.63}$$

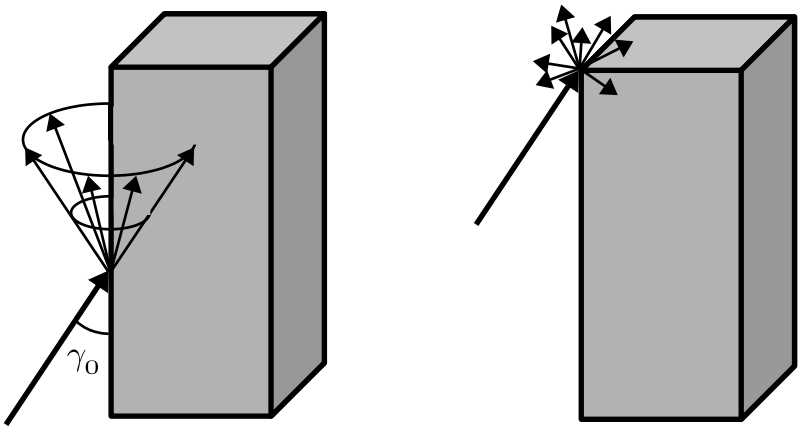
where $\kappa = \pi/\beta$. Note that (3.63) reduces to (3.55) when $\beta = 2\pi$.

3.3.5.4 Edge diffraction in 3D

It was proposed by Keller ([48]) that a ray incident on an edge in 3D gives rise to a *cone* of diffracted rays, with apex at the point at which the incident ray meets the edge and semi-angle equal to the angle γ_0 between the incident ray and the edge, as illustrated in Figure 3.6(a) in the special case of a 90° wedge. At leading order the diffracted field takes the form

$$\phi_{\text{incident}} \frac{D(\theta)}{\sin \gamma_0} \frac{e^{ikR}}{\sqrt{kR}}, \tag{3.64}$$

where R is the distance to the edge, measured along the diffracted ray (i.e. a generator of the cone), and θ is the angular coordinate in the plane perpendicular to the edge. Here ϕ_{incident} is the value of the incident field at the point at which the diffracted ray leaves the edge, and $D(\theta)$ is the diffraction coefficient (3.63) associated with the corresponding 2D wedge diffraction problem. The theory has been verified in the case of an infinite wedge in 3D, both for a plane wave at oblique incidence and for a 3D point source (see e.g. [45], p. 560-563).



(a) Edge diffraction (b) Vertex diffraction

Figure 3.6: (a) The cone of diffracted rays produced by a ray (thick arrow) incident on an edge in 3D (after [48], Figure 1). The semi-angle of the cone is equal to the angle γ_0 between the incident ray and the edge. (b) A ray incident on a vertex gives rise to diffracted rays emanating from the vertex in all directions.

3.3.5.5 Vertex diffraction in 3D

It was proposed by Keller ([48]) that a ray incident on a vertex gives rise to diffracted rays emanating from the vertex in all directions, as illustrated in Figure 3.6(b) in the special case of the vertex of a cuboid. At leading order the vertex-diffracted field takes the form

$$\phi_{\text{incident}} D(\theta, \varphi) \frac{e^{ikr}}{kr}, \tag{3.65}$$

where (r, θ, φ) are spherical coordinates with origin at the vertex, and $D(\theta, \varphi)$ is the diffraction coefficient. Note that magnitude of the vertex-diffracted field is $O(1/k)$ times that of the incident field, in contrast to an edge-diffracted field, which, in general, has magnitude $O\left(1/\sqrt{k}\right)$ times that of the incident field.

The diffraction coefficient $D(\theta, \varphi)$ can only be determined analytically in special cases for which exact solutions exist, for example the case of a circular cone (see e.g. [33], p. 703, or [67]) and an elliptic cone (see e.g. [53]), while in the general case it can be evaluated via analytic-numerical hybrid approaches (see e.g. [7, 11, 80]).

3.4 Acoustic energy

In principle, GTD reduces the calculation of the sound field in a domain containing multiple scatterers to the geometrical 'ray tracing' problem of determining all the rays (incident, reflected and diffracted) emanating from the source that reach the receiver location, and summing their respective contributions. This task clearly becomes more difficult as the domain becomes more complicated; however, as is well-known in the radar industry, this approach is usually easier than attempting to solve the full wave problem numerically.

Because of the highly oscillatory nature of the sound field in the short wavelength regime, the precise details of the sound field are sensitive to small perturbations in domain characteristics, such as street widths or lengths and source or receiver locations. As remarked in section 1.1, in practical situations such characteristics may be known only to a certain degree of accuracy, and may best be considered random variables. Hence a full description of the details of the sound field in one particular realisation of the domain will be of limited relevance (see e.g. [31, 40]).

To obtain a more robust measure of the broad spatial variation of the sound field, the approach taken by many authors in the urban acoustics literature (see e.g. [14, 27, 91]) is to study the distribution of *acoustic energy* across the domain, and this is the approach we take in this thesis. The acoustic energy and the associated *acoustic intensity* are quadratic quantities (i.e. involving products of two primed variables in the acoustic approximation). They can be averaged both temporally and spatially to provide useful measures of the magnitude of the sound field that are less sensitive to perturbations in the domain characteristics than are the full details of the sound field. Moreover, as we shall show, in the short wavelength regime the leading-order behaviour of the time-averaged acoustic energy and intensity have very simple representations in terms of the leading-order amplitude of the ray approximation, and, even more importantly, the acoustic energy can be shown to be directly proportional to the mean-square pressure, a more easily measurable quantity.

It is important to remark that the acoustic energy differs from the full energy of the fluid considered in section 2.1, and the relationship between the two will be discussed in the next section.

3.4.1 Definition of acoustic energy and intensity

In Chapter 1 of [58] the *instantaneous acoustic energy density* $W(\mathbf{x}, t)$ associated with a sound wave is defined in terms of the acoustic pressure and velocity fluctuations p' and $\mathbf{u}'$ by

$$W(\mathbf{x}, t) := \frac{1}{2}\rho_0 |\mathbf{u}'(\mathbf{x}, t)|^2 + \frac{1}{2}\frac{(p'(\mathbf{x}, t))^2}{\rho_0 c_0^2}. \tag{3.66}$$

The first term in (3.66) represents the kinetic energy associated with the sound wave. The second term can be interpreted as representing the potential energy of compression[4] per unit volume ([58], p. 13). The *instantaneous acoustic intensity* $\mathbf{I}(\mathbf{x}, t)$ is defined by

$$\mathbf{I}(\mathbf{x}, t) := p'(\mathbf{x}, t)\mathbf{u}'(\mathbf{x}, t). \tag{3.67}$$

For any unit vector $\mathbf{n}$, the product $\mathbf{I} \cdot \mathbf{n}$ represents the rate per unit area at which work is being done by the excess pressure p' on a small plane element orthogonal to $\mathbf{n}$ located at the point $\mathbf{x}$. For homentropic flow it can be shown using the linearised equations (2.9)-(2.11) that W and $\mathbf{I}$ satisfy the equation of conservation of acoustic energy

$$\frac{\partial W}{\partial t} = -\nabla \cdot \mathbf{I}, \tag{3.68}$$

so that $\mathbf{I}$ strictly describes the instantaneous acoustic energy flux at a given point in space.

The instantaneous acoustic energy flux (or *power flow*) P across a surface S is then given by the integral

$$P = \iint_S \mathbf{I} \cdot \mathbf{n}\, dS, \tag{3.69}$$

where $\mathbf{n}$ is the positively-oriented unit normal vector to S.

We remark that the definition of the acoustic intensity (3.67) captures only the work done by the pressure perturbation p', and ignores the contribution from the background pressure p_0, which one would expect to give rise to a linear term $p_0\mathbf{u}'$ in the expression for the full energy flux. It would seem reasonable to assume that the

[4]This quantity is analogous to the elastic strain energy for an elastic material with $\rho_0 c_0^2$ as its bulk modulus. In the gas dynamics setting, the quantity $\rho_0 c_0^2 = \gamma p_0$ can be thought of as the adiabatic bulk modulus of the gas. Here γ is the ratio of specific heats of the gas as before.

background pressure should not play a role in the net transport of acoustic energy; indeed for time-harmonic disturbances, the linear term $p_0\mathbf{u}'$ will average to zero over each period of oscillation. However, it is nonetheless important to discuss briefly[5] how (3.68) is related to the full energy conservation equation (2.3).

We begin by noting that substitution of the constitutive law (2.7) into the unintegrated energy conservation equation (2.5) gives

$$\rho\mathbf{u}\cdot\frac{D\mathbf{u}}{Dt}+\frac{p}{\rho}\frac{D\rho}{Dt}=-\nabla\cdot(p\mathbf{u}). \tag{3.70}$$

Direct linearisation of (3.70) produces

$$\frac{p_0}{\rho_0}\frac{\partial\rho'}{\partial t}=-p_0\nabla\cdot\mathbf{u}', \tag{3.71}$$

which is simply p_0/q_0 times the linearised mass conservation equation (2.9). However, if we return to (3.70) and subtract the same multiple of the *full* mass conservation equation (2.1), then the linear terms cancel out exactly when the acoustic approximation is substituted, and the acoustic energy conservation equation (3.68) emerges as the quadratic approximation of the resulting equation (i.e. involving products of two primed variables, with higher order terms neglected).

3.4.2 Time-averaged acoustic energy in the frequency domain

Use of (2.14) allows us to express the instantaneous acoustic energy (3.66) and intensity (3.67) in terms of the velocity potential Φ, so that in the time-harmonic case we have

$$W(\mathbf{x},t)=\frac{\rho_0}{2}\left(\left|\mathrm{Re}\left[\boldsymbol{\nabla}\phi(\mathbf{x})\,e^{-i\omega t}\right]\right|^2+k^2\left(\mathrm{Im}\left[\phi(\mathbf{x})\,e^{-i\omega t}\right]\right)^2\right), \tag{3.72}$$

$$\mathbf{I}(\mathbf{x},t)=-\rho_0\omega\,\mathrm{Im}\left[\phi(\mathbf{x})\,e^{-i\omega t}\right]\,\mathrm{Re}\left[\boldsymbol{\nabla}\phi(\mathbf{x})\,e^{-i\omega t}\right], \tag{3.73}$$

in dimensional variables.

To remove the temporal oscillations we consider the average values of (3.72) and (3.73) over one period of oscillation, denoting these quantities by $\langle W\rangle(\mathbf{x})$ and $\langle\mathbf{I}\rangle(\mathbf{x})$,

[5]For a more detailed discussion the reader is encouraged to consult [58] pp. 14-16. For more information on the measurement of acoustic intensity see e.g. [31].

respectively. Expanding (3.72) and (3.73), we find that the only non-zero contributions come from terms involving $\sin^2 \omega t$ and $\cos^2 \omega t$, with the result that

$$\langle W \rangle(\mathbf{x}) = \frac{\rho_0}{4} \left(\boldsymbol{\nabla}\phi(\mathbf{x}) \cdot \overline{\boldsymbol{\nabla}\phi(\mathbf{x})} + k^2 \phi(\mathbf{x}) \overline{\phi(\mathbf{x})} \right), \tag{3.74}$$

$$\langle \mathbf{I} \rangle(\mathbf{x}) = \frac{\rho_0 \omega}{2} \operatorname{Im}[\overline{\phi}(\mathbf{x}) \boldsymbol{\nabla}\phi(\mathbf{x})], \tag{3.75}$$

where the overbar denotes complex conjugation.

In terms of the nondimensional variables introduced in (3.1) (denoted here with hats), (3.74) and (3.75) become

$$\langle W \rangle = \frac{\rho_0 \phi_0^2}{2L^2} \langle \hat{W} \rangle, \tag{3.76}$$

$$\langle \mathbf{I} \rangle = \frac{\rho_0 c_0 \phi_0^2}{2L^2} \langle \hat{\mathbf{I}} \rangle, \tag{3.77}$$

where

$$\langle \hat{W} \rangle = \frac{1}{2} \left(\hat{\boldsymbol{\nabla}}\hat{\phi} \cdot \overline{\hat{\boldsymbol{\nabla}}\hat{\phi}} + \hat{k}^2 \hat{\phi} \overline{\hat{\phi}} \right), \tag{3.78}$$

$$\langle \hat{\mathbf{I}} \rangle = \hat{k} \operatorname{Im}[\overline{\hat{\phi}} \hat{\boldsymbol{\nabla}}\hat{\phi}], \tag{3.79}$$

and $\hat{k} = \omega L / c_0$.

3.4.2.1 Acoustic energy associated with a single ray expansion

In the short-wavelength regime $\hat{k} \gg 1$, assuming that $\hat{\phi}$ can be approximated by a single ray expansion of the form (3.3), we have, to leading order,

$$\hat{\phi} \sim A_0 e^{i\hat{k}U}, \tag{3.80}$$

$$\hat{\boldsymbol{\nabla}}\hat{\phi} \sim i\hat{k} \hat{\boldsymbol{\nabla}} U A_0 e^{i\hat{k}U}, \tag{3.81}$$

and substituting (3.80) and (3.81) in (3.78) and (3.79) gives

$$\langle \hat{W} \rangle \sim \hat{k}^2 |A_0|^2, \tag{3.82}$$

$$\langle \hat{\mathbf{I}} \rangle \sim \hat{k}^2 |A_0|^2 \hat{\boldsymbol{\nabla}} U. \tag{3.83}$$

Hence, to leading order, the acoustic energy is proportional to the square of the modulus of the leading-order amplitude A_0 of the ray approximation, with the energy flow being in the ray direction[6].

[6]This justifies our interpretation of equation (3.22) in section 3.2.1.

Another justification for studying the acoustic energy is that in the ray approximation, it is directly proportional to an experimentally measurable quantity, the *mean-square pressure*, $\langle (p')^2 \rangle$. Specifically, when $\hat{k} \gg 1$, use of (3.80) gives

$$\langle (p')^2 \rangle = \frac{\rho_0^2 \omega^2}{2} |\phi|^2 \sim \frac{\rho_0^2 \phi_0^2 c_0^2}{2L^2} \hat{k}^2 |A_0|^2, \tag{3.84}$$

so that

$$\langle (p')^2 \rangle \sim \rho_0 c_0^2 \langle W \rangle \tag{3.85}$$

in dimensional terms.

For the remainder of this chapter we work exclusively in nondimensional variables, but drop hats for ease of presentation.

As an illustration we consider the case of a point source in 2D free space, the ray expansion for which is given by (3.24). Using (3.82) and (3.83), we find that

$$\langle W \rangle \sim \frac{k}{8\pi r}, \tag{3.86}$$

$$\langle \mathbf{I} \rangle \sim \frac{k}{8\pi r} \mathbf{e_r}, \tag{3.87}$$

where $\mathbf{e_r}$ denotes the outward radial unit vector. The energy flow is purely in the radial direction, and the magnitude of $\langle \mathbf{I} \rangle(\mathbf{x})$ decays like the inverse of the distance from the source. The (nondimensional) time-averaged power flow P across the circle of radius r centered at the source is then approximated by

$$P \sim \int_0^{2\pi} \frac{k}{8\pi r} \, r \, d\theta = \frac{k}{4}, \tag{3.88}$$

since the outward normal vector on the circle is simply $\mathbf{e_r}$. P is independent of the radius of the circle, and represents the total power output of the source. More generally, the power flow across a surface S described in polar coordinates (r, θ) by $r = R(\theta)$ is proportional to the angle subtended at the source by the surface, with the constant of proportionality being $\frac{k}{8\pi}$. This can easily be verified by an application of the divergence theorem (we note that the vector field (3.87) is divergence free, and is smooth everywhere except at $r = 0$).

In the case of a point source in 3D free space we find that

$$\langle W \rangle \sim \frac{k^2}{16\pi^2 r^2}, \tag{3.89}$$

$$\langle \mathbf{I} \rangle \sim \frac{k^2}{16\pi^2 r^2} \, \mathbf{e_r}. \tag{3.90}$$

The magnitude of $\langle \mathbf{I} \rangle$ now decays with increasing distance from the source according to an inverse square law. The power flow P across the sphere of radius r centered at the source is found to be

$$P = \frac{k^2}{4\pi}, \tag{3.91}$$

which represents the total power output of the source. More generally, the power flow across any surface S described by an equation $r = R(\theta, \phi)$ in spherical coordinates is proportional to the solid angle subtended at the source by the surface, with the constant of proportionality being $\frac{k^2}{16\pi^2}$.

3.4.2.2 Acoustic energy associated with a sum of ray expansions (GTD approximation)

We now consider the more general case, where, due to the scattering effect of obstacles, the sound field is approximated, according to GTD, by a *sum* of ray expansions

$$\phi \sim \sum_i \phi_i, \tag{3.92}$$

where, for each i, ϕ_i is of the form (3.3). According to (3.79), the time-averaged acoustic intensity is then given by

$$\langle \mathbf{I} \rangle = k \operatorname{Im} \left[\overline{\left(\sum_i \phi_i \right)} \left(\sum_j \boldsymbol{\nabla} \phi_j \right) \right], \tag{3.93}$$

which can be rewritten as

$$\langle \mathbf{I} \rangle = k \operatorname{Im} \left[\sum_i \overline{\phi}^{(i)} \boldsymbol{\nabla} \phi_i \quad + \sum_i \sum_{i \neq j} \overline{\phi}^{(i)} \boldsymbol{\nabla} \phi_j \right]. \tag{3.94}$$

The first sum in (3.94) is simply an 'incoherent' summation of the intensities associated with each of the ray fields. The second (double) sum represents the effects of interference between ray fields. Each interference term $\overline{\phi}^{(i)} \boldsymbol{\nabla} \phi_j$ may make a positive contribution (constructive interference) or a negative contribution (destructive interference) to the intensity, depending on the phase difference between the ray fields ϕ_i and ϕ_j.

In this thesis we make the simplifying assumption that the contribution of the second sum can be neglected, so that acoustic intensities can be computed by incoherent

summation of the energy flows along individual rays[7]. This is a standard assumption in the urban acoustics literature (see e.g. [35, 51, 91]), and we refer to it as the *ray model of acoustic energy propagation*.

In a highly reverberant environment for which there is some uncertainty in domain characteristics, the validity of this model can be justified by assuming that the phases of each of the ray fields ϕ_i are independent random variables, so that the expected contribution of the interference terms is zero in the ensemble average. This reasoning has similarities to the method of 'Statistical Energy Analysis' (SEA), a technique used to predict the distribution of vibrational energy in complex mechanical structures (see e.g. [40, 62]).

Even in the fully deterministic case, it is sometimes possible to justify the neglect of the interference terms by performing some sort of spatial averaging over either the source or receiver location, provided that the averaging region is chosen so that the interference terms oscillate sufficiently to average to zero in the short wavelength limit. In the following section we verify this statement in the case of a single 2D street. A natural choice of averaging region in this case is a street cross-section, and in fact, we consider only the component of the acoustic intensity vector normal to the cross-section, which, after integration, gives the acoustic power flow down the street. We show that the prediction of the incoherent ray model does indeed approximate the exact acoustic power flow in the short wavelength limit, provided that the source is not too close to either of the street walls and that the effects of resonance are dealt with appropriately.

[7]We remark that, under this incoherent summation assumption, the same relationship (3.85) between the acoustic energy and the mean-square pressure holds for a sum of ray expansions as for a single ray expansion.

3.5 The acoustic power flow in a single 2D street

According to the ray model, the acoustic power flow across a street cross-section at distance x from the source is equal to the incoherent sum of the free space power flows across the street cross-section from each of the image sources of section 3.3.4.2. By the remark following (3.88), the power flow from the nth image source is equal to $\frac{k}{8\pi}$ times the angular width $\Theta_n = \Theta_n(x, y_0)$ of the tube of rays from that image source that intersect the street cross-section at x (see Figure 3.7(a)). The ray model therefore gives the power flow down the street as

$$P_{\text{ray}} = \frac{k}{8\pi} \sum_{n \in \mathbf{Z}} \Theta_n, \tag{3.95}$$

where

$$\Theta_n = \arctan \frac{y_n}{x} - \arctan \frac{y_n - 1}{x} \tag{3.96}$$

$$= \begin{cases} \arctan \frac{n+y_0}{x} - \arctan \frac{n-(1-y_0)}{x}, & n \text{ even}, \\ \arctan \frac{n+(1-y_0)}{x} - \arctan \frac{n-y_0}{x}, & n \text{ odd}. \end{cases} \tag{3.97}$$

The analysis simplifies somewhat if we rewrite (3.95) as

$$P_{\text{ray}} = \frac{k}{8\pi} \sum_{n \in \mathbf{Z}} \tilde{\Theta}_n, \tag{3.98}$$

where

$$\tilde{\Theta}_n = \begin{cases} \Theta_{-n}, & n \text{ even}, \\ \Theta_n, & n \text{ odd}. \end{cases} \tag{3.99}$$

Then we have

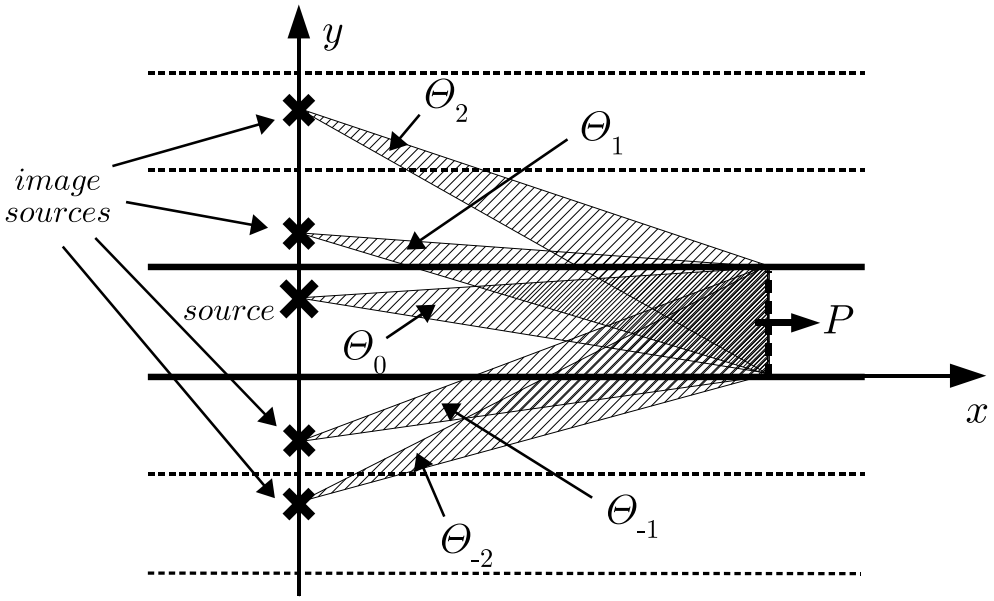
$$\tilde{\Theta}_n = \tilde{\theta}_n^+ - \tilde{\theta}_n^-, \tag{3.100}$$

where

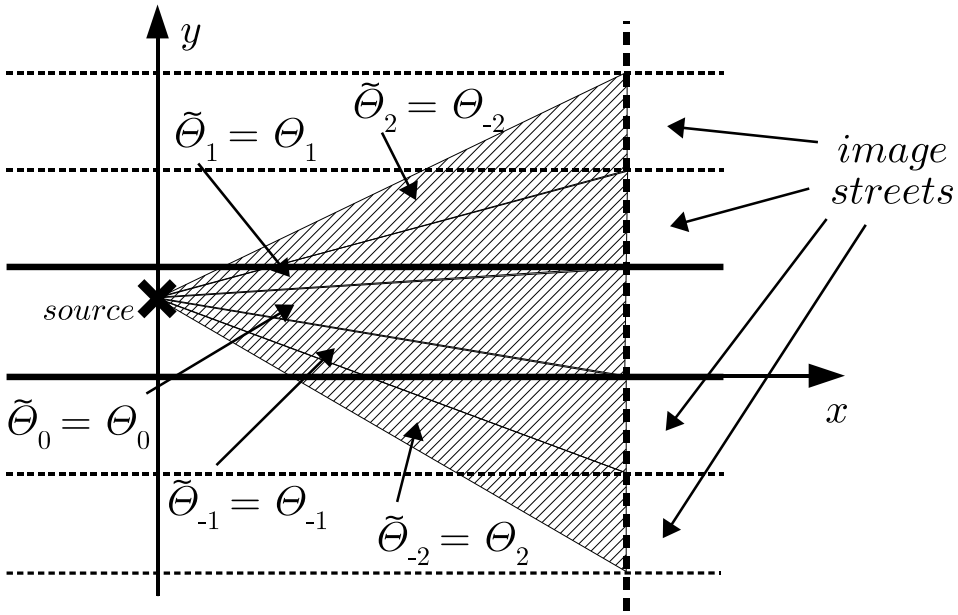
$$\begin{aligned} \tilde{\theta}_n^+ &= \arctan \frac{n + 1 - y_0}{x}, \\ \tilde{\theta}_n^- &= \arctan \frac{n - y_0}{x}, \end{aligned} \tag{3.101}$$

and since $\tilde{\theta}_n^+ = \tilde{\theta}_{n+1}^-$, we find that (3.98) is a telescoping sum which collapses to give

$$P_{\text{ray}} = \frac{k}{8\pi} \left(\arctan(\infty) - \arctan(-\infty) \right) = \frac{k}{8}. \tag{3.102}$$



(a) Image source interpretation



(b) Image street interpretation

Figure 3.7: The geometrical interpretation of Θ_n and $\tilde{\Theta}_n$ in a single 2D street.

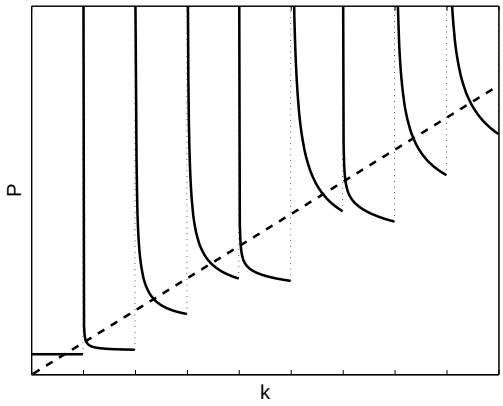


Figure 3.8: Typical plot of P (solid line) and P_{ray} (dashed line) as a function of the wavenumber k. Here the singularities in P occur at integer multiples of π.

Note that (3.102) is independent of the distance x down the street. In fact, by comparing (3.102) with (3.88) we see that the combined contribution from all the image sources is simply the total free space power output in the positive x-direction of a source at the point $(0, y_0)$.

Geometrically, the manipulation of (3.95) into (3.102) corresponds to moving all the image sources (and their respective ray tubes) to the point $(0, y_0)$ and considering the total power flow from a single source located at that point across an infinite array of *image street* cross-sections (i.e. across the line $\{x\} \times (-\infty, \infty)$). After reflecting the ray tubes corresponding to the odd image sources in the line $y = y_0$ we obtain the picture in Figure 3.7(b).

The exact value of the power flow is computed most conveniently from the modal decomposition (3.38). After use of the orthogonality relations (3.31) we find that

$$P = \frac{k}{4} \sum_{m=0}^{\lfloor k/\pi \rfloor} \frac{\cos^2 m\pi y_0}{\sigma_m \kappa_m}, \tag{3.103}$$

since the evanescent modes do not make any contribution to the power flow. Note that (3.103) is, like (3.102), independent of x.

The exact power flow (3.103) possesses inverse square root singularities at the resonant wavenumbers $k = m\pi$, $m \in \mathbf{Z}$, which are not discovered by the ray model. Away from resonance, however, the behaviour of (3.103) does broadly follow the linear growth in k of (3.102), as Figure 3.8 illustrates. One way to make this statement more precise is to consider the *average* behaviour of (3.103) between any two neighbouring

resonances, which is well-defined because the singularities are integrable. For any positive integer K we define

$$\begin{aligned} P^{\mathrm{av}}(K) :&= \frac{1}{\pi}\int_{K\pi}^{(K+1)\pi} P\,dk \\ &= \frac{1}{4}\sum_{m=0}^{K}\frac{1}{\pi}\int_{K\pi}^{(K+1)\pi}\frac{k\cos^2 m\pi y_0}{\sigma_m\sqrt{k^2-(m\pi)^2}}\,dk \\ &= \frac{1}{2}\left(\sum_{m=0}^{K}\cos^2 m\pi y_0\left(\sqrt{(K+1)^2-m^2}-\sqrt{K^2-m^2}\right)-\frac{1}{2}\right). \end{aligned} \tag{3.104}$$

Using the relation $\cos^2 z = \frac{1}{2}(1+\cos 2z)$ we can rewrite (3.104) as

$$P^{\mathrm{av}}(K) = \frac{1}{4}\left(S_1(K)+S_2(K)-1\right), \tag{3.105}$$

where

$$S_1(K) = \sum_{m=0}^{K}\sqrt{(K+1)^2-m^2}-\sqrt{K^2-m^2} \tag{3.106}$$

and

$$S_2(K) = \sum_{m=0}^{K}\cos 2m\pi y_0\left(\sqrt{(K+1)^2-m^2}-\sqrt{K^2-m^2}\right). \tag{3.107}$$

Because of the oscillatory factor $\cos 2m\pi y_0$ in the summand of (3.107), S_1 dominates S_2 as $K\to\infty$, unless y_0 is close to 0 or 1. The details of the analysis can be found in Appendix A, and we find that

$$S_1(K) \sim \frac{K\pi}{2}+O(\sqrt{K}), \quad K\to\infty, \tag{3.108}$$

and

$$S_2(K) = O\left(\frac{\sqrt{K}}{y_*}\right), \qquad K\to\infty, \quad y_*\gg 1/\sqrt{K}, \tag{3.109}$$

where

$$y_* = \min\{y_0, 1-y_0\}. \tag{3.110}$$

Thus, provided that $y_*\gg 1/\sqrt{K}$, we have $S_2(K)\ll S_1(K)$ and

$$P^{\mathrm{av}}(K) \sim \frac{K\pi}{8}, \quad K\to\infty. \tag{3.111}$$

This clearly agrees with the leading order behaviour (as $K \to \infty$) of the prediction of the ray model, which is

$$P_{\text{ray}}^{\text{av}}(K) = \frac{1}{\pi} \int_{K\pi}^{(K+1)\pi} P_{\text{ray}}\, dk = \frac{(K + \frac{1}{2})\pi}{8}. \tag{3.112}$$

The requirement that $y_* \gg 1/\sqrt{K}$ corresponds to y_0 not being too close to either of the street walls. The need for this restriction is completely intuitive when one considers the geometry of the image source representation (3.40), as illustrated in Figure 3.2, since the effect of moving the source close to one of the walls is to cause neighbouring image sources to coalesce, which invalidates the neglect of the relevant interference effects.

3.5.1 Energy absorption at walls

So far we have assumed that the street walls are perfectly reflecting. In practice a small amount of the energy incident on the walls will be absorbed. The standard method of including the effects of this absorption in the ray model (see e.g. [91, 44]) is to assume that there exists a constant $\alpha \in [0, 1]$, called the *absorption coefficient*, such that the magnitude I of the intensity along a ray undergoing a reflection at the boundary is attenuated according to the rule

$$I_{\text{reflected}} = (1 - \alpha)\, I_{\text{incident}}. \tag{3.113}$$

As a crude first approximation, α is usually taken to be independent of the angle of incidence/reflection, and this is the approach we take in this thesis. The relationship between this simplistic ray-based absorption model and full wave-based models such as impedance boundary conditions is rather subtle (see e.g. [28, 36, 43, 68]), and will not be discussed here. However, we remark that the form of the integral approximations derived in the remainder of this chapter would make generalisation to angle-dependent absorption coefficients a possibility for future work.

Experimental studies have shown that the absorption coefficient of a material also depends weakly on the frequency of the incident wave (see e.g. [25], Chapter 57). Most common building materials are very good reflectors of sound, with the value of α at normal incidence and in the frequency range of interest to Dstl typically lying in the range $0 < \alpha < 0.1$. For example, $\alpha = 0.04$ for an unpainted brick wall and $\alpha = 0.02$ for a painted brick wall at 1KHz ([25], p. 708).

In practice, the absorption coefficient may vary along the street depending on the nature of the building facades, but for simplicity we assume that the effects of wall absorption can be represented by an effective absorption coefficient that is a known characteristic of each street.

Under the absorption coefficient model (3.113), the expression (3.98) for the power flow down the street is modified to

$$P(x) = \frac{1}{2\pi} \sum_{n \in \mathbf{Z}} (1-\alpha)^{|n|} \tilde{\Theta}_n, \tag{3.114}$$

where, for ease of presentation, we have dropped the subscript $_{\text{ray}}$ and have normalised P by a factor $\frac{k}{4}$, so that (3.114) represents the power flow relative to the total transmitted power in free space, as computed in (3.88). This normalisation will be the convention for the remainder of this chapter.

3.5.2 Asymptotic behaviour far from the source

With the inclusion of wall absorption, the power flow down the street is no longer independent of x, and in this section we study the asymptotic behaviour of (3.114) when the receiver is far from the source ($x \gg 1$). As we shall see, the qualitative nature of this behaviour is dependent on the size of the absorption coefficient α.

When α is not too small (exactly how small will be determined shortly), the main contribution to the sum comes from near $n = 0$, because of the exponentially decaying factor $(1-\alpha)^{|n|}$ in the summand. More precisely, if we split the sum into

$$P(x) = \frac{1}{2\pi} \left(\sum_{|n| \leq N} (1-\alpha)^{|n|} \tilde{\Theta}_n + \sum_{|n| > N} (1-\alpha)^{|n|} \tilde{\Theta}_n \right), \tag{3.115}$$

then the second sum is exponentially small compared to the first, and can be neglected, provided that $|N \log(1-\alpha)| \gg 1$. If also $N \ll x$, then we can Taylor-expand the function $\tilde{\Theta}_n$ inside the first sum, giving

$$P(x) \sim \frac{1}{2\pi} \sum_{|n| \leq N} (1-\alpha)^{|n|} \frac{1}{x} \left(1 - \frac{1}{x^2} \left((n+1-y_0)(n-y_0) + \frac{1}{3} \right) + O\left(\frac{1}{x^4} \right) \right). \tag{3.116}$$

By re-extending the summation range to the whole of $\mathbf{Z}$, again introducing only exponentially small errors, we obtain sums which can be evaluated explicitly using

the formula for the sum of a geometric progression (and formulae derived from it), giving the result

$$P(x) \sim \frac{2-\alpha}{2\pi\alpha x}\left(1+\frac{1}{x^2}\left(y_0(1-y_0)-\frac{1}{3}-\frac{2(1-\alpha)}{\alpha^2}\right)+O\left(\frac{1}{x^4}\right)\right), \quad x\to\infty. \tag{3.117}$$

To answer the question of how small α may be for this approach to be valid, we note that the expression (3.117) is a valid asymptotic expansion only when $\alpha \gg 1/x$; this restriction is entirely consistent with the two conditions obtained for the choice of the truncation point N, since when $\alpha = O(1/x)$ the condition $|N\log(1-\alpha)| \gg 1$ is equivalent to requiring that $N \gg 1/\alpha$, which is clearly incompatible with the requirement that $N \ll x$.

To deal with the case where $\alpha = O(1/x)$, we first note that using the trigonometric identity

$$\arctan z_1 \pm \arctan z_2 = \arctan\frac{z_1 \pm z_2}{1 \mp z_1 z_2}, \tag{3.118}$$

we can rewrite $\tilde{\Theta}_n$ in the form

$$\tilde{\Theta}_n = \arctan\frac{1}{x+\frac{(n+1-y_0)(n-y_0)}{x}}. \tag{3.119}$$

We then approximate

$$\tilde{\Theta}_n \sim \frac{1}{x+\frac{n^2}{x}}\left(1+O\left(\frac{1}{x}\right)\right), \quad x\to\infty, \tag{3.120}$$

which, crucially, is valid uniformly for all n. Inserting this into (3.114) gives

$$P(x) \sim \frac{1}{2\pi}\left(-\frac{1}{x}+\frac{2}{x}\sum_{n=0}^{\infty}(1-\alpha)^n\frac{1}{1+\frac{n^2}{x^2}}\right), \quad x\to\infty, \tag{3.121}$$

where the $-1/x$ correction is required because we have included the $n=0$ term twice. The key step now is to recognise the second term as an approximation of the integral[8]

$$\int_0^\infty \frac{(1-\alpha)^{xt}}{1+t^2}\,dt, \tag{3.122}$$

with the result that

$$P(x) \sim \frac{1}{\pi}\int_0^\infty \frac{(1-\alpha)^{xt}}{1+t^2}\,dt + O\left(\frac{1}{x}\right), \quad x\to\infty. \tag{3.123}$$

[8]We remark that (3.122) can be written in terms of exponential integrals.

In fact, it is possible to show that the integral approximation (3.123) is valid not just for $\alpha = O(1/x)$, but for all $\alpha \ll 1$. Indeed, when $1/x \ll \alpha \ll 1$ (3.123) is a Laplace-type integral with large parameter αx. The main contribution to the integral comes from the endpoint $t = 0$, and a local expansion around this point gives the leading order behaviour

$$\frac{1}{\pi}\int_0^\infty \frac{(1-\alpha)^{xt}}{1+t^2}\,dt \sim \frac{1}{\pi\alpha x}, \tag{3.124}$$

which clearly agrees with the leading order term in (3.117) when $1/x \ll \alpha \ll 1$.

3.5.3 Interpretation in terms of ray angles at small absorption ($\alpha \ll 1$)

We have seen that in the case of small absorption ($\alpha \ll 1$), the power flow down the street far from the source ($x \gg 1$) can be approximated by (3.123). By the change of variable $t = \tan\theta$, this integral approximation can be rewritten as

$$P(x) \sim \frac{1}{\pi}\int_0^{\frac{\pi}{2}} (1-\alpha)^{x\tan\theta}\,d\theta, \quad x \to \infty, \tag{3.125}$$

where we identify the integration variable θ with the absolute value of the launch angle of a ray emanating from the source (as defined in Figure 3.3). Then (3.125) states that the power flow far from the source takes the form of an integral over launch angles of a 'power density' propagating at each value of θ, after attenuation by wall absorption. The exponent $x\tan\theta$ in the integral (3.125) represents a continuous approximation to the discrete number of reflections undergone by a ray of launch angle $\pm\theta$.

This interpretation will offer considerable conceptual advantages in the section that follows, where we come to study the way that the energy propagating along a street is redistributed at a junction with another street.

3.6 Energy redistribution at a junction in 2D

In this section we use the ray model to study the way that the acoustic energy from a point source is redistributed at a junction between two 2D streets. Asymptotic approximations to the acoustic power flows out of the junction are obtained in the form of integral representations that are a generalisation of the results of the previous section, with a natural interpretation in terms of power densities propagating at ray launch angles.

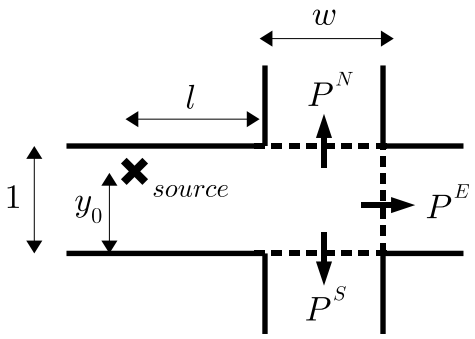
3.6.1 Energy redistribution at a crossroads

We consider first the case of a right-angled crossroads, as illustrated in Figure 3.9(a). As in section 3.3.4, we choose as our characteristic lengthscale L the width of the street containing the source. In the short wavelength regime $k \gg 1$, GTD represents the sound field in this domain as the sum over all of the geometrical rays that exist between source and receiver. These rays can be put into two categories: those rays which involve either direct propagation or one or more reflections at the street walls, and those which involve diffraction at one or more of the sharp edges of the junction. Motivated by the observations of section 3.3.5.2, we expect that the diffracted field constitutes a higher-order correction to the field due to the direct and (multiply-)reflected rays. Therefore, as a first approximation, we propose to estimate the acoustic power flows P^N, P^E and P^S out of the North, East and South exits of the junction by considering the contribution of the incident and (multiply-)reflected ray fields alone.

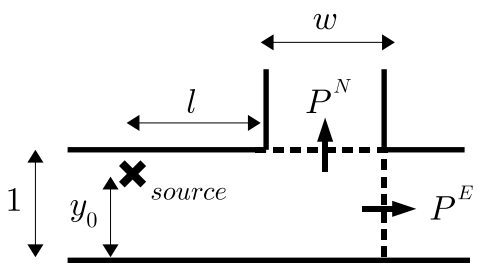
3.6.1.1 Neglect of diffraction effects

The assumption that diffraction effects can be neglected offers a considerable analytical simplification; however, it is important to discuss the conditions under which we expect it to be valid. In particular, the nonuniformity in the GTD approximation means that we must be careful in applying ray theory in such a domain, because the shadow boundary regions in which the ray approximation fails become increasingly important with increasing distance down the streets leading off the junction.

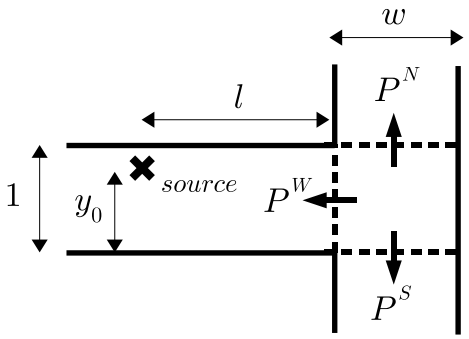
As an illustration of this point, consider the situation depicted in Figure 3.10, where a plane wave is incident on the open end of a semi-infinite street. As usual



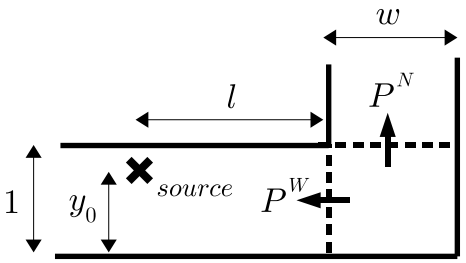
(a) Crossroads



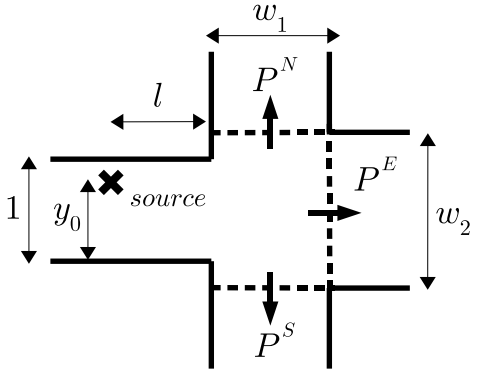
(b) Side street



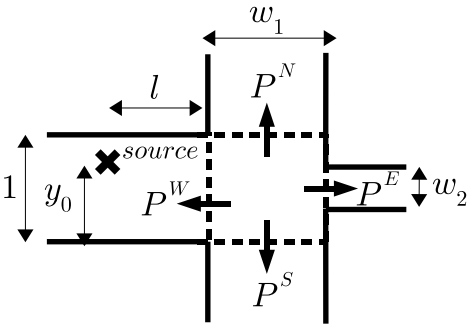
(c) T-junction



(d) Right-angled bend



(e) Asymmetric crossroads (w_2>1)



(f) Asymmetric crossroads (w_2<1)

Figure 3.9: Common junction types

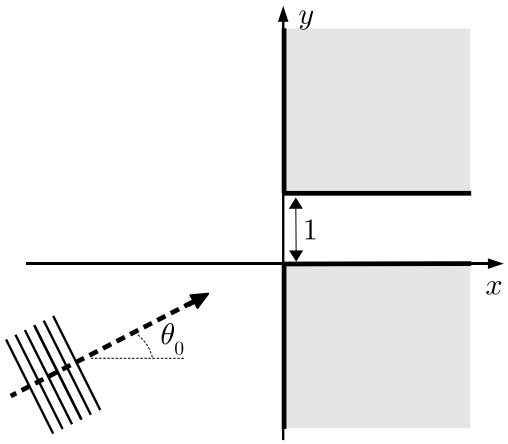


Figure 3.10: A plane wave incident on the open end of a semi-infinite street.

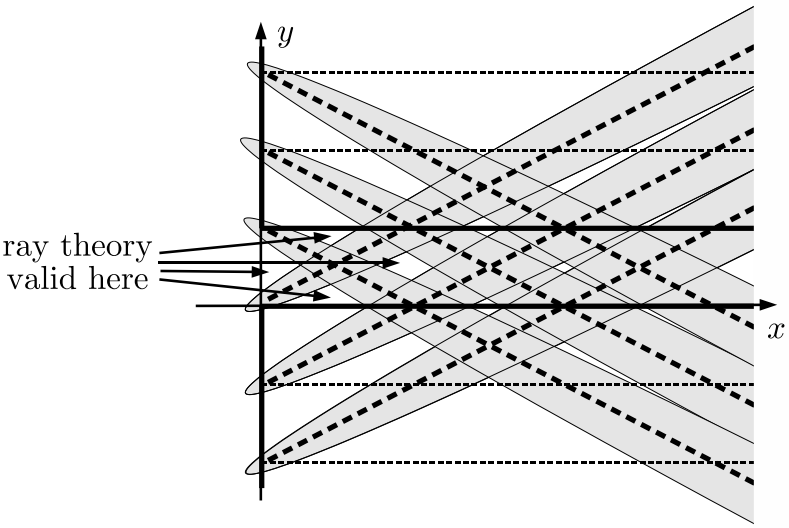


Figure 3.11: Schematic showing the shadow boundary regions arising inside the street for the problem considered in Figure 3.10. Only the singly-diffracted fields are considered here - the multiple reflections of these fields give rise to an infinite set of shadow boundary regions in the image plane, associated with the appropriate 'image edges'. Away from these regions ray theory is valid - note that the width of each shadow boundary region has been exaggerated to make the presentation clearer.

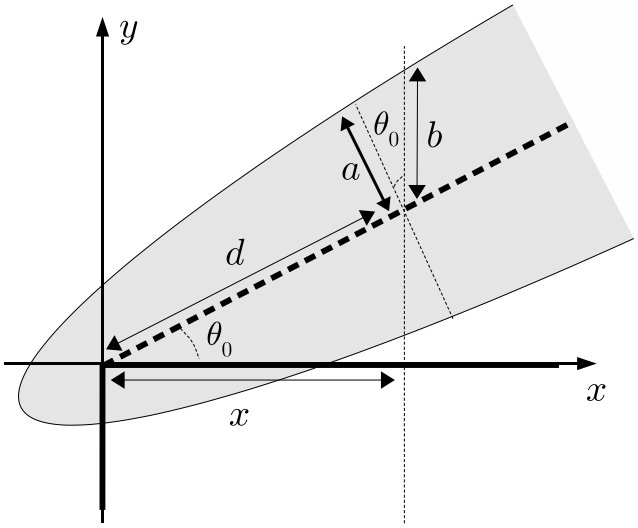


Figure 3.12: Schematic of one of the shadow boundary regions for the problem considered in Figure 3.10.

we nondimensionalise lengths with respect to the street width and consider the case where the nondimensional wavenumber $k \gg 1$. According to GTD, the field inside the street is a sum of the incident wave and its multiple reflections in the street walls, and diffracted ray fields emanating from the edges at $(0, 0)$ and $(0, 1)$, which contribute a higher order correction to the incident and reflected fields. However, because of the nonuniformity of the GTD approximation, this picture is only valid close to the opening, because of the way the shadow boundary regions associated with the edge-diffracted fields 'spread out' with increasing distance down the street (see Figure 3.11).

In order to derive an estimate for how far down the street the ray model holds, let us consider the geometry of one of the shadow boundary regions in more detail (see the schematic in Figure 3.12). We begin by noting that the bounding parabola of the shaded region in Figure 3.12 may be described, as in equation (3.58) of section 3.3.5.1, by the equation

$$k(\sqrt{d^2 + a^2} - d) = \eta, \tag{3.126}$$

where d is distance along the axis of the parabola, a is the half-width (measured normal to the axis), and η is a constant. When $kd \gg 1$ it is easily shown that a

grows like $a \propto \sqrt{d/k}$. Thus when $kx \gg 1$ we find that b, the half-width measured in the y-direction, grows like

$$b \propto \frac{1}{\cos\theta_0}\sqrt{\frac{x}{k\cos\theta_0}}. \tag{3.127}$$

A sufficient condition for the ray approximation to hold across the majority of the street cross-section (which is what we require in order to compute acoustic power flows) is that $b \ll 1$, or equivalently

$$\frac{k}{x}\cos^3\theta_0 \gg 1 \tag{3.128}$$

in our nondimensional variables. In dimensional variables (3.128) is

$$\frac{kw^2}{x}\cos^3\theta_0 \gg 1, \tag{3.129}$$

where w is the street width. The quantity $kw^2\cos^3\theta_0$ is sometimes referred to in optics as the *Rayleigh distance* (or sometimes as the *Fresnel distance*), and (3.129) tells us that ray theory becomes invalid once x is of the order of the Rayleigh distance. Note that the presence of the factor $\cos^3\theta_0$ in (3.129) implies that the Rayleigh distance decreases as the incidence angle θ_0 increases.

In the case of a junction between two streets the situation is more complicated. However, by the modal decomposition of section 3.3.4.1, we may represent the field incident on the junction from the West street as a sum of plane wave 'beams' that are incident on the East street, as illustrated in Figure 3.13 (we shall return to this representation in section 3.6.5). Following the discussion of the previous paragraphs, for each of these plane waves we expect the ray approximation to be valid in the East street, up to the appropriate Rayleigh distance from the junction. By geometrical considerations, we need only consider those modal plane waves for which $|\theta_0| < \theta_* = \arctan w_0/w_1$, where w_0 and w_1 are the widths of the East-West and the North-South streets, respectively, since for larger values of $|\theta_0|$ the beam propagates entirely into the North or South street. For example, when the street widths are equal we have $\theta_* = \pi/4$. In contrast, there is no such restriction on the incidence angle of the plane wave beams which propagate into the North or South streets, and because of this we expect the distance over which the ray model can be used in these streets to be somewhat shorter than in the East street, although we have not, as yet, been able to quantify this difference.

We now attempt to estimate the order of magnitude of the Rayleigh distance in the parameter regime of interest to Dstl. Dstl are interested in frequencies of up to 1kHz,

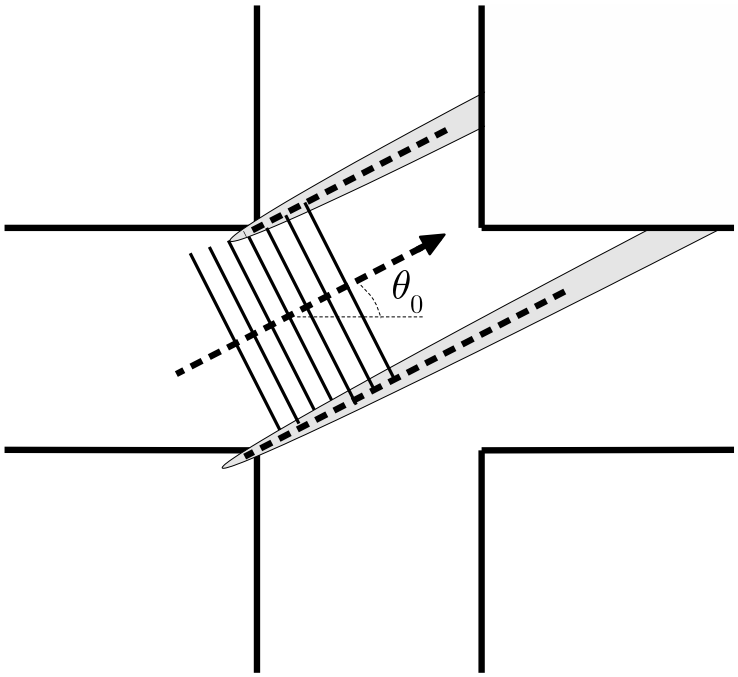


Figure 3.13: Junction between two streets - a modal plane wave 'beam' incident on the open end of the right-hand street.

which corresponds to a spatial wavelength of around 30cm, and hence a dimensional wavenumber $k \approx 20\text{m}^{-1}$. Typical street widths and lengths vary considerably between different urban areas, but as a test case we have considered downtown Manhattan, New York City. In this environment, street widths w and lengths l (as measured from a satellite photograph) typically lie in the range

$$w \in (20\text{m}, 40\text{m}), \tag{3.130}$$

$$l \in (100\text{m}, 200\text{m}). \tag{3.131}$$

For example, with $w = 30\text{m}$ we have $kw^2 \approx 18000\text{m}$, so that for $\theta_0 = 0$ the Rayleigh distance is 18000m, considerably larger than the typical street lengths. For $\theta_0 = \pi/4$ we have $\cos^3\theta_0 = 1/(2\sqrt{2})$, which reduces the Rayleigh distance to around 6000m, although this is still considerably larger than the typical street lengths.

We therefore conclude that the parameter range in which the ray theory limit is valid does overlap with the regime of interest to Dstl. However, it should be remarked that for narrower streets or lower frequencies the Rayleigh distances will be shorter, and a more careful treatment of the diffraction effects may be required (see e.g. [77, 92]), although we do not pursue this matter further here.

3.6.1.2 Calculation of power flows

Under the assumption that diffraction effects can be neglected, the power flow P^E out of the East exit of the junction is computed by incoherently summing the power flows along the ray tubes reaching the exit from each of the image sources defined in (3.39), so that

$$P^E = \frac{1}{2\pi} \sum_{n \in \mathbf{Z}} (1-\alpha)^{|n|} \Theta_n, \tag{3.132}$$

where α is the absorption coefficient of the street containing the source and $\Theta_n = \Theta_n(l, w, y_0)$ is the angular width of the tube of rays from the nth image source reaching the East exit. The geometry of the ray tubes in this case is shown in Figure 3.14(a). Note that all of the image sources, except for the original source, have their 'line-of-sight' partially (or fully) obscured by the presence of the side street exits. Hence (3.132) is actually a finite sum, since only a finite number of image sources can 'see' the East exit of the junction at all. Rewriting (3.132) in terms of the image street representation (see Figure 3.14(b)) simplifies the presentation slightly, so that

$$P^E = \frac{1}{2\pi} \sum_{n=-\left\lfloor \frac{l}{w}+1-y_0 \right\rfloor}^{\left\lfloor \frac{l}{w}+y_0 \right\rfloor} (1-\alpha)^{|n|} \tilde{\Theta}_n, \tag{3.133}$$

where

$$\tilde{\Theta}_n = \tilde{\theta}_n^+ - \tilde{\theta}_n^-, \tag{3.134}$$

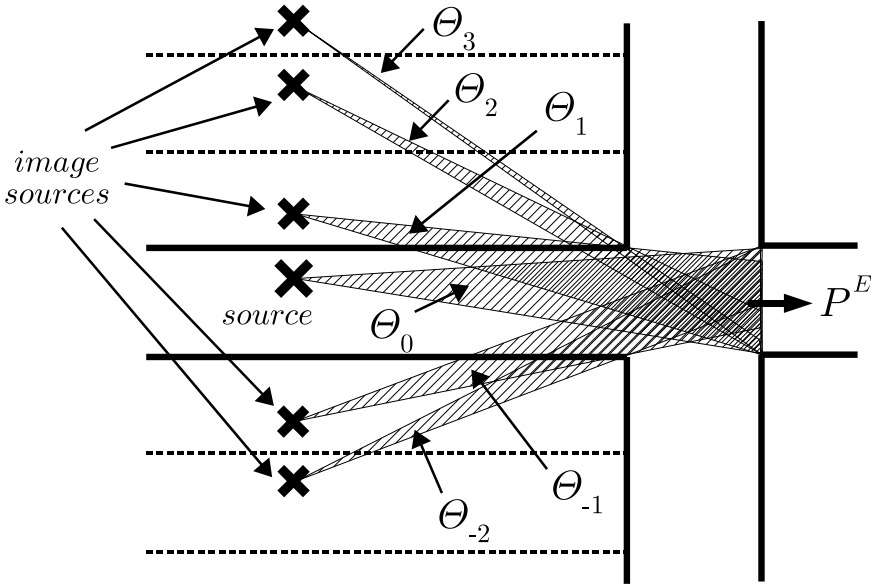
and

$$\begin{aligned} \tilde{\theta}_n^+ &= \begin{cases} \arctan \frac{n+1-y_0}{l+w}, & 0 \le n \le \left\lfloor \frac{l}{w} + y_0 \right\rfloor, \\ \arctan \frac{n+1-y_0}{l}, & -\left\lfloor \frac{l}{w} + 1 - y_0 \right\rfloor \le n < 0, \end{cases} \\ \tilde{\theta}_n^- &= \begin{cases} \arctan \frac{n-y_0}{l}, & 0 < n \le \left\lfloor \frac{l}{w} + y_0 \right\rfloor, \\ \arctan \frac{n-y_0}{l+w}, & -\left\lfloor \frac{l}{w} + 1 - y_0 \right\rfloor \le n \le 0. \end{cases} \end{aligned} \tag{3.135}$$

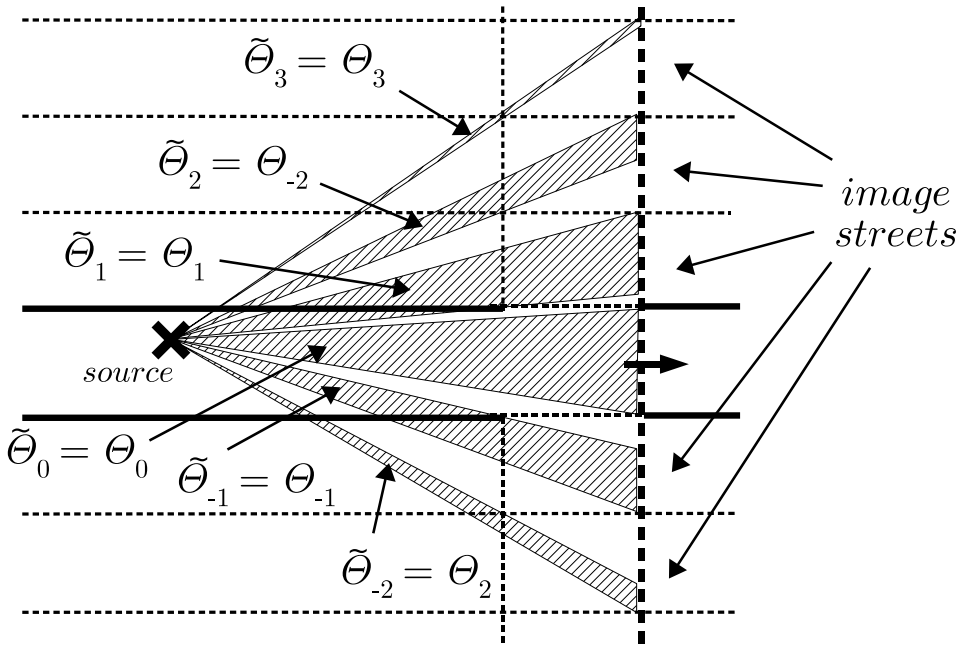
As was found for the sum (3.114), the qualitative behaviour of (3.133) in the limit $l \to \infty$ is dependent on the size of the absorption coefficient α. In the case $\alpha \gg 1/l$ we find that

$$P^E \sim \frac{2-\alpha}{2\pi l \alpha} - \frac{w(2-\alpha)}{2\pi (l\alpha)^2} + O\left(\frac{1}{l^3}\right), \quad l \to \infty, \;\; w = O(1). \tag{3.136}$$

We remark that the parameter w does not enter the expansion until the second order term, and by comparing (3.136) with (3.95), we see that the leading order behaviour



(a) Image source interpretation



(b) Image street interpretation

Figure 3.14: The geometrical interpretation of $\Theta_n(l, w, y_0)$ and $\tilde{\Theta}_n(l, w, y_0)$ - crossroads case.

is the same as if there were no junction at all. The dependence on y_0 does not enter until the $O\left(1/l^3\right)$ term, which has been omitted in (3.136).

When $\alpha = O(1/l)$ we seek to approximate the sum (3.133) by an integral. We first note that, by (3.118),

$$\tilde{\Theta}_n = \begin{cases} \arctan \frac{l+w(n+1-y_0)}{l(l+w)+(n+1-y_0)(n-y_0)}, & -\left\lfloor \frac{l}{w} + 1 - y_0 \right\rfloor \leq n \leq -1, \\ \arctan \frac{l+w}{(l+w)^2-y_0(1-y_0)}, & n = 0, \\ \arctan \frac{l-w(n-y_0)}{l(l+w)+(n+1-y_0)(n-y_0)}, & 1 \leq n \leq \left\lfloor \frac{l}{w} + y_0 \right\rfloor, \end{cases} \tag{3.137}$$

so that

$$\tilde{\Theta}_n \sim \frac{1 - |\frac{wn}{l}|}{l + \frac{n^2}{l}} \left(1 + O\left(\frac{1}{l}\right)\right), \quad l \to \infty, \;\; w = O(1), \tag{3.138}$$

uniformly for all n. Inserting (3.138) into (3.133) and approximating the sums by the appropriate integrals[9], we find that

$$P^E \sim \frac{1}{\pi} \int_0^{\frac{1}{w}} (1-\alpha)^{lt} \frac{1-wt}{1+t^2}\, dt + O\left(\frac{1}{l}\right), \quad l \to \infty, \;\; w = O(1). \tag{3.139}$$

As in the single street case, a Laplace analysis reveals that (3.139) is valid for all $\alpha \ll 1$, agreeing with (3.136) to leading order for $1/l \ll \alpha \ll 1$.

Approximations to the power flows P^N and P^S can be obtained similarly. The ray tube summations are now infinite, with P^N being a sum solely over the image sources $n \leq 0$ and P^S being a sum solely over the image sources $n \geq 0$. We find that for $\alpha \gg 1/l$,

$$\begin{aligned} P^N &\sim \frac{w(1-\alpha)(2-\alpha(1-y_0))}{2\pi l^2 \alpha^2 (2-\alpha)} + O\left(\frac{1}{l^3}\right), \quad l \to \infty, \;\; w = O(1), \\ P^S &\sim \frac{w(1-\alpha)(2-\alpha y_0)}{2\pi l^2 \alpha^2 (2-\alpha)} + O\left(\frac{1}{l^3}\right), \quad l \to \infty, \;\; w = O(1). \end{aligned} \tag{3.140}$$

Unlike in (3.136), the dependence on the parameter y_0 enters at leading order, although the leading order behaviour is now $O\left(1/l^2\right)$, as opposed to the $O\left(1/l\right)$ decay we found for P^E. When $y_0 = 1/2$ the expansions for P^N and P^S coincide, as one would expect.

For $\alpha = O(1/l)$, both P^N and P^S are found to have the same leading order asymptotic behaviour, independent of y_0, namely

$$P^N \sim P^S \sim \frac{1}{2\pi} \left(\int_0^{\frac{1}{w}} (1-\alpha)^{lt} wt\, dt + \int_{\frac{1}{w}}^{\infty} (1-\alpha)^{lt}\, dt \right), \quad l \to \infty, \;\; w = O(1). \tag{3.141}$$

[9]We remark that, like (3.122), (3.139) can be written in terms of exponential integrals.

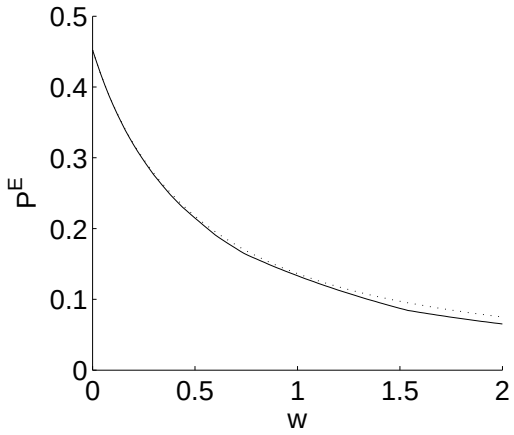


Figure 3.15: Comparison of ray tube sum (3.133) (solid line) and the corresponding integral approximation (3.139) (dotted line) for the power flow past a crossroads, plotted against the side street width w. Parameter values are $l = 2$, $y_0 = 0.3$, $\alpha = 0.02$.

Again, it can be shown that the integral approximations (3.141) are, in fact, valid for $\alpha \ll 1$.

3.6.2 Range of applicability

Although the integral approximations presented in this section have been derived for $l \gg 1$, good agreement with numerical evaluations of the ray tube sums is observed even when l is not particularly large. For example, Figure 3.15 shows a comparison between the ray tube sum (3.133) and the corresponding integral approximation (3.139) in the case $l = 2$.

3.6.3 Interpretation in terms of ray launch angles

The integral approximations (3.139) and (3.141) for the power flows out of the junction in the regime $l \gg 1$, $\alpha \ll 1$ can be rewritten after a change of integration variable $t = \tan\theta$ as

$$P^E \sim \frac{1}{\pi} \int_0^{\theta_*} (1-\alpha)^{l \tan\theta} \, (1 - w \tan\theta) \; d\theta, \tag{3.142}$$

$$P^N \sim P^S \sim \frac{1}{2\pi} \left(\int_0^{\theta_*} (1-\alpha)^{l \tan\theta} w \tan\theta \; d\theta + \int_{\theta_*}^{\frac{\pi}{2}} (1-\alpha)^{l \tan\theta} \, d\theta \right), \tag{3.143}$$

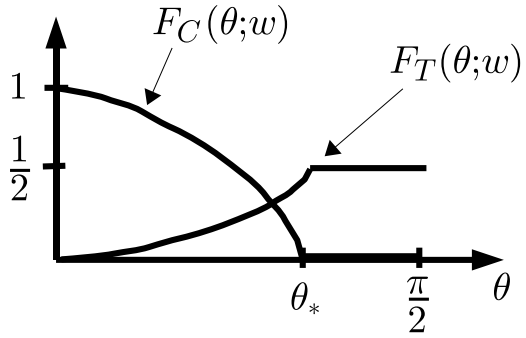


Figure 3.16: The functions F_C and F_T

where $\theta_* = \arctan 1/w$. As in section 3.5.3 we identify θ with the absolute value of the launch angle of a ray emanating from the source. Introducing the functions

$$F_C(\theta; w) := \max\{1 - w\tan\theta, 0\}, \tag{3.144}$$

$$F_T(\theta; w) := \frac{1}{2}\min\{w\tan\theta, 1\}, \tag{3.145}$$

which are plotted in Figure 3.16 for a fixed value of the side street width w, we can rewrite (3.142) and (3.143) as integrals over $\theta \in (0, \pi/2)$ by

$$P^E \sim \frac{1}{\pi}\int_0^{\frac{\pi}{2}} (1-\alpha)^{l\tan\theta} F_C(\theta; w)\, d\theta, \tag{3.146}$$

$$P^N \sim P^S \sim \frac{1}{\pi}\int_0^{\frac{\pi}{2}} (1-\alpha)^{l\tan\theta} F_T(\theta; w)\, d\theta. \tag{3.147}$$

The representations (3.146) and (3.147) imply that the power flows out of the junction can be expressed as integrals of appropriate θ-resolved power densities. The functions $F_C(\theta; w)$ and $F_T(\theta; w)$ describe the way that the power density incident on the junction at a given value of θ is redistributed between the exits of the junction: the function $F_C(\theta; w)$ gives the proportion of the power density that crosses the junction, flowing out of the East exit, and the function $F_T(\theta; w)$ gives the proportion that 'turns the corner' and flows out of each of the North and South exits[10].

3.6.4 Probabilistic interpretation

We now discuss a second interpretation of the functions $F_C(\theta; w)$ and $F_T(\theta; w)$. We first note that upon reaching the junction, a ray emanating from the source with

[10]The fact that $F_C(\theta; w) = 0$ for $\theta > \theta_*$ reflects the geometrical fact that any ray with launch angle greater than θ_* must leave the junction by either the North or South exit (cf. the discussion in section 3.6.1.1).

launch angle θ has a certain offset $q \in (0,1)$ from the bottom wall of the main street and a certain orientation $O = \pm 1$, depending on the sign of the angle between the ray and the horizontal. The exit by which the ray leaves the junction can be determined from the parameters θ, q and O by geometrical considerations.

First suppose that $0 < \theta < \theta_*$. Then for $O = +1$, the ray leaves by the East exit if $0 < q < 1 - w\tan\theta$ and by the North exit if $1 - w\tan\theta < q < 1$. For $O = -1$, the ray leaves by the East exit if $w\tan\theta < q < 1$ and by the South exit if $0 < q < w\tan\theta$. When $\theta > \theta_*$, however, the ray must always leave by either the North exit (if $O = +1$) or the South exit (if $O = -1$), regardless of the value of q.

Now, in the limit $l \to \infty$ the rays in a narrow ray tube of fixed width $d\theta$ around the launch angle θ have their offsets and orientations uniformly and independently distributed over $(0,1)$ and $\{\pm 1\}$, respectively, because of the effect of geometrical spreading. By the observations of the previous paragraph, the probability of a given ray in the ray tube crossing the junction, or turning and exiting by the North or South exits is given exactly by the functions $F_C(\theta; w)$ and $F_T(\theta; w)$, respectively. The expressions (3.146) and (3.147) then imply that the power flows out of the junction can be approximated by integrating the probability densities $F_C(\theta; w)$ and $F_T(\theta; w)$ with respect to the ray angle θ, after multiplication by the relevant absorption factor.

3.6.5 Comparison with [26]

In the case $\alpha = 0$, explicit evaluation of the integral (3.139) gives

$$P^E \sim \frac{1}{2\pi}\left(2\arctan\frac{1}{w} - w\log\left(1 + \left(\frac{1}{w}\right)^2\right)\right), \quad l \to \infty, \;\; w = O(1). \tag{3.148}$$

It is interesting to note that (3.148) agrees exactly with the formula for the power flow past a crossroads from a point source in a network of 3D corridors, as obtained in [26], section II. The correspondence between this 3D problem and our 2D problem will be established shortly; however, we first remark that the method used by Davies to derive his result provides us with an alternative derivation of (3.148) for our 2D problem, based not on an image source method, but on modal decomposition.

Davies' approach is to assume that the field in the street containing the source is given by the modal expansion (3.38). In doing so, Davies implicitly assumes that $l \gg 1$, which also permits the neglect of the exponentially-decaying evanescent terms.

Each propagating mode can be further decomposed into the sum of two plane waves, propagating at angles $\pm\vartheta_m$ relative to the x-axis, where

$$\vartheta_m = \arctan \frac{m\pi}{\kappa_m}. \tag{3.149}$$

For each of these plane waves, the proportion of the associated power incident on the junction that crosses the junction is found by a geometrical argument to be equal to $F_C(\vartheta_m, w)$, as defined in (3.144), diffraction effects being neglected (cf. section 3.6.1.1). Summing over all of the propagating modes and letting $k \to \infty$, Davies claims that the total power flow past the junction can be approximated by an integral, which can be evaluated exactly to give formula (3.148). What is not mentioned in Davies' paper is that before the sum can be replaced by an integral, it is necessary to deal with the problem of resonance in an appropriate way, e.g. by averaging the power flow between two neighbouring resonances, as in section 3.5. We have checked that by treating the resonances in this way, Davies' approach does indeed return the formula (3.148) for our 2D problem.

Note that both our image source method and Davies' modal expansion method require us to take two limits: $k \to \infty$ and $l \to \infty$. In our image source approach, we first took $k \to \infty$, to justify the adoption of the ray approximation, the neglect of diffraction effects and the incoherent summation of the power flows due to each image source, before taking $l \to \infty$ to justify the replacement of the ray tube sum (3.132) by the integral (3.139). In Davies' modal expansion approach, the limits are taken in the opposite order. The fact that the two methods produce the same result proves, importantly, that these two limits commute.

One advantage of the image source method over the modal expansion approach is the ease with which the effects of wall absorption can be included, since the absolute value $|n|$ of the index of each term in the ray tube sum corresponds to the number of wall reflections undergone by the rays in the corresponding ray tube. As an illustration of this, we apply the image source approach to the problem of sound propagation in a network of 3D corridors considered in [26]. As well as demonstrating the correspondence between this 3D problem and our 2D problem, we also generalise Davies' result to the case where the walls of the corridor are absorbing with absorption coefficient α.

With lengths nondimensionalised by the width of the corridor, we denote the height of the corridor by h and assume a point source at $(0, y_0, z_0)$ with $0 < y_0 < 1$ and

$0 < z_0 < h$. To deal with the wall and floor/ceiling reflections we introduce a doubly-infinite array of image sources at the points $(0, y_n, z_m)$, $n, m \in \mathbf{Z}$, where y_n are defined as in (3.39) and

$$z_m = \begin{cases} hm + z_0, & m \text{ even}, \\ hm + (h - z_0), & m \text{ odd}. \end{cases} \tag{3.150}$$

Assuming that the floor/ceiling are perfectly reflecting and that $k \gg 1$, an argument similar to that following (3.287) in Section 3.9.2 proves that for each n the total contribution to the power flow from the image sources $(0, y_n, z_m)$, $m \in \mathbf{Z}$, is proportional to Θ_n, the angular width of the ray tube from the nth image source in the 2D problem. After taking into account wall absorption, summing over n then produces (3.132), and hence the integral approximation (3.139) when $l \gg 1$ and $\alpha \ll 1$.

3.6.6 Other junctions

The integral approximation procedure of section 3.6.1 can be used to calculate acoustic power flows at junctions other than crossroads. For example, in the 'side street' geometry of Figure 3.9(b), the ray tube sums correspoding to the power flows P^E and P^N may be approximated for $l \gg 1$ and $\alpha \ll 1$ by the integrals

$$P^E \sim \frac{1}{\pi} \int_0^{\frac{\pi}{2}} (1 - \alpha)^{l \tan \theta} F_C(\theta; w/2)\, d\theta, \tag{3.151}$$

$$P^N \sim \frac{2}{\pi} \int_0^{\frac{\pi}{2}} (1 - \alpha)^{l \tan \theta} F_T(\theta; w/2)\, d\theta. \tag{3.152}$$

Note that the power loss to a single side street of width w is exactly the same as the combined losses to the two side streets at a crossroads where the ratio between the main and crossing streets is $w/2$. This result is completely intuitive when one considers the geometrical correspondence between these two junction types: reflecting the single side street in the lower wall produces a crossroads with the same side street width w but with a main street width of 2.

Such reflection arguments can be used to study the energy redistribution at other junction types, without the need to repeat the full approximation procedure of section 3.6.1. For example, reflection of the 'T-junction' geometry of Figure 3.9(c) in the far-right wall produces a crossroads of side street width $2w$, so that

$$\begin{aligned} P^W &\sim \frac{1}{\pi} \int_0^{\frac{\pi}{2}} (1 - \alpha)^{l \tan \theta} F_C(\theta; 2w)\, d\theta, \\ P^N \sim P^S &\sim \frac{1}{\pi} \int_0^{\frac{\pi}{2}} (1 - \alpha)^{l \tan \theta} F_T(\theta; 2w)\, d\theta, \end{aligned} \tag{3.153}$$

where P^W should be interpreted as the power flow back down the main street due to reflection off the far wall. Power flows in the 'right-angled bend' geometry of Figure 3.9(d) can be treated similarly.

Asymmetric junctions such as that of Figures 3.9(e) and 3.9(f) can also be considered, although such geometries cannot be treated by a reflection argument. However, it is possible to avoid carrying out the full approximation procedure of section 3.6.1, by appealing to the probabilistic interpretation of section 3.6.4.

We first consider the case depicted in Figure 3.9(e), where $w_2 > 1$. Assuming that the offset and orientation of a ray incident on the junction are random, uniform and independent, geometrical considerations reveal that the probability that the ray crosses the junction and leaves by the East exit is given by the function

$$\tilde{F}_C(\theta; w_1, w_2) = \begin{cases} 1, & 0 < \theta < \theta_*^-, \\ \frac{w_2+1}{2} - w_1 \tan\theta, & \theta_*^- < \theta < \theta_*^+, \\ 0, & \theta_*^+ < \theta < \frac{\pi}{2}, \end{cases} \tag{3.154}$$

where θ_*^-, θ_*^+ are given by

$$\theta_*^- = \arctan \frac{w_2 - 1}{2w_1}, \tag{3.155}$$

$$\theta_*^+ = \arctan \frac{w_2 + 1}{2w_1}. \tag{3.156}$$

The probability that the ray leaves by the North exit is equal to the probability that it leaves by the South exit, and is given by

$$\tilde{F}_T(\theta; w_1, w_2) = \begin{cases} 0, & 0 < \theta < \theta_*^-, \\ \frac{w_1 \tan\theta}{2} - \frac{w_2-1}{2}, & \theta_*^- < \theta < \theta_*^+, \\ \frac{1}{2}, & \theta_*^+ < \theta < \frac{\pi}{2}. \end{cases} \tag{3.157}$$

We then propose the approximations

$$P^E \sim \frac{1}{\pi} \int_0^{\frac{\pi}{2}} (1-\alpha)^{l \tan\theta} \tilde{F}_C(\theta; w_1, w_2)\, d\theta, \tag{3.158}$$

$$P^N \sim P^S \sim \frac{1}{\pi} \int_0^{\frac{\pi}{2}} (1-\alpha)^{l \tan\theta} \tilde{F}_T(\theta; w_1, w_2)\, d\theta. \tag{3.159}$$

In the case of Figure 3.9(f), where $w_2 < 1$, the approximations (3.158) and (3.159) still hold, provided that we modify (3.154) and (3.157) to

$$\tilde{F}_C(\theta; w_1, w_2) = \begin{cases} w_2, & 0 < \theta < \theta_*^-, \\ \frac{w_2+1}{2} - w_1 \tan\theta, & \theta_*^- < \theta < \theta_*^+, \\ 0, & \theta_*^+ < \theta < \frac{\pi}{2}, \end{cases} \tag{3.160}$$

and

$$\tilde{F}_T(\theta; w_1, w_2) = \begin{cases} 2w_1 \tan\theta & 0 < \theta < \theta_*^- \\ \frac{w_1 \tan\theta}{2} - \frac{w_2 - 1}{4} & \theta_*^- < \theta < \theta_*^+ \\ \frac{1}{2} & \theta_*^+ < \theta < \frac{\pi}{2}, \end{cases} \tag{3.161}$$

where now

$$\theta_*^- = \arctan \frac{1 - w_2}{2w_1}. \tag{3.162}$$

There is now the further possibility that the ray is reflected back down the main street towards the source. This occurs with probability

$$\tilde{F}_B(\theta; w_1, w_2) = \begin{cases} 1 - w_2 - 2w_1 \tan\theta, & 0 < \theta < \theta_*^-, \\ 0, & \theta_*^- < \theta < \theta_*^+, \\ 0, & \theta_*^+ < \theta < \frac{\pi}{2}, \end{cases} \tag{3.163}$$

and we then have

$$P^W \sim \frac{1}{\pi} \int_0^{\frac{\pi}{2}} (1 - \alpha)^{l \tan\theta} \tilde{F}_B(\theta; w_1, w_2)\, d\theta. \tag{3.164}$$

To end this section, we remark that this probabilistic approach could, in principle, be applied to the study of a much more general class of junctions than those presented here. For example, it should be possible to remove the requirement that intersecting streets meet at right angles.

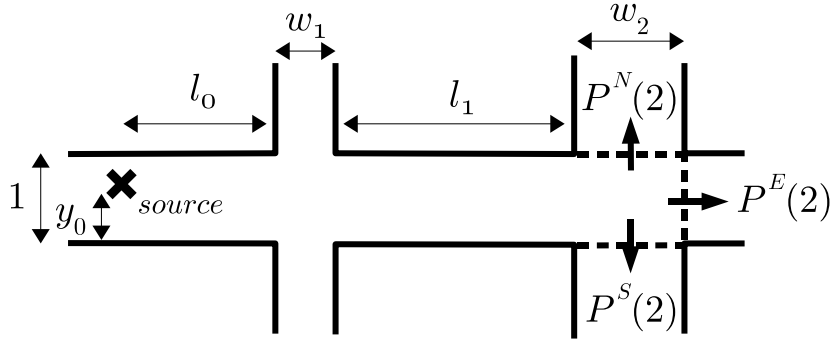


Figure 3.17: Energy redistribution at a second crossroads

3.7 Multiple junctions in 2D

The acoustic power flows in domains involving more than one junction can also be computed using the ray tube model.

3.7.1 Energy redistribution at a second junction in 2D

We begin by considering the two-junction domain illustrated in Figure 3.17. According to the ray tube model[11], the power flow $P^E(2)$ out of the East exit of the second crossroads can be written as a sum

$$P^E(2) = \frac{1}{2\pi} \sum_{n \in \mathbf{Z}} (1-\alpha)^{|n|} \Theta_n, \tag{3.165}$$

where α is the absorption coefficient of the main street and $\Theta_n = \Theta_n(l_0, l_1, w_1, w_2, y_0)$ is the sum of the angular widths of the ray tubes from the nth image source in (3.39) that are incident on the exit in question (in general there may be up to two such ray tubes, as we shall see shortly).

The summation of (3.165) is slightly easier when we transform to the image street representation

$$P^E(2) = \frac{1}{2\pi} \sum_{n \in \mathbf{Z}} (1-\alpha)^{|n|} \tilde{\Theta}_n, \tag{3.166}$$

[11] As discussed in section 3.6.1.1, in order for this approximation to be valid we require $l_1 \ll k w_0^2$.

where, as before,

$$\tilde{\Theta}_n = \begin{cases} \Theta_{-n}, & n \text{ even}, \\ \Theta_n, & n \text{ odd}, \end{cases} \tag{3.167}$$

is the contribution from the nth image street cross-section.

To compute $\tilde{\Theta}_n$ for a given n we must determine the sum of the angular widths of the ray tubes from the source that are incident on the nth image street cross-section. These ray tubes are found by taking the ray tube that would be incident on the nth image street cross-section if the first junction were *not* present and removing those rays which intersect any of the images of the side street entrances of the first junction.

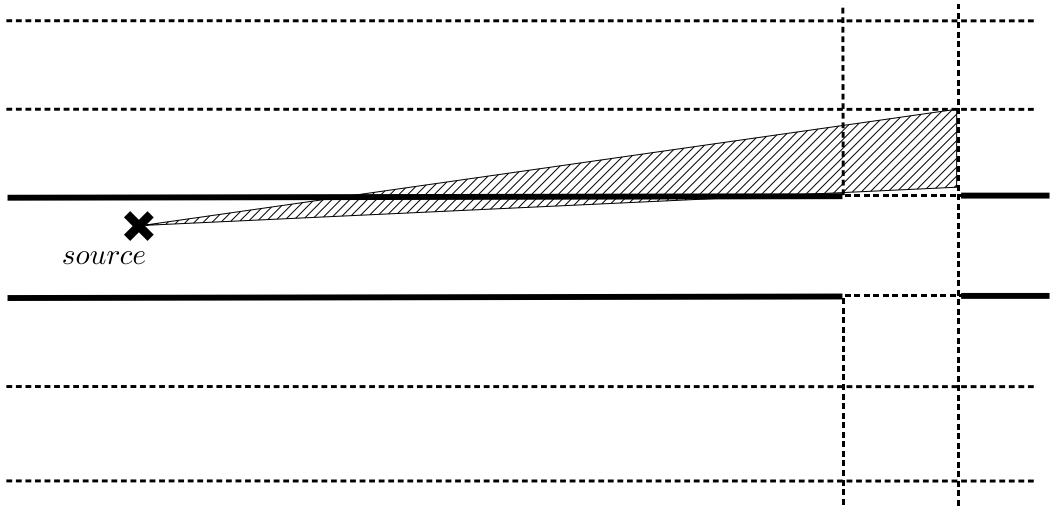
The procedure is illustrated for the case $n = 1$ in Figure 3.18. In this case, the removal of rays lost to the side streets at the first junction divides the ray tube in Figure 3.18(a) into two sub-tubes of angular widths $\tilde{\Theta}_{1,1}$ and $\tilde{\Theta}_{1,2}$ in Figure 3.18(b). We then have that $\tilde{\Theta}_1 = \tilde{\Theta}_{1,1} + \tilde{\Theta}_{1,2}$. A portion of the full ray tube diagram is shown in Figure 3.19.

This algorithmic method of calculating $\tilde{\Theta}_n$ is easily implemented on a computer, and the sum (3.165) can therefore be evaluated numerically. However, a simple closed-form analytical expression for $\tilde{\Theta}_n$ encompassing the algorithmic calculation does not seem to exist.

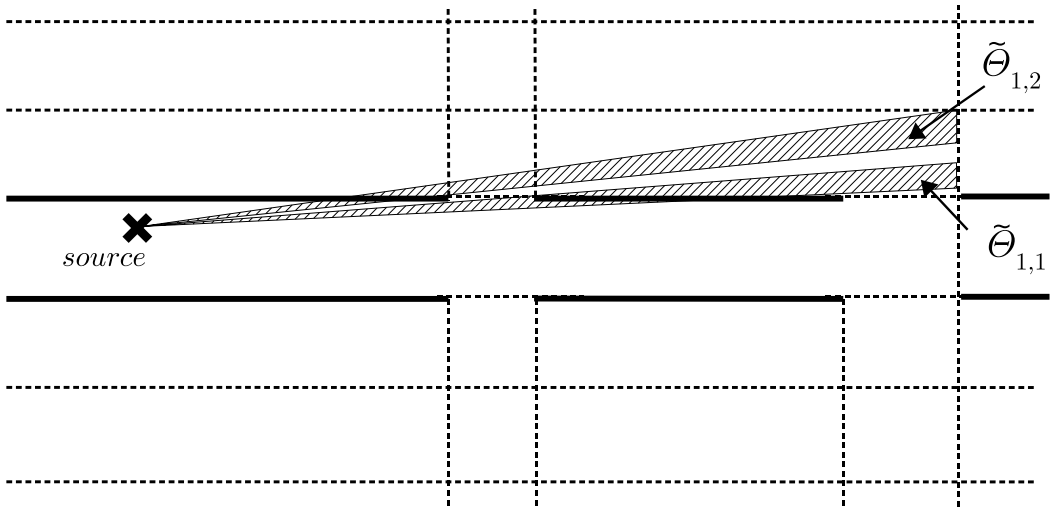
In the single junction case it was found that when $l_0 \gg 1$ and $\alpha \ll 1$ the ray tube sum could be approximated by an integral over power densities propagating at each ray angle θ. We now proceed by assuming that the same is true in the two junction case when $l_0, l_1 \gg 1$ and $\alpha \ll 1$, and the integral approximation we propose is

$$P^E_{\text{app}}(2) = \frac{1}{\pi} \int_0^{\frac{\pi}{2}} (1-\alpha)^{l_0 \tan\theta} F_C(\theta; w_1)(1-\alpha)^{l_1 \tan\theta} F_C(\theta; w_2)\, d\theta. \tag{3.168}$$

Comparing (3.168) with (3.146), we note that the extra factors $(1-\alpha)^{l_1 \tan\theta}$ and $F_C(\theta; w_2)$ in the integrand in (3.168) represent the effects of wall absorption in the second street and energy redistribution at the second junction, respectively.



(a) The ray tube incident on the first image street cross-section in the *absence* of the first junction.



(b) The ray tubes incident on the first image street cross-section in the *presence* of the first junction.

Figure 3.18: Determining the ray tubes incident on the first image street cross-section

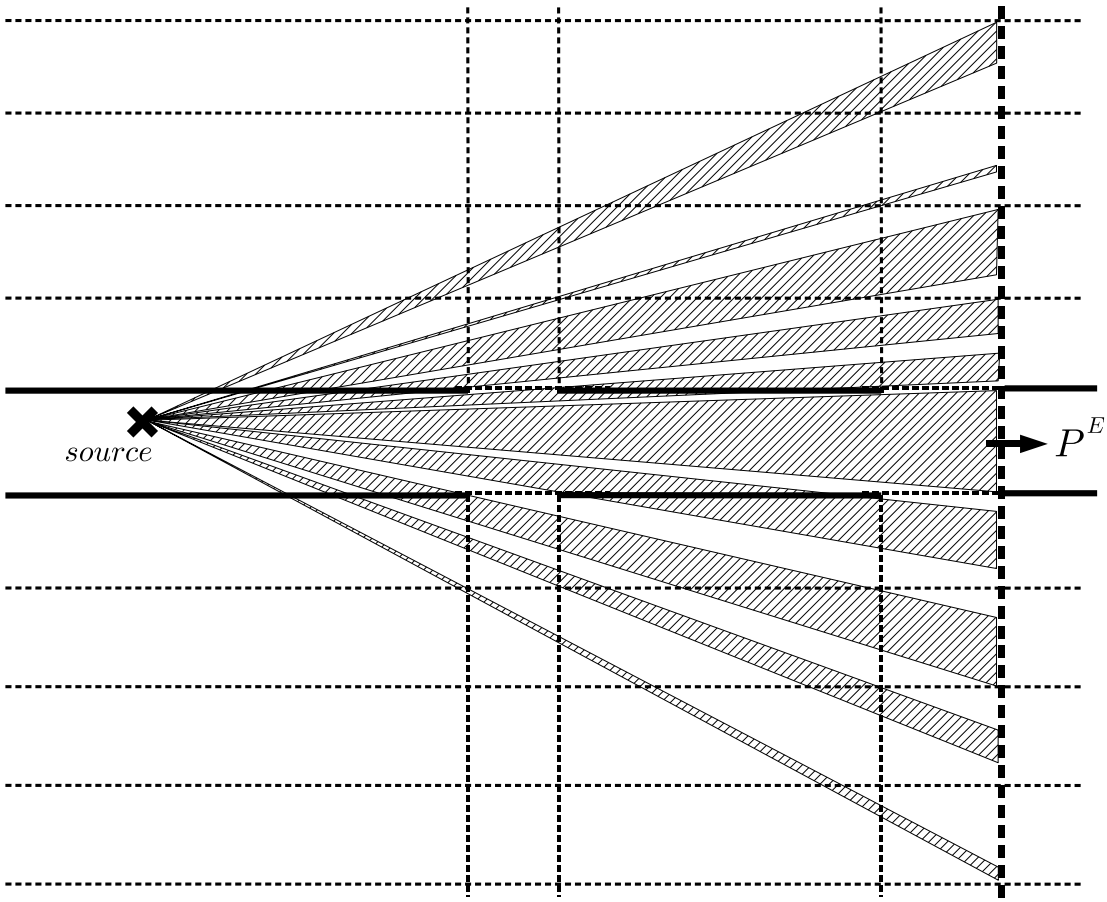


Figure 3.19: A portion of the ray tube diagram at a second crossroads

3.7.2 Validity of integral approximation: expected power flows

As Figure 3.20 demonstrates, numerical experiments do indeed validate (3.168) as a good approximation to (3.165), even for values of l_0 and l_1 as small as 2. However, the lack of a convenient analytical expression for $\tilde{\Theta}_n$ makes it difficult to determine whether (3.168) is truly an asymptotic approximation to (3.165) in the joint limit $l_0, l_1 \gg 1$ with $\alpha \ll 1$. In this section we investigate this question by means of numerical experiments, and make a conjecture about the sense in which the approximation holds.

We note that the discrepancies exhibited in plots (a)-(c) of Figure 3.20, in which $l_1 = l_0$, appear to be larger than those exhibited in plots (d)-(f), in which $l_1 = 1.2l_0$. In Figures 3.21 and 3.22 we plot the error $R = P^E_{\text{app}}(2) - P^E(2)$ as a function of the ratio $\lambda = l_0/l_1$ for three different values of l_0, and for two sets of the other parameter

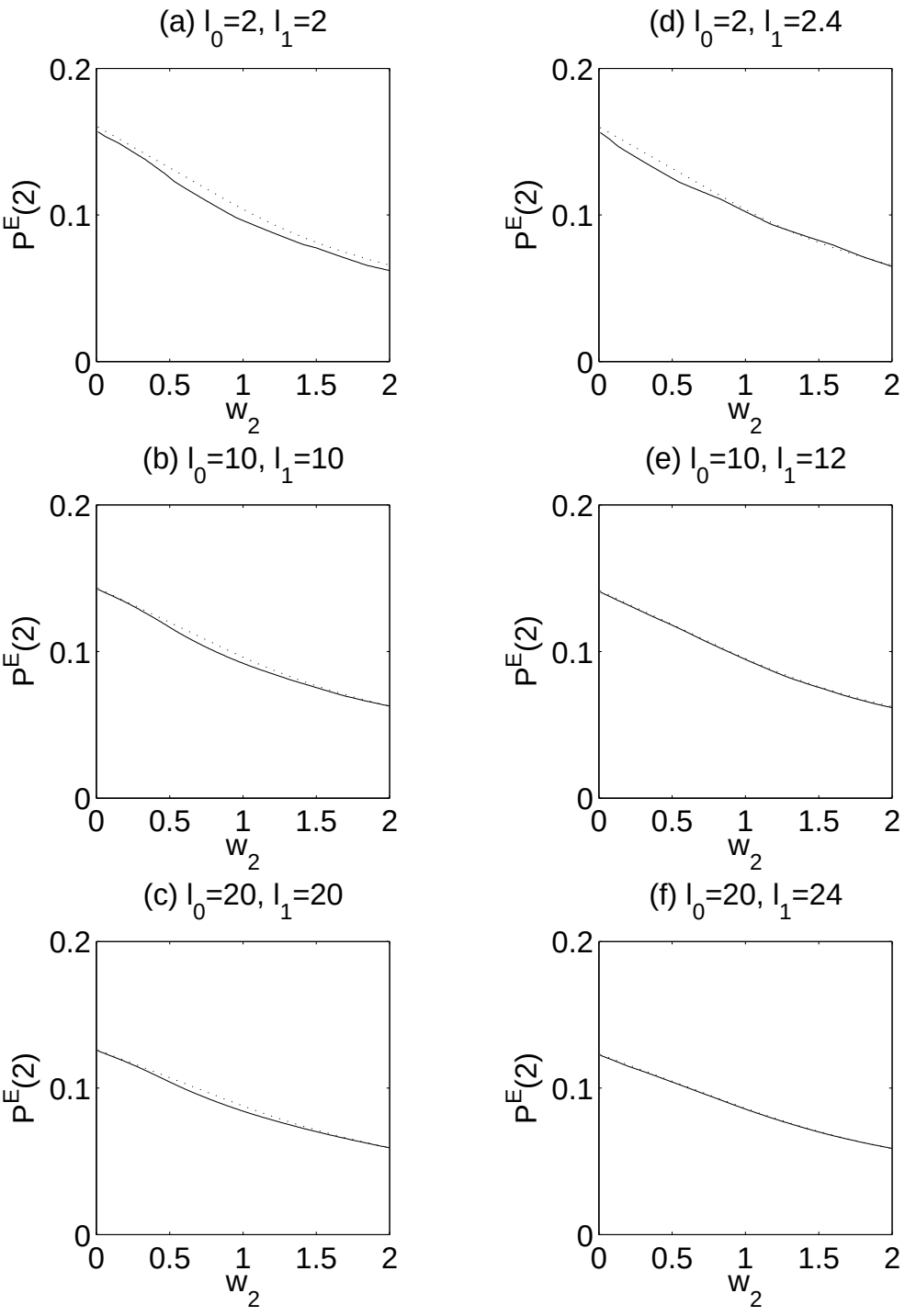


Figure 3.20: Comparison of (3.166) (solid line) and (3.168) (dotted line) for parameter values $y_0 = 0.4$, $w_1 = 0.8$, $\alpha = 0.02$.

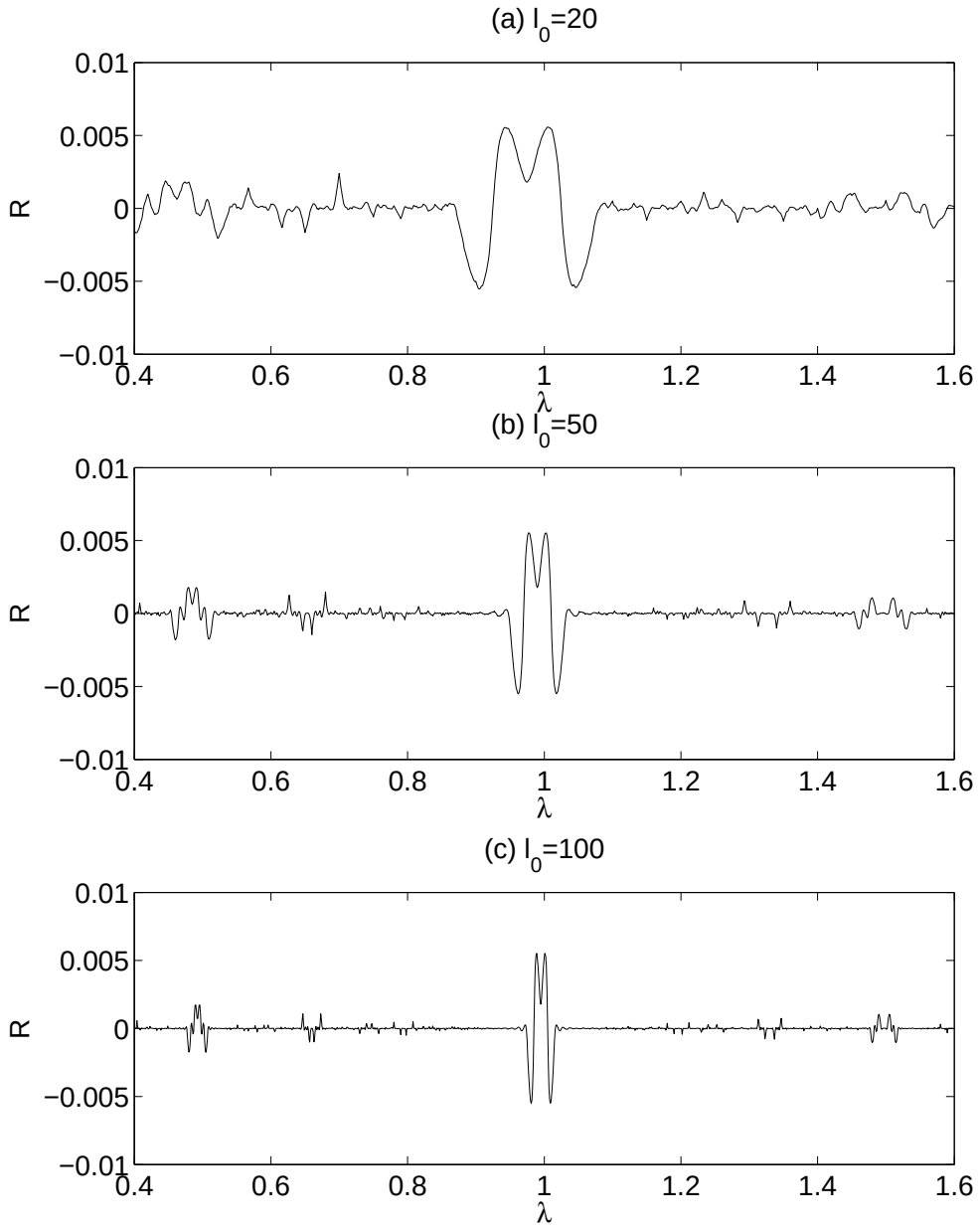


Figure 3.21: Plot of the error R as a function of λ for parameter values $y_0 = 0.5$, $w_1 = 1$, $w_2 = 1$, $\alpha = 0$.

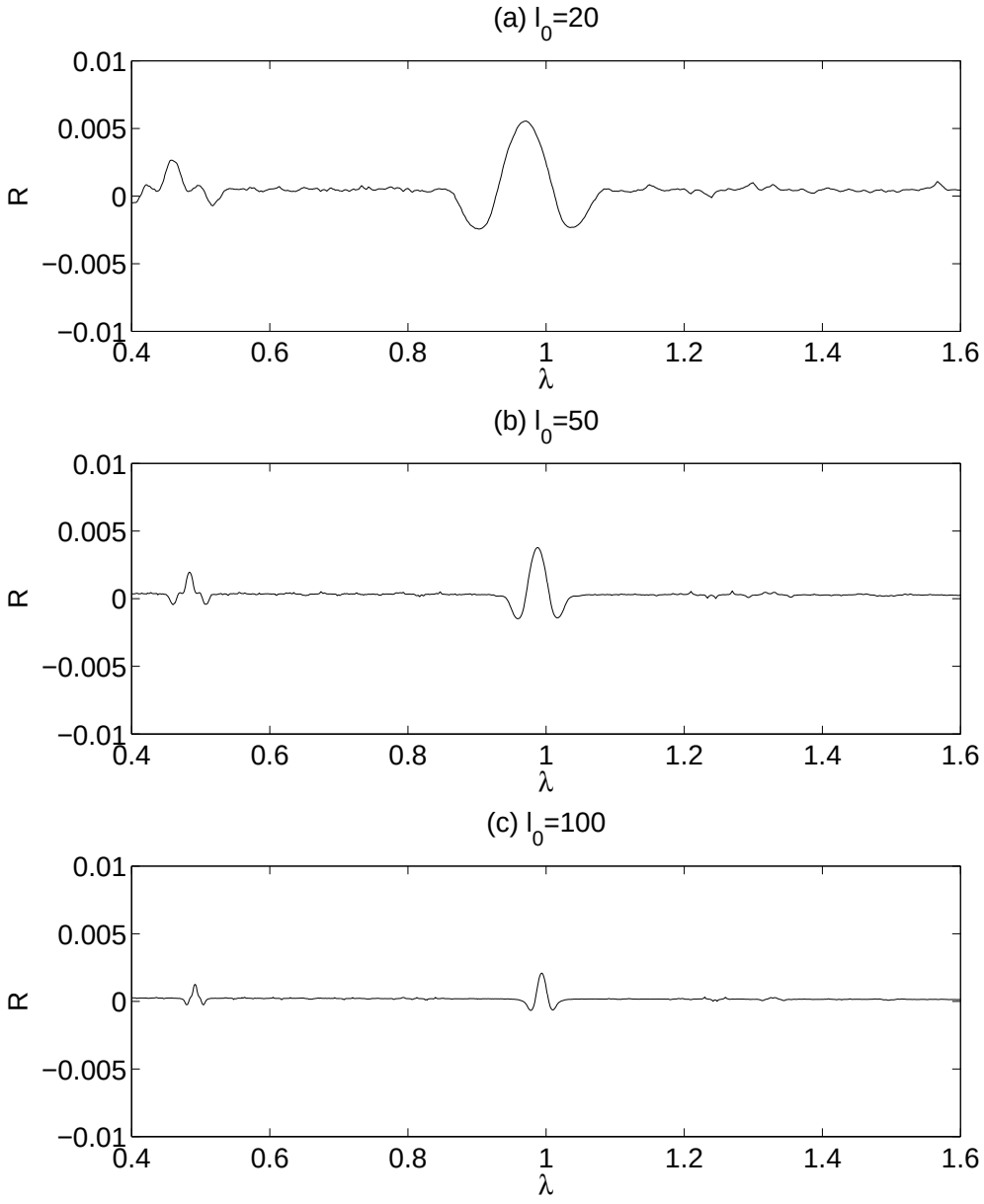


Figure 3.22: Plot of the error R as a function of λ for parameter values $y_0 = 0.4$, $w_1 = 0.8$, $w_2 = 1.2$, $\alpha = 0.02$.

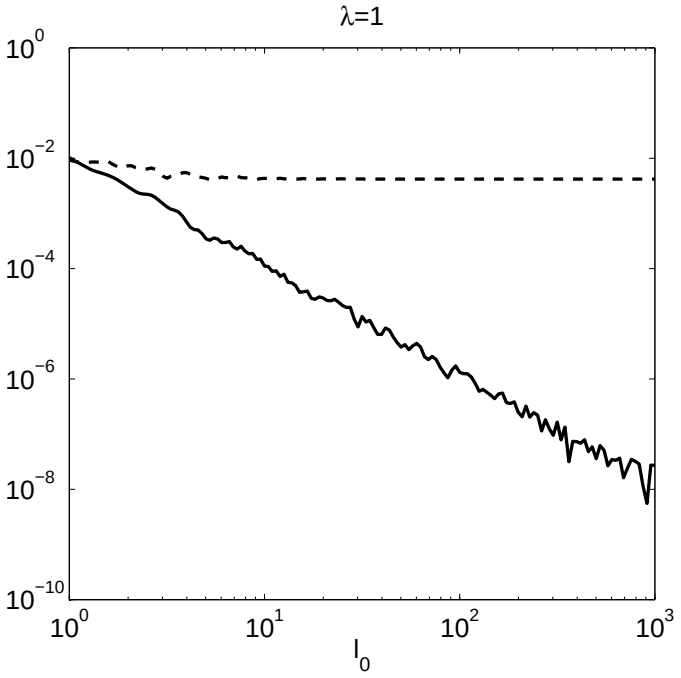


Figure 3.23: Logarithmic plot of $|\langle R\rangle|$ (solid line) and $|R|$ (dashed line) as a function of l_0 for $\lambda = 1$, $\lambda' = \frac{1}{\sqrt{l_0}}$ and parameter values $y_0 = 0.4$, $w_1 = 0.8$, $w_2 = 1$, $\alpha = 0$.

values. In both Figures, the maximum errors are about 0.005, and the largest errors occur near the points vicinity of the points $\lambda = 1, 1/2, 3/2, 2/3, 4/3$, where there are oscillatory regions. In fact, such oscillations are observed on a smaller scale around any rational value of λ, although the amplitude of the oscillations seems to decrease as the denominator in the fractional representation of λ increases. Further numerical experiments suggest that the oscillations persist even for very large l_0, and we conjecture that the convergence is not uniform in λ.

One possible approach to deal with such difficulties is to weaken the notion of convergence required. Suppose we consider a local average of $P^E(2)$ in the vicinity of λ, defining

$$\left\langle P^E(2)\right\rangle := \frac{1}{2\lambda'}\int_{\lambda-\lambda'}^{\lambda+\lambda'} P^E(2)(\tilde{\lambda})\,d\tilde{\lambda}, \tag{3.169}$$

for some $\lambda' > 0$. We conjecture that if λ' is chosen appropriately, the oscillations observed in $P^E(2)$ will average out in the limit as $l_0 \to \infty$, with the averaged behaviour being given by $P^E_{\rm app}(2)$. Numerical experiments suggest that the oscillations in R have a typical wavelength of order $1/l_0$, so we certainly need to choose $\lambda' \gg 1/l_0$. Figure 3.23 shows the average error $\langle R\rangle = P^E_{\rm app}(2) - \left\langle P^E(2)\right\rangle$ in the case where $\lambda' = 1/\sqrt{l_0}$,

alongside the unaveraged error R. The gradient of the solid line is found to be approximately 2, which leads us to conjecture that, in this case, $\langle R \rangle \propto \frac{1}{l_0^2}$ as $l_0 \to \infty$.

We therefore conjecture that $P^E_{\text{app}}(2) \sim \left\langle P^E(2) \right\rangle$ as $l_0 \to \infty$, so that our integral approximation represents an *expected* power flow, in the sense of (3.169). In assessing this interpretation we need to remember our assumption that the street geometry may be known only to a certain degree of accuracy.

The case where the absorption coefficient α takes a value α_0 between the source and the first junction, and a different value α_1 between the first and second junctions, can easily be treated by modifying (3.168) to

$$P^E_{\text{app}}(2) = \frac{1}{\pi} \int_0^{\frac{\pi}{2}} (1-\alpha_0)^{l_0 \tan\theta} F_C(\theta; w_1)\, (1-\alpha_1)^{l_1 \tan\theta} F_C(\theta; w_2)\, d\theta. \tag{3.170}$$

Expected values of the power flows $P^N(2)$ and $P^S(2)$ out of the North and South exits of the second junction can be obtained by replacing the factor of $F_C(\theta; w_2)$ in (3.170) by a factor of $F_T(\theta; w_2)$, so that

$$P^N_{\text{app}}(2) = P^S_{\text{app}}(2) = \frac{1}{\pi} \int_0^{\frac{\pi}{2}} (1-\alpha_0)^{l_0 \tan\theta} F_C(\theta; w_1)\, (1-\alpha_1)^{l_1 \tan\theta} F_T(\theta; w_2)\, d\theta. \tag{3.171}$$

In Figure 3.24 we consider another two-junction geometry. The integral approximations we propose for the expected power flows out of the second junction are

$$P^N_{\text{app}}(2) = \frac{1}{\pi} \int_0^{\frac{\pi}{2}} (1-\alpha_0)^{l_0 \tan\theta} F_T(\theta; w_1)\, (1-\alpha_1)^{\frac{l_1}{w_1} \tan\left(\frac{\pi}{2}-\theta\right)} F_C\left(\frac{\pi}{2} - \theta; \frac{w_2}{w_1}\right) d\theta, \tag{3.172}$$

$$P^E_{\text{app}}(2) = P^W_{\text{app}}(2) = \frac{1}{\pi} \int_0^{\frac{\pi}{2}} (1-\alpha_0)^{l_0 \tan\theta} F_T(\theta; w_1)\, (1-\alpha_1)^{\frac{l_1}{w_1} \tan\left(\frac{\pi}{2}-\theta\right)} F_T\left(\frac{\pi}{2} - \theta; \frac{w_2}{w_1}\right) d\theta. \tag{3.173}$$

The replacement of θ by $\frac{\pi}{2} - \theta$ in the factors for the second street is necessary because of the change of orientation from an East-West street to a North-South street after turning at the first junction.

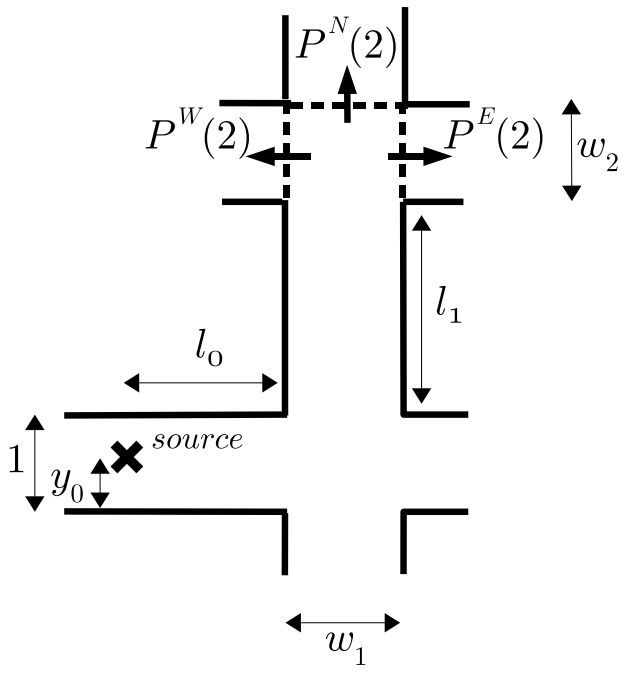


Figure 3.24: Another two-junction geometry

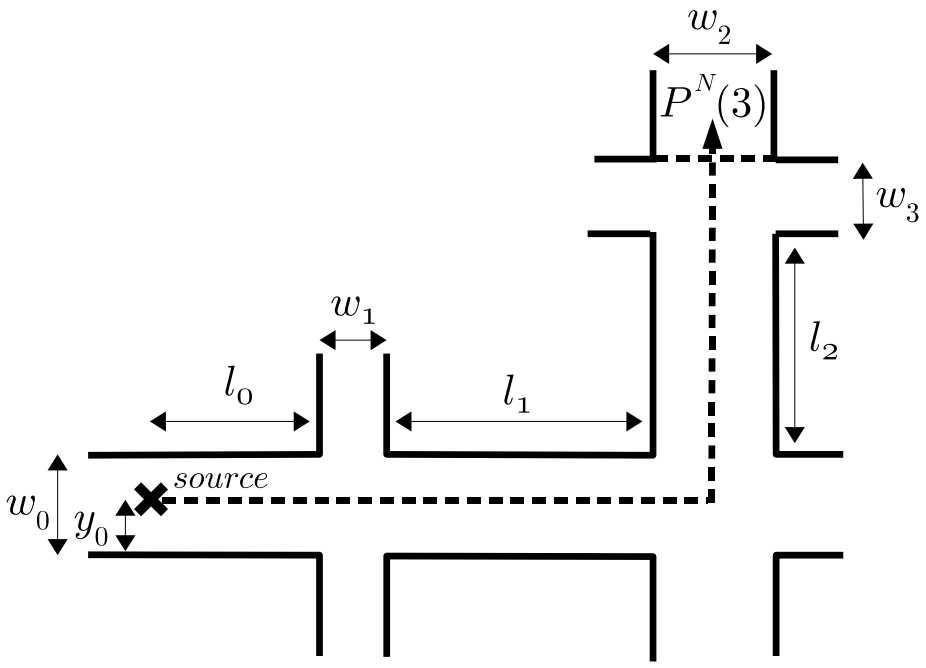


Figure 3.25: A three-junction geometry

3.7.3 More than two junctions

Integral approximations for the expected power flows in domains involving more than two junctions can be constructed similarly.

For example, consider the path shown in Figure 3.25. For generality, the street width w_0 is assumed to be of the same order of magnitude, but not the exactly equal to, the characteristic lengthscale L used in the nondimensionalisation. The expected power flow $P^N(3)$ out of the North exit of the third junction is then approximated by the integral

$$P^N_{\text{app}}(3) = \frac{1}{\pi}\int_0^{\frac{\pi}{2}} (1-\alpha_0)^{\frac{l_0}{w_0}\tan\theta} F_C\left(\theta; \frac{w_1}{w_0}\right) (1-\alpha_1)^{\frac{l_1}{w_0}\tan\theta} F_T\left(\theta; \frac{w_2}{w_0}\right) \tag{3.174}$$

$$\times (1-\alpha_2)^{\frac{l_2}{w_2}\tan\left(\frac{\pi}{2}-\theta\right)} F_C\left(\frac{\pi}{2}-\theta; \frac{w_3}{w_2}\right) d\theta. \tag{3.175}$$

Noting that the function $F_C(\theta; \frac{w_1}{w_0})$ vanishes for $\theta \geq \arctan\frac{w_0}{w_1}$, and that the function $F_R(\frac{\pi}{2}-\theta; \frac{w_3}{w_2})$ vanishes for $\theta \leq \arctan\frac{w_3}{w_2}$, we find that if

$$\frac{w_3}{w_2} \geq \frac{w_0}{w_1}, \tag{3.176}$$

then the expected power flow is zero, since the integrand vanishes completely on the range $(0, \pi/2)$.

The above example illustrates a more general result. Suppose that an arbitrary path through a network of streets crosses a junction in the East-West direction, with the ratio between the widths of the 'side street' and the 'main street' given by R_{EW}, and that this path also crosses a junction in the North-South direction, with the ratio between the widths of the 'side street' and the 'main street' given by R_{NS}. Then if $R_{EW}R_{NS} \geq 1$, the expected power flow along the path is zero.

In particular, in the special case where the street widths are all equal, there is no expected power flow along any path which crosses junctions in both the East-West and North-South directions.

3.8 A network of streets in 2D

In this section we apply the ideas of the previous section to estimate the power flows in an infinite rectangular network of streets intersecting at right-angled crossroads. Indexing the crossroads by $(x, y) \in \mathbf{Z} \times \mathbf{Z}$, we let $l^S_{x,y}, w^S_{x,y}, \alpha^S_{x,y}$ and $l^W_{x,y}, w^W_{x,y}, \alpha^W_{x,y}$ denote the lengths, widths[12] and absorption coefficients of the streets to the South and West respectively of junction (x, y), and we assume that a source lies in the street between junctions $(0, 0)$ and $(1, 0)$, a distance d_0 from the junction $(1, 0)$.

The net power flows $P^N_{x,y}$, $P^E_{x,y}$, $P^S_{x,y}$ and $P^W_{x,y}$ out of a junction (x, y) are made up of contributions from the infinitely many propagation paths that exist between the source and the junction. The expected power flow along any particular path can be estimated by the integral approximation method developed in sections 3.5-3.7, provided that the street lengths are much larger than the street widths, and that the absorption coefficients are small.

Some paths make a positive contribution to the power flow, and others make a negative one, depending on the direction in which the energy is propagating when it crosses the junction exit in question. Some paths make no contribution at all to the power flow, as remarked in section 3.7.3. However, classifying all of the infinitely many paths and explicitly summing their respective contributions to the net power flows would seem to be impracticable in the general case.

To simplify the problem somewhat we consider the special case of a *regular* network in which $l^S_{x,y} = l^W_{x,y} = l$, $w^S_{x,y} = w^W_{x,y} = w$ and $\alpha^S_{x,y} = \alpha^W_{x,y} = \alpha$ for all (x, y), where l, w and α are constant. Furthermore we assume, without loss of generality, that $x \geq 1$ and $y \geq 0$, and try to find the net power flow $P^E_{x,y}$ out of the East exit of the junction (x, y).

3.8.1 Paths of minimal length

Since the power flow along any path through the network decreases with each junction encountered, a crude estimate of $P^E_{x,y}$ can be obtained by considering only those paths that have *minimal length*, in the sense that they encounter exactly $x + y$ junctions.

The number of such paths is shown in Appendix B to be equal to $\binom{x+y-1}{x-1}$. However, only a subset of these paths make a non-zero contribution to the net power flow, since

[12]Note that $w^S_{x,y}$ is constant in y for fixed x and $w^W_{x,y}$ is constant in x for fixed y.

there is no propagation along any path that crosses junctions in both the West-East and South-North directions (see section 3.7.3). The number $M_{x,y}$ of paths of minimal length that do contribute is shown in Appendix B to be

$$M_{x,y} = \begin{cases} \binom{x}{y}, & x \geq y \\ \binom{y-1}{x-1}, & x < y. \end{cases} \tag{3.177}$$

According to the integral approximation method, each of these paths makes the *same* contribution to the power flow, namely

$$P_{x,y}^{E,\text{path}} = \frac{1}{\pi} \int_0^{\frac{\pi}{2}} \beta^{(x-\frac{d_0}{l})\tan\theta + y\tan(\frac{\pi}{2}-\theta)} f(\theta)\, d\theta, \tag{3.178}$$

where

$$\beta = (1-\alpha)^{l/w}, \tag{3.179}$$

and

$$f(\theta) = \begin{cases} F_C(\theta,1)^{x-y} F_T(\theta,1)^y F_T(\frac{\pi}{2}-\theta,1)^y, & x \geq y, \\ F_C(\frac{\pi}{2}-\theta,1)^{y-x} F_T(\theta,1)^x F_T(\frac{\pi}{2}-\theta,1)^x, & x < y. \end{cases} \tag{3.180}$$

Our estimate for the net power flow $P_{x,y}^E$ is then

$$P_{x,y}^E = M_{x,y} P_{x,y}^{E,\text{path}}. \tag{3.181}$$

Plots of (3.181) for different values of β can be found in Figure 3.26. Examination of these plots reveals that the power flow appears to decay *exponentially* with increasing distance from the source, with the fastest decay rate being along the diagonal $x = y$. This result can be verified by direct analysis of (3.181), as we now show.

For ease of presentation we consider the case where $\alpha = 0$ (so that $\beta = 1$). Setting $N = x + y$, $\lambda = y/N = 1 - x/N$ and

$$P_\lambda^E(N) := P_{x,y}^E = P_{(1-\lambda)N,\lambda N}^E, \tag{3.182}$$

$$P_\lambda^{E,\text{path}}(N) := P_{x,y}^{E,\text{path}} = P_{(1-\lambda)N,\lambda N}^{E,\text{path}}, \tag{3.183}$$

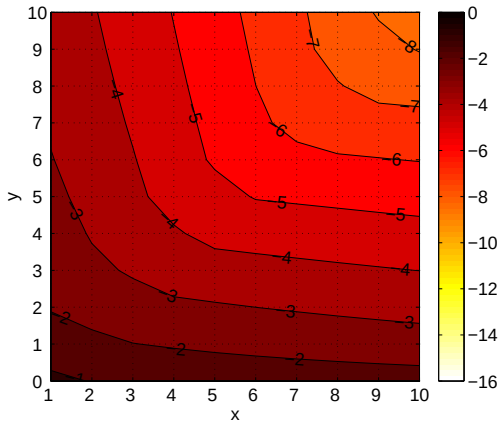
$$M_\lambda(N) := M_{x,y} = M_{(1-\lambda)N,\lambda N}, \tag{3.184}$$

$$\tag{3.185}$$

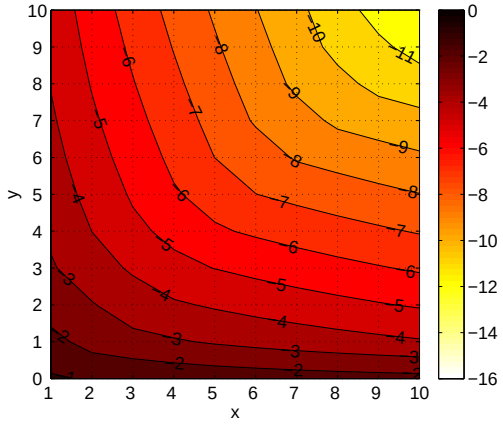
(3.181) becomes

$$P_\lambda^E(N) = M_\lambda(N) P_\lambda^{E,\text{path}}(N). \tag{3.186}$$

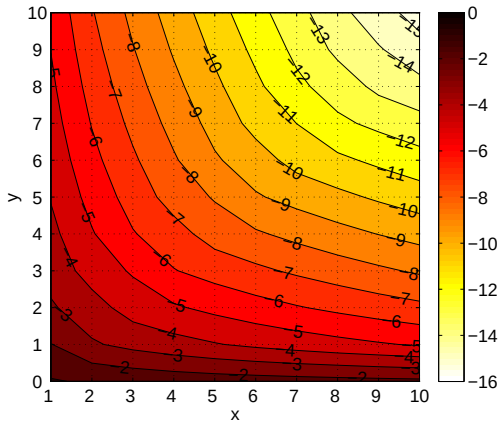
We now investigate the behaviour of $P_\lambda^E(N)$ for N large and $0 \leq \lambda < 1$ fixed.



(a) $\beta = 0.9$



(b) $\beta = 0.6$



(c) $\beta = 0.4$

Figure 3.26: Contour plots of $\log_{10} P^E_{x,y}$ for different values of β, computed by (3.181) (i.e. using only paths of minimal length).

- When $\lambda = 0$ we have $M_0(N) = 1$ and our estimate for $P_0^E(N)$ is

$$P_0^E(N) = \frac{1}{\pi} \int_0^{\frac{\pi}{2}} F_C(\theta; 1)^N \, d\theta, \tag{3.187}$$

or, using (3.144),

$$P_0^E(N) = \frac{1}{\pi} \int_0^{\frac{\pi}{4}} \exp\left[N \log\left(1 - \tan\theta\right)\right] d\theta, \tag{3.188}$$

which is a Laplace-type integral with large parameter N. The main contribution to (3.188) comes from the left endpoint $\theta = 0$, and a local expansion around this point reveals that

$$P_0^E(N) \sim \frac{1}{N\pi}, \quad N \to \infty, \tag{3.189}$$

so that the decay is *algebraic* in the number of junctions encountered.

- Along the diagonal $\lambda = 1/2$ (with N even) there is again only one contributing path of minimal length ($M_{1/2}(N) = 1$ for all N even) and our estimate for $P_{1/2}^E(N)$ is

$$P_{1/2}^E(N) = \frac{1}{\pi} \int_0^{\frac{\pi}{2}} F_T\left(\theta; 1\right)^{N/2} F_T\left(\frac{\pi}{2} - \theta; 1\right)^{N/2} d\theta, \tag{3.190}$$

or, using (3.144),

$$P_{1/2}^E(N) = \frac{2}{\pi} \int_0^{\frac{\pi}{4}} \exp\left[N \left(\frac{1}{2} \log\left(\frac{\tan\theta}{4}\right)\right)\right] d\theta, \tag{3.191}$$

where we have used the symmetry of the integrand to reduce the range of integration to $\theta \in (0, \pi/4)$. Again, this is a Laplace-type integral, although this time the main contribution comes from the right endpoint $\theta = \pi/4$. A local expansion around this point reveals that

$$P_{1/2}^E(N) \sim \frac{2}{N\pi} \left(\frac{1}{2}\right)^N \quad N \to \infty, \ (N \text{ even}), \tag{3.192}$$

and the decay is *exponential* in the number of junctions encountered.

- In the intermediate case $0 < \lambda < 1/2$, we first note that by Stirling's approximation,

$$\begin{aligned} M_\lambda(N) &= \frac{((1-\lambda)N)!}{(\lambda N)!((1-2\lambda)N)!} \\ &\sim \sqrt{\frac{(1-\lambda)}{2\pi N\lambda(1-2\lambda)}} \left(\left(\frac{(1-2\lambda)^2}{\lambda(1-\lambda)}\right)^\lambda \left(\frac{1-\lambda}{1-2\lambda}\right)\right)^N, \quad N \to \infty. \end{aligned} \tag{3.193}$$

Along each of the contributing paths we have

$$P_\lambda^{E,\text{path}}(N) = \frac{1}{\pi}\int_0^{\frac{\pi}{2}} F_T(\theta;1)^{\lambda N} F_T(\pi/2-\theta;1)^{\lambda N} F_C(\theta;1)^{(1-2\lambda)N}\, d\theta, \quad (3.194)$$

or, using (3.144),

$$P_\lambda^{E,\text{path}}(N) = \frac{1}{\pi}\int_0^{\frac{\pi}{4}} \exp\left[N\left(\lambda\log\left(\frac{\tan\theta}{4}\right) + (1-2\lambda)\log\left(1-\tan\theta\right)\right)\right] d\theta, \quad (3.195)$$

since $F_C(\theta;1) = 0$ for $\theta > \pi/4$. The main contribution now comes from the interior point $\theta = \arctan\frac{\lambda}{1-\lambda}$, and we find that

$$P_\lambda^{E,\text{path}}(N) \sim \frac{1}{\pi}\sqrt{\frac{2}{N}}\frac{\sqrt{(1-2\lambda)(1-\lambda)\lambda}}{(1-\lambda)^2+\lambda^2}\left(\left(\frac{\lambda(1-\lambda)}{4(1-2\lambda)^2}\right)^\lambda\left(\frac{1-2\lambda}{1-\lambda}\right)\right)^N, \quad N\to\infty. \quad (3.196)$$

Combining (3.193) and (3.196), we conclude that (3.186) has the asymptotic behaviour

$$P_\lambda^E(N) \sim \frac{1}{N\pi}\left(\frac{1-\lambda}{(1-\lambda)^2+\lambda^2}\right)\left(\frac{1}{2}\right)^{2\lambda N}, \quad N\to\infty. \quad (3.197)$$

- Finally, when $1/2 < \lambda < 1$ a similar analysis reveals that

$$P_\lambda^E(N) \sim \frac{1}{N\pi}\left(\frac{\lambda}{(1-\lambda)^2+\lambda^2}\right)\left(\frac{1}{2}\right)^{2(1-\lambda)N}, \quad N\to\infty. \quad (3.198)$$

We therefore conclude that the power flow decays exponentially in N for all $0 < \lambda < 1$, with the maximum decay rate occurring along the diagonal $\lambda = 1/2$. Note that setting $\lambda = 0$ in expression (3.197) returns the algebraic decay predicted by (3.189). However, with $\lambda = 1/2$ (and N even), both (3.197) and (3.198) return precisely $1/2$ times the prediction of (3.192). The reason for this apparent inconsistency is that in the cases $0 < \lambda < 1/2$ and $1/2 < \lambda < 1$ energy propagates only along rays with launch angles in the ranges $\theta \in (0, \frac{\pi}{4})$ and $\theta \in (\frac{\pi}{4}, \frac{\pi}{2})$, respectively, whereas in the special case $\lambda = 1/2$ energy propagates along rays of all angles $\theta \in (0, \frac{\pi}{2})$. The correct behaviour for $\lambda = 1/2$ can therefore only be recovered by considering the *sum* of the limiting values of (3.197) and (3.198) as $\lambda \to 1/2$ from below and above:

$$P_{1/2}^E(N) \sim P_{1/2-}^E(N) + P_{1/2+}^E(N), \quad N\to\infty. \quad (3.199)$$

3.8.2 Network model

Up to this point we have considered only the contribution from a finite subset of the propagation paths from source to receiver, namely those which have minimal length. In this section we generalise our model to take into account the contribution of *all* the propagation paths through the network.

At each junction in the lattice we define $p^N_{x,y}(\theta)$, $p^E_{x,y}(\theta)$, $p^S_{x,y}(\theta)$, $p^W_{x,y}(\theta)$ to be the θ-resolved power flows out of the junction (x, y) in the North, East, South and West directions, respectively. We expect that the energy redistribution and absorption rules suggested by the integral approximations we have developed will allow us to rewrite our model as a coupled system of partial difference equations satisfied by these quantities. For example, the power flow $p^N_{x,y}(\theta)$ out of the North exit is a sum of contributions flowing in from the East, South and West streets, each involving an appropriate choice of the redistribution functions F_C and F_T.

The appropriate system of partial difference equations for the case of a general network of streets is

$$\begin{aligned}
p^N_{x,y} &= F_C\left(\frac{\pi}{2}-\theta;\frac{w^W_{x,y}}{w^S_{x,y}}\right)(\beta^N_{x,y-1})^{1/t}p^N_{x,y-1} \\
&\quad + F_T\left(\theta;\frac{w^S_{x,y}}{w^W_{x,y}}\right)\left((\beta^E_{x-1,y})^t p^E_{x-1,y}+(\beta^W_{x+1,y})^t p^W_{x+1,y}\right)+\Phi^N_{x,y}, \qquad (3.200)\\
p^E_{x,y} &= F_C\left(\theta;\frac{w^S_{x,y}}{w^W_{x,y}}\right)(\beta^E_{x-1,y})^t p^E_{x-1,y} \\
&\quad + F_T\left(\frac{\pi}{2}-\theta;\frac{w^W_{x,y}}{w^S_{x,y}}\right)\left((\beta^N_{x,y-1})^{1/t}p^N_{x,y-1}+(\beta^S_{x,y+1})^{1/t}p^S_{x,y+1}\right)+\Phi^E_{x,y}, \qquad (3.201)\\
p^S_{x,y} &= F_C\left(\frac{\pi}{2}-\theta;\frac{w^W_{x,y}}{w^S_{x,y}}\right)(\beta^S_{x,y+1})^{1/t}p^S_{x,y+1} \\
&\quad + F_T\left(\theta;\frac{w^S_{x,y}}{w^W_{x,y}}\right)\left((\beta^E_{x-1,y})^t p^E_{x-1,y}+(\beta^W_{x+1,y})^t p^W_{x+1,y}\right)+\Phi^S_{x,y}, \qquad (3.202)\\
p^W_{x,y} &= F_C\left(\theta;\frac{w^S_{x,y}}{w^W_{x,y}}\right)(\beta^W_{x+1,y})^t p^W_{x+1,y} \\
&\quad + F_T\left(\frac{\pi}{2}-\theta;\frac{w^W_{x,y}}{w^S_{x,y}}\right)\left((\beta^N_{x,y-1})^{1/t}p^N_{x,y-1}+(\beta^S_{x,y+1})^{1/t}p^S_{x,y+1}\right)+\Phi^W_{x,y}, \qquad (3.203)
\end{aligned}$$

where

$$t = \tan\theta, \tag{3.204}$$

$$\beta^S_{x,y} = (1-\alpha^S_{x,y})^{\frac{l^S_{x,y}}{w^S_{x,y}}}, \tag{3.205}$$

$$\beta^W_{x,y} = (1-\alpha^W_{x,y})^{\frac{l^W_{x,y}}{w^W_{x,y}}}, \tag{3.206}$$

$$\beta^N_{x,y} = \beta^S_{x,y+1}, \tag{3.207}$$

$$\beta^E_{x,y} = \beta^W_{x+1,y}, \tag{3.208}$$

and Φ^N, Φ^E Φ^S and Φ^W are source terms to be specified according to the distribution of sources in the network. For example, in the case where the source lies in the street between junctions $(0,0)$ and $(1,0)$, the appropriate source functions are zero everywhere except for

$$\Phi^N_{0,0} = \Phi^S_{0,0} = \left(\beta^W_{1,0}\right)^{\frac{\left(l^W_{1,0}-d\right)t}{l^W_{1,0}}} F_T\left(\theta, \frac{w^S_{0,0}}{w^W_{1,0}}\right), \tag{3.209}$$

$$\Phi^W_{0,0} = \left(\beta^W_{1,0}\right)^{\frac{\left(l^W_{1,0}-d\right)t}{l^W_{1,0}}} F_C\left(\theta, \frac{w^S_{0,0}}{w^W_{1,0}}\right), \tag{3.210}$$

$$\Phi^N_{1,0} = \Phi^S_{1,0} = \left(\beta^W_{1,0}\right)^{\frac{d}{l^W_{1,0}}t} F_T\left(\theta, \frac{w^S_{1,0}}{w^W_{1,0}}\right), \tag{3.211}$$

$$\Phi^E_{1,0} = \left(\beta^W_{1,0}\right)^{\frac{d}{l^W_{1,0}}t} F_C\left(\theta, \frac{w^S_{1,0}}{w^W_{1,0}}\right), \tag{3.212}$$

where d is the distance from the source to the junction $(1,0)$.

3.8.2.1 Calculation of net power flows and mean-square pressures

If the system (3.200)-(3.203) can be solved for each θ, net power flows in the network can be found by integrating appropriate combinations of the solutions over $\theta \in (0, \frac{\pi}{2})$. For example, the net power flow $P^E_{x,y}$ out of the East exit of the junction (x,y) is

$$P^E_{x,y} = \int_0^{\frac{\pi}{2}} p^E_{x,y}(\theta) - \left(\beta^W_{x+1,y}\right)^t p^W_{x+1,y}(\theta)\, d\theta. \tag{3.213}$$

Furthermore, knowledge of the θ-resolved power densities also allows us to calculate the average value of the acoustic energy density over a street cross-section. For

example, the average nondimensional (cf. (3.76)) energy density $W_{x,y}$ over the street cross-section halfway between junctions (x, y) and $(x + 1, y)$ is given by

$$W^E_{x,y} = \frac{1}{w^W_{x+1,y}} \int_0^{\frac{\pi}{2}} \frac{\left(\beta^W_{x+1,y}\right)^{t/2} \left(p^E_{x,y}(\theta) + p^W_{x+1,y}(\theta)\right)}{\cos\theta}\, d\theta. \tag{3.214}$$

As explained in section 3.4.2, (3.214) is proportional to the average value of the mean-square pressure over the same street cross-section.

3.8.2.2 Exact solution in a regular network

The system (3.200)-(3.203) is difficult to solve analytically. However, in the special case of a regular network the system decouples and an analytical solution can be found, as we now demonstrate.

The resulting equations have different forms depending on whether $\theta < \pi/4$ or $\theta > \pi/4$, and we first consider the case $0 < \theta < \pi/4$. For notational convenience we introduce the shift operators X, Y defined on a quantity $f_{x,y}$ by

$$(Xf)_{x,y} = f_{x+1,y}, \tag{3.215}$$

$$(Yf)_{x,y} = f_{x,y+1}. \tag{3.216}$$

In this notation the system (3.200)-(3.203) becomes

$$p^N = \frac{t}{2}\beta^t(X^{-1}p^E + Xp^W) + \Phi^N, \tag{3.217}$$

$$p^E = (1-t)\beta^t X^{-1}p^E + \frac{1}{2}\beta^{1/t}(Y^{-1}p^N + Yp^S) + \Phi^E, \tag{3.218}$$

$$p^S = \frac{t}{2}\beta^t(X^{-1}p^E + Xp^W) + \Phi^S, \tag{3.219}$$

$$p^W = (1-t)\beta^t Xp^W + \frac{1}{2}\beta^{1/t}(Y^{-1}p^N + Yp^S) + \Phi^W, \tag{3.220}$$

and by eliminating p^E, p^S and p^W from (3.217)-(3.220) we may obtain a single partial difference equation satisfied by p^N of the form

$$L[p^N] = \psi, \tag{3.221}$$

where

$$\begin{aligned} L &:= \frac{\beta^{1/t}}{4}\left(X + X^{-1} - 2\rho\right)\left(Y + Y^{-1}\right) + \frac{(1-t)}{t}\left(X + X^{-1} - (\rho^{-1} + \rho)\right) \\ \psi &:= -\frac{\beta^{1/t}}{4}\left(X + X^{-1} - 2\rho\right) Y\left(\Phi^S - \Phi^N\right) - \frac{1}{2}\left(\left(X^{-1} - \rho\right)\Phi^E + (X - \rho)\Phi^W\right) \\ &\qquad + \frac{(1-t)}{t}\left(X + X^{-1} - (\rho^{-1} + \rho)\right)\Phi^N, \end{aligned} \tag{3.222}$$

and $\rho = (1-t)\beta^t$.

The source functions (3.209)-(3.212) become

$$\Phi^N_{0,0} = \Phi^S_{0,0} = \beta^{\frac{(l-d)t}{l}} \left(\frac{t}{2\pi}\right), \tag{3.223}$$

$$\Phi^W_{0,0} = \beta^{\frac{(l-d)t}{l}} \left(\frac{1-t}{\pi}\right), \tag{3.224}$$

$$\Phi^N_{1,0} = \Phi^S_{1,0} = \beta^{\frac{dt}{l}} \left(\frac{t}{2\pi}\right), \tag{3.225}$$

$$\Phi^E_{1,0} = \beta^{\frac{dt}{l}} \left(\frac{1-t}{\pi}\right), \tag{3.226}$$

and ψ is found to be zero everywhere except for

$$\psi_{0,0} = \frac{1}{2\pi}\left(\beta^{\frac{dt}{l}}(1-t) - \beta^{-\frac{dt}{l}}\right), \tag{3.227}$$

$$\psi_{1,0} = \frac{1}{2\pi}\left(\beta^{\frac{(l-d)t}{l}}(1-t) - \beta^{-\frac{(l-d)t}{l}}\right). \tag{3.228}$$

To solve equation (3.221) we first note that by analogy to the theory of linear partial differential equations with constant coefficients, if we can find a 'fundamental solution' $G_{x,y}$ satisfying the equation

$$L[G_{x,y}] = \delta_{x,y}, \tag{3.229}$$

where

$$\delta_{x,y} = \begin{cases} 1, & (x,y) = (0,0), \\ 0, & \text{otherwise}, \end{cases} \tag{3.230}$$

then a formal solution of the original problem (3.221) is provided by the convolution

$$p^N_{x,y} = (\psi * G)_{x,y} := \sum_{i,j} \psi_{i,j} X^{-i} Y^{-j} G_{x,y}. \tag{3.231}$$

Equation (3.229) can be solved by an application of the transform methods employed in [87], p. 365, or [89] to solve similar problems. We form the double Fourier series

$$F(\xi,\eta) := \sum_{x=-\infty}^{\infty} \sum_{y=-\infty}^{\infty} G_{x,y}\, e^{i(\xi x + \eta y)}, \tag{3.232}$$

and note that applying the translations X and Y to $G_{x,y}$ corresponds to multiplying $F(\xi,\eta)$ by $e^{-i\xi}$ and $e^{-i\eta}$, respectively. Under the transformation (3.232), equation (3.229) becomes

$$F(\xi,\eta) = \frac{1}{K(\xi,\eta)}, \tag{3.233}$$

where

$$K(\xi,\eta) = \beta^{1/t}\,(\cos\xi - \rho)\cos\eta + \frac{(1-t)}{t}\left(2\cos\xi - (\rho^{-1}+\rho)\right). \tag{3.234}$$

A formal solution of (3.229) is then given by

$$\begin{aligned} G_{x,y} &= \frac{1}{4\pi^2}\int_{-\pi}^{\pi}\int_{-\pi}^{\pi}\frac{e^{-i(\xi x+\eta y)}}{K(\xi,\eta)}\,d\xi d\eta \\ &= \frac{1}{\pi^2}\int_{0}^{\pi}\int_{0}^{\pi}\frac{\cos\xi x\cos\eta y}{K(\xi,\eta)}\,d\xi d\eta, \end{aligned} \tag{3.235}$$

since $K(\xi,\eta)$ is even in both ξ and η. We remark that for $0<t<1$ and $0<\beta<1$, $K(\xi,\eta)$ is continuous and does not vanish on the square $[0,\pi]\times[0,\pi]$, which is enough to guarantee convergence of the integral in (3.235) for all $(x,y)\in\mathbf{Z}\times\mathbf{Z}$.

In Appendix C we show how the η-integration in (3.235) can be carried out explicitly to give

$$G_{x,y} = -\frac{1}{\pi}\int_{0}^{\pi}\frac{\cos\xi x\, z^{|y|}}{\sqrt{b^2-a^2}}\,d\xi, \tag{3.236}$$

where[13]

$$a = \beta^{1/t}(\cos\xi - \rho), \tag{3.237}$$

$$b = \frac{(1-t)}{t}\left(2\cos\xi - (\rho^{-1}+\rho)\right), \tag{3.238}$$

$$z = -\frac{1}{a}\left(b + \sqrt{b^2-a^2}\right). \tag{3.239}$$

With p^N determined by (3.231) and (3.236), the other variables p^E, p^S and p^W can be expressed in terms of p^N as follows:

$$p^S = p^N + (\Phi^S - \Phi^N), \tag{3.240}$$

$$p^E = \left[1-\rho X^{-1}\right]^{-1}\left(\frac{\beta^{1/t}}{2}\left((Y+Y^{-1})p^N + Y(\Phi^S-\Phi^N)\right) + \Phi^E\right), \tag{3.241}$$

$$p^W = \left[1-\rho X\right]^{-1}\left(\frac{\beta^{1/t}}{2}\left((Y+Y^{-1})p^N + Y(\Phi^S-\Phi^N)\right) + \Phi^W\right). \tag{3.242}$$

[13]For the purposes of Appendix C we remark that $b<0$ in (3.238).

The inverse operators $[1-\rho X^{\pm 1}]^{-1}$ in (3.241) and (3.242) are given formally by the sums

$$\left[1-\rho X^{\pm 1}\right]^{-1} = \sum_{n=0}^{\infty} (\rho X^{\pm 1})^n, \tag{3.243}$$

which converge under fairly weak assumptions on p^N, Φ^N, Φ^E, Φ^S and Φ^W (e.g. boundedness), because $0 < \theta < \frac{\pi}{4}$ implies that $0 < \rho < 1$. In fact the action of (3.243) on p^N can be evaluated explicitly using the trigonometric identity

$$\sum_{n=0}^{\infty} \rho^n \cos\xi(x \pm n) = \frac{\cos\xi x - \rho\cos\xi(x \mp 1)}{1+\rho^2 - 2\rho\cos\xi}, \tag{3.244}$$

a proof of which is given in Appendix C.

The result of this calculation is that the solution of (3.217)-(3.220) can be written as

$$p^N = \psi * G, \tag{3.245}$$

$$p^E = \psi * H^+ + S_1, \tag{3.246}$$

$$p^S = \psi * G + S_2, \tag{3.247}$$

$$p^W = \psi * H^- + S_3, \tag{3.248}$$

where

$$H^{\pm}_{x,y} = -\frac{\beta^{1/t}}{2\pi} \int_0^{\pi} \frac{(\cos\xi x - \rho\cos\xi(x \pm 1))\ \left(z^{|y+1|} + z^{|y-1|}\right)}{(1+\rho^2 - 2\rho\cos\xi)\sqrt{b^2-a^2}}\, d\xi, \tag{3.249}$$

and

$$S_1 = \sum_{n=0}^{\infty} \left(\rho X^{-1}\right)^n \left(\frac{\beta^{1/t}}{2} Y(\Phi^S - \Phi^N) + \Phi^E\right), \tag{3.250}$$

$$S_2 = \Phi^S - \Phi^N, \tag{3.251}$$

$$S_3 = \sum_{n=0}^{\infty} (\rho X)^n \left(\frac{\beta^{1/t}}{2} Y(\Phi^S - \Phi^N) + \Phi^W\right). \tag{3.252}$$

When $\pi/4 < \theta < \pi/2$, the system (3.217)-(3.220) is replaced by

$$p^N = \left(1 - \frac{1}{t}\right) \beta^{1/t} Y^{-1} p^N + \frac{1}{2}\beta^t \left(X^{-1} p^E + X p^W\right) + \Phi^N, \tag{3.253}$$

$$p^E = \frac{1}{2t}\beta^{1/t} \left(Y^{-1} p^N + Y p^S\right) + \Phi^E, \tag{3.254}$$

$$p^S = \left(1 - \frac{1}{t}\right) \beta^{1/t} Y p^S + \frac{1}{2}\beta^t \left(X^{-1} p^E + X p^W\right) + \Phi^S, \tag{3.255}$$

$$p^W = \frac{1}{2t}\beta^{1/t} \left(Y^{-1} p^N + Y p^S\right) + \Phi^W. \tag{3.256}$$

and the source functions are now zero everywhere except for

$$\Phi^N_{0,0} = \Phi^S_{0,0} = \beta^{\frac{(l-d)t}{l}} \left(\frac{1}{2\pi}\right), \tag{3.257}$$

$$\Phi^N_{1,0} = \Phi^S_{1,0} = \beta^{\frac{dt}{l}} \left(\frac{1}{2\pi}\right). \tag{3.258}$$

Noting that (3.253)-(3.256) is simply (3.217)-(3.220) with

$$N \leftrightarrow E \tag{3.259}$$

$$S \leftrightarrow W \tag{3.260}$$

$$t \leftrightarrow 1/t \tag{3.261}$$

$$X \leftrightarrow Y, \tag{3.262}$$

the solution of (3.253)-(3.256) is easily found to be

$$p^N = \tilde{\psi} * \tilde{H}^+ + \tilde{S}_1 \tag{3.263}$$

$$p^E = \tilde{\psi} * \tilde{G} \tag{3.264}$$

$$p^S = \tilde{\psi} * \tilde{H}^- + \tilde{S}_3 \tag{3.265}$$

$$p^W = \tilde{\psi} * \tilde{G} + \tilde{S}_2, \tag{3.266}$$

where $\tilde{\psi}$, $\tilde{S}_i$ are the previously defined expressions ψ, S_i under the transformations (3.259)-(3.262), and

$$\tilde{G}_{x,y} = G_{y,x}, \tag{3.267}$$

$$\tilde{H}^{\pm}_{x,y} = H^{\pm}_{y,x}, \tag{3.268}$$

under the transformation $t \leftrightarrow 1/t$. By (3.257)-(3.258) we find that $\tilde{\psi}$ is zero everywhere except for

$$\tilde{\psi}_{0,0} = -\frac{1-t}{2\pi t}\beta^{1/t+\frac{(l-d)t}{l}}, \tag{3.269}$$

$$\tilde{\psi}_{1,0} = -\frac{1-t}{2\pi t}\beta^{1/t+\frac{dt}{l}}, \tag{3.270}$$

$$\tilde{\psi}_{0,-1} = \tilde{\psi}_{0,1} = -\frac{1}{4\pi}\beta^{\frac{(l-d)t}{l}}, \tag{3.271}$$

$$\tilde{\psi}_{1,-1} = \tilde{\psi}_{1,1} = -\frac{1}{4\pi}\beta^{\frac{dt}{l}}. \tag{3.272}$$

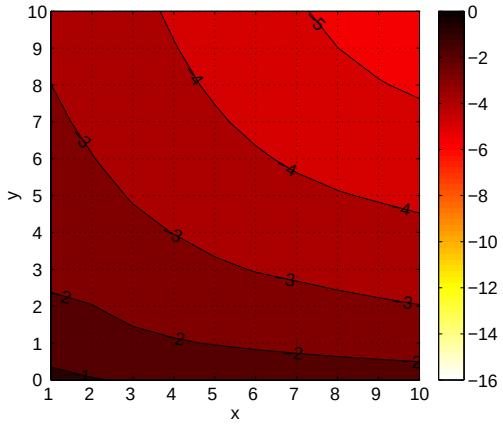
In Figure 3.27 we show logarithmic plots of the net power flow P^E defined by (3.213) for three different values of β. Comparing these to Figure 3.26 we note

that the anisotropic decay predicted by the minimal length paths approach is clearly visible, although, as might have been expected, the minimal length path calculation underestimates the power flow derived via the full network model. The modulus of the relative error between the minimal path length calculation (3.181) and the full network model result (3.213) is plotted in Figure 3.28. Note that the relative error decreases as β decreases, so that the contribution of the non-minimal-length paths becomes less important as the amount of wall absorption increases.

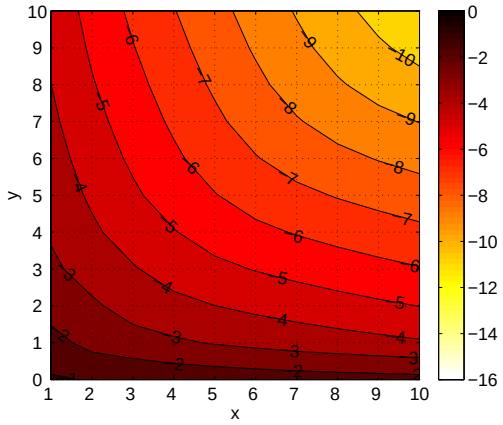
As remarked in section 3.8.2.1, knowledge of the power densities $p^N_{x,y}(\theta)$, $p^E_{x,y}(\theta)$, $p^S_{x,y}(\theta)$, $p^W_{x,y}(\theta)$ also allows us to estimate average energy densities and mean-square pressures in the network. For example, in Figure 3.29 we show logarithmic plots of the average energy density W^E defined by (3.214) for three different values of β.

3.8.2.3 The case $\beta = 1$ ($\alpha = 0$)

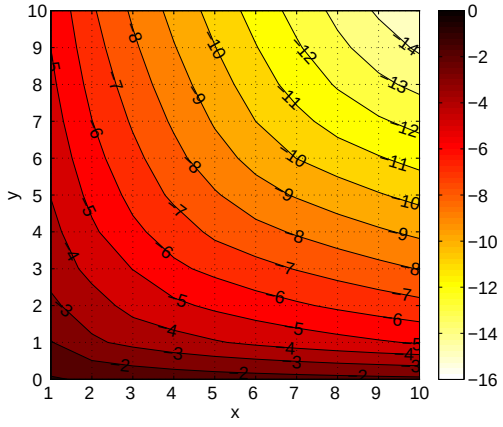
We remark that when $\beta = 1$ ($\alpha = 0$) the integral (3.235) is no longer convergent, and the θ-resolved power flows are no longer well-defined. However, it is still possible to compute net power flows such as (3.213) by considering the limiting value of the net power flow as $\beta \to 1$, which is well-defined because the singularities in $p^E_{x,y}$ and $p^W_{x,y+1}$ for $\beta = 1$ exactly cancel.



(a) $\beta = 0.9$

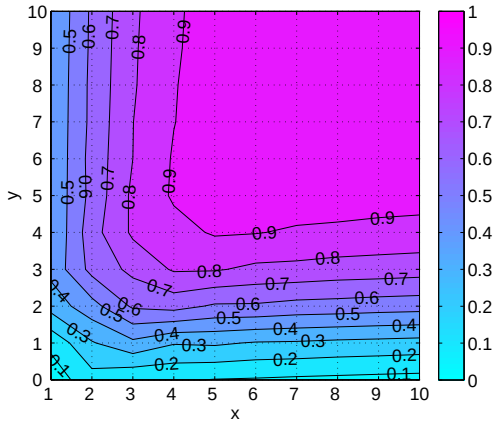


(b) $\beta = 0.6$

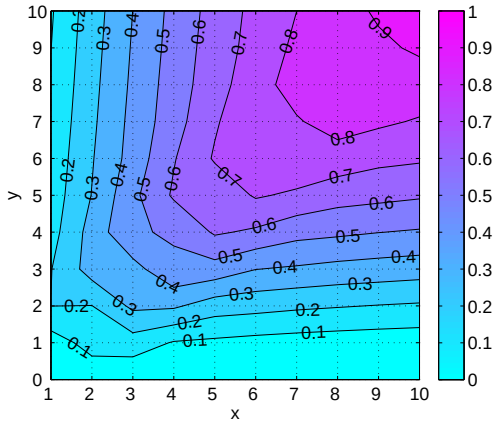


(c) $\beta = 0.4$

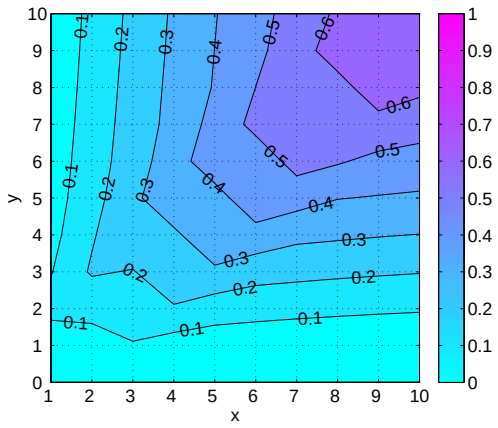
Figure 3.27: Contour plots of $\log_{10} P^E_{x,y}$ for different values of β, computed by (3.213) using the exact solution of the network model.



(a) $\beta = 0.9$

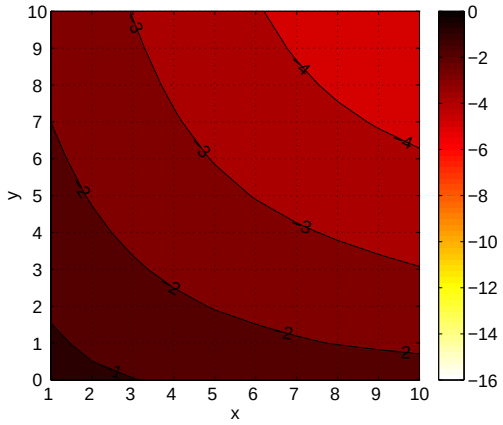


(b) $\beta = 0.6$

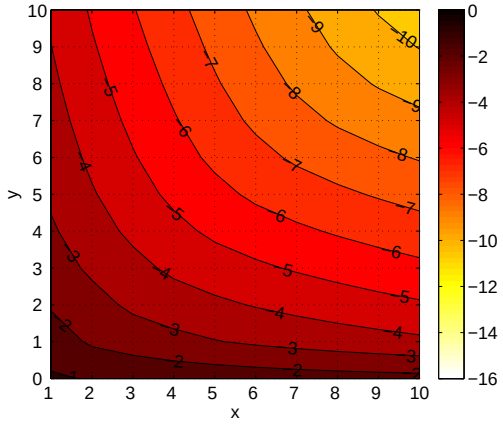


(c) $\beta = 0.4$

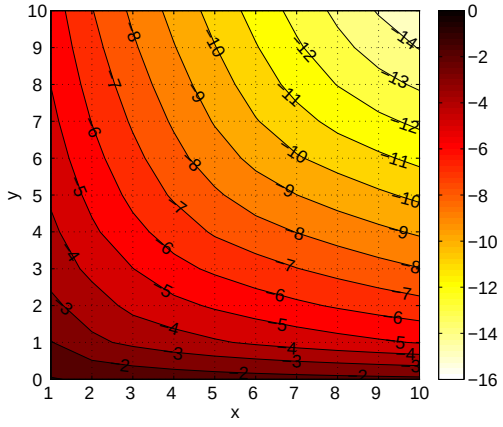
Figure 3.28: Contour plots of the relative error between the value of $P^E_{x,y}$ computed using paths of minimal length and the exact result computed using the network model.



(a) $\beta = 0.9$



(b) $\beta = 0.6$



(c) $\beta = 0.4$

Figure 3.29: Contour plots of $\log_{10} W^E_{x,y}$ (defined in (3.214)) for different values of β, computed from solution of network model. Here the street width $w = 1$.

3.9 The 3D case

In this section we briefly discuss the extent to which the results of the preceding sections might be generalized to 3D urban environments. The main ways in which the 3D problem differs from the 2D problem are the higher rate of geometrical spreading, the presence of a ground reflection, and the fact that energy emitted from the source can escape to the atmosphere.

3.9.1 Ray approximation in a single street

As a simple model of a single street in 3D, we consider an infinitely-long channel running parallel to the x-axis, as illustrated in Figure 3.30. As in the 2D case, we choose as our typical lengthscale the street width, so that, after nondimensionalisation, the channel is bounded by buildings $(-\infty,\infty)\times(-\infty,0)\times(0,h)$ and $(-\infty,\infty)\times(1,\infty)\times(0,h)$, where $h>0$ is the (nondimensional) building height, assumed constant along the length of the street, and a rigid ground $(-\infty,\infty)\times(0,1)\times\{0\}$. We assume that a point source is located within the street at $(0,y_0,z_0)$, where $0<y_0<1$ and $0<z_0<h$.

Under our short wavelength assumption, GTD represents the field inside the street as a sum of ray fields (incident, reflected and diffracted). As in the 2D case, we simplify the analysis by neglecting the effects of diffraction, and consider the contribution of

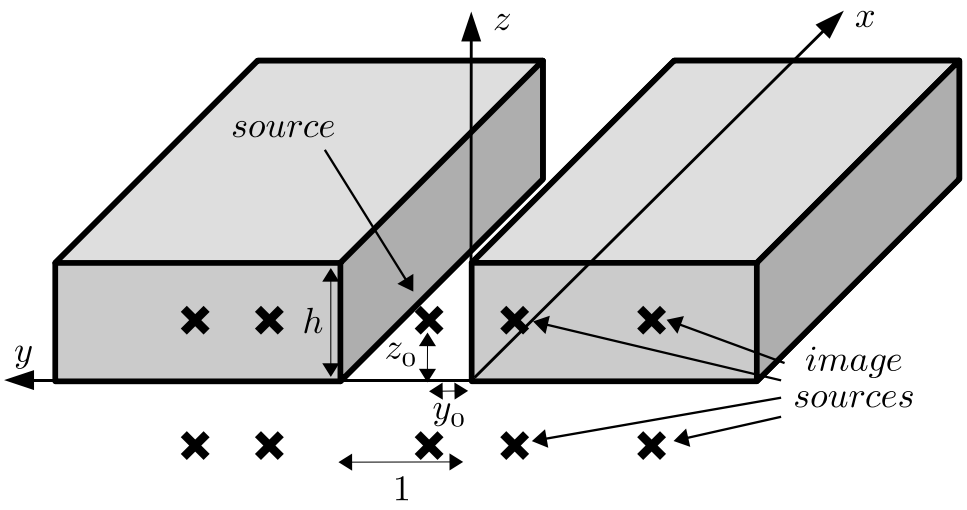


Figure 3.30: A single street in a 3D urban environment - image source configuration.

the multiply-reflected field alone. This can be computed by the introduction of image sources[14] at the points $(0, y_n, \pm z_0)$, $n \in \mathbf{Z}$, with y_n defined as in (3.39) (see Figure 3.30). The field is then approximated by

$$\phi \sim -\frac{1}{4\pi} \sum_{z \in \mathbf{Z}} \frac{e^{ikr_n^-}}{r_n^-} + \frac{e^{ikr_n^+}}{r_n^+}, \tag{3.273}$$

where $r_n^\pm = \sqrt{x^2 + (y - y_n)^2 + (z \pm z_0)^2}$.

For simplicity we consider only the case where the source is close enough to the ground to ensure that the interference between each image source and its corresponding ground-reflected image source in (3.273) is entirely constructive[15]. Each pair of image sources at $(0, y_n, \pm z_0)$ can then be replaced by a single image source at $(0, y_n, 0)$ of double the amplitude (four times the power output), i.e.

$$\phi \sim -\frac{1}{2\pi} \sum_{z \in \mathbf{Z}} \frac{e^{ikr_n}}{r_n}, \tag{3.274}$$

where $r_n = \sqrt{x^2 + (y - y_n)^2 + z^2}$.

To determine exactly how small z_0 must be for this to hold, we begin by writing the summand in (3.273) as

$$\frac{e^{ikr_n^-}}{r_n^-} \left(1 + \frac{r_n^- e^{ik(r_n^+ - r_n^-)}}{r_n^+} \right). \tag{3.275}$$

Then, noting that

$$r_n^\pm = r_n \sqrt{1 + \frac{z_0(z_0 \pm 2z)}{r_n^2}} \tag{3.276}$$

$$= r_n \left(1 + \frac{z_0(z_0 \pm 2z)}{2r_n^2} + \dots \right), \qquad \left| \frac{z_0(z_0 \pm 2z)}{r_n^2} \right| < 1, \tag{3.277}$$

we have

$$r_n^\pm \sim r_n, \tag{3.278}$$

$$r_n^+ - r_n^- \sim \frac{2zz_0}{r_n^2} \tag{3.279}$$

[14] We note that although a ray can undergo an arbitrarily large number of reflections in the walls of the street, no ray undergoes more than one ground reflection.

[15] The general case would require a more careful treatment of the ground reflection, and will not be considered here.

for all $0 < z < h$, provided that $z_0 \ll \frac{r_n^2}{h}$. Finally, when also $z_0 \ll \frac{r_n}{kh}$ we may approximate the second term inside the brackets in (3.275) by 1, to give

$$\frac{e^{ikr_n^-}}{r_n^-} + \frac{e^{ikr_n^+}}{r_n^+} \sim 2\frac{e^{ikr_n}}{r_n}. \tag{3.280}$$

In fact, assuming that $x \gg 1/k$ (so we are not too close to the source), the condition

$$z_0 \ll \frac{x}{kh} \tag{3.281}$$

is sufficient to ensure that (3.280) holds for each $n \in \mathbf{Z}$, and hence that the field can be well-approximated by (3.274).

3.9.2 The acoustic power flow in a single street

As in the 2D case (cf. section 3.4.2.2), we assume that the intensity contributions from the infinitely many image sources in (3.274) can be summed incoherently, with the effect of interference being neglected. The power flow P across the street cross-section $\{x\} \times (0,1) \times (0,h)$ is then given, as a fraction of the total free space power output of the source (which was found in (3.91) to be $\frac{k^2}{4\pi}$), by the ray tube sum

$$P = \frac{1}{\pi}\sum_n (1-\alpha)^{|n|}\tilde{\Omega}_n, \tag{3.282}$$

where α is the absorption coefficient of the street walls and $\tilde{\Omega}_n$ is the solid angle subtended at the source location by the ray tube incident on the nth image street cross-section (cf. equation (3.98) in the 2D case). In terms of the spherical coordinates[16]

$$\begin{aligned} x &= \cos\phi\cos\theta, \\ y - y_0 &= \cos\phi\sin\theta, \\ z &= \sin\phi, \end{aligned} \tag{3.283}$$

we have

$$\tilde{\Omega}_n = \int_{\tilde{\theta}_n^-}^{\tilde{\theta}_n^+} \int_0^{\phi^+(\theta)} \cos\phi \, d\phi d\theta, \tag{3.284}$$

[16]Here the angle ϕ represents 'latitude' on the unit sphere, so that ϕ equals $\pi/2$ minus the usual spherical polar angle.

where $\tilde{\theta}_n^{\pm}$ are defined as in (3.101) and

$$\phi^+(\theta) = \arctan \frac{h \cos\theta}{x}. \tag{3.285}$$

The ϕ-integration in (3.284) is trivial, and we have

$$\begin{aligned} \tilde{\Omega}_n &= \int_{\tilde{\theta}_n^-}^{\tilde{\theta}_n^+} \sin\left(\phi^+(\theta)\right) d\theta \\ &= \int_{\tilde{\theta}_n^-}^{\tilde{\theta}_n^+} \frac{1}{\sqrt{1 + \left(\frac{x}{h\cos\theta}\right)^2}} \, d\theta. \end{aligned} \tag{3.286}$$

In the special case $\alpha = 0$ the sum (3.282) is telescoping, and

$$\begin{aligned} P &= \frac{2}{\pi} \int_0^{\frac{\pi}{2}} \frac{1}{\sqrt{1 + \left(\frac{x}{h\cos\theta}\right)^2}} \, d\theta \\ &= \frac{2}{\pi} \arctan \frac{h}{x}. \end{aligned} \tag{3.287}$$

In this case P is proportional to the power flow due to a single source at $(0, y_0, 0)$ across the infinite strip $C = \{x\} \times (-\infty, \infty) \times (0, h)$, which, in turn, is proportional to the solid angle subtended by C at the source location. This is equal to the area formed by the inverse stereographic projection of C onto the unit sphere centred at $(0, y_0, 0)$, which is the 'orange segment' illustrated in Figure 3.31. There is a bias towards rays with small θ, since these rays gain less height with every unit travelled in the x-direction than those with larger θ. Note that when $x \gg h$ we have

$$P \sim \frac{2h}{x\pi}, \tag{3.288}$$

and the decay in power due to losses to the atmosphere is found to be *algebraic* in the distance down the street.

More generally, when $x \gg 1$ and $\alpha \ll 1$ we may, as in the 2D case, approximate the sum (3.282) by an integral, giving

$$P \sim \frac{2}{\pi} \int_0^{\frac{\pi}{2}} \frac{(1-\alpha)^{x\tan\theta}}{\sqrt{1 + \left(\frac{x}{h\cos\theta}\right)^2}} \, d\theta. \tag{3.289}$$

When also $x \gg h$, (3.289) can be further approximated to give

$$P \sim \frac{2h}{x\pi} \int_0^{\frac{\pi}{2}} (1-\alpha)^{x\tan\theta} \cos\theta \, d\theta. \tag{3.290}$$

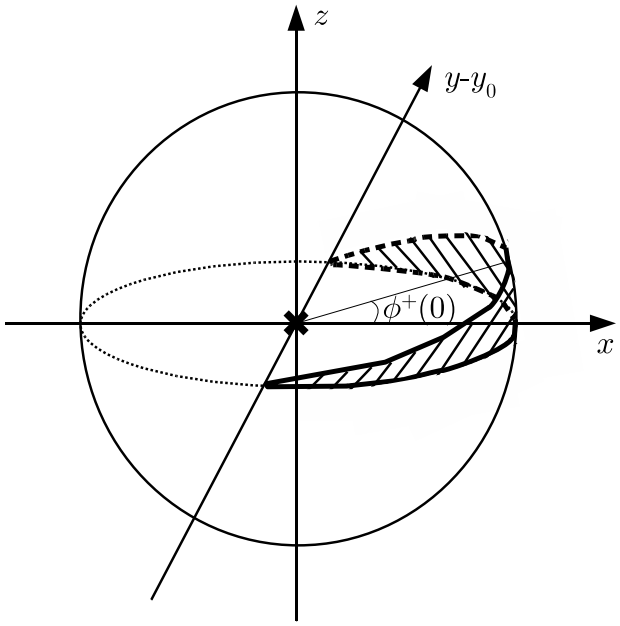


Figure 3.31: The inverse stereographic projection onto the unit sphere centred at the source of the infinite strip C formed by the union of the image street cross-sections forms a segment, bounded by the curves parametrized by $(r, \theta, \phi) = (1, \theta, 0)$ and $(r, \theta, \phi) = (1, \theta, \phi^+(\theta))$ for $-\pi/2 \leq \theta \leq \pi/2$.

3.9.3 Acoustic power flows in a network of streets

In this section we propose a method for estimating acoustic power flows across street cross-sections in a network of streets in 3D, which generalises that developed in sections 3.5-3.8 for the 2D problem. To simplify the analysis we assume, as in the 2D case, that diffraction effects at junctions can be neglected (see the discussion in section 3.6.1.1). We therefore consider only the contributions from the direct and (multiply-)reflected rays, which we sum incoherently. We also assume, for simplicity, that the buildings all have equal height h.

We first introduce the method in general terms, then illustrate it in a number of examples, comparing the results to those for the corresponding 2D problems.

Suppose that, as a fraction of the total free space power output of the source, the power flow P across the street cross-section is given by a ray tube sum of the general form

$$P = \frac{1}{\pi} \sum_n B_n \tilde{\Omega}_n. \tag{3.291}$$

Here B_n represents the effect of wall absorption, and is the same as in the analogous 2D problem. $\tilde{\Omega}_n$ is the solid angle subtended by the nth ray tube at the source

location, given by

$$\tilde{\Omega}_n = \int_{\tilde{\theta}_n^-}^{\tilde{\theta}_n^+} \int_0^{\phi^+(\theta)} \cos\phi \, d\phi d\theta, \tag{3.292}$$

where $\tilde{\theta}_n^{\pm}$ are the launch angles of the rays bounding the corresponding ray tube in the analogous 2D problem, and

$$\phi^+(\theta) = \arctan \frac{h}{L(\theta)}, \tag{3.293}$$

where $L(\theta)$ is the length of a ray of launch angle θ reaching the street cross-section in the analogous 2D problem.

The ϕ-integration in (3.292) is trivial, so that

$$\tilde{\Omega}_n = \int_{\tilde{\theta}_n^-}^{\tilde{\theta}_n^+} G(\theta) \, d\theta, \tag{3.294}$$

where

$$G(\theta) = \sin\phi^+(\theta) = \frac{1}{\sqrt{1 + \left(\frac{L(\theta)}{h}\right)^2}}. \tag{3.295}$$

We then propose to approximate (3.291) by the integral

$$P_{\text{app}} := \frac{2}{\pi} \int_0^{\frac{\pi}{2}} A(\theta)F(\theta)G(\theta) \, d\theta, \tag{3.296}$$

where the absorption factor $A(\theta)$ and the energy redistribution factor $F(\theta)$ are exactly as in the analogous 2D problem. We expect (3.296) to provide a good approximation to (3.291) only when the streets in the network are long and the typical absorption coefficient is small. Furthermore, when multiple junctions are involved, we conjecture, as in the 2D case, that the approximations represent *expected* power flows after averaging over a suitable range of street lengths.

Note that when also $L(\theta) \gg h$ we can further approximate

$$G(\theta) \sim \frac{h}{L(\theta)}, \tag{3.297}$$

to give

$$P_{\text{app}} \sim \frac{2h}{\pi} \int_0^{\frac{\pi}{2}} \frac{A(\theta)F(\theta)}{L(\theta)} \, d\theta. \tag{3.298}$$

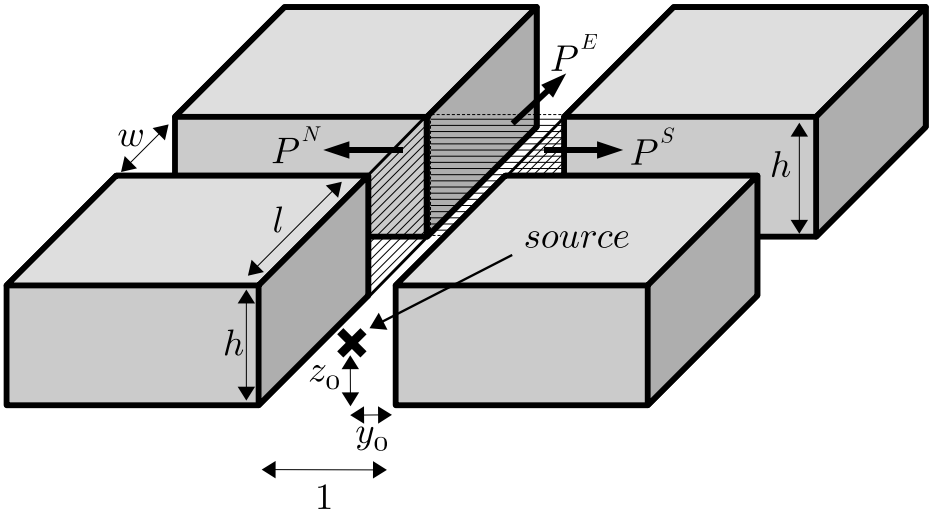


Figure 3.32: A crossroads in 3D.

One example has already been considered in section 3.9.2 - the power flow in a single street. In this case (cf. (3.289) and (3.290)) we have

$$B_n = (1-\alpha)^{|n|}, \tag{3.299}$$

$$A(\theta) = (1-\alpha)^{x\tan\theta}, \tag{3.300}$$

$$F(\theta) = 1, \tag{3.301}$$

$$L(\theta) = \frac{x}{\cos\theta}. \tag{3.302}$$

We now consider a number of other examples.

3.9.4 Energy redistribution at a crossroads

Let us consider the case of a right-angled crossroads, where a street of width w intersects a main street at a distance l from the source (see Figure 3.32 for an illustration). In the ray tube sum (cf. (3.291) and (3.292)) for the power flow P^E out of the East exit of the junction we have

$$B_n = (1-\alpha)^{|n|}, \tag{3.303}$$

and $\tilde{\theta}_n^{\pm}$ are now defined as in (3.135). Accordingly, in the integral approximations (3.296) and (3.298) we have

$$A(\theta) = (1-\alpha)^{l\tan\theta}, \tag{3.304}$$

$$F(\theta) = F_C(\theta; w), \tag{3.305}$$

$$L(\theta) = \frac{l}{\cos\theta}. \tag{3.306}$$

For example, in the case $l \gg h$ this gives

$$P_{\text{app}}^E = \frac{2h}{\pi l}\int_0^{\frac{\pi}{2}} (1-\alpha)^{l\tan\theta} F_C(\theta; w)\cos\theta\, d\theta. \tag{3.307}$$

It is interesting to compare (3.307) with the corresponding two-dimensional formula (3.146). For simplicity we assume[17] that $\alpha = 0$. By comparison with (3.288), we see that the prefactor $\frac{2h}{\pi l}$ in (3.307) represents the power incident on the junction. Thus the fraction E_{3D} of energy incident on the junction that carries on down the main street is given as a function of w by

$$E_{3D}(w) = \int_0^{\frac{\pi}{2}} F_C(\theta; w)\cos\theta\, d\theta. \tag{3.309}$$

The corresponding expression in two dimensions is

$$E_{2D}(w) = \frac{2}{\pi}\int_0^{\frac{\pi}{2}} F_C(\theta; w)\, d\theta. \tag{3.310}$$

A plot of the functions E_{2D} and E_{3D} is presented in Figure 3.33. Note that in three dimensions a greater proportion of the incident energy passes the junction than in two dimensions. This is because in three dimensions the energy incident on the junction is not distributed uniformly over all $\theta \in (0, \pi/2)$, as it is in the two dimensional case; rather there is a bias towards rays with small θ, as remarked at the end of section 3.9.2, and as illustrated in Figure 3.31. Such rays contribute more to the power flow than those with larger θ because $F_C(\theta, w)$ is a decreasing function of θ.

[17] Note that in this special case the integral in (3.307) can be evaluated explicitly to give

$$P_{\text{app}}^E = \frac{2h}{\pi l}\left(\sqrt{1+\left(\frac{w}{2}\right)^2} - \frac{w}{2}\right). \tag{3.308}$$

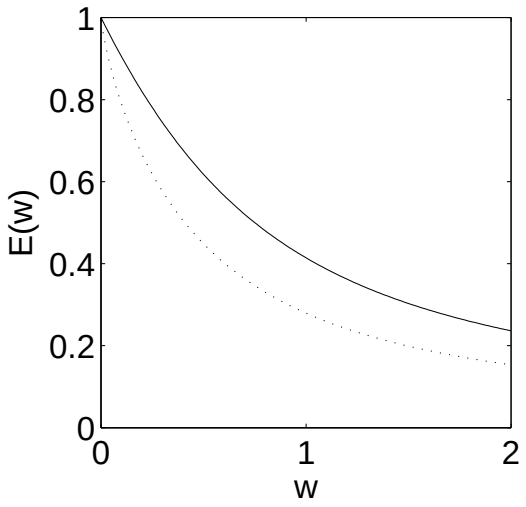


Figure 3.33: A plot of the functions E_{2D} (dotted line) and E_{3D} (solid line).

3.9.5 A two-junction environment

As a further example, we consider the 3D analogue of the 2D two-junction environment illustrated in Figure 3.24, for which the approximations (3.172) and (3.173) were obtained. In the 3D case the integral approximation (3.296) of the power flows $P^E(2)$ and $P^W(2)$ would have

$$A(\theta) = (1-\alpha_0)^{l_0 \tan\theta}(1-\alpha_1)^{\frac{l_1}{w_1}\tan\left(\frac{\pi}{2}-\theta\right)}, \tag{3.311}$$

$$F(\theta) = F_T(\theta; w_1) F_T\left(\frac{\pi}{2}-\theta; \frac{w_2}{w_1}\right), \tag{3.312}$$

$$L(\theta) = \frac{l_0}{\cos\theta} + \frac{l_1}{\cos\left(\frac{\pi}{2}-\theta\right)}, \tag{3.313}$$

and to obtain the integral approximation of $P^N(2)$ we must replace (3.312) by

$$F(\theta) = F_T(\theta; w_1) F_C\left(\frac{\pi}{2}-\theta; \frac{w_2}{w_1}\right). \tag{3.314}$$

3.9.6 A regular network of streets

The integral approximation method proposed in the previous section can be used to estimate the power flows in a network of streets in 3D. For simplicity we consider the case of a regular network in which the street length l, width w, and height h are constant across the network, and there is no wall absorption. We also assume that

$l \gg h$ so that the simplified form (3.298) applies, although we expect similar results in the more general case.

As in the 2D case, one way to proceed is to consider only those paths which have minimal length. Defining $P_\lambda^E(N)$ as in (3.186), we may investigate the behaviour of $P_\lambda^E(N)$ for large N. For simplicity we consider only the cases $\lambda = 0, 1/2$; in both cases there is only one path of minimal length.

- When $\lambda = 0$ we have

$$F(\theta) = F_C(\theta; 1)^N, \tag{3.315}$$

$$L(\theta) = \frac{Nl}{\cos\theta}, \tag{3.316}$$

and our estimate for $P_0^E(N)$ is

$$P_0^E(N) = \frac{2h}{\pi N l} \int_0^{\frac{\pi}{4}} \exp\left[N \log\left(1 - \tan\theta\right)\right] \cos\theta \, d\theta. \tag{3.317}$$

The Laplace analysis is similar to that in the 2D case, with the main contribution to (3.317) coming from the endpoint $\theta = 0$. We find that

$$P_0^E(N) \sim \frac{2h}{\pi N^2 l}, \quad N \to \infty, \tag{3.318}$$

so that the decay is *algebraic* in the number of junctions encountered.

- Along the diagonal $\lambda = 1/2$ (with N even) we have

$$F(\theta) = F_C(\theta; 1)^{N/2} F_T\left(\frac{\pi}{2} - \theta; 1\right)^{N/2}, \tag{3.319}$$

$$L(\theta) = \frac{Nl}{2}\left(\frac{1}{\cos\theta} + \frac{1}{\sin\theta}\right), \tag{3.320}$$

and our estimate for $P_{1/2}^E(N)$ is

$$P_{1/2}^E(N) = \frac{8h}{\pi N l} \int_0^{\frac{\pi}{4}} \exp\left[N\left(\frac{1}{2}\log\left(\frac{\tan\theta}{4}\right)\right)\right] \frac{1}{\left(\frac{1}{\cos\theta} + \frac{1}{\sin\theta}\right)} \, d\theta. \tag{3.321}$$

As in the 2D case the main contribution comes from the right endpoint $\theta = \pi/4$, where we note that $\left(\frac{1}{\cos\theta} + \frac{1}{\sin\theta}\right) = 2\sqrt{2}$. We therefore have

$$P_{1/2}^E(N) \sim \frac{2\sqrt{2}h}{\pi N^2 l}\left(\frac{1}{2}\right)^N, \quad N \to \infty, \ (N \text{ even}), \tag{3.322}$$

and the decay is *exponential* in the number of junctions encountered.

However, at this stage it is not clear whether the integral approximations can be used to formulate a network model analogous to that proposed for the 2D case in section 3.8.2. There we were able to relate the θ-resolved power flows into one junction to the θ-resolved power flows out of the neighbouring junctions, which allowed us to write down a system of coupled partial difference equations at each value of θ. This formulation relied crucially on the fact that the absorption and energy redistribution factors $A(\theta)$ and $F(\theta)$ in our integral approximations were 'multiplicative', in the sense that with each additional street/junction encountered, $A(\theta)$ and $F(\theta)$ were multiplied by a factor. In the 3D case, however, the factor $G(\theta)$ in the integrand in (3.296) does not follow the same rule. Indeed, the length $L(\theta)$ in (3.295) is 'additive', in the sense that with each additional street/junction encountered, we must add a term to $L(\theta)$, rather than multiply it by a factor.

Whether or not these difficulties can be resolved is still an open question, and we leave any further discussion of these issues for future work.

3.10 Summary

In this chapter we have derived a model for the propagation of acoustic energy from a time-harmonic point source through a network of interconnecting streets. Our analysis was based on a number of simplifying assumptions:

- The wavelength was assumed to be short compared to typical lengthscales such as street widths, lengths and heights, justifying the use of the geometrical acoustics approximation.
- Diffraction effects were neglected - only the contribution of the direct and (multiply)-reflected ray fields was considered. As discussed in section 3.6.1.1, we expect this assumption to be valid provided that street lengths are much shorter than the Rayleigh distance kw^2, where k is the wavenumber and w is a typical street width.
- Acoustic intensities were computed by incoherent summation of the intensities along individual rays - the effect of interference between ray fields was neglected.
- The effect of energy absorption at building walls was modelled by an absorption coefficient, which was assumed to be small.
- Streets were assumed to intersect at right-angles.
- Street lengths were assumed large compared to street widths.
- The source was assumed to be located within a street, not close to a junction or to a street wall.

Our model represents the acoustic power flow from the source along any pathway through the network as the integral of a power density over the launch angle θ of a ray emanating from the source. The dependence of the power density on θ takes into account the key phenomena involved in the propagation, namely energy loss by wall absorption, energy redistribution at junctions, and, in 3D, energy loss to the atmosphere. We have shown, by means of a number of examples, how the appropriate power density for a given propagation pathway may be explicitly computed. The model is not only concerned with the calculation of acoustic power flows - once the power density has been determined, an elementary modification of the integral allows us to compute the acoustic energy density and the mean-square pressure, averaged over the street cross-section (see section 3.8.2.1).

We have proved the validity of the model analytically in the cases of a single street and a single junction between two intersecting streets. In the latter case the integral representation generalises the result derived previously in [26] to the case of non-zero wall absorption. In the multiple-junction case, we have investigated the validity of the model using numerical experiments, the results of which suggest that the integral expressions represent expected power flows after averaging over a range of street lengths. This interpretation is consistent with the fact that in practical applications, the street geometry may be known only to a certain degree of accuracy.

In an infinite network of streets, computing the total net power flow across a street cross-section would require the summation of the power flows along each of the infinitely many propagation pathways between the source and cross-section in question. We have explained the circumstances under which an estimate of this summation can be obtained by considering only paths of minimal length. The resulting estimate exhibits strongly anisotropic decay away from the source, with the power flow decaying exponentially in the number of junctions from the source, except along the axial directions of the network, where the decay is algebraic.

In the 2D case, we have shown how the full summation can be computed implicitly, by formulating a system of partial difference equations for the power densities flowing out of the exits of each junction in the network. In the special case where the street widths, lengths, and absorption coefficients are constant across the network, we have been able to obtain an exact solution to this system. This solution exhibits the same qualitative anisotropic decay observed in the minimal length estimate, with the quantitative agreement between the two improving as the absorption coefficient is increased. However, the generalisation of this formulation to the 3D case remains an area for future research.

Chapter 4

Time domain analysis - forward problem

4.1 Introduction

In this chapter we study the propagation of sound waves with arbitrary time dependence. In particular, we consider the propagation of singularities in the wave field, another situation in which the theory of geometrical acoustics, discussed in the previous chapter in the context of short-wavelength time-harmonic waves, applies.

In section 4.2 we review the theory of characteristics, which are the manifolds in space-time on which singularities are supported. In section 4.3 we illustrate the theory by means of a number of specific domains in which an exact solution of the wave equation is available. In each case the geometrical acoustics approximation is shown to arise from an asymptotic approximation of the exact solution in the vicinity of the characteristics.

In section 4.4 we consider more general pulses, which can be dealt with by convolution. The exact solutions for edge and vertex diffraction suggest a general principle which governs the weakening of singularities when they are diffracted, which is proved in section 4.4.1.

Section 4.5 concerns the switching on of time-harmonic acoustic waves. We consider three specific cases: a point source in an infinite domain in 3D, a point source in an infinite domain in 2D, and the diffraction of a plane wave by a rigid half-line in 2D. In each case we determine the conditions under which the field is well-approximated by the solution of the corresponding frequency domain problem.

Finally, in section 4.6 we comment on some experimental data from an investigation into the propagation of sound pulses arising from gunshots.

4.2 Propagation of singularities in solutions of the wave equation

The hyperbolic nature of the time-dependent wave equation (2.16) means that its solution Φ and the derivatives thereof are permitted to have discontinuities or other singularities, even away from the source, provided that the derivatives in (2.16) are interpreted in the weak or distributional sense. This is in sharp contrast to the elliptic Helmholtz equation, the solution of which is analytic away from the source. The relevance of this for our purposes is that the arrivals of the singularities at receivers are well-defined acoustic 'events', which can be used to solve the inverse problem, as will be discussed in Chapter 5.

The propagation of singularities of the solutions of (2.16) is governed by the theory of geometrical acoustics. In the next section we review the standard theory. Following [23], pp. 618-619 and [71], pp. 66-67, we work, not in terms of the wave equation (2.16), but rather in terms of the first-order equations (2.9)-(2.11). An alternative derivation of the key results directly from the wave equation can be found in [34], Chapter 3.

4.2.1 Characteristics, wavefronts and rays

Consider the general first-order system of PDEs

$$L[\mathbf{v}] := \sum_{i=1}^{m} \mathbf{A_i} \frac{\partial \mathbf{v}}{\partial x_i} = 0, \tag{4.1}$$

where the coefficient matrices $\mathbf{A_i}$ are assumed to be constant. Suppose that across some surface $\varphi(x_1, ..., x_m) = 0$ the solution $\mathbf{v}$ is continuous, but that the normal derivative $\frac{\partial \mathbf{v}}{\partial \varphi}$ experiences a jump discontinuity. Changing variables to $(\varphi, \psi_1, ..., \psi_{m-1})$, where the ψ_i are tangential coordinates, gives

$$L[\mathbf{v}] = \sum_{i=1}^{m} \mathbf{A_i} \frac{\partial \varphi}{\partial x_i} \frac{\partial \mathbf{v}}{\partial \varphi} + \sum_{i=1}^{m} \mathbf{A_i} \left(\sum_{j=1}^{m-1} \frac{\partial \psi_j}{\partial x_i} \frac{\partial \mathbf{v}}{\partial \psi_j} \right) = 0, \tag{4.2}$$

where the first term represents a derivative normal to the surface and the remaining terms represent tangential derivatives. Assuming that the tangential derivatives $\frac{\partial \mathbf{v}}{\partial \psi_j}$ are all continuous across the surface $\varphi = 0$, taking the difference of $L[\mathbf{v}]$ across the surface (and denoting this operation by $[\cdot]^+_-$) gives

$$[L[\mathbf{v}]]^+_- = \mathbf{A}\left[\frac{\partial \mathbf{v}}{\partial \varphi}\right]^+_- = 0, \tag{4.3}$$

where the *characteristic matrix* $\mathbf{A}$ is defined by

$$\mathbf{A} := \sum_{i=1}^{m} \mathbf{A_i} \frac{\partial \varphi}{\partial x_i}. \tag{4.4}$$

Equation (4.3) implies that if there is a discontinuity in $\frac{\partial \mathbf{v}}{\partial \varphi}$ across the surface, then the matrix $\mathbf{A}$ must be singular on the surface, i.e.

$$\det\left(\sum_{i=1}^{m} \mathbf{A_i} \frac{\partial \varphi}{\partial x_i}\right) = 0. \tag{4.5}$$

Surfaces for which the eikonal equation (4.5) hold are called *characteristics* of the system (4.1). The above argument shows that discontinuities in the derivatives of solutions of (4.1) can only occur across characteristics.

To determine how the size of the discontinuity $\left[\frac{\partial \mathbf{v}}{\partial \varphi}\right]^+_-$ varies as a function of position in the characteristic surface we return to equation (4.2) and compute $\left[\frac{\partial}{\partial \varphi} L[\mathbf{v}]\right]^+_-$, which gives

$$\mathbf{A}\frac{\partial^2 \mathbf{v}}{\partial \varphi^2} + \sum_{i=1}^{m} \mathbf{A_i}\left(\sum_{j=1}^{m-1} \frac{\partial \psi_j}{\partial x_i}\frac{\partial}{\partial \psi_j}\left[\frac{\partial \mathbf{v}}{\partial \varphi}\right]^+_-\right) = 0. \tag{4.6}$$

Since $\mathbf{A}$ is singular, it has left and right nullvectors $\mathbf{l}$ and $\mathbf{r}$, which are uniquely defined up to rescaling when $\mathbf{A}$ has rank $m-1$ (as we shall see, this the case of interest to us). Then, multiplying equation (4.6) on the left by $\mathbf{l}$ removes the first term, giving

$$\mathbf{l}\left(\sum_{i=1}^{m} \mathbf{A_i}\left(\sum_{j=1}^{m-1} \frac{\partial \psi_j}{\partial x_i}\frac{\partial}{\partial \psi_j}\left[\frac{\partial \mathbf{v}}{\partial \varphi}\right]^+_-\right)\right) = 0. \tag{4.7}$$

Also, by (4.3) we have

$$\left[\frac{\partial \mathbf{v}}{\partial \varphi}\right]^+_- = \sigma \mathbf{r}, \tag{4.8}$$

where σ is a scalar, and substituting (4.8) in (4.7) then gives

$$\left(\mathbf{l}\sum_{i=1}^{m}\mathbf{A_i r}\right)\sum_{j=1}^{m-1}\frac{\partial\psi_j}{\partial x_i}\frac{\partial\sigma}{\partial\psi_j}+\left(\mathbf{l}\sum_{i=1}^{m}\mathbf{A_i}\sum_{j=1}^{m-1}\frac{\partial\psi_j}{\partial x_i}\frac{\partial\mathbf{r}}{\partial\psi_j}\right)\sigma=0. \tag{4.9}$$

Finally, by introducing the zero term $\mathbf{l}\,\mathbf{A}\frac{\partial\mathbf{r}}{\partial\varphi}$ inside the parentheses of the second term, we can rewrite (4.9) as

$$(\mathbf{a}\cdot\tilde{\nabla})\sigma+\mathbf{l}\,L[\mathbf{r}]\sigma=0, \tag{4.10}$$

where

$$(\mathbf{a}\cdot\tilde{\nabla}):=\mathbf{l}\sum_{i=1}^{m}\mathbf{A_i r}\sum_{j=1}^{m-1}\frac{\partial\psi_j}{\partial x_i}\frac{\partial}{\partial\psi_j}. \tag{4.11}$$

The operator (4.11) represents differentiation in a particular direction in the characteristic surface, called the *bicharacteristic* direction. Equation (4.10) is called the *transport equation* and describes how the size of the discontinuity $\left[\frac{\partial\mathbf{v}}{\partial\varphi}\right]_-^+$ varies along the *bicharacteristic rays*, defined to be the tangent curves of the vector field of bicharacteristic directions[1].

4.2.2 Singularities

In the previous section we showed that discontinuities in the derivatives of a continuous solution of the system (4.1) could only occur across characteristics. In fact, characteristics can also support discontinuities or even singularities in the solution itself, provided that we interpret the equations in a distributional sense. The singularities may be algebraic singularities, or delta-functions, for example. Furthermore, it can be shown that the magnitude of the discontinuity, or the coefficient function in front of the singularity, must satisfy the transport equation (4.10). For more detail see e.g. [24], pp. 624-626.

4.2.3 Application to the acoustics equations

We now specialise the general theory of section 4.2.1 to the equations of acoustics. We first substitute the linearised constitutive law (2.11) in the mass and momentum

[1]We remark that, in the scalar case with $\mathbf{l}=\mathbf{r}=1$, equation (4.10) reduces to $(\mathbf{a}\cdot\tilde{\nabla})\sigma=0$, so that the size of the discontinuity remains constant along bicharacteristics (see [71], p. 27).

conservation equations (2.9) and (2.10) to obtain the equations

$$\frac{1}{\rho_0}\frac{\partial \rho'}{\partial t} + \nabla \cdot \mathbf{u}' = 0, \tag{4.12}$$

$$\frac{\partial \mathbf{u}'}{\partial t} + \frac{c_0^2}{\rho_0}\nabla \rho' = \mathbf{0}. \tag{4.13}$$

We then set $\mathbf{v} = (\rho', \mathbf{u}')^\top$ and rewrite (4.12)-(4.13) as

$$L[\mathbf{v}] := \mathbf{A_t}\frac{\partial \mathbf{v}}{\partial t} + \mathbf{A_x}\frac{\partial \mathbf{v}}{\partial x} + \mathbf{A_y}\frac{\partial \mathbf{v}}{\partial y} + \mathbf{A_z}\frac{\partial \mathbf{v}}{\partial z} = 0, \tag{4.14}$$

where

$$\mathbf{A_t} = \begin{pmatrix} \frac{1}{\rho_0} & 0 & 0 & 0 \\ 0 & 1 & 0 & 0 \\ 0 & 0 & 1 & 0 \\ 0 & 0 & 0 & 1 \end{pmatrix}, \qquad \mathbf{A_x} = \begin{pmatrix} 0 & 1 & 0 & 0 \\ \frac{c_0^2}{\rho_0} & 0 & 0 & 0 \\ 0 & 0 & 0 & 0 \\ 0 & 0 & 0 & 0 \end{pmatrix}, \tag{4.15}$$

$$\mathbf{A_y} = \begin{pmatrix} 0 & 0 & 1 & 0 \\ 0 & 0 & 0 & 0 \\ \frac{c_0^2}{\rho_0} & 0 & 0 & 0 \\ 0 & 0 & 0 & 0 \end{pmatrix}, \qquad \mathbf{A_z} = \begin{pmatrix} 0 & 0 & 0 & 1 \\ 0 & 0 & 0 & 0 \\ 0 & 0 & 0 & 0 \\ \frac{c_0^2}{\rho_0} & 0 & 0 & 0 \end{pmatrix}, \tag{4.16}$$

which is clearly of the form (4.1). The characteristic matrix (4.4) is then found to be

$$\mathbf{A} = \begin{pmatrix} \frac{1}{\rho_0}\frac{\partial \varphi}{\partial t} & \frac{\partial \varphi}{\partial x} & \frac{\partial \varphi}{\partial y} & \frac{\partial \varphi}{\partial z} \\ \frac{c_0^2}{\rho_0}\frac{\partial \varphi}{\partial x} & \frac{\partial \varphi}{\partial t} & 0 & 0 \\ \frac{c_0^2}{\rho_0}\frac{\partial \varphi}{\partial y} & 0 & \frac{\partial \varphi}{\partial t} & 0 \\ \frac{c_0^2}{\rho_0}\frac{\partial \varphi}{\partial z} & 0 & 0 & \frac{\partial \varphi}{\partial t} \end{pmatrix}, \tag{4.17}$$

so that

$$\det \mathbf{A} = \frac{1}{\rho_0}\left(\frac{\partial \varphi}{\partial t}\right)^2 \left(\left(\frac{\partial \varphi}{\partial t}\right)^2 - c_0^2 \left|\nabla \varphi\right|^2\right). \tag{4.18}$$

Assuming that $\frac{\partial \varphi}{\partial t} \neq 0$, we say that a surface $\varphi = 0$ is a characteristic for the acoustic equations (and the associated wave equation) if

$$\left(\frac{\partial \varphi}{\partial t}\right)^2 = c_0^2 \left|\nabla \varphi\right|^2. \tag{4.19}$$

The evolving surface formed by intersecting a characteristic $\varphi = 0$ with the planes of constant t is called a *wavefront*. With $\varphi(t, \mathbf{x}) = t - \tau(\mathbf{x})$, where $\tau(\mathbf{x})$ is defined to be the time when the wavefront passes through the point $\mathbf{x}$, the characteristic matrix takes the form

$$\mathbf{A} = \begin{pmatrix} \dfrac{1}{\rho_0} & -\dfrac{\partial\tau}{\partial x} & -\dfrac{\partial\tau}{\partial y} & -\dfrac{\partial\tau}{\partial z} \\ -\dfrac{c_0^2}{\rho_0}\dfrac{\partial\tau}{\partial x} & 1 & 0 & 0 \\ -\dfrac{c_0^2}{\rho_0}\dfrac{\partial\tau}{\partial y} & 0 & 1 & 0 \\ -\dfrac{c_0^2}{\rho_0}\dfrac{\partial\tau}{\partial z} & 0 & 0 & 1 \end{pmatrix}, \tag{4.20}$$

and equation (4.19) becomes

$$|\nabla\tau|^2 = \frac{1}{c_0^2}, \tag{4.21}$$

which we recognise as the eikonal equation (cf. equation (3.4)).

When (4.21) holds, left and right nullvectors of the matrix $\mathbf{A}$ are[2]

$$\mathbf{l} = \begin{pmatrix} 1, & \dfrac{\partial\tau}{\partial x}, & \dfrac{\partial\tau}{\partial y}, & \dfrac{\partial\tau}{\partial z} \end{pmatrix}, \quad \mathbf{r} = \begin{pmatrix} \dfrac{\rho_0}{c_0^2} \\ \dfrac{\partial\tau}{\partial x} \\ \dfrac{\partial\tau}{\partial y} \\ \dfrac{\partial\tau}{\partial z} \end{pmatrix}, \tag{4.22}$$

and we have

$$\mathbf{l}L[\mathbf{r}] = \nabla^2\tau, \qquad \mathbf{a} = 2\begin{pmatrix} \dfrac{1}{c_0^2} \\ \dfrac{\partial\tau}{\partial x} \\ \dfrac{\partial\tau}{\partial y} \\ \dfrac{\partial\tau}{\partial z} \end{pmatrix}. \tag{4.23}$$

If σ represents the magnitude of a discontinuity in $\mathbf{v}$, or the coefficient in front of a singularity of $\mathbf{v}$, then σ must satisfy the transport equation (4.10), which becomes

$$2\left(\frac{1}{c_0^2}\frac{\partial}{\partial t} + \nabla\tau\cdot\nabla\right)\sigma + \nabla^2\tau\sigma = 0. \tag{4.24}$$

[2]In this case the rank of $\mathbf{A}$ is equal to 3, so that the left and right nullvectors are unique up to rescaling, as remarked after equation (4.6).

We remark that this PDE is defined only on the characteristic surface. Equation (4.24) can be rewritten as

$$2\frac{d\sigma}{ds} + \nabla^2\tau\sigma = 0, \tag{4.25}$$

where s is a parameter along the bicharacteristic curve $\mathbf{x} = \mathbf{x}(s)$, $t = \tau(\mathbf{x}(s))$, which satisfies the bicharacteristic equations

$$\frac{dt}{ds} = \frac{1}{c_0^2}, \qquad \frac{d\mathbf{x}}{ds} = \nabla\tau. \tag{4.26}$$

The projections of the bicharacteristic curves onto the physical space are called *rays*. By (4.21) and (4.26) the rays are normal to the wavefronts, and the wavefronts propagate normal to themselves (i.e. in the ray direction) at speed c_0.

The function σ, which is defined on the characteristic surface, naturally gives rise to the function $\sigma_{\text{spatial}}(\mathbf{x}) := \sigma(\mathbf{x}, \tau(\mathbf{x}))$, which represents the magnitude of the discontinuity or the coefficient in front of the singularity when the wavefront arrives at the point $\mathbf{x}$ at time $t = \tau(\mathbf{x})$. Since

$$\nabla\sigma_{\text{spatial}} = \left(\nabla + \nabla\tau\frac{\partial}{\partial t}\right)\sigma, \tag{4.27}$$

we have by (4.24) and (4.21) that

$$2\nabla\tau\cdot\nabla\sigma_{\text{spatial}} + \nabla^2\tau\sigma_{\text{spatial}} = 0, \tag{4.28}$$

which is precisely the leading order transport equation (3.5) of the geometrical acoustics approximation for short wavelength time-harmonic waves.

4.2.4 Geometrical acoustics in the time domain and frequency domain

We now nondimensionalise by

$$\mathbf{x} = L\hat{\mathbf{x}}, \qquad t = \frac{L}{c_0}\hat{t}, \qquad \Phi = \phi_0\hat{\Phi}, \tag{4.29}$$

where L and ϕ_0 are reference values of $|\mathbf{x}|$ and Φ, respectively, and immediately drop hats. We suppose that in the vicinity of a wavefront $t = \tau(\mathbf{x})$, the wave field can be expanded as an asymptotic series

$$\Phi \sim \sum_{n=0}^{\infty}\sigma_n(\mathbf{x})H(\xi)\xi^{\lambda+n}, \qquad \xi \to 0, \tag{4.30}$$

where $\xi = t - \tau(\mathbf{x})$, λ is a real constant and $H(\xi)$ is the Heaviside function. When $\lambda > 0$ the wave field is continuous across the wavefront; when $\lambda = 0$ the wave field has a jump discontinuity across the wavefront, and when $-1 < \lambda < 0$ the wave field is (integrably) singular on the wavefront. In each case, the leading order coefficient σ_0 satisfies the transport equation (4.28), which, as remarked in the previous section, is identical to the leading order transport equation (3.5) of the frequency domain case. Furthermore, it can be shown that the higher order coefficients $\sigma_n(\mathbf{x})$, $n > 0$, satisfy transport equations which are identical to the higher order transport equations (3.6) of the frequency domain case (see e.g. [24], pp. 624-626 or [34], p. 56), although we do not present the details here.

The link with the ray approximation of the frequency domain case can be made explicit via the Fourier transform, as has been elucidated in [12]. We first recall that if $\Phi(\mathbf{x}, t)$ is a solution of the wave equation then the Fourier transform with respect to time[3],

$$\phi(k, \mathbf{x}) := \int_{-\infty}^{\infty} \Phi(\mathbf{x}, t) e^{ikt}\, dt, \tag{4.31}$$

is a solution of the Helmholtz equation. The asymptotic behaviour of $\phi(k, \mathbf{x})$ for large k is governed by the singularities of $\Phi(\mathbf{x}, t)$. If, in the vicinity of $t = \tau(\mathbf{x})$, $\Phi(\mathbf{x}, t)$ is the sum of a smooth summand (corresponding to the waves whose wavefronts have already passed through the point $\mathbf{x}$) and an expansion of the form (4.30), then formally taking a Fourier transform of (4.30) in a term-by-term way, we see that the singularity at $t = \tau(\mathbf{x})$ makes a contribution

$$\sum_{n=0}^{\infty} \Gamma(\lambda + n + 1)\sigma_n(\mathbf{x}) \left(\frac{i}{k}\right)^{\lambda+n+1} e^{ik\tau(\mathbf{x})} \tag{4.32}$$

to the asymptotic behaviour of $\phi(k, \mathbf{x})$ as $k \to \infty$. The series (4.32) is clearly of the form of a ray expansion (3.3), with

$$U(\mathbf{x}) = \tau(\mathbf{x}), \tag{4.33}$$

$$A_n(\mathbf{x}) = \Gamma(\lambda + n + 1) \left(\frac{i}{k}\right)^{\lambda+1} (-1)^n \sigma_n(\mathbf{x}). \tag{4.34}$$

In a similar way, Fourier inversion implies that any frequency domain ray expansion of the form (3.3) corresponds formally to a singularity supported on a wavefront in

[3]The use of k rather than ω as the transform variable is justified by the fact that under the scaling (4.29) the nondimensional frequency and wavenumber of a time-harmonic wave are equal ($\omega = k$).

the time domain. This formal correspondence allows us to use our knowledge of short wavelength propagation in the frequency domain to make certain predictions about the reflection and diffraction of pulses in the time domain.

In section 3.3.3 we saw that, in the frequency domain, a ray incident on a rigid boundary gives rise to a reflected ray satisfying the specular reflection law, with the limiting values of the phase and amplitude on the reflected ray being equal to those on the incident ray. The implication of this in the time domain is that a wavefront incident on a rigid boundary should give rise to a reflected wavefront, on which a singularity of the same order as that on the incident wavefront is supported.

In section 3.3.5 we saw that, in the frequency domain, a ray incident on an edge gives rise to a family of diffracted rays, on which the amplitude is, in general, $O\left(1/k^{1/2}\right)$ smaller than that on the incident ray. In the time domain this implies that a wavefront incident on an edge should give rise to a diffracted wavefront, on which a singularity half a power of ξ weaker than that on the incident wavefront is supported. The amplitude on a vertex-diffracted ray is, in general, $O\left(1/k\right)$ smaller than that on the incident ray, and in the time domain this implies that the singularity on a vertex-diffracted wavefront should be a whole power of ξ weaker than that on the incident wavefront.

We now verify these statements in a number of situations for which exact solutions of the time domain problem exist.

4.3 Review of exact solutions

In principle, the exact solutions reviewed in this section can be obtained by Fourier inversion of the appropriate frequency domain solutions discussed in section 3.3. However, in certain cases (see e.g. sections (4.3.4.3), (4.3.4.3) and (4.3.4.4)) it is also possible to obtain the time domain solution by alternative means, without taking a Fourier transform in time.

4.3.1 Fundamental solutions

The free-space solution of

$$\frac{\partial^2 \Phi}{\partial t^2} - c_0^2 \nabla^2 \Phi = \delta(\mathbf{x} - \mathbf{x}_0)\delta(t), \qquad \Phi = 0, \quad t < 0, \tag{4.35}$$

is called the *fundamental solution* of the wave equation. In three dimensions we have ([29], p. 382)

$$\Phi = F_{3D}(\mathbf{x_0}; \mathbf{x}, t) := \frac{H(t)}{4\pi c_0 r}\delta(c_0 t - r), \tag{4.36}$$

where $r = \sqrt{(x-x_0)^2 + (y-y_0)^2 + (z-z_0)^2}$. The disturbance is supported entirely on the characteristic half-cone $r = c_0 t$, $t > 0$, with the leading wavefront being the sphere $r = c_0 t$. Across this wavefront the solution possesses a delta function singularity $\delta(\xi)$, where $\xi = c_0 t - r$ measures the distance from the wavefront. With the leading wavefront described by $t - \tau(\mathbf{x}) = 0$, where $\tau(\mathbf{x}) = r/c_0$, we have $\nabla\tau\cdot\nabla = \frac{1}{c_0}\frac{\partial}{\partial r}$ and $\nabla^2\tau = \frac{2}{c_0 r}$, so that the transport equation (4.28) becomes

$$\frac{\partial \sigma_{\text{spatial}}}{\partial r} + \frac{1}{r}\sigma_{\text{spatial}} = 0. \tag{4.37}$$

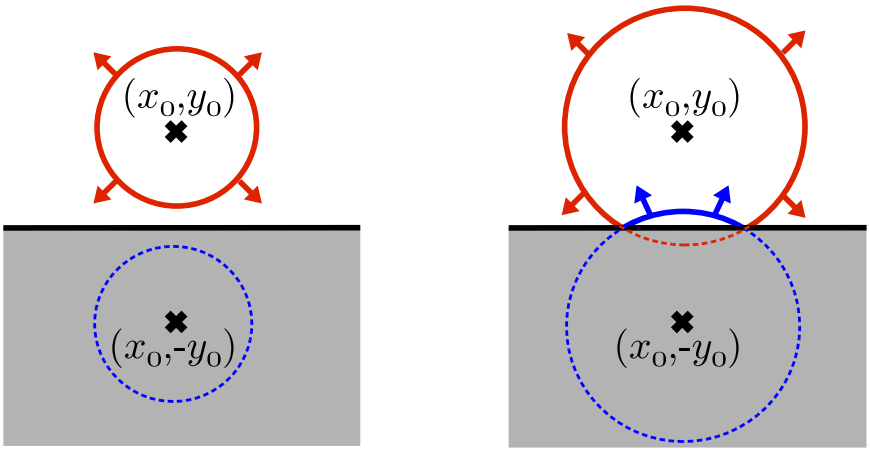
We remark that the coefficient $\frac{1}{4\pi c_0 r}$ multiplying the delta function singularity in (4.36) does indeed satisfy (4.37).

In two dimensions the fundamental solution is ([29], p. 384)

$$\Phi = F_{2D}(\mathbf{x_0}; \mathbf{x}, t) := \frac{H(t)H(c_0 t - r)}{2\pi c_0 \sqrt{c_0^2 t^2 - r^2}}, \tag{4.38}$$

where $r = \sqrt{(x-x_0)^2 + (y-y_0)^2}$. The leading wavefront is the circle $r = c_0 t$, across which there is a $\frac{H(\xi)}{\sqrt{\xi}}$ singularity. In contrast to the 3D case, behind the sharp leading wavefront there is a lingering disturbance[4], with the support of the solution being

[4]This difference between 3D and 2D propagation is a manifestation of *Huygens' principle* - see e.g. [71], pp. 368-369.



(a) $0 < t < y_0/c_0$ (b) $t > y_0/c_0$

Figure 4.1: Wavefront diagram for a 2D point source in the presence of a rigid half-plane, showing the incident (red) and reflected (blue) wavefronts. The arrows indicate the direction in which the wavefronts propagate.

the *interior* of the characteristic half-cone $r = c_0 t$, $t > 0$. With $\tau(\mathbf{x}) = r/c_0$, we have $\nabla\tau \cdot \nabla = \frac{1}{c_0}\frac{\partial}{\partial r}$ and $\nabla^2\tau = \frac{1}{c_0 r}$, so that the transport equation (4.28) is

$$\frac{\partial \sigma_{\text{spatial}}}{\partial r} + \frac{1}{2r}\sigma_{\text{spatial}} = 0. \tag{4.39}$$

We remark that the coefficient $\frac{1}{2\pi c_0\sqrt{2r}}$ multiplying the inverse square root singularity in (4.38) does indeed satisfy the transport equation (4.39).

4.3.2 Reflection by a half-space

The solution of (4.35) in a half-space with rigid boundary is trivially constructed from the fundamental solution by the method of images. For example, in the two-dimensional case where the propagation domain is the half-plane $y > 0$, we extend the propagation domain to the whole plane and insert a second source, identical to the first, at the image point $\tilde{\mathbf{x}}_\mathbf{0} = (x_0, -y_0)$, giving

$$\Phi(\mathbf{x}, t) = F_{2D}(\mathbf{x_0}, \mathbf{x}, t) + F_{2D}(\tilde{\mathbf{x}}_\mathbf{0}, \mathbf{x}, t). \tag{4.40}$$

A diagram of the wavefronts for $t > y_0/c_0$ is shown in Figure 4.1. The singularity on the reflected wavefront is the same as that on the incident wavefront, and the rays incident on the boundary give rise to reflected rays satisfying the specular reflection law: angle of reflection equals angle of incidence.

4.3.3 A point source in a single 2D street

Similarly, the method of images provides an exact solution of (4.35) in the case of a single 2D street, as modelled in section 3.3.4, namely

$$\Phi(\mathbf{x}, t) = \sum_{n \in \mathbf{Z}} F_{2D}(\mathbf{x_n}, \mathbf{x}, t), \tag{4.41}$$

where $\mathbf{x_n} = (0, y_n)$, with y_n defined as in (3.39).

4.3.4 Diffraction by a wedge

The first non-trivial domain of relevance is the exterior of a rigid wedge, described in cylindrical polar coordinates (r, θ, z) (with the z axis along the edge) by $0 < r < \infty$, $0 < \theta < \beta$, with $\pi < \beta \leq 2\pi$. As remarked in section 3.3.5.3, the special case $\beta = 2\pi$ corresponds to the problem of scattering from a half-line.

4.3.4.1 Incoming planar step discontinuity at parallel incidence

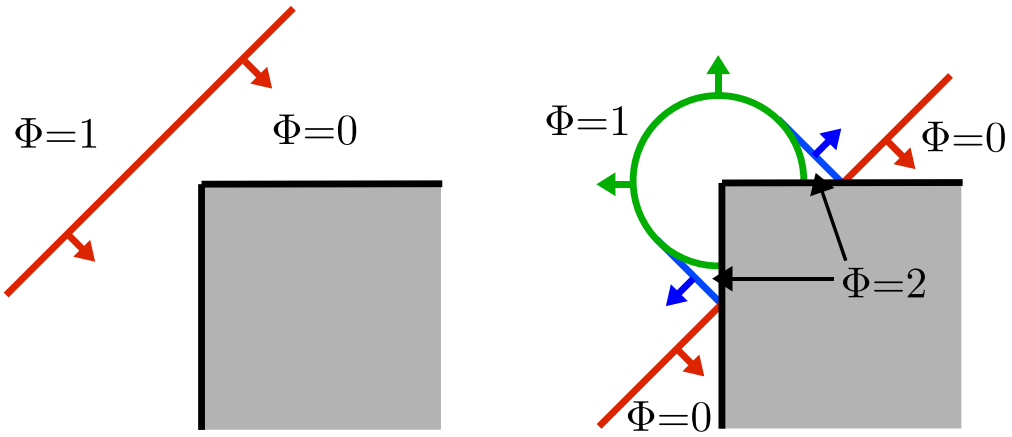
We consider first the case where the incident pulse is a unit step discontinuity supported on a planar wavefront parallel to the edge (so that the field is independent of z) and advancing towards the wedge from the direction θ_0. By symmetry it suffices to consider only the case $0 < \theta_0 < \beta/2$. In principle, the solution to this pulse diffraction problem can, of course, be found by Fourier inversion of the corresponding frequency domain solution, which was discussed in section 3.3.5. However, alternative derivations have been proposed which do not involve transforming to the frequency domain (see e.g. [49, 55, 64] and [34], p. 123). The approach we present here is due to Keller [49], and we review the derivation in some detail since it will be of use in later sections.

When $\pi/2 < \theta_0 < \beta/2$ the incident wave is represented by the condition

$$\Phi = H(c_0 t + r\cos(\theta - \theta_0)), \quad t < 0, \tag{4.42}$$

so that for $t < 0$ the incident wavefront (i.e. the plane $c_0 t + r\cos(\theta - \theta_0) = 0$) separates the domain into two regions, with $\Phi = 0$ ahead of the wavefront and $\Phi = 1$ behind it (see Figure 4.2(a)).

At $t = 0$ the wavefront arrives at the edge $r = 0$ and the solution gains additional structure. The region of influence of the point $r = 0$, $t = 0$, in space-time is the



(a) $t < 0$ (b) $t > 0$

Figure 4.2: Wavefront diagram for diffraction of a plane step discontinuity by a wedge of exterior angle $\beta = 3\pi/2$, showing the incident (red), reflected (blue) and diffracted (green) wavefronts. The arrows indicate the direction in which the wavefronts propagate.

sector of the interior of the characteristic half-cone with vertex at $r = 0$, $t = 0$, (i.e. $r < c_0 t$) bounded by the planes $\theta = 0$, $\theta = \beta$, and we refer to this as the *diffracted region*. The diffracted wavefront is the circle $r = c_0 t$, with the associated diffracted rays being radial lines.

Outside the diffracted region the solution is unaffected by the presence of the edge, and can be constructed using the reflection law discussed in the previous section, as if the walls extended to infinity in both directions. In the region $0 < \theta < \pi - \theta_0$, $c_0 t < r < -c_0 t/\cos(\theta + \theta_0)$, we have $\Phi = 2$ because of the presence of a reflected wave from the wall $\theta = 0$. If $\beta - \pi < \theta_0 < \beta/2$ there is also a reflected wave from the wall $\theta = \beta$, so that $\Phi = 2$ in the region $2\beta - \pi - \theta_0 < \theta < \beta$, $c_0 t < r < -c_0 t/\cos(\theta - (2\beta - \theta_0))$. An illustration of the resulting wavefront configuration for this case can be found in Figure 4.2(b).

We now proceed to construct the solution in the diffracted region $r < c_0 t$. We consider first the case where $\beta - \pi < \theta_0 < \beta/2$ (as in Figure 4.2). Applying the Principle of Minimum Singularity (see section 2.4), we assume that Φ is continuous[5] across the diffracted wavefront $r = c_0 t$. Then, inside the diffracted region Φ must

[5]The reasoning behind this assumption is that if Φ had a jump discontinuity across the diffracted wavefront, the size of the jump would necessarily tend to infinity as $t \to 0$ from above, since the diffracted rays converge at the edge. Since the incident wave is finite at the edge, such singular behaviour in the diffracted field cannot be allowed.

satisfy the wave equation

$$\frac{\partial^2\Phi}{\partial t^2} - c_0^2\left[\frac{\partial^2\Phi}{\partial r^2} + \frac{1}{r}\frac{\partial\Phi}{\partial r} + \frac{1}{r^2}\frac{\partial^2\Phi}{\partial\theta^2}\right] = 0, \qquad 0 < r < c_0 t, \tag{4.43}$$

and the boundary conditions

$$\Phi = \begin{cases} 2, & r = c_0 t,\ \ 0 < \theta < \pi - \theta_0, \\ 1, & r = c_0 t,\ \ \pi - \theta_0 < \theta < 2\beta - \pi - \theta_0, \\ 2, & r = c_0 t,\ \ 2\beta - \pi - \theta_0 < \theta < \beta, \end{cases} \tag{4.44}$$

$$\frac{\partial\Phi}{\partial\theta} = 0, \qquad 0 < r < c_0 t,\ \ \theta = 0, \beta. \tag{4.45}$$

Noting that the transformation $t = \lambda\tilde{t}$, $r = \lambda\tilde{r}$ leaves equation (4.43) and the boundary conditions (4.44)-(4.45) unchanged, we seek a similarity solution of the form $\Phi = \Phi(\zeta, \theta)$, where the similarity variable $\zeta = r/(c_0 t)$. Equation (4.43) then becomes

$$\zeta^2(1-\zeta^2)\frac{\partial^2\Phi}{\partial\zeta^2} + \zeta(1-2\zeta^2)\frac{\partial\Phi}{\partial\zeta} + \frac{\partial^2\Phi}{\partial\theta^2} = 0, \qquad 0 < \zeta < 1. \tag{4.46}$$

Making the further change of variable $\zeta = \frac{2\eta}{1+\eta^2}$ gives

$$\frac{\partial^2\Phi}{\partial\eta^2} + \frac{1}{\eta}\frac{\partial\Phi}{\partial\eta} + \frac{1}{\eta^2}\frac{\partial^2\Phi}{\partial\theta^2} = 0, \qquad 0 < \eta < 1 \tag{4.47}$$

which we recognise as Laplace's equation in the 2D polar coordinates (η, θ). The boundary conditions (4.44)-(4.45) become

$$\Phi = \begin{cases} 2, & \eta = 1,\ \ 0 < \theta < \pi - \theta_0, \\ 1, & \eta = 1,\ \ \pi - \theta_0 < \theta < 2\beta - \pi - \theta_0, \\ 2, & \eta = 1,\ \ 2\beta - \pi - \theta_0 < \theta < \beta, \end{cases} \tag{4.48}$$

$$\frac{\partial\Phi}{\partial\theta} = 0, \qquad 0 < \eta < 1,\ \ \theta = 0, \beta. \tag{4.49}$$

The solution of (4.47)-(4.49) is readily found by complex variable methods. We begin by writing $\Phi = \mathrm{Re}[f(w)]$, where $w = \eta e^{i\theta}$ and $f(w)$ is analytic in the sector of the unit disc $0 < \eta < 1$, $0 < \theta < \beta$. The transformation $v = w^\kappa$, $\kappa = \pi/\beta$ maps this domain to the upper half disc in the complex v-plane. The boundary condition on $\mathrm{Im}[v] = 0$ can be satisfied by seeking a solution in the *whole* unit disc with *symmetric* boundary conditions on the unit circle. We thus seek a function of $v = \rho e^{i\gamma}$, $\gamma \in [-\pi, \pi)$, which is analytic in the unit disc and whose real part takes the values

$$\Phi = \begin{cases} 2, & \eta = 1,\ \ 0 < |\gamma| < \kappa(\pi - \theta_0), \\ 1, & \eta = 1,\ \ \kappa(\pi - \theta_0) < |\gamma| < 2\pi - \kappa(\pi + \theta_0), \\ 2, & \eta = 1,\ \ 2\pi - \kappa(\pi + \theta_0) < |\gamma| < \pi. \end{cases} \tag{4.50}$$

The canonical problem with boundary values

$$\Phi = \begin{cases} 1, & \eta = 1, \;\; \gamma_1 < \gamma < \gamma_2, \\ 0, & otherwise, \end{cases} \tag{4.51}$$

with $0 < \gamma_2 - \gamma_1 < 2\pi$, is readily solved (e.g. by conformally mapping to the upper half plane) to give

$$\Phi = \frac{1}{\pi} \arctan \left[\frac{(1-\rho^2) \sin \frac{\gamma_2 - \gamma_1}{2}}{(1+\rho^2) \cos \frac{\gamma_2 - \gamma_1}{2} - 2\rho \cos\left(\gamma - \frac{\gamma_2 - \gamma_1}{2}\right)} \right], \tag{4.52}$$

where the arctangent is taken in the interval between 0 and π. Cancelling a factor of ρ from numerator and denominator in the argument of the arctangent, substituting $\rho = \eta^\kappa$ and noting that

$$\eta^\kappa + \eta^{-\kappa} = 2 \cosh\left(\kappa \operatorname{arcosh} \frac{1}{\zeta}\right), \tag{4.53}$$

$$\eta^\kappa - \eta^{-\kappa} = -2 \sinh\left(\kappa \operatorname{arcosh} \frac{1}{\zeta}\right), \tag{4.54}$$

the solution satisfying (4.50) is then

$$\Phi = \frac{1}{\pi} \sum_{\pm} \arctan \left[\frac{\sinh\left(\kappa \operatorname{arcosh} \frac{1}{\zeta}\right) \sin \kappa\pi}{\cosh\left(\kappa \operatorname{arcosh} \frac{1}{\zeta}\right) \cos \kappa\pi - \cos \kappa\left(\theta \pm \theta_0\right)} \right]. \tag{4.55}$$

In the original variables this is

$$\Phi = \frac{1}{\pi} \sum_{\pm} \arctan \left[\frac{\sinh\left(\kappa \operatorname{arcosh} \frac{c_0 t}{r}\right) \sin \kappa\pi}{\cosh\left(\kappa \operatorname{arcosh} \frac{c_0 t}{r}\right) \cos \kappa\pi - \cos \kappa\left(\theta \pm \theta_0\right)} \right], \tag{4.56}$$

which agrees[6] with the result in [34], equation (5.5.7).

In the case where $\pi/2 < \theta_0 < \beta - \pi$ there is no longer a reflection from $\theta = \beta$ and the boundary conditions (4.50) must be altered to

$$\Phi = \begin{cases} 2, & \eta = 1, \;\; 0 < |\gamma| < \kappa(\pi - \theta_0), \\ 1, & \eta = 1, \;\; \kappa(\pi - \theta_0) < |\gamma| < \kappa(\pi + \theta_0), \\ 0, & \eta = 1, \;\; \kappa(\pi + \theta_0) < |\gamma| < \pi, \end{cases} \tag{4.57}$$

but the same formula (4.56) is obtained.

[6] We remark, however, that Friedlander's formula contains two typographical errors.

When $0 < \theta_0 < \pi/2$ the reflected wave due to the wall $\theta = 0$ is present even for $t < 0$, so that

$$\Phi = \sum_{\pm} H(\pi - (\theta \pm \theta_0))H(c_0 t + r\cos(\theta \pm \theta_0)), \qquad t < 0. \tag{4.58}$$

Remarkably, the same formula (4.56) is again obtained for the field inside the diffracted region. In fact, symmetry arguments reveal that the same is true even of the case $\beta/2 < \theta_0 < \beta$, and we therefore conclude that (4.56) provides the solution in the diffracted region $r < c_0 t$ for all $0 < \theta_0 < \beta$.

4.3.4.2 Behaviour near diffracted wavefront

We now determine the behaviour of (4.56) near the diffracted wavefront. Let $\xi = c_0 t - r$ be the distance from the diffracted wavefront, and set $\varepsilon = \frac{\xi}{r}$. Then $\frac{c_0 t}{r} = \varepsilon + 1$, and when $\varepsilon \ll 1$ we can expand

$$\operatorname{arcosh}\frac{c_0 t}{r} \sim \sqrt{2\varepsilon} - \frac{1}{6\sqrt{2}}\varepsilon^{3/2} + \ldots, \tag{4.59}$$

$$\sinh\left(\kappa \operatorname{arcosh}\frac{c_0 t}{r}\right) \sim \kappa\sqrt{2\varepsilon} + \kappa\left(\frac{\sqrt{2}\kappa^2}{3} - \frac{\kappa}{6\sqrt{2}}\right)\varepsilon^{3/2} + \ldots, \tag{4.60}$$

$$\cosh\left(\kappa \operatorname{arcosh}\frac{c_0 t}{r}\right) \sim 1 + \kappa^2\varepsilon + \ldots. \tag{4.61}$$

A uniform approximation to (4.56), valid for all θ, is then

$$\Phi \sim \sum_{\pm} \frac{1}{\pi}\arctan\left[\frac{\kappa\sqrt{2\varepsilon}\sin\kappa\pi}{\cos\kappa\pi - \cos\kappa(\theta \pm \theta_0) + \kappa^2\varepsilon\cos\kappa\pi}\right], \qquad \varepsilon \ll 1. \tag{4.62}$$

When $\sqrt{\varepsilon} \ll \cos\kappa\pi - \cos\kappa(\theta \pm \theta_0)$ we can use the following approximation, valid for small δ,

$$\arctan\delta \sim \begin{cases} \delta - \frac{1}{3}\delta^3 + \ldots, & \delta > 0, \\ \pi + \delta - \frac{1}{3}\delta^3 + \ldots, & \delta < 0, \end{cases} \tag{4.63}$$

to get

$$\Phi \sim \sum_{\pm} H(\cos\kappa\pi - \cos\kappa(\theta \pm \theta_0)) + \frac{\sqrt{2\varepsilon}\sin\kappa\pi}{\beta(\cos\kappa\pi - \cos\kappa(\theta \pm \theta_0))}. \tag{4.64}$$

This approximation (4.64) becomes invalid when θ approaches a value for which one of the terms $\cos\kappa\pi - \cos\kappa(\theta \pm \theta_0)$ vanishes. Writing

$$\cos\kappa\pi - \cos\kappa(\theta \pm \theta_0) = -2\sin\kappa\left(\frac{\pi + (\theta \pm \theta_0)}{2}\right)\sin\kappa\left(\frac{\pi - (\theta \pm \theta_0)}{2}\right) \tag{4.65}$$

reveals that this occurs whenever

$$\kappa(\pi \pm (\theta \pm \theta_0)) = 2n\pi \tag{4.66}$$

for some integer n, and any combination of the $\pm$ signs. For example, when $0 < \theta_0 < \beta - \pi$ the only cases for which a relevant solution $0 < \theta < \beta$ exists are

$$\kappa(\pi - (\theta + \theta_0)) = 0 \;\; \Rightarrow \;\; \theta = \pi - \theta_0, \tag{4.67}$$

$$\kappa(\pi - (\theta - \theta_0)) = 0 \;\; \Rightarrow \;\; \theta = \pi + \theta_0. \tag{4.68}$$

These special values of θ correspond to the boundaries in $r > c_0 t$ between the incident and reflected regions and the incident and shadow regions, respectively. In the shadow region $\pi + \theta_0 < \theta < \beta$ both Heaviside terms in (4.64) vanish, so that

$$\Phi \sim C(\theta) H(\varepsilon)\sqrt{\varepsilon} = \frac{C(\theta)}{\sqrt{r}} H(\xi)\sqrt{\xi}, \tag{4.69}$$

where

$$C(\theta) = \frac{\sqrt{2}\kappa}{\pi} \sum_{\pm} \frac{\sin \kappa\pi}{\cos \kappa\pi - \cos \kappa\,(\theta \pm \theta_0)}. \tag{4.70}$$

The step discontinuity $H(\xi)$ on the incident wavefront has given rise to $H(\xi)\sqrt{\xi}$ behaviour on the diffracted wavefront. We remark that the coefficient $C(\theta)/\sqrt{r}$ multiplying $H(\xi)\sqrt{\xi}$ clearly satisfies the transport equation (4.39) associated with the circular wavefronts. Moreover, as is to be expected following the remarks made in section 4.2.4, $C(\theta)$ is simply a constant multiple of the diffraction coefficient $D(\theta)$ of the corresponding frequency domain problem, given by (3.63). Specifically,

$$C(\theta) = \frac{2e^{-i\pi/4}}{\sqrt{\pi}} D(\theta). \tag{4.71}$$

4.3.4.3 Oblique incidence

Now suppose the incident planar wavefront intersects the wedge obliquely, arriving from the direction $(\sin\gamma_0, \theta_0, \cos\gamma_0)$ in cylindrical polar co-ordinates. Without loss of generality we assume $0 < \theta_0 < \beta/2$ and $0 < \gamma_0 < \pi/2$. The incident wavefront now intersects the edge $r = 0$ for all times t, with the point of intersection $z(t)$ satisfying $\frac{dz}{dt} = -\frac{c_0}{\cos\gamma_0}$. Assuming that $z(0) = 0$, the incident wavefront is then the plane $c_0 t + r\cos(\theta - \theta_0)\sin\gamma_0 + z\cos\gamma_0 = 0$, restricted to $0 < \theta < \pi + \theta_0$ if $0 < \theta_0 < \beta - \pi$. There is a planar reflected wavefront $c_0 t + r\cos(\theta + \theta_0)\sin\gamma_0 + z\cos\gamma_0 = 0$ in the

region $0 < \theta < \pi - \theta_0$, due to the wall $\theta = 0$. When $\beta - \pi < \theta_0 < \beta/2$ there is also a planar reflected wavefront $c_0 t + r\cos(\theta - (2\beta - \theta_0))\sin\gamma_0 + z\cos\gamma_0 = 0$ in the region $0 < \theta < \pi - \theta_0$, due to the wall $\theta = \beta$.

We expect there to be a diffracted wave contained in the region of influence of the line $r = 0$, $z = z(t)$ in space-time, and we refer to this as the diffracted region. The intersection of this region with a plane of constant t is the interior of the cone $z = \frac{r\sin\gamma_0 - c_0 t}{\cos\gamma_0}$, restricted to $0 < \theta < \beta$, and we call this cone the diffracted wavefront, with the associated diffracted rays being straight lines emanating from the point $(0, 0, z(t))$, forming a cone of semi-angle γ_0 with axis the z-axis.

Noting that the wave equation and the value of Φ on the diffracted wavefront are invariant under transformations $t = \tilde{t} + \lambda$, $z = \tilde{z} - \lambda\frac{c_0}{\cos\gamma_0}$, we are motivated to look for a similarity solution $\Phi = \Phi(r, \theta, \mu)$ where the similarity variable $\mu = \frac{z\cos\gamma_0 + c_0 t}{c_0 \sin\gamma_0}$, say. The 3D wave equation transforms to

$$\frac{\partial^2\Phi}{\partial\mu^2} - c_0^2\left[\frac{\partial^2\Phi}{\partial r^2} + \frac{1}{r}\frac{\partial\Phi}{\partial r} + \frac{1}{r^2}\frac{\partial^2\Phi}{\partial\theta^2}\right] = 0, \tag{4.72}$$

which we recognise as the 2D wave equation (4.43) with t replaced by μ. The incident wavefront transforms to the plane $c_0 t + r\cos(\theta - \theta_0)$, and the reflected wavefronts transform to $c_0 t + r\cos(\theta + \theta_0)$ and $c_0 t + r\cos(\theta - (2\beta - \theta_0))$, respectively. The diffracted wavefront transforms to the cone $r = c_0\mu$, and the problem is therefore equivalent to the problem of parallel incidence, discussed in the previous sections, with t replaced by μ.

Formula (4.56) then provides the solution in the diffracted region:

$$\Phi = \frac{1}{\pi}\sum_{\pm}\arctan\left[\frac{\sinh\left(\kappa\,\mathrm{arcosh}\left(\frac{z\cos\gamma_0 + c_0 t}{r\sin\gamma_0}\right)\right)\sin\kappa\pi}{\cosh\left(\kappa\,\mathrm{arcosh}\left(\frac{z\cos\gamma_0 + c_0 t}{r\sin\gamma_0}\right)\right)\cos\kappa\pi - \cos\kappa(\theta \pm \theta_0)}\right], \tag{4.73}$$

where, as in (4.56), the arctangent is taken in the interval between 0 and π.

To determine the behaviour near the diffracted wavefront we first note that the distance from the diffracted wavefront, measured in the normal direction, is $\xi = z\cos\gamma_0 + c_0 t - r\sin\gamma_0$. Then, setting $\varepsilon = \frac{\xi}{r\sin\gamma_0}$ we have $\frac{z\cos\gamma_0 + c_0 t}{r\sin\gamma_0} = 1 + \varepsilon$, so that when $\varepsilon \ll 1$,

$$\Phi \sim \frac{C(\theta)}{\sqrt{r\sin\gamma_0}} H(\xi)\sqrt{\xi}, \tag{4.74}$$

where $C(\theta)$ is defined as in (4.70).

4.3.4.4 Incident delta-pulse

We remark that by differentiating (4.56) and (4.73) with respect to t, the response to an incident delta-pulse can be obtained[7]. In both cases the leading order behaviour near the diffracted wavefront is found to be proportional to $H(\xi)/\sqrt{\xi}$, although we do not present the details here.

4.3.4.5 A point source in 2D

When the incident wave is due to a 2D point source rather than a plane pulse, the boundary conditions on the diffracted wavefront cannot be expressed in terms of a similarity variable, and the method described in section 4.3.4 no longer applies. The solution can, of course, be obtained by Fourier inversion of the corresponding frequency domain solution, as described in [69]. An alternative derivation, based on an application of Sommerfeld's Riemann-surface method (see [81]) in the time domain has been given by Friedlander ([34]). For a source at (r_0, θ_0) the solution may be written [34]:

$$\begin{aligned}\Phi = &\frac{\sigma(\theta-\theta_0)H(c_0t-\overline{r})}{2\pi c_0\sqrt{c_0^2t^2-\overline{r}^2}} + \frac{\sigma(\theta+\theta_0)H(c_0t-\overline{r}_*)}{2\pi c_0\sqrt{c_0^2t^2-\overline{r}_*^2}} \\ &+ \frac{H(c_0t-(r+r_0))}{4\pi\beta c_0\sqrt{2rr_0}}\int_0^{\operatorname{arcosh} Z}\frac{Q(s,\theta-\theta_0)+Q(s,\theta+\theta_0)}{\sqrt{Z-\cosh s}}\,ds, \qquad (4.75)\end{aligned}$$

where

$$\sigma(\psi) = \begin{cases}1, & |\psi_*|<\pi,\\ 0, & |\psi_*|>\pi,\end{cases} \qquad (4.76)$$

$$\psi_* = \psi \pmod{2\beta}, \quad \psi_* \in (-\beta,\beta), \qquad (4.77)$$

$$\overline{r} = \sqrt{r^2+r_0^2-2rr_0\cos(\theta-\theta_0)}, \qquad (4.78)$$

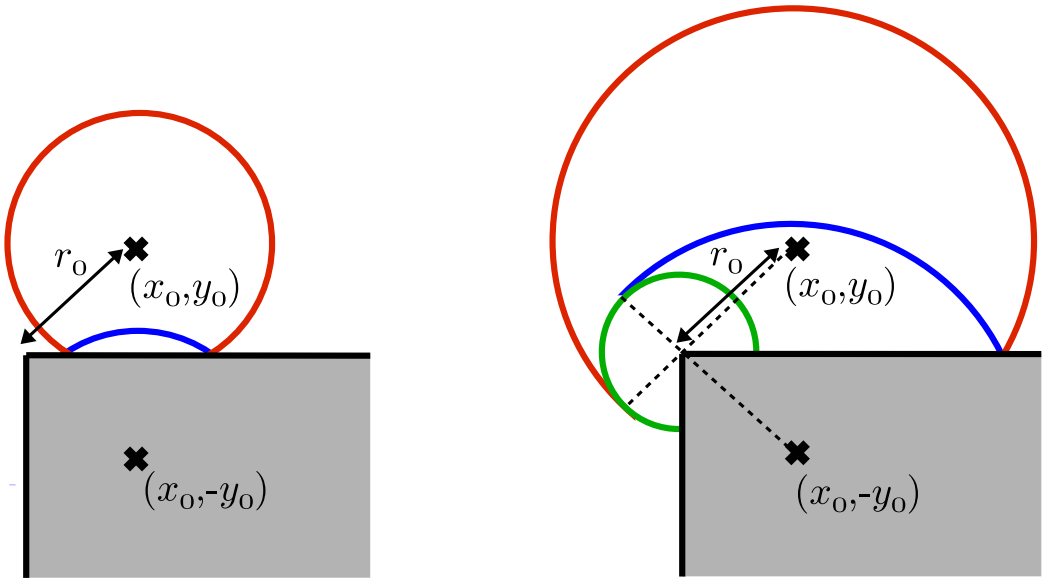
$$\overline{r}_* = \sqrt{r^2+r_0^2-2rr_0\cos(\theta+\theta_0)_*}, \qquad (4.79)$$

$$Z = \frac{c_0^2t^2-r^2-r_0^2}{2rr_0}, \qquad (4.80)$$

$$Q(s,\psi) = \sum_{\pm} -\frac{\sin\kappa(\pi\pm\psi)}{\cosh\kappa s-\cos\kappa(\pi\pm\psi)}. \qquad (4.81)$$

We now provide a brief interpretation of this result, assuming as before that $0 < \theta_0 < \beta/2$. The first term in (4.75) represents the incident wave, with $\overline{r}$ denoting the

[7] An explicit example of this will be presented in section 4.5.4, equation (4.163).



(a) $0 < t < r_0/c_0$ (b) $t > r_0/c_0$

Figure 4.3: Wavefront diagram for 2D point source in the presence of a wedge of exterior angle $\beta = 3\pi/2$, showing the incident (red), reflected (blue) and diffracted (green) wavefronts. The source location is indicated by the small red circle.

distance from the observation point to the source location. The second term represents the reflected wave. When $0 < \theta_0 < \beta - \pi$ there is just one reflected wave due to the wall $\theta = 0$, with $\overline{r}_*$ denoting the distance from the observation point to the image source location $(r_0, -\theta_0)$. When $\beta - \pi < \theta < \beta/2$ there is an additional reflected wave due to the wall $\theta = \beta$, and in the region where this wave exists, $\overline{r}_*$ denotes the distance from the observation point to the image source location $(r_0, 2\beta - \theta_0)$. The third term, present only inside the diffracted region $r < c_0 t - r_0$, represents the diffracted field, and has jump discontinuities across the shadow boundaries of the incident and reflected waves to compensate for the corresponding discontinuities in the first two terms. The corresponding wavefront diagram for the case $0 < \theta_0 < \beta - \pi$ is illustrated in Figure 4.3.

The behaviour of the solution near the diffracted wavefront can be found by a careful analysis of the third term in (4.75), which we denote Φ_{diff}. The distance from the diffracted wavefront is $\xi = c_0 t - r - r_0$, and setting $\varepsilon = \frac{\xi}{r} + \frac{\xi}{r_0} + \frac{\xi^2}{2rr_0}$ we have $Z = 1 + \varepsilon$. If both $\frac{\xi}{r} \ll 1$ and $\frac{\xi}{r_0} \ll 1$, then $\varepsilon \ll 1$ and we can approximate

$$\operatorname{arcosh}(Z) \sim \sqrt{2\varepsilon} - \frac{1}{6\sqrt{2}}\varepsilon^{3/2} + \ldots, \tag{4.82}$$

so that

$$\Phi_{\text{diff}} \sim \frac{H(\xi)}{4\pi\beta c_0\sqrt{2rr_0}} \int_0^{\sqrt{2\varepsilon}} \frac{Q(s,\theta-\theta_0)+Q(s,\theta+\theta_0)}{\sqrt{1+\varepsilon-\cosh s}}\, ds. \tag{4.83}$$

Expanding the integrand for small s we note that

$$1+\varepsilon-\cosh s \sim \varepsilon - \frac{s^2}{2} + \ldots \tag{4.84}$$

and

$$\begin{aligned} Q(s,\psi) &\sim \sum_{\pm} -\frac{\sin\kappa\,(\pi\pm\psi)}{\left(1+\frac{(\kappa s)^2}{2}+\ldots\right)-\cos\kappa\,(\pi\pm\psi)} \\ &\sim \sum_{\pm} -\frac{\sin\kappa\,(\pi\pm\psi)}{1-\cos\kappa\,(\pi\pm\psi)} \\ &= \frac{2\sin\kappa\pi}{\cos\kappa\pi-\cos\kappa\psi}, \end{aligned} \tag{4.85}$$

provided that $\frac{(\kappa s)^2}{2} \ll 1-\cos\kappa\,(\pi\pm\psi)$. Then[8]

$$\begin{aligned} \Phi_{\text{diff}} &\sim \frac{C(\theta)H(\xi)}{4\pi c_0\sqrt{rr_0}} \int_0^{\sqrt{2\varepsilon}} \frac{1}{\sqrt{\varepsilon-\frac{s^2}{2}}}\, ds \\ &= \frac{C(\theta)H(\xi)}{4c_0\sqrt{2rr_0}}, \end{aligned} \tag{4.86}$$

where $C(\theta)$ is defined as in (4.70). The approximation is valid if $\varepsilon \ll 1-\cos\kappa\,(\pi\pm\psi)$, which, as before, means that we are not too close to one of the shadow boundaries.

When $0<\theta_0<\beta-\pi$ the solution in the shadow region $2\beta-\pi-\theta_0<\theta<\beta$ is given by Φ_{diff} alone. Hence we see that the $\frac{H(\xi)}{\sqrt{\xi}}$ singularity on the incident wavefront gives rise to a jump discontinuity $H(\xi)$ across the diffracted wavefront.

4.3.4.6 A point source in 3D

The exact solution for a 3D point source in the presence of a rigid wedge is also well-known (see e.g. [69, 86, 93]), and for a source at $(r_0,\theta_0,0)$ in cylindrical coordinates

[8] We remark that (4.86) disagrees with the corresponding result in [34], equation (5.4.10), by a minus sign. Having compared the approximation (4.86) with the results of a numerical integration of (4.75) we conclude that the discrepancy must be due to a typographical error in Friedlander's book.

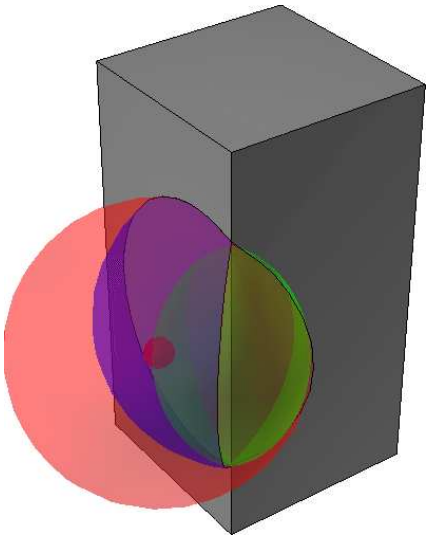


Figure 4.4: Wavefront diagram for 3D point source in the presence of a wedge of exterior angle $\beta = 3\pi/2$, showing the incident (red), reflected (blue) and diffracted (green) wavefronts. The source location is indicated by the small red sphere.

with the z-axis along the edge we have

$$\Phi = \frac{\sigma(\theta-\theta_0)\delta(c_0t-\overline{r})}{4\pi c_0\overline{r}} + \frac{\sigma(\theta+\theta_0)\delta(c_0t-\overline{r}_*)}{4\pi c_0\overline{r}_*} + \frac{H(c_0t-\sqrt{(r+r_0)^2+z^2})}{8\pi c_0\beta r r_0\sqrt{Z^2-1}}\left[Q(\operatorname{arcosh} Z,\theta-\theta_0)+Q(\operatorname{arcosh} Z,\theta+\theta_0)\right], \tag{4.87}$$

where

$$\overline{r} = \sqrt{r^2+r_0^2-2rr_0\cos(\theta-\theta_0)+z^2}, \tag{4.88}$$

$$\overline{r}_* = \sqrt{r^2+r_0^2-2rr_0\cos(\theta+\theta_0)_*+z^2}, \tag{4.89}$$

$$Z = \frac{c_0^2t^2-r^2-r_0^2-z^2}{2rr_0}, \tag{4.90}$$

and $Q(s,\psi)$ is defined as in (4.81).

The structure of the solution (4.87) is essentially the same as that of (4.75), with the first and second terms representing the incident and reflected fields, respectively. The third term represents the diffracted field, which we again denote by Φ_{diff}. The diffracted wavefront, described by $Z = 1$, or equivalently, by $c_0t = \sqrt{(r+r_0)^2+z^2}$, is the rugby-ball-shaped surface of revolution shaded in green in Figure 4.4. The associated diffracted rays are straight lines emanating from the z-axis, making an angle $\gamma = \arctan r_0/z$ with the z-axis (where z denotes the point of origin of the ray).

To determine the behaviour of Φ_{diff} near the diffracted wavefront, we first note that the distance from the diffracted wavefront, measured in the normal direction, is given by $\xi = c_0 t - \sqrt{(r+r_0)^2+z^2}$. Setting $\varepsilon = \frac{2\xi\sqrt{(r+r_0)^2+z^2}+\xi^2}{2rr_0}$, we have $Z = 1+\varepsilon$, and when $\varepsilon \ll 1$ we can approximate

$$\sqrt{Z^2-1} \sim \sqrt{2\varepsilon} + \ldots. \tag{4.91}$$

Then, using (4.82) and (4.85) with $s = \operatorname{arcosh} Z$ we obtain

$$\Phi_{\text{diff}} \sim \frac{C(\theta)H(\varepsilon)}{8\pi c_0 r r_0 \sqrt{2\varepsilon}}. \tag{4.92}$$

For $\xi \ll \sqrt{(r+r_0)^2+z^2}$ we have

$$\varepsilon \sim \frac{\xi\sqrt{(r+r_0)^2+z^2}}{rr_0}, \tag{4.93}$$

so that

$$\Phi_{\text{diff}} \sim \frac{C(\theta)}{8\pi c_0\sqrt{2rr_0}((r+r_0)^2+z^2)^{1/4}} \frac{H(\xi)}{\sqrt{\xi}}. \tag{4.94}$$

For the approximation to be valid we need $\varepsilon \ll 1-\cos\kappa\,(\pi \pm \psi)$. We find that the delta-function singularity on the incident wavefront gives rise to an inverse square root singularity $H(\xi)/\sqrt{\xi}$ on the diffracted wavefront. Finally, we note that the transport equation (4.28) in this case can be written as

$$\left(2(r+r_0)\frac{\partial}{\partial r} + 2z\frac{\partial}{\partial z}\right)\sigma_{\text{spatial}} + \frac{2r+r_0}{r}\sigma_{\text{spatial}} = 0, \tag{4.95}$$

and it is easily verified that the coefficient $\frac{C(\theta)}{8\pi c_0\sqrt{2rr_0}((r+r_0)^2+z^2)^{1/4}}$ in (4.94) satisfies (4.95).

4.3.5 Diffraction by a cone

According to the correspondence discussed in section 4.2.4, we expect the singularity on a vertex-diffracted wavefront to be a whole power of ξ weaker than that on the incident wavefront. Furthermore, we expect a delta-function singularity on the incident wavefront to give rise to a jump discontinuity on the vertex-diffracted wavefront.

The verification of these statements is complicated by the fact that exact solutions for the diffraction of pulses by cones are available only in certain special cases. The solution for a 3D point source in the presence of a circular or elliptical cone can be

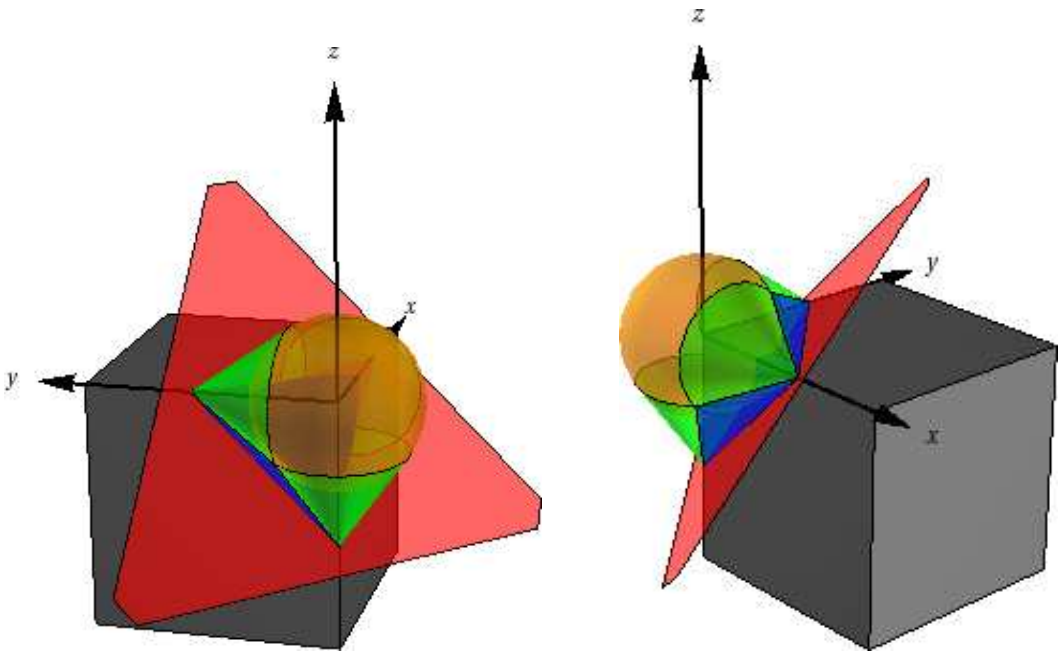


Figure 4.5: Wavefront diagram for diffraction of a planar pulse by a polyhedral cone, showing the incident (red), reflected (blue), edge-diffracted (green) and vertex-diffracted (orange) wavefronts. In this example the cone is the region $x > 0$, $y > 0$, $z < 0$ and the pulse is incident from the direction $(-1, -1, 1)$.

expressed as the inverse Fourier transform of the corresponding frequency domain solution mentioned in section 3.3.5.5, but the resulting formulae are rather cumbersome (see e.g. [19]). However, in the case of a narrow circular cone, it has been shown in [19] that the delta-function singularity on the incident field does indeed give rise to a jump discontinuity on the vertex-diffracted wavefront.

Pulse diffraction by more general cones has been considered by Borovikov and Kinber in [12], Section 9.5. For simplicity we consider here the special case of a planar pulse incident on a polyhedral cone, which could, for example, represent the corner of a building. An example of a wavefront diagram corresponding to this situation can be found in Figure 4.5. Assuming that the incident wavefront arrives at the vertex $r = 0$ at time $t = 0$, the vertex-diffracted wavefront is the sphere $r = c_0 t$ centred at the vertex. The faces of the cone give rise to planar reflected wavefronts, and the edges between the faces give rise to conical edge-diffracted wavefronts.

The method of analysis proposed in [12] is a direct generalisation of Keller's method, described in section 4.3.4, for the solution of the 2D wedge diffraction problem. We begin by rewriting the wave equation in spherical coordinates (r, θ, φ) with

origin at the vertex of the cone, which gives

$$\frac{\partial^2\Phi}{\partial t^2} - c_0^2\left[\frac{\partial^2\Phi}{\partial r^2} + \frac{2}{r}\frac{\partial\Phi}{\partial r} + \frac{1}{r^2}\Delta_\Omega\Phi\right] = 0, \qquad 0 < r < c_0 t, \tag{4.96}$$

where

$$\Delta_\Omega = \frac{\partial^2}{\partial\varphi^2} + \frac{1}{\tan\varphi}\frac{\partial}{\partial\varphi} + \frac{1}{\sin^2\varphi}\frac{\partial^2}{\partial\theta^2}, \tag{4.97}$$

and assume an incident pulse of the form

$$\Phi = H(\xi_{\text{inc}})\xi_{\text{inc}}^{\mu}, \qquad t < 0; \tag{4.98}$$

here μ is yet to be chosen and $\xi_{\text{inc}} = c_0 t + r(\mathbf{\Omega}\cdot\mathbf{\Omega_0})$, where $\mathbf{\Omega} = (\cos\varphi\cos\theta, \cos\varphi\sin\theta, \sin\varphi)$, so that (4.98) represents a planar pulse propagating towards the cone from the direction $\mathbf{\Omega_0}$. Note that the form of (4.98) implicitly assumes that the cone lies entirely in the half-space $\mathbf{\Omega}\cdot\mathbf{\Omega_0} < 0$, so that there is no reflected or edge-diffracted wave for $t < 0$.

Noting that the transformation $t = \lambda\tilde{t}$, $r = \lambda\tilde{r}$, $\Phi = \lambda^{-\mu}\tilde{\Phi}$ leaves the equation (4.96) and the incident field (4.98) unchanged, we seek a similarity solution inside the vertex-diffracted region (the interior of the cone $r = c_0 t$) of the form $\Phi = (c_0 t)^\mu \Psi(\zeta, \mathbf{\Omega})$, where the similarity variable $\zeta = r/(c_0 t)$. The equation (4.96) then becomes

$$\zeta^2(1-\zeta^2)\frac{\partial^2\Psi}{\partial\zeta^2} + 2\zeta(1 + (\mu-1)\zeta^2)\frac{\partial\Psi}{\partial\zeta} - \mu(\mu-1)\zeta^2\Psi + \Delta_\Omega\Psi = 0, \qquad 0 < \zeta < 1. \tag{4.99}$$

Making the further change of variables

$$\zeta = \frac{2\eta}{1+\eta^2}, \tag{4.100}$$

$$\Psi = \left(\frac{2}{1+\eta^2}\right)^\mu (1-\eta^2)^{\mu+1/2}\Upsilon, \tag{4.101}$$

gives, after some manipulation[9],

$$\frac{\partial^2\Upsilon}{\partial\eta^2} + \frac{2}{\eta}\frac{\partial\Upsilon}{\partial\eta} + \frac{1}{\eta^2}\Delta_\Omega\Upsilon - \frac{(2\mu+3)(2\mu+1)}{(1-\eta^2)^2}\Upsilon = 0, \qquad 0 < \eta < 1. \tag{4.102}$$

In the special cases $\mu = -3/2$, $\mu = -1/2$, equation (4.102) is simply Laplace's equation[10] in the spherical coordinates (η, Ω). In order that the change of variable (4.101) be nondegenerate at $\eta = 1$, we consider the case $\mu = -1/2$. We then expect the singularity on the vertex-diffracted wavefront to be $H(\xi)\sqrt{\xi}$.

[9]Formula (4.102) corrects a typographical error in [12], p. 357.

[10]We remark that in the 2D wedge diffraction case, a similar analysis produces Laplace's equation only when $\mu = -1$ or $\mu = 0$. The latter case corresponds to an incident jump discontinuity, which has been discussed in section 4.3.4.

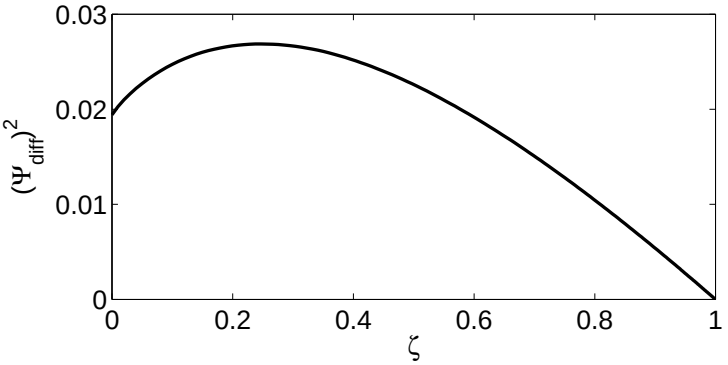


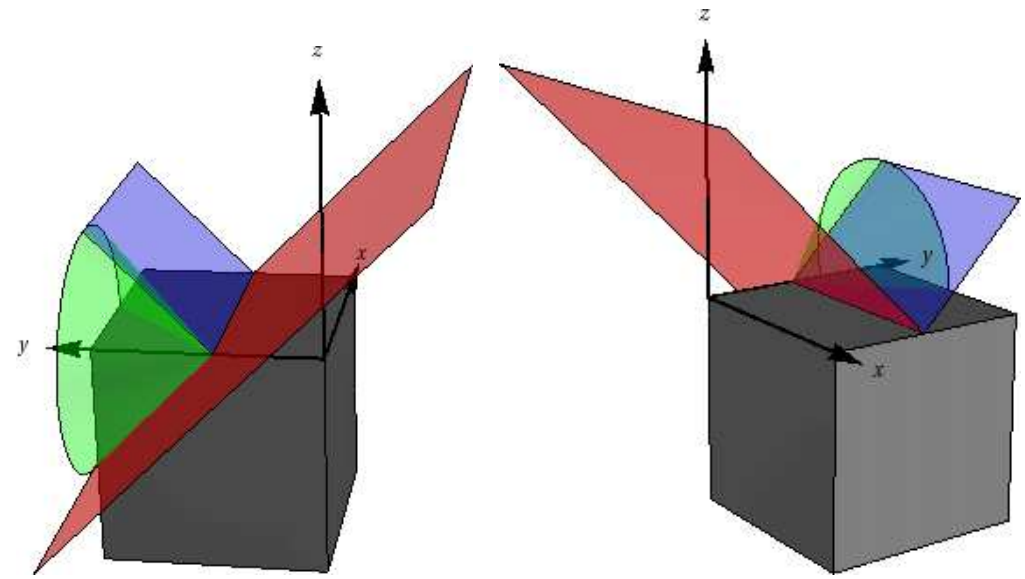
Figure 4.6: Result of FEM solution for diffraction of a planar pulse by a polyhedral cone, with the geometry of Figure 4.5 and an inverse square root singularity on the incident wavefront. The plot shows how the square of Ψ_{diff} varies as a function of ζ in the direction $(-1,-1,1)$, the direction from which the wave was incident. The linear behaviour observed near $\zeta = 1$ confirms our expectation that Ψ_{diff} should have a square-root singularity on the diffracted wavefront.

Assuming that the field is continuous across the diffracted wavefront, the boundary conditions on the diffracted wavefront ($\eta = 1$) are obtained from the field outside the diffracted region, which can be constructed using the wedge diffraction solutions discussed in section 4.3.4.3. The resulting boundary value problem can then be solved numerically, e.g. using FEM. Such a solution has been performed for the case illustrated in Figure 4.5 using the FEM package Comsol. A sample output of the calculation can be found in Figure 4.6. The function Ψ_{diff} is the diffracted component of the solution, defined by

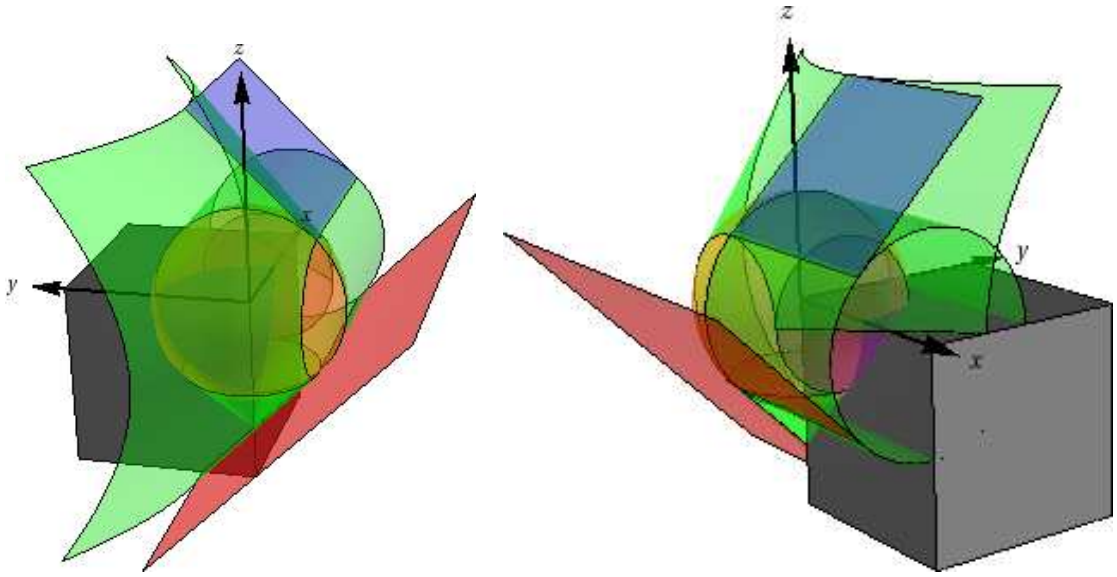
$$\Psi_{\text{diff}} = \Psi - \Psi_{\text{incident}}, \tag{4.103}$$

where Ψ_{incident} is the component of the solution corresponding to the incident wave (4.98). The plot in 4.6 shows how Ψ^2_{diff} varies as a function of ζ in the direction $(-1,-1,1)$, the direction from which the wave was incident. The expected square-root singularity on the diffracted wavefront is indeed observed in this case.

Figure 4.5 represents a rather special case, and in general a more complicated wavefront configuration may arise. In Figure 4.7 we consider a different case, where the wave is incident on the same cone, but now from the direction $(0,1,1)$. The planar incident wavefront is then perpendicular to the xz-plane, and inclined at 45° to the xy-plane. With the incident wave assumed to reach the vertex at $t = 0$, the wavefront configuration for $t < 0$ is as illustrated in Figure 4.7(a). We have a planar reflected wavefront due to reflection from the xy-plane, and a conical edge-diffracted



(a) $t < 0$



(b) $t > 0$

Figure 4.7: Wavefront diagrams for diffraction of a planar pulse by a polyhedral cone, showing the incident (red), reflected (blue), singly-edge-diffracted (green), doubly-edge-diffracted (purple) and vertex-diffracted (orange) wavefronts. In this example the cone is the region $x > 0$, $y > 0$, $z < 0$ and the pulse is incident from the direction $(0, 1, 1)$, with the incident wavefront assumed to reach the vertex $(0, 0, 0)$ at $t = 0$.

wavefront due to diffraction from the y-axis. For $t > 0$ the wavefront configuration is as illustrated in Figure 4.7(b). The incident and reflected wavefronts no longer intersect, and the conical edge-diffracted wavefront due to diffraction from the y-axis no longer has a 'tip'. We now have a two new singly-edge-diffracted wavefronts, one cylindrical and one conical, resulting from diffraction of the incident wave by the x-axis and the z-axis, respectively. We also have a conical doubly-edge-diffracted wavefront due to secondary diffraction by the x-axis of the original conical edge-diffracted wavefront associated with the y-axis. Finally, we have the spherical vertex-diffracted wavefront.

4.4 Pulses with arbitrary time-dependence

If the solution of

$$\frac{\partial^2 \Phi_\delta}{\partial t^2}(\mathbf{x}, t) - c_0^2 \nabla^2 \Phi_\delta(\mathbf{x}, t) = \delta(\mathbf{x} - \mathbf{x_0})\delta(t) \tag{4.104}$$

is known in some domain, then the solution of

$$\frac{\partial^2 \Phi}{\partial t^2}(\mathbf{x}, t) - c_0^2 \nabla^2 \Phi(\mathbf{x}, t) = \delta(\mathbf{x} - \mathbf{x_0})g(t) \tag{4.105}$$

for arbitrary $g(t)$ in the same domain is given formally by the convolution

$$\Phi = (\Phi_\delta * g)(t) = \int_{-\infty}^{\infty} \Phi_\delta(t - s)g(s)\, ds \tag{4.106}$$

(this is Duhamel's Principle). Similarly, if the solution Φ_δ corresponding to an incident δ-pulse supported on a planar wavefront is known, then the solution corresponding to an incident pulse with profile $g(t)$ is also given by the formula (4.106).

In both cases, the pressure perturbation p' is given by

$$\begin{aligned} p' = -\rho_0 \frac{\partial(\Phi_\delta * g)}{\partial t} &= -\rho_0 \Phi_\delta(t) * \frac{dg}{dt}(t) \\ &= -\rho_0 \int_{-\infty}^{\infty} \Phi_\delta(t - s)\frac{dg}{ds}(s)\, ds. \end{aligned} \tag{4.107}$$

Note that in the special case of a point source in 3D free space, the particular form of the fundamental solution (4.36) means that (4.106) and (4.107) can be evaluated exactly to give

$$\Phi = \frac{1}{4\pi c_0^2 r} g(t - r/c_0), \tag{4.108}$$

$$p' = -\frac{\rho_0}{4\pi c_0^2 r} \dot{g}(t - r/c_0), \tag{4.109}$$

where $\dot{g}$ denotes $\frac{dg}{ds}$.

4.4.1 General principles for diffraction of pulses by edges and vertices

In this section we state more precisely the general rules suggested at the end of section 4.2.4 concerning the weakening of singularities in the wave field when they are diffracted by edges and vertices.

We begin by noting that if an incident δ-pulse produces a diffracted field

$$\Phi_\delta \sim \sum_{n=0}^{\infty} \sigma_n(\mathbf{x}) H(\xi) \xi^{\lambda+n} \tag{4.110}$$

near some diffracted wavefront $\xi = 0$, then, by (4.106), an incident pulse $H(\xi_{\text{inc}})\xi_{\text{inc}}^{\alpha}$ will give rise to

$$\begin{aligned} \Phi = (\Phi_\delta * H(t)t^\alpha)(t) &\sim H(\xi) \int_0^\xi s^\alpha \sum_{n=0}^{\infty} \sigma_n(\mathbf{x})(\xi - s)^{\lambda+n}\, ds \\ &= H(\xi) \sum_{n=0}^{\infty} \sigma_n(\mathbf{x}) \xi^{\alpha+1+\lambda+n} B(1+\alpha, 1+\lambda+n), \end{aligned} \tag{4.111}$$

where

$$B(z,w) = \int_0^1 s^{z-1}(1-s)^{w-1}\, ds = \frac{\Gamma(z)\Gamma(w)}{\Gamma(z+w)}, \qquad \operatorname{Re}[z], \operatorname{Re}[w] > 0, \tag{4.112}$$

is the Beta function (see e.g. [2], Section 6.2).

In the case of diffraction by an edge, we have seen that an incoming δ-pulse gives rise to a diffracted pulse of the form (4.110) with $\lambda = -1/2$. Then (4.111) implies that an incident pulse $H(\xi_{\text{inc}})\xi_{\text{inc}}^{\alpha}$ will give rise to the leading order behaviour $H(\xi)\xi^{\alpha+1/2}$ on the edge-diffracted wavefront.

Similarly, in the case of vertex diffraction, an incoming δ-pulse gives rise to a diffracted pulse of the form (4.110) with $\lambda = 0$, which means that an incident pulse $H(\xi_{\text{inc}})\xi_{\text{inc}}^{\alpha}$ will give rise to the leading order behaviour $H(\xi)\xi^{\alpha+1}$ on the vertex-diffracted wavefront.

4.5 Switching on a time-harmonic source

In this section we apply the results of sections 4.2-4.4 to the problem of switching on a time-harmonic source, where both the time domain and frequency domain theories are in evidence[11]. We consider three cases: a point source in an infinite domain in 3D, a point source in an infinite domain in 2D, and the diffraction of a 2D plane wave by a rigid half-line (the Sommerfeld problem). In each case we determine the conditions under which the time-dependent field is well-approximated by the solution of the corresponding frequency domain problem.

4.5.1 Problem statement

In the case of a point source in 2D or 3D free space, the time-dependent problem to be solved is

$$\frac{\partial^2 \Phi}{\partial t^2} - c_0^2 \nabla^2 \Phi = \delta(\mathbf{x}) H(t) e^{-i\omega t}, \tag{4.113}$$

with $\Phi = 0$ for $t < 0$. The resulting velocity potential Φ is complex-valued, with $\mathrm{Re}\,[\Phi]$ and $\mathrm{Im}\,[\Phi]$ representing the responses to the source functions $H(t)\cos\omega t$ and $-H(t)\sin\omega t$, respectively.

In the case of plane wave diffraction by a rigid half-line $x > 0$, $y = 0$, the time-dependent problem is

$$\frac{\partial^2 \Phi}{\partial t^2} - c_0^2 \nabla^2 \Phi = 0, \qquad\qquad 0 < \theta < 2\pi, \tag{4.114}$$

subject to the rigid boundary condition

$$\frac{\partial \Phi}{\partial \theta} = 0, \qquad\qquad \theta \in \{0, 2\pi\}, \tag{4.115}$$

and a suitable prescription of the 'switched-on' incident plane wave. The simplest case is when the wave is incident from the direction $\theta_0 = 0^+$, with

$$\Phi = H(\pi - \theta) H(t + x/c_0) e^{-i(\omega t + kx)}, \qquad\qquad t < 0. \tag{4.116}$$

Again the velocity potential Φ is complex-valued, with $\mathrm{Re}\,[\Phi]$ and $\mathrm{Im}\,[\Phi]$ representing the responses to the incident waves $H(\pi - \theta)H(t + x/c_0)\cos(\omega t + kx)$ and $-H(\pi - \theta)H(t + x/c_0)\sin(\omega t + kx)$, respectively.

[11] The results of this section form the basis of the forthcoming journal article [38].

In all three cases we proceed to show that over a suitable timescale (which we shall determine), $\mathrm{Re}\,[\Phi]$ and $\mathrm{Im}\,[\Phi]$ converge to the real and imaginary parts, respectively, of $\Phi_{\mathrm{freq}} = e^{-i\omega t}\phi$, where ϕ is the solution of the corresponding frequency domain problem. In the point source cases, this comprises the Helmholtz equation

$$\left(\nabla^2 + k^2\right)\phi = -\frac{1}{c_0^2}\delta(\mathbf{x}), \qquad k = \frac{\omega}{c_0}, \tag{4.117}$$

along with an outgoing radiation condition at infinity.

In the plane wave diffraction case, the frequency domain problem is

$$\left(\nabla^2 + k^2\right)\phi = 0, \qquad 0 < \theta < 2\pi, \tag{4.118}$$

$$\frac{\partial\phi}{\partial\theta} = 0, \qquad \theta \in \{0, 2\pi\}, \tag{4.119}$$

along with the assumption that

$$\phi - H(\pi - \theta)e^{-ikx} \tag{4.120}$$

should satisfy an outgoing radiation condition for $\theta \neq \pi$.

In all three examples we wish to determine the conditions under which $\mathrm{Re}\,[\Phi]$ and $\mathrm{Im}\,[\Phi]$ are well-approximated by $\mathrm{Re}[\Phi_{\mathrm{freq}}]$ and $\mathrm{Im}[\Phi_{\mathrm{freq}}]$, respectively, in the sense that for a given observation point, the graphs of the functions (as functions of t) look alike. When comparing two oscillatory functions f, g possessing multiple zeros, the standard notion of asymptotic approximation $f/g \to 1$ (or equivalently $(g-f)/g \to 0$) is unsuitable since the quotient f/g is not defined at points where g vanishes (unless f also vanishes at those points). A more appropriate convergence criterion is $(g-f)/g_* \to 0$, where $g_* > 0$ represents the local amplitude of oscillation of the function g.

In our case the local amplitude of oscillation of $\mathrm{Re}\,[\Phi]$ and $\mathrm{Im}\,[\Phi]$ is given by $|\Phi_{\mathrm{freq}}| = |\phi|$. We therefore define

$$\delta\Phi := \Phi_{\mathrm{freq}} - \Phi, \tag{4.121}$$

we proceed to determine the conditions under which

$$\delta_{\mathrm{R}} := \frac{\mathrm{Re}[\delta\Phi]}{|\Phi_{\mathrm{freq}}|} \to 0, \tag{4.122}$$

$$\delta_{\mathrm{I}} := \frac{\mathrm{Im}[\delta\Phi]}{|\Phi_{\mathrm{freq}}|} \to 0. \tag{4.123}$$

4.5.2 A point source in 3D free space

The solution of (4.113) in free space satisfying $\Phi = 0$ for $t < 0$ can be found by convolution of the source function $H(t)e^{-i\omega t}$ with the fundamental solution of the wave equation. In 3D this gives

$$\Phi = \int_{-\infty}^{\infty} \frac{\delta(s - r/c_0)}{4\pi c_0^2 r} H(t-s) e^{-i\omega(t-s)}\, ds \tag{4.124}$$

$$= H(t - r/c_0) \frac{e^{-i(\omega t - kr)}}{4\pi c_0^2 r}, \quad k = \omega/c_0. \tag{4.125}$$

We see from (4.124) that when the source is switched on, an expanding spherical wavefront $r = c_0 t$ is born. The behaviour of Φ near the leading wavefront $r = c_0 t$ is found by approximating (4.124) in the limit as $\xi \to 0$, where the nondimensional parameter $\xi = \omega t - kr$ represents 2π times the number of periods of oscillation since the arrival of the leading wavefront, or, equivalently, 2π times the number of wavelengths from the observation point to the leading wavefront. This gives

$$\mathrm{Re}[\Phi] = \frac{H(\xi)}{4\pi c_0^2 r} + O(\xi), \tag{4.126}$$

$$\mathrm{Im}[\Phi] = -\frac{H(\xi)}{4\pi c_0^2 r}\xi + O(\xi^2), \tag{4.127}$$

so that $\mathrm{Re}[\Phi]$ undergoes a jump discontinuity across the leading wavefront of magnitude $4\pi c_0^2 r$, while $\mathrm{Im}[\Phi]$ is continuous across the leading wavefront, with a discontinuity in the normal derivative.

The frequency domain solution (cf. (3.25))

$$\Phi_{\mathrm{freq}} = \frac{e^{-i(\omega t - kr)}}{4\pi c_0^2 r} \tag{4.128}$$

is immediately attained after the arrival of the leading wavefront.

4.5.3 A point source in 2D free space

In the 2D case we have

$$\Phi = \int_{-\infty}^{\infty} \frac{H(s - r/c_0)}{2\pi c_0^2 \sqrt{s^2 - (r/c_0)^2}} H(t-s) e^{-i\omega(t-s)}\, ds$$

$$= \frac{H(t - r/c_0) e^{-i\omega t}}{2\pi c_0^2} \int_{r/c_0}^{t} \frac{e^{i\omega s}}{\sqrt{s^2 - (r/c_0)^2}}\, ds, \tag{4.129}$$

and the leading wavefront is the circle $r = c_0 t$. Equation (4.129) can be conveniently rewritten as[12]

$$\Phi = \frac{H(t - r/c_0)}{2\pi c_0^2} \int_0^\xi \frac{e^{i(s-\xi)}}{\sqrt{s(s+2\eta)}}\, ds, \tag{4.131}$$

in terms of the nondimensional parameters $\xi = \omega t - kr$ and $\eta = kr$, and a new dimensionless integration variable. Note that ξ represents 2π times the number of periods of oscillation since the arrival of the leading wavefront at time $t = r/c_0$, and η represents 2π times the number of wavelengths from the observation point to the source.

4.5.3.1 Behaviour near the leading wavefront

To determine the behaviour of Φ near the leading wavefront (i.e. as $\xi \to 0$) we note that (4.131) can be expanded as

$$\Phi = \frac{H(\xi)}{2\pi c_0^2} \int_0^\xi \frac{1 + i(s-\xi) + \dots}{\sqrt{s}\sqrt{s+2\eta}}\, ds, \tag{4.132}$$

and for $\xi < 2\eta$ we can also expand the denominator to get

$$\Phi = \frac{H(\xi)}{2\pi c_0^2} \frac{1}{\sqrt{2\eta}} \int_0^\xi \frac{(1 + i(s-\xi) + ...)}{\sqrt{s}} \left(1 - \frac{s}{4\eta} + \dots\right) ds, \tag{4.133}$$

with the result that

$$\mathrm{Re}[\Phi] \sim \frac{H(\xi)}{\sqrt{2}\pi c_0^2 \sqrt{\eta}} \xi^{1/2}, \qquad \xi \to 0,\ \xi \ll \eta, \tag{4.134}$$

$$\mathrm{Im}[\Phi] \sim -\frac{\sqrt{2} H(\xi)}{3\pi c_0^2 \sqrt{\eta}} \xi^{3/2}, \qquad \xi \to 0,\ \xi \ll \eta. \tag{4.135}$$

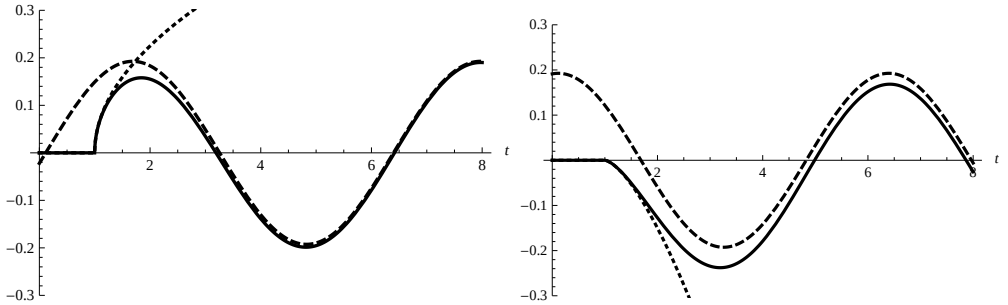
4.5.3.2 Convergence to the frequency domain solution

The frequency domain solution is (cf. (3.23))

$$\Phi_{\mathrm{freq}} = \frac{i e^{-i\omega t}}{4 c_0^2} H_0^{(1)}(\eta). \tag{4.136}$$

[12] An equivalent representation is

$$\Phi = \frac{H(t - r/c_0) e^{-i\omega t}}{2\pi c_0^2} \int_0^{\cosh^{-1} c_0 t/r} e^{ikr\cosh\theta}\, d\theta. \tag{4.130}$$



(a) Re[Φ] (b) Im[Φ]

Figure 4.8: Switching on a time-harmonic point source in 2D free space. Comparison of Φ (solid curves), Φ_{freq} (dashed curves) and the wavefront approximations (4.134) and (4.135) (dotted curves). Parameter values are $\omega = 1$, $c_0 = 1$, $r = 1$, so that the leading wavefront arrives at $t = 1$.

Plots of Φ, Φ_{freq} and the wavefront approximations (4.134) and (4.135) as functions of t, with the other parameters fixed, can be found in Figure 4.8. In this case the leading wavefront arrives at $t = 1$, with the local behaviour being governed by the wavefront approximations (4.134) and (4.135). As time progresses, Re[Φ] and Im[Φ] gradually approach the appropriate frequency domain solutions. Note that the convergence of Re[Φ] appears to be faster than that of Im[Φ].

To study the convergence in more detail we first use the integral representation 9.1.24 in [2] to rewrite (4.136) in the form[13]

$$\Phi_{\text{freq}} = \frac{1}{2\pi c_0^2} \int_0^\infty \frac{e^{i(s-\xi)}}{\sqrt{s(s+2\eta)}}\, ds, \tag{4.138}$$

so that with $r < c_0 t$ (i.e. $\xi > 0$),

$$\delta\Phi = \frac{1}{2\pi c_0^2} \int_\xi^\infty \frac{e^{i(s-\xi)}}{\sqrt{s(s+2\eta)}}\, ds. \tag{4.139}$$

Integration by parts then gives

$$\delta\Phi = \frac{1}{2\pi c_0^2} \left[\frac{i}{\sqrt{\xi(\xi+2\eta)}} + \frac{(\xi+\eta)}{(\xi(\xi+2\eta))^{3/2}} - \int_\xi^\infty \frac{(2s^2+4s\eta+3\eta^2)e^{i(s-\xi)}}{(s(s+2\eta))^{5/2}}\, ds \right], \tag{4.140}$$

[13] An equivalent representation is

$$\Phi_{\text{freq}} = \frac{e^{-i\omega t}}{2\pi c_0^2} \int_0^\infty e^{ikr\cosh\theta}\, d\theta \tag{4.137}$$

and it is easily shown that

$$\mathrm{Re}[\delta\Phi] \sim \frac{(\xi+\eta)}{2\pi c_0^2(\xi(\xi+2\eta))^{3/2}}\left(1+O\left(\frac{1}{\xi^2}\right)\right), \qquad \xi\to\infty, \tag{4.141}$$

$$\mathrm{Im}[\delta\Phi] \sim \frac{1}{2\pi c_0^2\sqrt{\xi(\xi+2\eta)}}\left(1+O\left(\frac{1}{\xi^2}\right)\right), \qquad \xi\to\infty, \tag{4.142}$$

uniformly for all $\eta > 0$.

- When[14] $\eta = \Theta(1)$ we have $|\Phi_{\mathrm{freq}}| = \Theta(1)$, and (4.122) and (4.123) hold with

$$\delta_{\mathrm{R}} = O\left(\frac{1}{\xi^2}\right), \qquad \xi\to\infty,\ \eta=\Theta(1), \tag{4.143}$$

$$\delta_{\mathrm{I}} = O\left(\frac{1}{\xi}\right), \qquad \xi\to\infty,\ \eta=\Theta(1), \tag{4.144}$$

  so that, as observed in Figure 4.8, the convergence of $\mathrm{Re}[\Phi]$ is indeed faster than that of $\mathrm{Im}[\Phi]$.

- When $\eta \ll 1$ the near field behaviour of the Hankel function (see e.g. [2], 9.1.12 and 9.1.13) gives

$$\Phi_{\mathrm{freq}} \sim \frac{e^{-i\omega t}}{2\pi c_0^2}\left(-\log(\eta)+(\log 2-\gamma)+\frac{i\pi}{2}+O\left(\eta^2\log\eta\right)\right), \quad \eta\ll 1, \tag{4.145}$$

  and combining (4.145) with (4.141) and (4.142) gives

$$\delta_{\mathrm{R}} = O\left(\frac{1}{\xi^2\log\eta}\right), \qquad \xi\to\infty,\ \eta\ll 1, \tag{4.146}$$

$$\delta_{\mathrm{I}} = O\left(\frac{1}{\xi\log\eta}\right), \qquad \xi\to\infty,\ \eta\ll 1. \tag{4.147}$$

  In fact, the assumption that $\eta \ll 1$ is enough to give convergence even when ξ is not large. For $\xi > 2\eta$ we can expand

$$\delta\Phi = \frac{e^{-i\xi}}{2\pi c_0^2}\int_\xi^\infty \frac{e^{is}}{s}\left(1-\frac{\eta}{s}+\ldots\right)ds, \tag{4.148}$$

  so that

$$\delta\Phi \sim \frac{e^{-i\xi}}{2\pi c_0^2}\int_\xi^\infty \frac{e^{is}}{s}\,ds, \qquad \eta\ll\xi. \tag{4.149}$$

[14] Here the notation $f(\xi) = \Theta(g(\xi))$ indicates that f is *strictly the same order as* g, as defined in [52]. That is, there exist positive constants C, C' and ξ_0 with $C\,f(\xi) \le g(\xi) \le C'\,f(\xi)$ for all $\xi > \xi_0$.

In particular, when $\xi = \Theta(1)$, (4.122) and (4.123) hold with

$$\delta_{\mathrm{R}},\, \delta_{\mathrm{I}} = O\left(\frac{1}{\log \eta}\right), \qquad \xi = \Theta(1),\, \eta \ll 1. \tag{4.150}$$

When $\xi \ll 1$ we have

$$\mathrm{Re}\left[\int_{\xi}^{\infty} \frac{e^{is}}{s}\, ds\right] \sim -\log \xi + O(1), \qquad \xi \ll 1, \tag{4.151}$$

$$\mathrm{Im}\left[\int_{\xi}^{\infty} \frac{e^{is}}{s}\, ds\right] \sim \frac{\pi}{2} + O(\xi), \qquad \xi \ll 1, \tag{4.152}$$

so that with $\eta \ll \xi \ll 1$, (4.122) and (4.123) hold with

$$\delta_{\mathrm{R}} = O\left(\frac{\log \xi}{\log \eta}\right), \qquad \eta \ll \xi \ll 1, \tag{4.153}$$

$$\delta_{\mathrm{I}} = O\left(\frac{1}{\log \eta}\right), \qquad \eta \ll \xi \ll 1. \tag{4.154}$$

For completeness we remark that with $\eta \ll 1$, the estimate (4.154) (and hence (4.123)) holds even for $\xi = O(\eta)$. This can be shown by combining the expansions (4.145) and (4.132), but we do not present the details here.

- When $\eta \gg 1$ the far-field behaviour of the Hankel function (cf. (3.24)) gives

$$\Phi_{\mathrm{freq}} \sim \frac{ie^{-i(\xi+\pi/4)}}{4c_0^2}\sqrt{\frac{2}{\pi\eta}}\left(1 - \frac{i}{8\eta} + \ldots\right), \qquad \eta \gg 1. \tag{4.155}$$

With $\xi \gg 1$, combining (4.155) with (4.141) and (4.142) gives

$$\delta_{\mathrm{R}} \sim \frac{\sqrt{2\eta}(\xi+\eta)}{\sqrt{\pi}(\xi(\xi+2\eta))^{3/2}}, \qquad \xi \to \infty,\, \eta \gg 1, \tag{4.156}$$

$$\delta_{\mathrm{I}} \sim \frac{\sqrt{2\eta}}{\sqrt{\pi}\sqrt{\xi(\xi+2\eta)}}, \qquad \xi \to \infty,\, \eta \gg 1. \tag{4.157}$$

The rate of convergence depends on the relative magnitudes of ξ and η. Specifically,

$$\delta_{\mathrm{R}} = O\left(\frac{1}{\xi^{3/2}}\right), \qquad 1 \ll \xi \ll \eta, \tag{4.158}$$

$$\delta_{\mathrm{I}} = O\left(\frac{1}{\sqrt{\xi}}\right), \qquad 1 \ll \xi \ll \eta, \tag{4.159}$$

and

$$\delta_{\mathrm{R}} = O\left(\frac{\sqrt{\eta}}{\xi^2}\right), \qquad 1 \ll \eta \ll \xi, \tag{4.160}$$

$$\delta_{\mathrm{I}} = O\left(\frac{\sqrt{\eta}}{\xi}\right), \qquad 1 \ll \eta \ll \xi. \tag{4.161}$$

4.5.4 A plane wave incident on a rigid half-line in 2D

We now apply a similar analysis to the case of diffraction of a plane wave by a rigid half-line.

To derive a solution of the time-dependent problem (4.114)-(4.116) we first note that the response to an incident step discontinuity $H(\pi-\theta)H(t+x/c_0)$ is given by $1/2$ times the limit of (4.56) as $\theta_0 \to 0^+$, namely[15]

$$\Phi_{\text{step}} = H(\pi-\theta)H(t+x/c_0) - \text{sgn}\,(\pi-\theta)\frac{H(t-r/c_0)}{\pi}\arctan\left[\sqrt{\frac{c_0t-r}{r(1+\cos\theta)}}\right]. \tag{4.162}$$

As remarked in section 4.3.4.4, the response to an incident δ-pulse $H(\pi-\theta)\delta\,(t+x/c_0)$ can be found by differentiating (4.162) with respect to t, which gives

$$\Phi_\delta = H(\pi-\theta)\delta\,(t+x/c_0) - \text{sgn}\,(\pi-\theta)\frac{H(t-r/c_0)}{2\pi}\frac{\sqrt{r(1+\cos\theta)}}{\sqrt{c_0t-r}(t+\frac{r}{c_0}\cos\theta)}. \tag{4.163}$$

Finally, by convolving (4.163) with the function $H(t)e^{-i\omega t}$, we obtain the solution to (4.114)-(4.116):

$$\begin{aligned}\Phi &= \int_{-\infty}^{\infty}\Phi_\delta(s)H(t-s)e^{-i\omega(t-s)}\,ds \\ &= H(\pi-\theta)H(t+x/c_0)e^{-i(\omega t+kx)} \\ &\qquad - \text{sgn}\,(\pi-\theta)\frac{H(t-r/c_0)}{2\pi}\sqrt{r(1+\cos\theta)}\int_{r/c_0}^{t}\frac{e^{-i\omega(t-s)}}{\sqrt{c_0s-r}(s+\frac{r}{c_0}\cos\theta)}\,ds.\end{aligned} \tag{4.164}$$

Changing variable $s = \frac{\tilde{s}}{\omega} + \frac{r}{c_0}$ (and immediately dropping tildes) simplifies the expression (4.164) slightly, giving

$$\Phi = H(t+x/c_0)H(\pi-\theta)e^{-i(\omega t+kx)} - \text{sgn}\,(\pi-\theta)\frac{H(t-r/c_0)}{2\pi}\sqrt{\eta}\int_0^{\xi}\frac{e^{i(s-\xi)}}{\sqrt{s}(s+\eta)}\,ds, \tag{4.165}$$

where $\xi = \omega t - kr$ and $\eta = kr(1+\cos\theta)$. The parameter ξ represents 2π times the number of periods of oscillation that have elapsed since the arrival of the diffracted wavefront, or equivalently, 2π times the number of wavelengths from the observation point to the diffracted wavefront. Curves of constant ξ are therefore circles centered

[15] In (4.162), and subsequently, the value of $H(0)$ is assigned to be $1/2$. The function (4.162) is then analytic in $r < c_0t$.

at the origin. As we shall see in section 4.5.4.2, the parameter η provides a measure of how close the observation point is to the shadow boundary $\theta = \pi$ of the frequency domain problem (cf. (3.58)). Curves of constant η are parabolae with focus at the origin and axis $\theta = \pi$ (which corresponds to $\eta = 0$).

4.5.4.1 Behaviour close to the leading wavefront

In the line-of-sight (LOS) region $\theta < \pi$ the leading wavefront is the incident wavefront $x = -c_0 t$. Defining $\xi_{\text{inc}} = \omega t + kx$, the behaviour near this wavefront is found by approximating (4.165) for $\xi_{\text{inc}} \to 0$. Provided that $r > c_0 t$ we have

$$\text{Re}[\Phi] \sim H(\xi_{\text{inc}}), \qquad \xi_{\text{inc}} \to 0, \tag{4.166}$$

$$\text{Im}[\Phi] \sim -H(\xi_{\text{inc}})\,\xi_{\text{inc}}, \qquad \xi_{\text{inc}} \to 0. \tag{4.167}$$

In the non-line-of-sight (NLOS) region $\theta > \pi$ the first term in (4.165) is not present, and the leading wavefront is the diffracted wavefront $\xi = 0$. Expanding (4.165) as

$$\Phi = \frac{H(\xi)\sqrt{\eta}}{2\pi} \int_0^{\xi} \frac{1 + i(s-\xi) + \dots}{\sqrt{s}(s+\eta)}\, ds, \tag{4.168}$$

we find that

$$\text{Re}[\Phi] \sim \frac{H(\xi)\sqrt{\eta}}{2\pi} \int_0^{\xi} \frac{1}{\sqrt{s}(s+\eta)}\, ds = \frac{1}{\pi} \arctan\sqrt{\frac{\xi}{\eta}}, \qquad \xi \to 0, \tag{4.169}$$

$$\text{Im}[\Phi] \sim \frac{H(\xi)\sqrt{\eta}}{2\pi} \int_0^{\xi} \frac{s-\xi}{\sqrt{s}(s+\eta)}\, ds = \frac{1}{\pi}\left(\sqrt{\eta\xi} - (\eta+\xi)\arctan\sqrt{\frac{\xi}{\eta}}\right), \quad \xi \to 0. \tag{4.170}$$

Provided that $\xi \ll \eta$ we can further expand to obtain the leading order behaviour

$$\text{Re}[\Phi] \sim \frac{H(\xi)}{\pi\sqrt{\eta}}\xi^{1/2}, \qquad \xi \to 0,\ \xi \ll \eta, \tag{4.171}$$

$$\text{Im}[\Phi] \sim -\frac{2H(\xi)}{3\pi\sqrt{\eta}}\xi^{3/2}, \qquad \xi \to 0,\ \xi \ll \eta. \tag{4.172}$$

Returning to the LOS region $\theta < \pi$, we note that the arrival of the diffracted wavefront provides a second pulse, following the incident pulse (which is described by

(4.166) and (4.167)). For $x > -c_0 t$ (i.e. $\xi_{\text{inc}} > 0$) we have

$$\text{Re}[\Phi] \sim \cos \xi_{\text{inc}} - \frac{H(\xi)}{\pi\sqrt{\eta}} \xi^{1/2}, \qquad \xi \to 0,\ \xi \ll \eta, \tag{4.173}$$

$$\text{Im}[\Phi] \sim -\sin \xi_{\text{inc}} + \frac{2H(\xi)}{3\pi\sqrt{\eta}} \xi^{3/2}, \qquad \xi \to 0,\ \xi \ll \eta. \tag{4.174}$$

We end this section by noting that curves on which $\lambda = \xi/\eta$ is constant have the equation

$$r = \frac{\frac{c_0 t}{\lambda+1}}{1 + (\frac{\lambda}{\lambda+1}) \cos\theta}, \tag{4.175}$$

which describes a family of ellipses, whose axes all lie on the shadow boundary $\theta = \pi$. Their foci are at $(0,0)$ and $\left(-\frac{c_0 t}{1+1/2\lambda}, 0\right)$, and they have eccentricity $\frac{\lambda}{\lambda+1}$, so that each ellipse intersects the circle $r = c_0 t$ at exactly one point, namely $r = c_0 t$, $\theta = \pi$. The region of validity of the approximations (4.171)-(4.174) can therefore be thought of as a thin annular region $0 < \xi \ll 1$, minus the interior of a thin ellipse $\lambda \ll 1$.

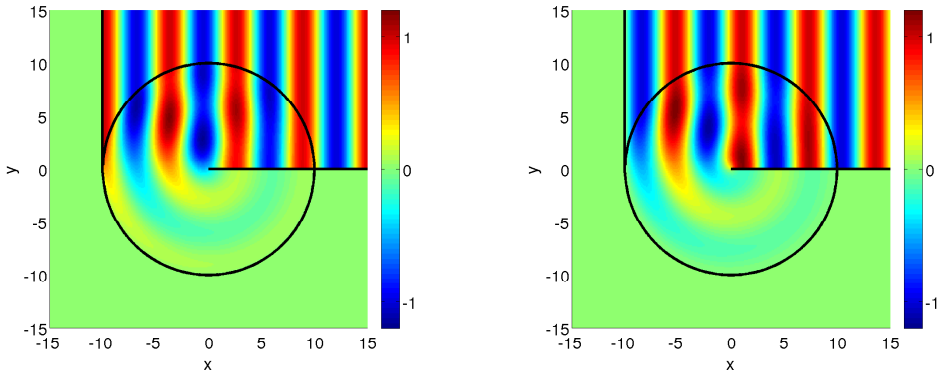
4.5.4.2 Convergence to the frequency domain solution

The solution of the frequency domain diffraction problem is given by 1/2 times the limiting value of (3.50) as $\theta_0 \to 0^+$, namely

$$\Phi_{\text{freq}} = \frac{e^{-i(\omega t + kx + \pi/4)}}{\sqrt{\pi}} \int_{-\sqrt{2kr}\cos\frac{\theta}{2}}^{\infty} e^{is^2}\, ds. \tag{4.176}$$

Typical plots of Φ and Φ_{freq} for fixed t can be found in Figure 4.9. Plots of Φ, Φ_{freq} and the wavefront approximations (4.171)-(4.174) as functions of t, with the other parameters fixed, can be found in Figure 4.10.

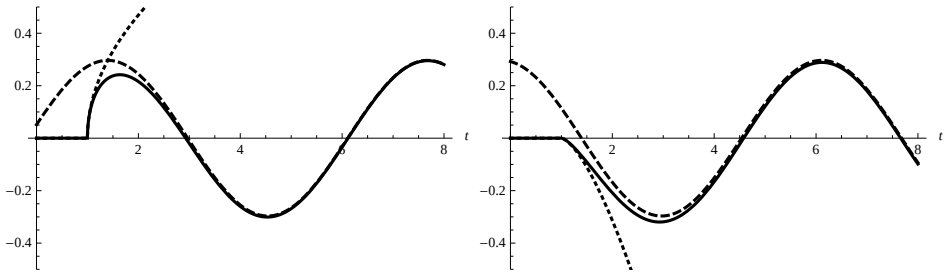
In Figures 4.10(a)-(d) the receiver is located in the NLOS region $\theta > \pi$, where the leading wavefront is the diffracted wavefront, which in this case arrives at $t = 1$. The local behaviour near this wavefront is governed by the wavefront approximations (4.171) and (4.172). In Figures 4.10(e)-(h) the receiver is located in the LOS region $\theta < \pi$, where the leading wavefront is the incident wavefront, which in this case arrives at $t = -\cos\theta$. The local behaviour near this wavefront is governed by the wavefront approximations (4.166) and (4.167). At time $t = 1$ the diffracted wavefront arrives, and the local behaviour is governed by (4.173) and (4.174). Magnified versions of Figures 4.10(c)-(f) can be found in Figure 4.11.



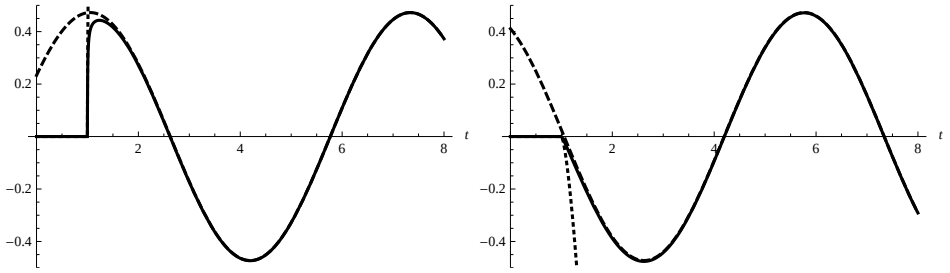
(a) $\mathrm{Re}[\Phi]$ (b) $\mathrm{Im}[\Phi]$

(c) $\mathrm{Re}[\Phi_{\mathrm{freq}}]$ (d) $\mathrm{Im}[\Phi_{\mathrm{freq}}]$

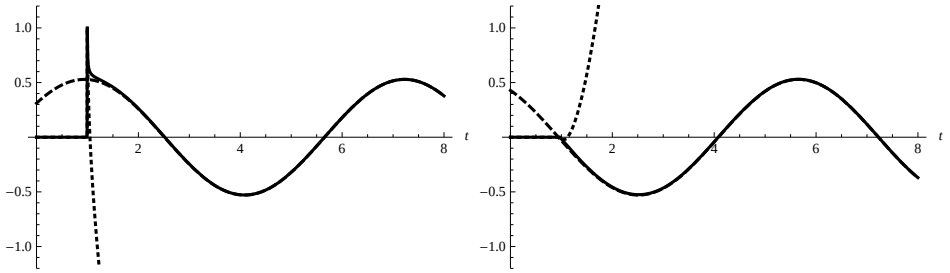
Figure 4.9: Switching on a time-harmonic source: diffraction of a plane wave by a rigid half-line. The half-line and the incident and diffracted wavefronts have been highlighted. Parameter values are $\theta_0 = 0^+$, $t = 10$, $\omega = 1$, $c_0 = 1$.



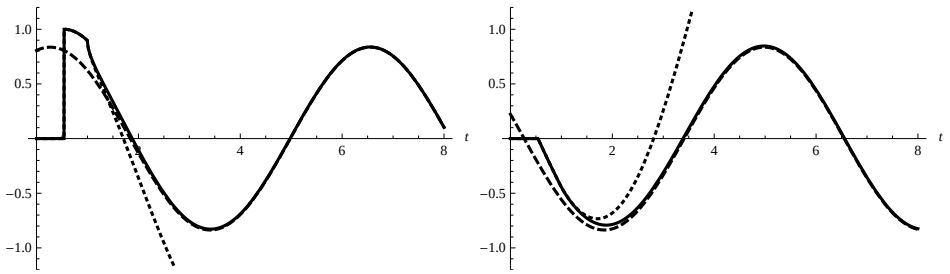
(a) Re[Φ], $\theta = \pi + 1$ (b) Im[Φ], $\theta = \pi + 1$



(c) Re[Φ], $\theta = \pi + 0.1$ (d) Im[Φ], $\theta = \pi + 0.1$

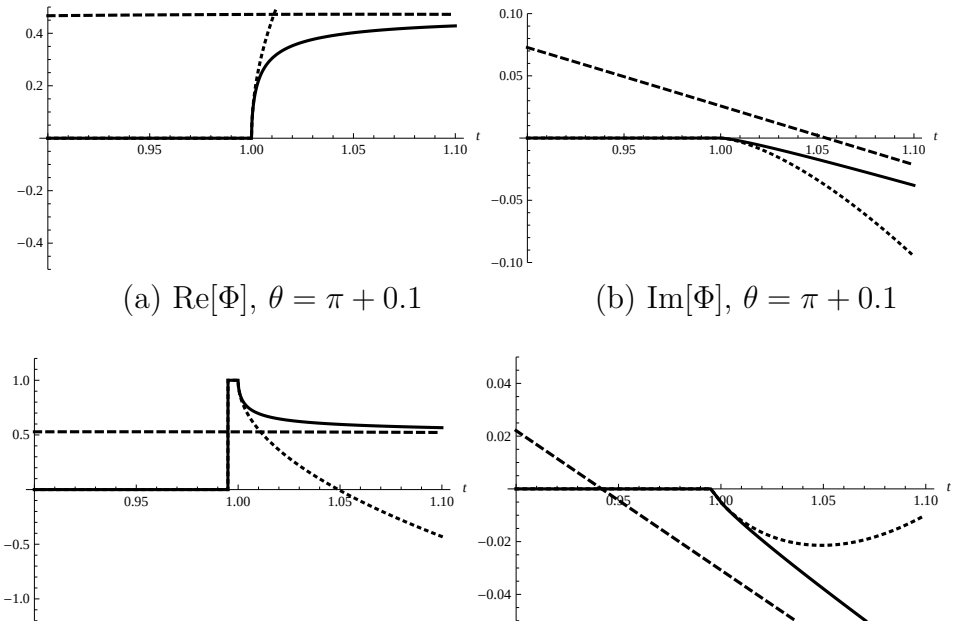


(e) Re[Φ], $\theta = \pi - 0.1$ (f) Im[Φ], $\theta = \pi - 0.1$



(g) Re[Φ], $\theta = \pi - 1$ (h) Im[Φ], $\theta = \pi - 1$

Figure 4.10: Switching on a time-harmonic source: diffraction of a plane wave by an edge. Comparison of Φ (solid curves), Φ_{freq} (dashed curves) and the wavefront approximations (4.171)-(4.174) (dotted curves). Magnified versions of plots (c)-(f) can be found in Figure 4.11. Parameter values are $\theta_0 = 0^+$, $\omega = 1$, $c_0 = 1$, $r = 1$.



(a) Re[Φ], $\theta = \pi + 0.1$ (b) Im[Φ], $\theta = \pi + 0.1$

(c) Re[Φ], $\theta = \pi - 0.1$ (d) Im[Φ], $\theta = \pi - 0.1$

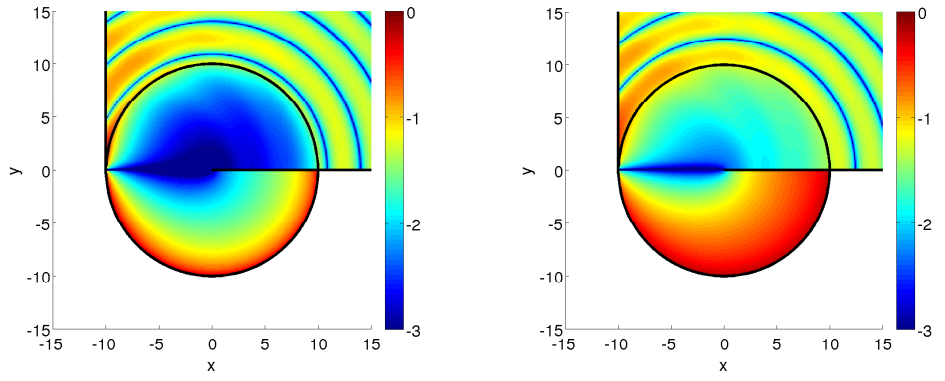
Figure 4.11: Magnified version of Figure 4.10(c)-(f).

As time progresses we observe that Re[Φ] and Im[Φ] gradually approach the appropriate frequency domain solutions. As in the 2D point source case, the convergence of Re[Φ] appears to be faster than that of Im[Φ]. Also, the convergence of both Re[Φ] and Im[Φ] appears to be faster for $\theta = \pi \pm 0.1$ than for $\theta = \pi \pm 1$, an indication that the convergence is not uniform with respect to θ. This is confirmed by plotting $|\delta_{\mathrm{R}}|$ and $|\delta_{\mathrm{I}}|$ as a function of position, for fixed t, which we do in Figures 4.12(a) and 4.12(b).

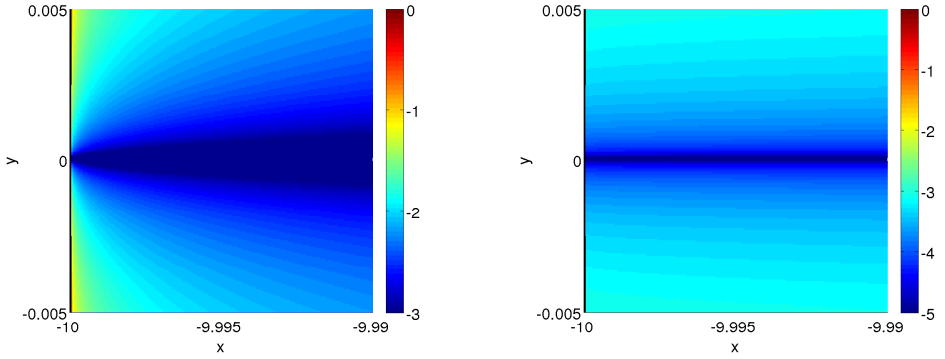
We remark that the concentric rings observed in Figures 4.12(a) and 4.12(b) in the region $r > c_0 t$ are due to the zeros of the diffracted component of Φ_{freq}, and do not represent regions of convergence to the frequency domain solution. Indeed, from this point on we shall restrict our attention almost exclusively to the behaviour of $|\delta_{\mathrm{R}}|$ and $|\delta_{\mathrm{I}}|$ *inside* the diffracted region $r < c_0 t$.

To allow analytical progress in studying $|\delta_{\mathrm{R}}|$ and $|\delta_{\mathrm{I}}|$ it is convenient to rewrite (4.176) in a form similar to (4.165). We begin by decomposing Φ_{freq} into a sum of an incident field and a diffracted field, writing

$$\Phi_{\mathrm{freq}} = H(\pi - \theta) e^{-i(\omega t + kx)} - \operatorname{sgn}(\pi - \theta) \frac{e^{-i(\omega t + kx + \pi/4)}}{\sqrt{\pi}} \int_{\sqrt{\eta}}^{\infty} e^{is^2}\, ds, \tag{4.177}$$



(a) $\log_{10}|\delta_{\mathrm{R}}|$ (b) $\log_{10}|\delta_{\mathrm{I}}|$



(c) $\log_{10}|\delta_{\mathrm{R}}|$ (d) $\log_{10}|\delta_{\mathrm{I}}|$

Figure 4.12: Switching on a time-harmonic source: diffraction of a plane wave by an edge. Logarithmic plots of $|\delta_{\mathrm{R}}|$ and $|\delta_{\mathrm{I}}|$ at $t = 10$, with $\theta_0 = 0^+$, $\omega = 1$, $c_0 = 1$. Regions coloured dark red indicate regions in which the relative error is greater than or equal to 1. We remark that the concentric rings observed in the region $r > c_0 t$ in (a) and (b) are due to the zeros of the diffracted component of Φ_{freq}, and do not represent regions of convergence to the frequency domain solution. The magnified plots in (c) and (d) show the behaviour near the point $(-10, 0)$. Near this point the contours of $|\delta_{\mathrm{R}}|$ appear to be ellipsoidal, and the contours of $|\delta_{\mathrm{I}}|$ appear to be horizontal, as is predicted by the analytical results for the regime $\eta \ll \xi \ll 1$.

where $\eta = kr(1 + \cos\theta)$ as before. We then apply the identity

$$\int_{\sqrt{\eta}}^{\infty} e^{is^2}\, ds = \frac{e^{i(\eta+\pi/4)}}{2\sqrt{\pi}}\sqrt{\eta}\int_0^{\infty} \frac{e^{is}}{\sqrt{s}(s+\eta)}\, ds, \qquad \eta > 0, \tag{4.178}$$

a proof of which is provided in Appendix D, to obtain the representation

$$\Phi_{\mathrm{freq}} = H(\pi-\theta)e^{-i(\omega t+kx)} - \operatorname{sgn}(\pi-\theta)\frac{1}{2\pi}\sqrt{\eta}\int_0^{\infty} \frac{e^{i(s-\xi)}}{\sqrt{s}(s+\eta)}\, ds. \tag{4.179}$$

Comparing (4.165) and (4.179), we immediately note that for $\theta = \pi$ (i.e. along the

shadow boundary) and $t > r/c_0$ we have

$$\Phi = \Phi_{\text{freq}} = \frac{1}{2} e^{-i(\omega t + kx)}, \tag{4.180}$$

so that the frequency domain solution is immediately attained once the leading wavefront has arrived.

Away from $\theta = \pi$, the frequency domain solution is only attained asymptotically in time. With $t > r/c_0$ we have

$$\delta\Phi = \pm \frac{\sqrt{\eta}}{2\pi} \int_{\xi}^{\infty} \frac{e^{i(s-\xi)}}{\sqrt{s}(s+\eta)}\, ds, \tag{4.181}$$

where $\pm$ denotes $\operatorname{sgn}(\theta - \pi)$. Integration by parts then gives

$$\begin{aligned} \delta\Phi = \pm \frac{\sqrt{\eta}}{2\pi} \Bigg[& \frac{i}{\sqrt{\xi}(\xi+\eta)} + \frac{3\xi + \eta}{2\xi^{3/2}(\xi+\eta)^2} \\ & - \int_{\xi}^{\infty} \frac{(15s^2 + 10s\eta + 3\eta^2) e^{i(s-\xi)}}{4s^{5/2}(s+\eta)^3}\, ds \Bigg], \end{aligned} \tag{4.182}$$

so that

$$\operatorname{Re}[\delta\Phi] \sim \pm \frac{\sqrt{\eta}(3\xi+\eta)}{4\pi\xi^{3/2}(\xi+\eta)^2} \left(1 + O\left(\frac{1}{\xi^2}\right)\right), \qquad \xi \to \infty, \tag{4.183}$$

$$\operatorname{Im}[\delta\Phi] \sim \pm \frac{\sqrt{\eta}}{2\pi\sqrt{\xi}(\xi+\eta)} \left(1 + O\left(\frac{1}{\xi^2}\right)\right), \qquad \xi \to \infty, \tag{4.184}$$

uniformly for all $\eta > 0$.

- When $\eta = \Theta(1)$ (e.g. when kr and θ are fixed) we have $|\Phi_{\text{freq}}| = \Theta(1)$, so that (4.122) and (4.123) hold with

$$\delta_{\text{R}} = O\left(\frac{1}{\xi^{5/2}}\right), \qquad \xi \to \infty,\ \eta = \Theta(1), \tag{4.185}$$

$$\delta_{\text{I}} = O\left(\frac{1}{\xi^{3/2}}\right), \qquad \xi \to \infty,\ \eta = \Theta(1), \tag{4.186}$$

  and, as observed in Figure 4.10, the convergence of $\operatorname{Re}[\Phi]$ is indeed faster than that of $\operatorname{Im}[\Phi]$.

- When $\eta \ll 1$ (which corresponds to the observation point being close to the shadow boundary $\theta = \pi$) the asymptotic behaviour of the Fresnel integral (see e.g. [2]) gives

$$\Phi_{\text{freq}} \sim \frac{e^{-i\xi}}{2} \left(1 \mp \frac{2e^{-i\pi/4}}{\sqrt{\pi}} \sqrt{\eta} + O(\eta)\right), \tag{4.187}$$

and combining (4.187) with (4.183) and (4.184) gives

$$\delta_{\mathrm{R}} = O\left(\frac{\sqrt{\eta}}{\xi^{5/2}}\right), \qquad \xi \to \infty,\ \eta \ll 1, \tag{4.188}$$

$$\delta_{\mathrm{I}} = O\left(\frac{\sqrt{\eta}}{\xi^{3/2}}\right), \qquad \xi \to \infty,\ \eta \ll 1. \tag{4.189}$$

The contours of δ_{R} and δ_{I} in this regime are, respectively, curves on which $\frac{\sqrt{\eta}}{\xi^{5/2}}$ and $\frac{\sqrt{\eta}}{\xi^{3/2}}$ are constant. See Figures 4.13(a) and 4.13(b) for an illustration.

In fact, the assumption that $\eta \ll 1$ is enough to give convergence even when ξ is not large. For $\xi > \eta$ we can expand

$$\delta\Phi = \pm\frac{\sqrt{\eta}}{2\pi}\int_{\xi}^{\infty} \frac{e^{i(s-\xi)}}{s^{3/2}}\left(1 - \frac{\eta}{s} + \ldots\right) ds, \tag{4.190}$$

so that

$$\delta\Phi \sim \pm\frac{\sqrt{\eta}}{2\pi}\int_{\xi}^{\infty} \frac{e^{i(s-\xi)}}{s^{3/2}}\, ds, \qquad \eta \ll \xi. \tag{4.191}$$

In particular, when $\xi = \Theta(1)$, (4.122) and (4.123) hold with

$$\delta_{\mathrm{R}}, \delta_{\mathrm{I}} = O\left(\sqrt{\eta}\right), \qquad \xi = \Theta(1),\ \eta \ll 1. \tag{4.192}$$

When $\xi \ll 1$, integration by parts gives

$$\mathrm{Re}\left[\int_{\xi}^{\infty} \frac{e^{i(s-\xi)}}{s^{3/2}}\, ds\right] \sim \frac{2}{\sqrt{\xi}} + O(1), \qquad \xi \ll 1, \tag{4.193}$$

$$\mathrm{Im}\left[\int_{\xi}^{\infty} \frac{e^{i(s-\xi)}}{s^{3/2}}\, ds\right] \sim \sqrt{2\pi} + O\left(\sqrt{\xi}\right), \qquad \xi \ll 1, \tag{4.194}$$

so that with $\eta \ll \xi \ll 1$, (4.122) and (4.123) hold with

$$\delta_{\mathrm{R}} = O\left(\frac{\sqrt{\eta}}{\sqrt{\xi}}\right), \qquad \eta \ll \xi \ll 1, \tag{4.195}$$

$$\delta_{\mathrm{I}} = O\left(\sqrt{\eta}\right), \qquad \eta \ll \xi \ll 1. \tag{4.196}$$

The contours of δ_{R} in this regime are curves on which ξ/η is constant, which, as we have already seen, are ellipses, whose axes all lie on the shadow boundary $\theta = \pi$. An illustration can be found in Figure 4.13(c). The ellipsoidal shape of the contours is clearly visible in Figure 4.12(c), which is a magnified version of Figure 4.12(a). The contours of δ_{I} are the curves of constant η, which are parabolae with axis $\theta = \pi$ and focus at the origin. An illustration can be found

in Figure 4.13(d). Near to the point $r = c_0 t$, $\theta = \pi$ they are approximately horizontal, as observed in Figure 4.12(d), which is a magnified version of Figure 4.12(b).

For completeness we remark that with $\eta \ll 1$, the estimate (4.196) (and hence (4.123)) holds even for $\xi = O(\eta)$, so that the horizontal contours described above go all the way to $\xi = 0$. This can be verified by combining the expansions (4.187) and (4.168), but we do not present the details here.

- When $\eta \gg 1$ the far-field behaviour of the Fresnel integral (see (3.54)) gives

$$\Phi_{\text{freq}} \sim H(\pi - \theta) e^{-i(\omega t + kx)} \pm \frac{e^{-i(\xi - \pi/4)}}{2\sqrt{\pi}\sqrt{\eta}} \left(1 + O\left(\frac{1}{\eta}\right)\right), \quad \eta \gg 1, \tag{4.197}$$

so that

$$|\Phi_{\text{freq}}| \sim \begin{cases} 1 & \eta \gg 1,\ \theta < \pi, \\ \dfrac{1}{2\sqrt{\pi}\sqrt{\eta}} & \eta \gg 1,\ \theta > \pi. \end{cases} \tag{4.198}$$

When $\xi \gg 1$ and $\theta > \pi$ (the NLOS region) the estimates (4.183) and (4.184) then give (4.122) and (4.123) with

$$\delta_{\text{R}} = O\left(\frac{1}{\xi^{3/2}}\right), \qquad 1 \ll \xi \ll \eta, \tag{4.199}$$

$$\delta_{\text{I}} = O\left(\frac{1}{\sqrt{\xi}}\right), \qquad 1 \ll \xi \ll \eta, \tag{4.200}$$

and

$$\delta_{\text{R}} = O\left(\frac{\eta}{\xi^{5/2}}\right), \qquad 1 \ll \eta \ll \xi, \tag{4.201}$$

$$\delta_{\text{I}} = O\left(\frac{\eta}{\xi^{3/2}}\right), \qquad 1 \ll \eta \ll \xi. \tag{4.202}$$

The contours of δ_{R} and δ_{I} in the regime $1 \ll \eta \ll \xi$ are, respectively, curves on which $\frac{\eta}{\xi^{5/2}}$ and $\frac{\eta}{\xi^{3/2}}$ are constant. See Figures 4.13(e) and 4.13(f) for an illustration.

When $\theta < \pi$ (the LOS region), however, (4.198) implies that we gain an extra factor of $1/\sqrt{\eta}$ in (4.199)-(4.202), giving closer agreement with the frequency domain solution than in the NLOS region. This far-field asymmetry about $\theta = \pi$ is clearly visible in Figures 4.12(a) and 4.12(b).

In fact, the assumption that $\eta \gg 1$ allows us to prove (4.122) and (4.123) in the LOS region even when ξ is not large. With $\xi = \Theta(1)$, (4.182) gives

$$\mathrm{Re}[\delta\Phi],\, \mathrm{Im}[\delta\Phi] = O\left(\frac{1}{\sqrt{\eta}}\right), \qquad \eta \to \infty,\, \xi = \Theta(1), \tag{4.203}$$

since

$$\begin{aligned}\left|\int_\xi^\infty \frac{(15s^2+10s\eta+3\eta^2)e^{i(s-\xi)}}{4s^{5/2}(s+\eta)^3}\,ds\right| &\le \int_\xi^\infty \frac{15s^2+10s\eta+3\eta^2}{4s^{5/2}(s+\eta)^3}\,ds \\ &= \frac{3\xi+\eta}{2\xi^{3/2}(\xi+\eta)^2} = O\left(\frac{1}{\eta}\right). \end{aligned} \tag{4.204}$$

The same estimates (4.203) can be obtained for the case $\eta \gg 1$, $\xi \ll 1$, since by splitting the integral we have

$$\begin{aligned}\int_\xi^\infty \frac{e^{i(s-\xi)}}{\sqrt{s}(s+\eta)}\,ds &\sim \frac{1}{\eta}\int_\xi^1 \frac{e^{i(s-\xi)}}{\sqrt{s}}\left(1-\frac{s}{\eta}+\ldots\right)ds + \int_1^\infty \frac{e^{i(s-\xi)}}{\sqrt{s}(s+\eta)}\,ds \\ &= O\left(\frac{1}{\eta}\right), \end{aligned} \tag{4.205}$$

where the estimate of the second term comes from applying the same procedure that led to (4.203) with $\xi = 1$. Thus in the LOS region $\theta < \pi$,

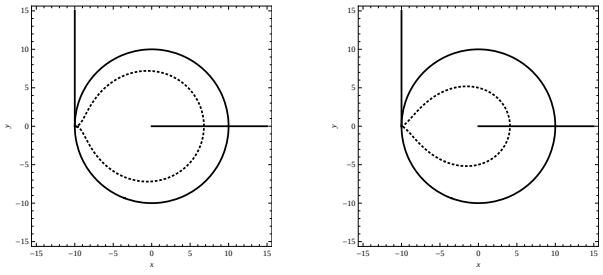
$$\delta_\mathrm{R},\, \delta_\mathrm{I} = O\left(\frac{1}{\sqrt{\eta}}\right), \qquad \eta \gg 1,\, \xi = O(1). \tag{4.206}$$

- Finally, for completeness we remark that in the region $\theta < \pi$, $r > c_0 t$, $x > -c_0 t$ (i.e. after the arrival of the incident wavefront but before the arrival of the diffracted wavefront), we have

$$\delta\Phi = -\frac{\sqrt{\eta}}{2\pi}\int_0^\infty \frac{e^{i(s-\xi)}}{\sqrt{s}(s+\eta)}\,ds. \tag{4.207}$$

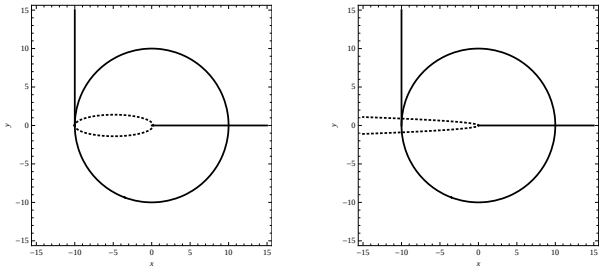
If $\eta \gg 1$ then (4.203) (and hence (4.206)) holds, so that the frequency domain solution provides the leading order behaviour, even though the diffracted wavefront has yet to arrive.

The results of this section are summarised in Table 4.1.



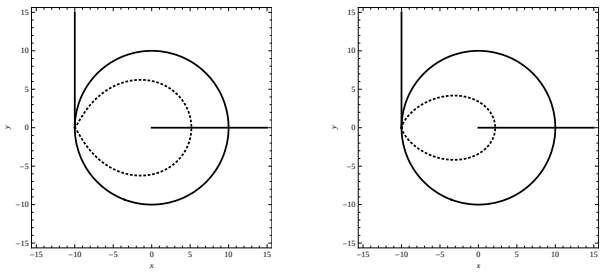
(a) $\varepsilon = \frac{\sqrt{\eta}}{\xi^{5/2}}$ (δ_{R}, $\xi \gg 1$, $\eta \ll 1$)

(b) $\varepsilon = \frac{\sqrt{\eta}}{\xi^{3/2}}$ (δ_{I}, $\xi \gg 1$, $\eta \ll 1$)



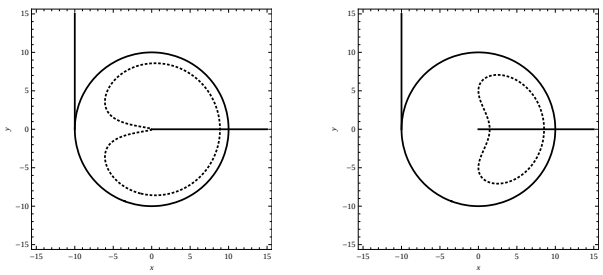
(c) $\varepsilon = \frac{\sqrt{\eta}}{\sqrt{\xi}}$ (δ_{R}, $\eta \ll \xi \ll 1$)

(d) $\varepsilon = \sqrt{\eta}$ (δ_{I}, $\eta \ll \xi \ll 1$)



(e) $\varepsilon = \frac{\eta}{\xi^{5/2}}$ (δ_{R}, $1 \ll \eta \ll \xi$)

(f) $\varepsilon = \frac{\eta}{\xi^{3/2}}$ (δ_{I}, $1 \ll \eta \ll \xi$)



(g) $\varepsilon = \frac{1}{\sqrt{\eta}\xi^{3/2}}$ (δ_{R}, $1 \ll \xi \ll \eta$, LOS)

(h) $\varepsilon = \frac{1}{\sqrt{\eta}\sqrt{\xi}}$ (δ_{I}, $1 \ll \xi \ll \eta$, LOS)

Figure 4.13: Illustration of contours of δ_{R}, δ_{I} as predicted by asymptotic analysis. In each plot $\varepsilon = 0.2$. For example, in (a), the plotted curve $\varepsilon = \frac{\sqrt{\eta}}{\xi^{5/2}}$ provides an illustration of a typical contour of δ_{R}, valid in the regime $\xi \gg 1$, $\eta \ll 1$. Other parameter values are $\theta_0 = 0^+$, $t = 10$, $\omega = 1$, $c_0 = 1$.

Size of η	Size of ξ	Size of δ_{R}	Size of δ_{I}
$\eta \ll 1$	$\xi = O(\eta)$	No convergence	$O\left(\sqrt{\eta}\right)$
	$\eta \ll \xi = O(1)$	$O\left(\sqrt{\frac{\eta}{\xi}}\right)$	$O\left(\sqrt{\eta}\right)$
	$\xi \gg 1$	$O\left(\frac{\sqrt{\eta}}{\xi^{5/2}}\right)$	$O\left(\frac{\sqrt{\eta}}{\xi^{3/2}}\right)$
$\eta = \Theta(1)$	$\xi \gg 1$	$O\left(\frac{1}{\xi^{5/2}}\right)$	$O\left(\frac{1}{\xi^{3/2}}\right)$
$\eta \gg 1$	$1 \ll \xi = O(\eta)$	$O\left(\frac{1}{\xi^{3/2}}\right)$	$O\left(\frac{1}{\sqrt{\xi}}\right)$
$\theta > \pi$ (NLOS)	$\xi \gg \eta$	$O\left(\frac{\eta}{\xi^{5/2}}\right)$	$O\left(\frac{\eta}{\xi^{3/2}}\right)$
$\eta \gg 1$	$\xi = O(1)$	$O\left(\frac{1}{\sqrt{\eta}}\right)$	$O\left(\frac{1}{\sqrt{\eta}}\right)$
$\pi < \theta$ (LOS)	$1 \ll \xi = O(\eta)$	$O\left(\frac{1}{\sqrt{\eta}\xi^{3/2}}\right)$	$O\left(\frac{1}{\sqrt{\eta}\sqrt{\xi}}\right)$
	$\xi \gg \eta$	$O\left(\frac{\sqrt{\eta}}{\xi^{5/2}}\right)$	$O\left(\frac{\sqrt{\eta}}{\xi^{3/2}}\right)$

Table 4.1: Switching on a time-harmonic source: diffraction of a plane wave by an edge. Summary of convergence results in the diffracted region $r < c_0 t$ (i.e. $\xi > 0$).

4.5.4.3 The case $\theta_0 \neq 0$

In this section we briefly consider the case where the plane wave is incident from an angle $0 < \theta_0 < \pi$. When $\pi/2 \leq \theta_0 < \pi$ the specification of the incident wave (4.116) is replaced by

$$\Phi = H(c_0 t + r\cos(\theta - \theta_0))e^{-i(\omega t + kr\cos(\theta - \theta_0))}, \qquad t < 0, \tag{4.208}$$

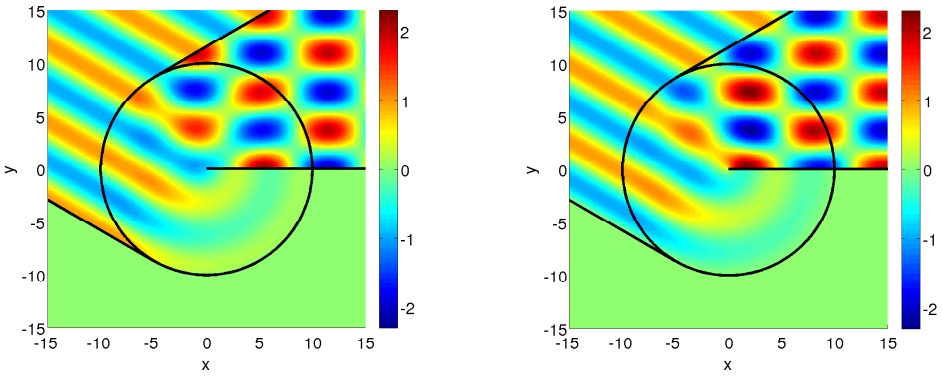
and when $0 < \theta_0 < \pi/2$ a reflected wave is also present, so that

$$\Phi = \sum_{\pm} H(\pi - (\theta \pm \theta_0))H(c_0 t + r\cos(\theta \pm \theta_0))e^{-i(\omega t + kr\cos(\theta \pm \theta_0))}, \quad t < 0. \tag{4.209}$$

In both cases the time-harmonic solution Φ_{freq} is the sum of two terms of the form (4.179), each associated with one of the two shadow boundaries $\theta = \pi \pm \theta_0$ (cf. equation (3.50)). Similarly, Φ is the sum of two terms of the form (4.165). Plots of Φ and Φ_{freq} for the case $\theta_0 = \pi/3$ and $\theta_0 = 2\pi/3$ are presented in Figures 4.14(a)-(d) and 4.15(a)-(d), respectively.

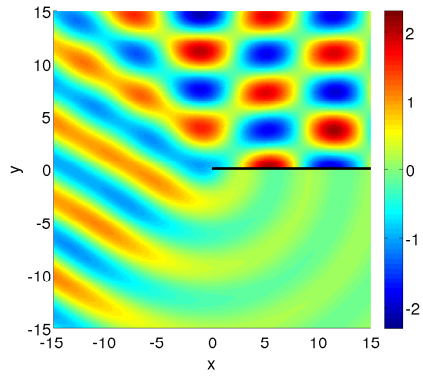
The corresponding plots of δ_R and δ_I can be found in Figures 4.14(e)-(f) and 4.15(e)-(f). Although we do not present a full analysis here, we make some remarks about the features of these plots.

We note first that, in contrast to the special case $\theta_0 = 0$, the frequency domain solution is not instantaneously attained along the shadow boundaries $\theta = \pi \pm \theta_0$.

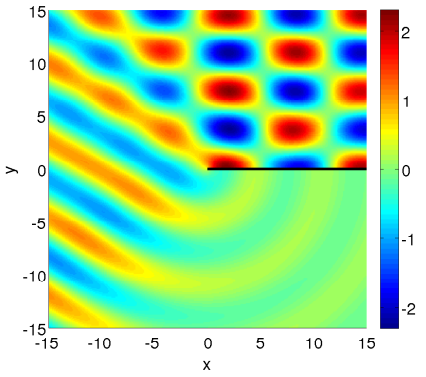


(a) $\mathrm{Re}[\Phi]$

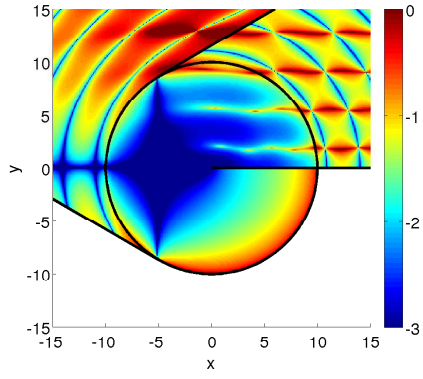
(b) $\mathrm{Im}[\Phi]$



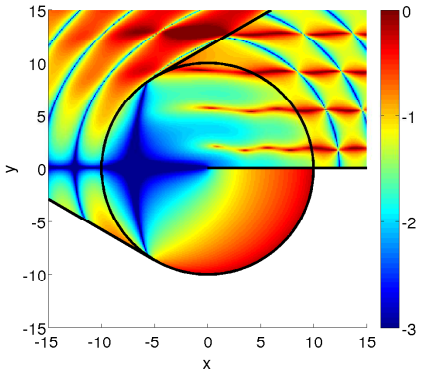
(c) $\mathrm{Re}[\Phi_{\mathrm{freq}}]$



(d) $\mathrm{Im}[\Phi_{\mathrm{freq}}]$

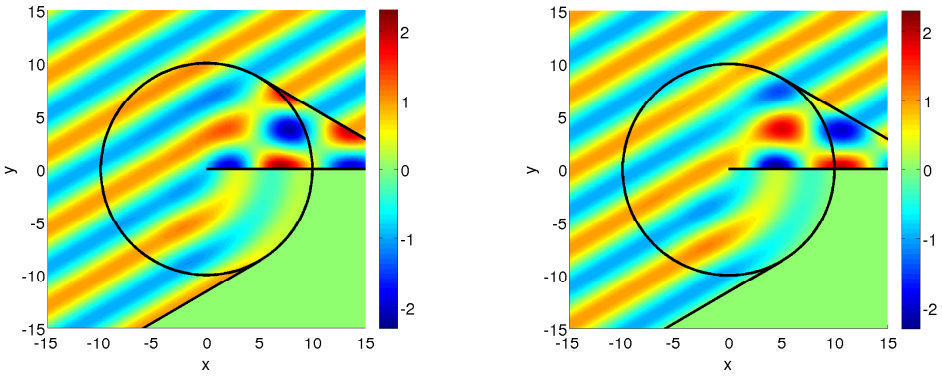


(e) $\log_{10}|\delta_{\mathrm{R}}|$



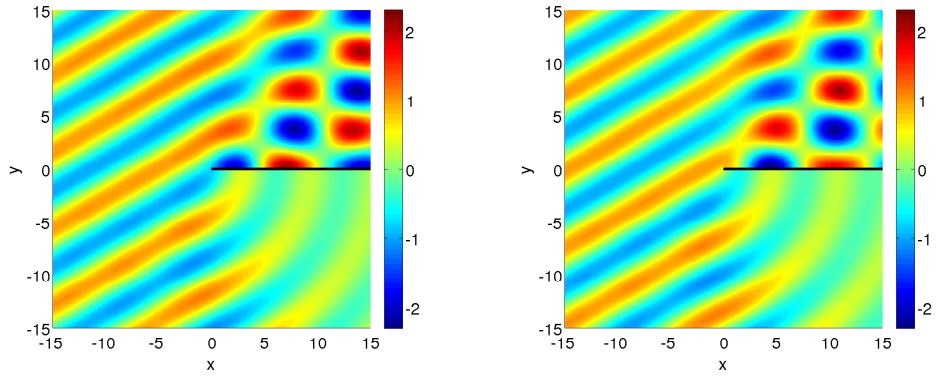
(f) $\log_{10}|\delta_{\mathrm{I}}|$

Figure 4.14: Switching on a time-harmonic source: diffraction of a plane wave by an edge. Plots of Φ, Φ_{freq}, $|\delta_{\mathrm{R}}|$ and $|\delta_{\mathrm{I}}|$ at $t = 10$, with $\theta_0 = \pi/3$, $\omega = 1$, $c_0 = 1$.



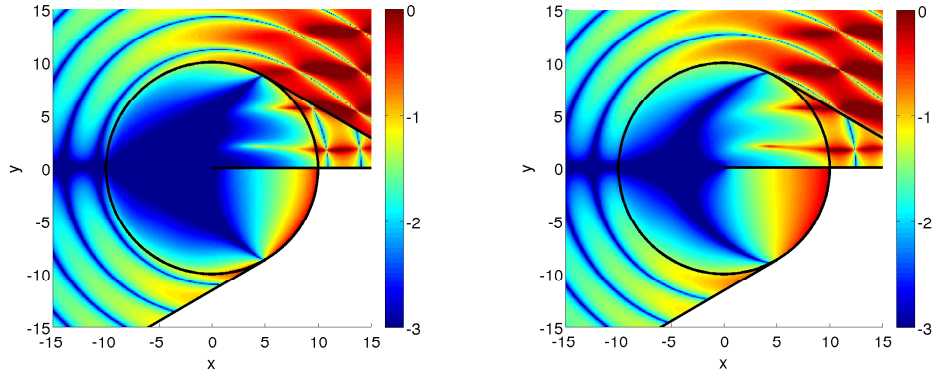
(a) $\mathrm{Re}[\Phi]$

(b) $\mathrm{Im}[\Phi]$



(c) $\mathrm{Re}[\Phi_{\mathrm{freq}}]$

(d) $\mathrm{Im}[\Phi_{\mathrm{freq}}]$



(e) $\log_{10}|\delta_{\mathrm{R}}|$

(f) $\log_{10}|\delta_{\mathrm{I}}|$

Figure 4.15: Switching on a time-harmonic source: diffraction of a plane wave by an edge. Plots of Φ, Φ_{freq}, $|\delta_{\mathrm{R}}|$ and $|\delta_{\mathrm{I}}|$ at $t = 10$, with $\theta_0 = 2\pi/3$, $\omega = 1$, $c_0 = 1$.

This is because along either shadow boundary, although one of the two terms making up Φ converges instantaneously, the other does not. However, the convergence is immediate along the line $\theta = \pi$ (i.e. the continuation of the half-line into $x < 0$). Once the incident wavefront has arrived we have

$$\Phi = \Phi_{\text{freq}} = e^{-i(\omega t - kr\cos\theta_0)}, \qquad \theta = \pi,\, t > -\frac{r\cos(\theta - \theta_0)}{c}. \tag{4.210}$$

Second, we remark on the 'tongue-like' features observed in Figures 4.14(e)-(f) and 4.15(e)-(f) in the reflected region $0 < \theta < \pi - \theta_0$. These are due to the effect of interference between the incident and reflected components of Φ_{freq}. Indeed, along the lines

$$y = \frac{(n + 1/2)\pi}{k\sin\theta_0}, \qquad n \in \mathbf{N}, \tag{4.211}$$

the incident and reflected components of Φ_{freq} cancel exactly, so that Φ_{freq} comprises only a (small) diffracted component in the far field. In the vicinity of these lines, δ_R and δ_I are therefore similar in magnitude to what they would be in the corresponding part of the NLOS region (i.e. at angle $2\pi - \theta$). Away from these lines, $\Phi_{\text{freq}} = \Theta(1)$, so that, as was found to be the case for $\theta_0 = 0$ (see the remark after (4.199)-(4.202)), δ_R and δ_I are smaller in the LOS region than in the corresponding part of the NLOS region.

4.6 Comparison with data from Bourges trials

In this section we use the theory of pulse propagation of sections 4.2-4.4 to comment on some experimental results obtained by Dstl as part of the NATO TG-53 Joint Field Experiment "Acoustic Detection of Weapon Firing", which took place in Bourges (France) in June 2008.

4.6.1 Background

The experiment involved the firing of a number of different weapons, including rifles of various calibres, heavy artillery, rocket-propelled grenades and C4 explosive, at certain locations within a large area of open farmland. Participants were permitted to set up microphones and recording equipment to measure the resulting sound pulses.

Although the primary objective of the experiment was to study sound propagation in open terrain, some measurements were taken by Dstl at microphone locations in and around a "disturbed zone", comprising two parallel concrete walls, as illustrated schematically in Figure 4.16 (note that this figure is not drawn to scale). The walls were each approximately 15m long, 5m tall, 0.9m thick and were positioned approximately 30m apart.

The data we consider here corresponds to "Event 154" (in Dstl's notation), which involved the firing of a single shot from a 7.62mm rifle from the source location "S2" (in Dstl's notation), represented by the cross in Figure 4.16. Simultaneous measurements were taken at four microphone locations ("dstl1-dstl4" in Dstl's notation) within the disturbed zone. The microphone and source locations, relative to the walls, were measured using a combination of GPS and tape measurements, and, for completeness, coordinates relative to the point W_1 in Figure 4.16 are given in Table 4.2. The source and the four microphones were all positioned 1m above the ground. An air temperature of 25.1°C was recorded at the time of the shot at the command post, a few hundred metres from the source location, and at a height of 5m. This corresponds (see e.g. [58], p. 7) to an approximate sound speed $c_0 = 345.8$m/s.

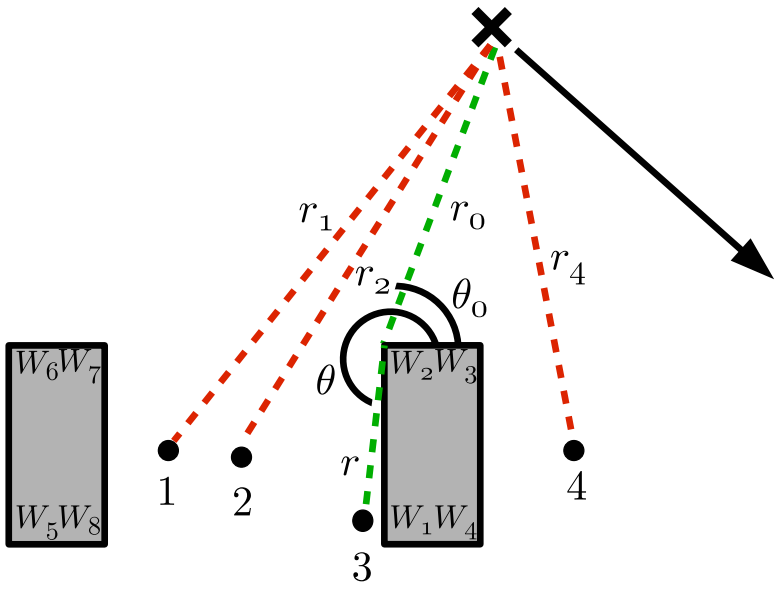


Figure 4.16: Schematic (not to scale) showing the geometry of the experimental setup, as viewed from above. The source location is indicated by a cross, and the firing direction by a thick black arrow. The four microphone receivers are indicated by black points. The wall vertices are labelled W_1-W_8. Parameter values are $r_1 = 308.7$m, $r_2 = 307.4$m, $r_4 = 301.7$m, $r_0 = 294.5$m $r = 14.6$m, $\theta_0 = 74°$, $\theta = 262°$.

	x	y
Microphone 1	-18.96	6.12
Microphone 2	-14.06	5.87
Microphone 3	-2.00	0.50
Microphone 4	10.90	4.61
Source	82.16	297.79

Table 4.2: Coordinates of microphone and source locations (in metres), relative to the wall vertex W_1 in Figure 4.16. Here the x- and y-axes run along W_1W_4 and W_1W_2, respectively.

4.6.2 Commentary on the data

10-second data samples containing the shot event are plotted in Figure 4.17. We assume that the microphone output is directly proportional to the excess pressure p'. The origin $t = 0$ in Figure 4.17 is arbitrary, and does not correspond to the time of firing. However, since the four microphones were all connected to the same tape deck, the recordings in Figure 4.17 are synchronised. At each of the four microphones, the pulse associated with the gunshot event arrives at around $t = 4.40$s, and appropriately magnified plots[16] showing the arrival of the gunshot event can be found in Figure 4.18.

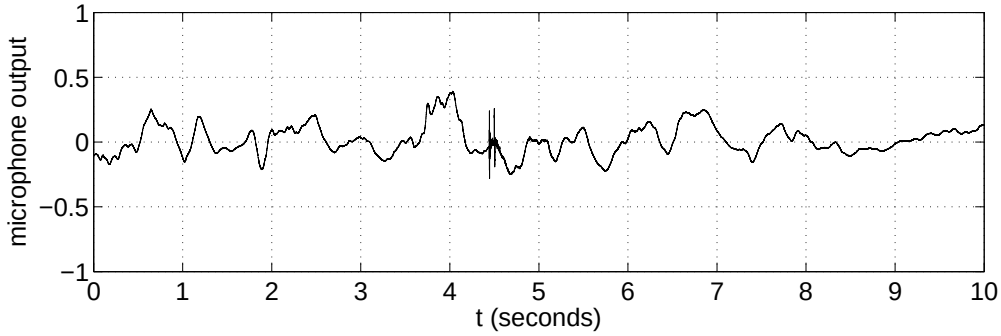
In each of the four plots (a)-(d) in Figure 4.18 the same qualitative behaviour is observed, with the single shot giving rise to two distinct pulse arrivals. We comment first on Figure 4.18(d). The initial pulse, which arrives at around $t = 4.40$s, is believed to be associated with the shockwave created by the supersonic flight of the bullet[17]. We focus our attention on the second pulse, arriving at around $t = 4.48$s, which is believed to be associated with the acoustic wave caused by the muzzle blast.

As Figure 4.18 shows, the muzzle blast pulse arrives at microphone 4 first, then at microphone 2, microphone 1, and shortly afterwards at microphone 3. The basic shape of the pulse is similar in all four plots, although the amplitude and arrival time of the pulse is different at each microphone.

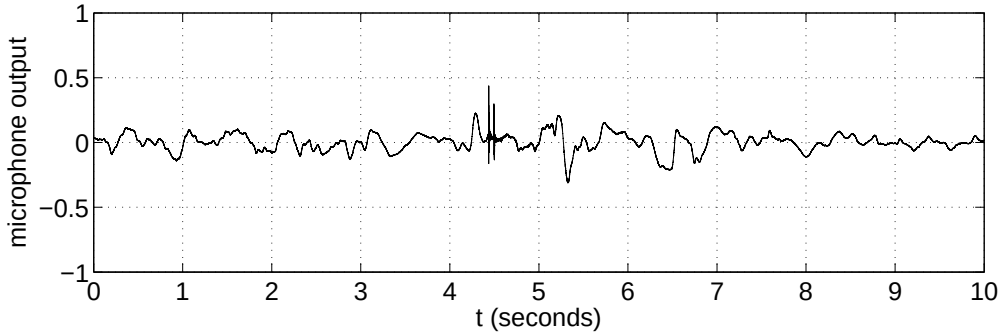
Microphones 1, 2 and 4 all have a direct line-of-sight (LOS) to the source, whereas microphone 3 is in the shadow of the right-hand wall, with the shortest propagation path involving a single edge diffraction around the right-hand wall (i.e. at W_2 in Figure 4.16). This provides a qualitative explanation of why the amplitude of the pulse at microphone 3 is the smallest of the four. We also note that no reflected pathways exist between the source and any of the microphones. Diffracted pathways from the source to the microphones 1, 2 and 4 exist, but the resulting pulses are not immediately discernable against the background noise.

[16] The low frequency oscillations observed in the remainder of the samples in Figure 4.17 correspond to background noise, not associated with the weapon firing.

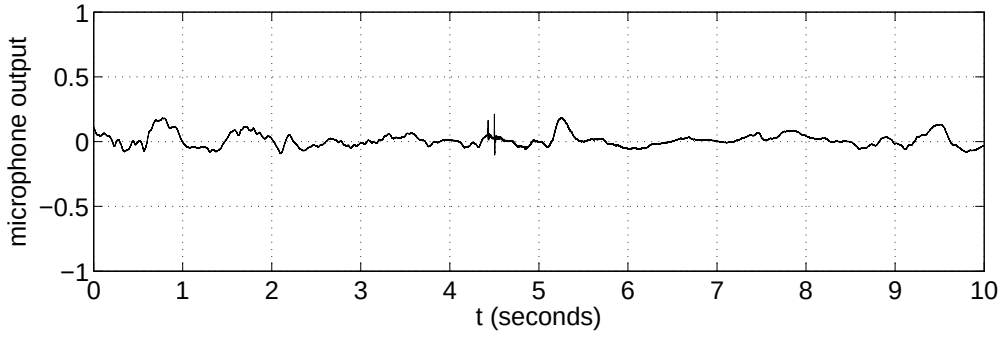
[17] We remark, however, that the highly oscillatory nature of this pulse does not match the N-wave profile typically associated with ballistic shockwaves (see e.g. [90], Section 9.3). The reasons for this are not yet clear, but similar observations have been made in other experiments (see e.g. [83]), especially in the case where the microphone location is far from the bullet trajectory (as is the case here). In [83] the loss of integrity of the shockwave profile was attributed to turbulent scattering.



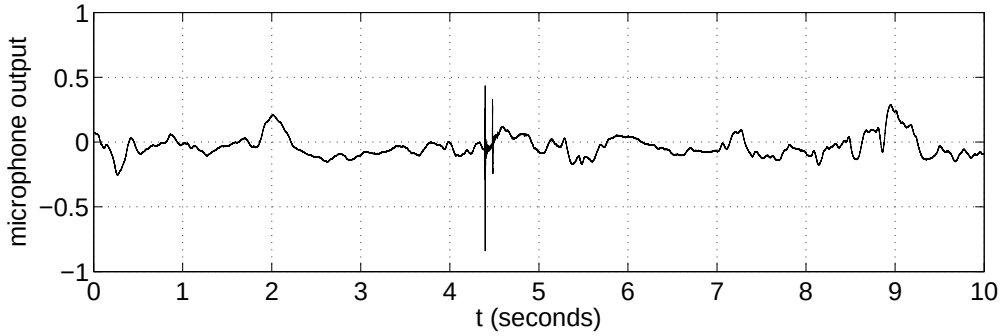
(a) Microphone 1



(b) Microphone 2

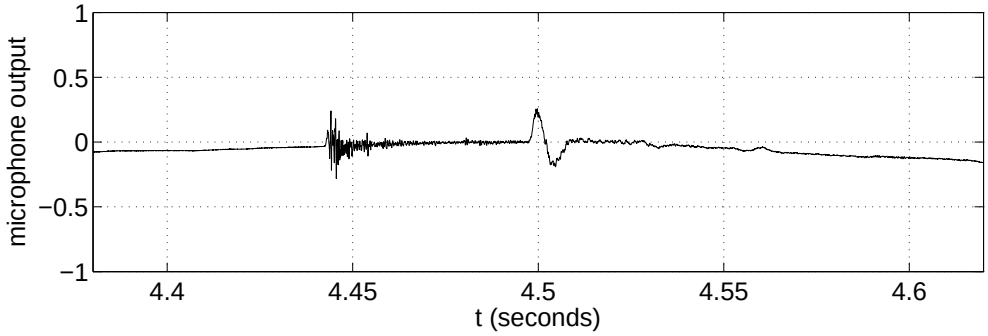


(c) Microphone 3

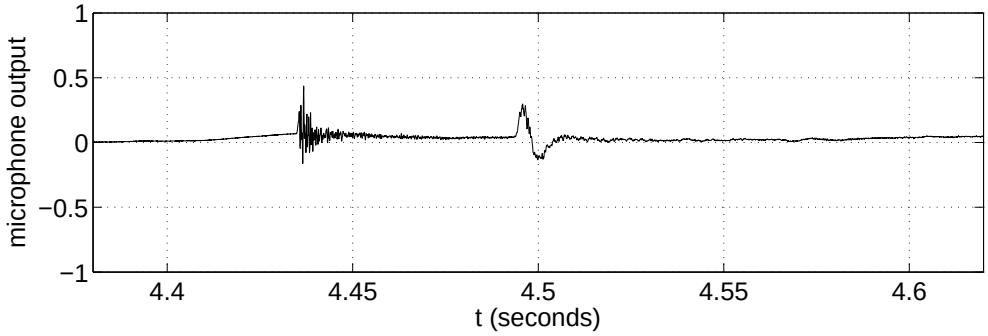


(d) Microphone 4

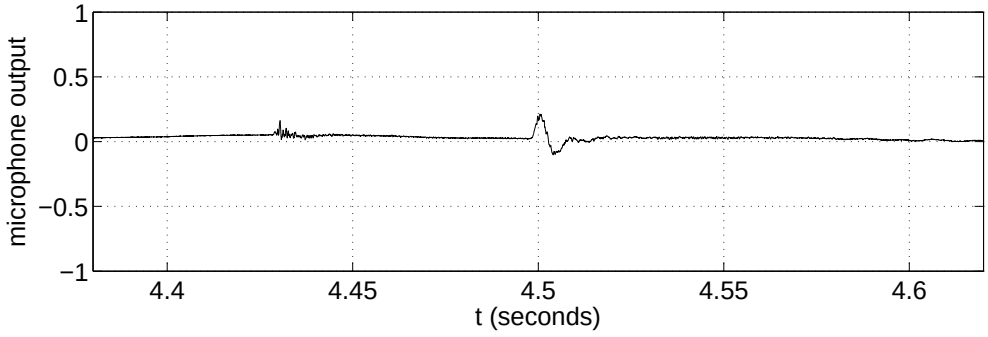
Figure 4.17: Typical data from Bourges trials. Event 154, 7.62mm rifle from S2.



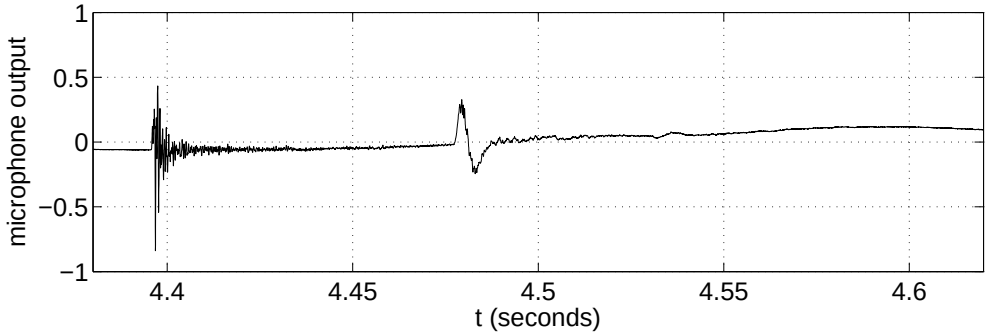
(a) Microphone 1



(b) Microphone 2



(c) Microphone 3



(d) Microphone 4

Figure 4.18: The two pulse arrivals: shockwave and muzzle blast.

4.6.3 Gaussian model of muzzle blast

We now attempt to reproduce the key aspects of the data, by modelling the muzzle blast pulse using the isotropic 3D point source model (4.105), with $g(t)$ a Gaussian

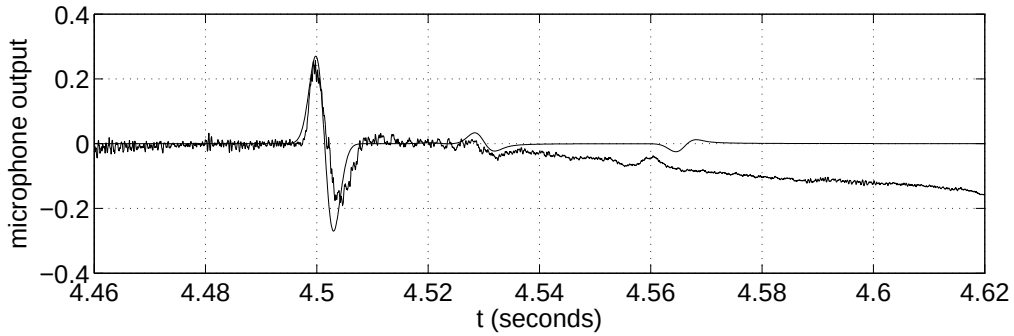
$$g(t) = -\frac{A}{\varepsilon} e^{-\pi(t-t_0)^2/\varepsilon^2}. \tag{4.212}$$

This choice of $g(t)$ is made simply for analytical convenience. Although (4.212) does qualitatively reproduce the key features of the data, as we shall shortly demonstrate, a different choice of $g(t)$ based on a physical modelling of the muzzle blast could provide even better agreement. Such a model is beyond the scope of this thesis, however, and is not considered here.

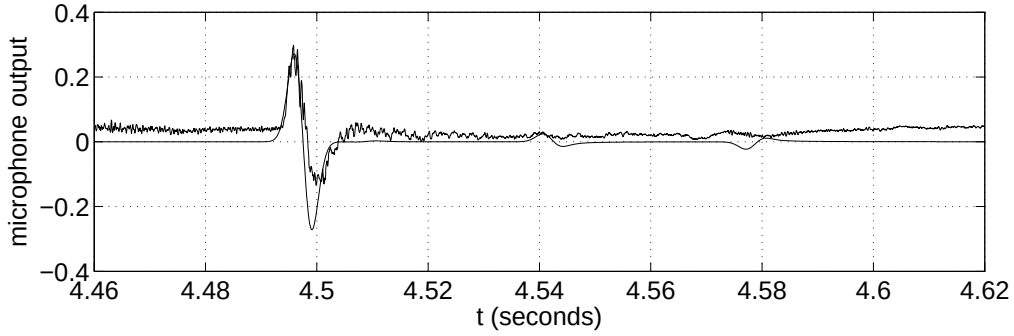
For simplicity, we neglect diffraction *over* the walls (which would involve either vertex-diffraction or double edge-diffraction) and consider the contribution of the LOS pulse (if it exists), calculated using formula (4.109), and singly-edge-diffracted pulses, calculated using formula (4.107) with Φ_δ given by the diffracted component of (4.87). At microphones 1 and 2 we have a LOS pulse, and diffracted pulses associated with the points W_2, W_7 and W_8 (see Figure 4.16). At microphone 3 we have no LOS pulse, only diffracted pulses associated with the points W_2, W_7 and W_8. At microphone 4 we have a LOS pulse, and diffracted pulses associated with the points W_3 and W_4.

With each pulse (direct or diffracted) we expect an associated ground-reflected pulse. The ground between the source and the disturbed area was flat, and covered with long grass of height between 0.5m and 0.75m. However, since detailed information concerning the acoustical properties of the ground is unavailable, for simplicity we model the ground as a rigid plane. Since the typical path length is approximately 300m, the length of a typical associated ground-reflected pathway is approximately $\sqrt{300^2 + 2^2}$m$= 300.0067$m. This corresponds to a delay in arrival time relative to the original pulse of approximately 0.00002s, and for our purposes it is reasonable to assume that the two pulses arrive simultaneously. The effect of ground reflection can therefore be included by absorbing a factor of 2 into the constant A in (4.212).

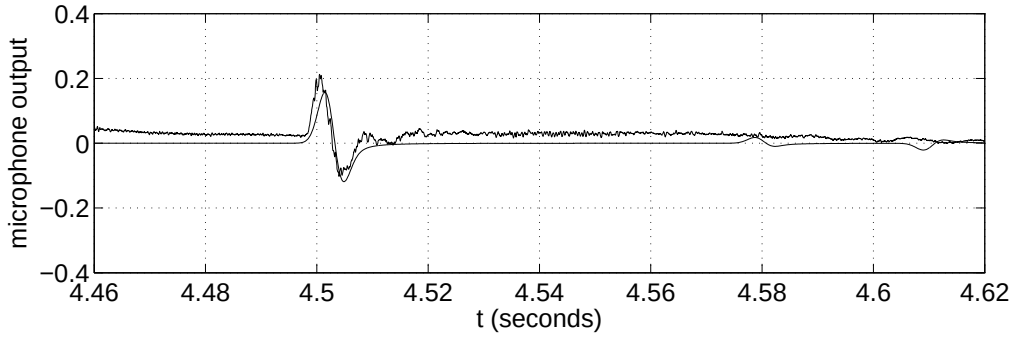
The parameters A, ε and t_0 in (4.212) have been chosen so as to provide a reasonable fit (by eye) to the direct pulse at microphone 4, as shown in Figure 4.19(d). The resulting diffracted pulses associated with the points W_3 and W_4 are clearly visible, arriving at around $t = 4.50$s and $t = 4.53$s, respectively. The latter pulse clearly reproduces a pulse observed in the measured data. However, the former pulse is harder to distinguish from the oscillations that are present in the measured data near



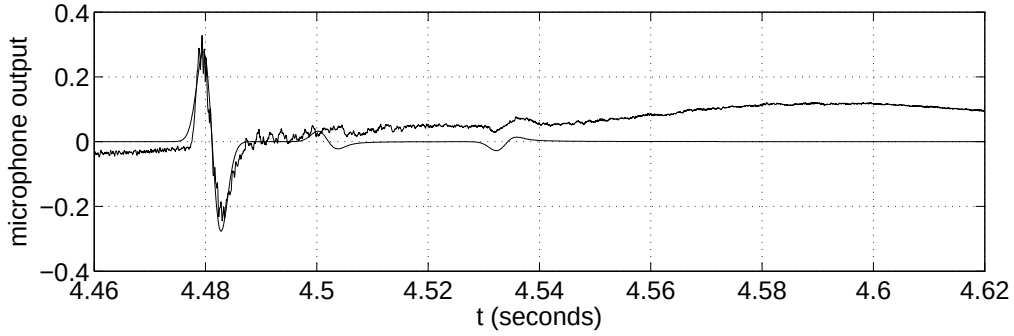
(a) Microphone 1



(b) Microphone 2



(c) Microphone 3



(d) Microphone 4

Figure 4.19: Muzzle blast for Event 154, along with the pressure pulse arising from the Gaussian model (4.212). Parameter values are $A = 1100\text{m}^5\text{s}^{-2}$, $\varepsilon = 0.004\text{s}$, $t_0 = 3.6087\text{s}$, $c_0 = 345.8\text{ms}^{-1}$, $\rho_0 = 1.2\text{kgm}^{-3}$.

$t = 4.50$s. The large discrepancy in pressure profiles between $t = 4.54$s and $t = 4.62$s is due to background noise (i.e. the low-frequency oscillations observed in Figure 4.17(d)).

The resulting predicted pressure profiles at microphones 1-3 (using the same parameter values) are shown in Figures 4.19(a)-(c), and also show good agreement with the measured data. In Figure 4.19(a) the LOS pulse arriving at around $t = 4.5$s is clearly reproduced, as are the diffracted pulses associated with the points W_7 and W_8, which arrive at around $t = 4.53$s and $t = 4.56$s, respectively, although the latter pulse is observed to arrive around 0.01s earlier in the measured data than predicted. The diffracted pulse associated with the point W_3 arrives at around $t = 4.52$s but is of too small an amplitude to be visible in Figure 4.19(a).

Similarly, in Figure 4.19(b) the LOS pulse is clearly reproduced, as are the diffracted pulses associated with the points W_7 and W_8, which arrive at around $t = 4.54$s and $t = 4.58$s, respectively, although the latter pulse is again observed to arrive earlier in the measured data than predicted. The diffracted pulse associated with the point W_2 arrives at around $t = 4.51$s but is of too small an amplitude to be visible.

In Figure 4.19(c) the diffracted pulse associated with the point W_3 arrives at around $t = 4.5$s and is clearly reproduced in the measured data. The fact that this diffracted pulse is so much stronger than the other diffracted pulses is due to the fact that microphone 3 'almost' has a LOS to the source, lying just 8° within the shadow region associated with the diffracting edge W_2. The diffracted pulse associated with the point W_7 arrives at around $t = 4.58$s, but is not so clearly reproduced. However, the diffracted pulse associated with the point W_8, which arrives at around $t = 4.61$s, is observed in the measured data, but arrives earlier than predicted.

The discrepancies in the arrival times of the diffracted pulses are most likely due to errors in measurement of geometry (receiver, source and wall locations), although the unknown local meteorological conditions (e.g. speed of sound, wind speed and direction) may also have been a contributing factor.

4.7 Summary

In this chapter we have studied the propagation of sound pulses in an urban environment. We first reviewed the standard theory of characteristics, which governs the propagation of singularities in the wave field, illustrating it by means of a number of specific examples in which an exact 'pulsed' solution of the wave equation is available. In particular, we focussed our attention on the diffraction of pulses by edges and vertices, and we stated and proved a general principle which governs the weakening of singularities when they are diffracted. The singularity on an edge-diffracted wavefront is half a power of ξ weaker than that on the incident wavefront, where ξ is the coordinate in the direction normal to the wavefront. In the case of vertex diffraction the singularity is a whole power of ξ weaker.

We then considered two applications. First, in section 4.5 we considered the problem of switching on a time-harmonic source. Here we concentrated on the rate at which the solution of the time-dependent problem converges to the corresponding frequency domain solution. In the case of a point source in free space we showed that, in 3D, the frequency domain solution is immediately attained after the arrival of the leading wavefront. In 2D we found that the rate of convergence depends on the strength of the singularity on the leading wavefront in the time-dependent problem, with a stronger singularity giving rise to faster convergence. This phenomenon was also observed in the case of a plane wave incident on a rigid half-line in 2D. Here we found that the rate of convergence also depends strongly on the observation point, and, in particular, the frequency domain solution is immediately attained along the extension of the half-line, after the arrival of the leading wavefront.

Second, in section 4.6 we commented on some experimental data collected by Dstl during an investigation into sound pulses arising from gunshots. We have shown that the mathematical theory of pulse propagation discussed in sections 4.2-4.4 can be used to model the propagation of the acoustic waves generated by the muzzle blast of a gun in the presence of obstacles. A rather simple mathematical model for the muzzle blast was adopted; namely, a isotropic point source with Gaussian time-dependence, but many of the key features of the data have been reproduced with reasonable accuracy, such as the arrival times and amplitudes of diffracted pulses. This analysis has put us in a position to apply the results concerning pulse propagation to the inverse problem of source localisation, and we will do this in the next chapter.

Chapter 5

Source localisation in the time domain

5.1 Introduction

This chapter concerns the inverse problem of localising an impulsive source using the Time Differences Of Arrival (TDOAs) of the pulse at multiple receivers distributed through the propagation domain. In section 5.2 we review the exact solution of the TDOA problem in 2D and 3D free space. We show that when there are errors in the measurement of arrival times, an estimate of the source location can be obtained by solving the TDOA equations in an approximate sense. In section 5.3 we show that in certain domains with boundaries, the arrival times of reflected pulses can be used to reduce the number of physical receivers needed to locate the source. In section 5.4 we propose a new method for solving the TDOA problem in a 2D urban environment in which a line-of-sight (LOS) between the source and each receiver is not available. We then consider the case where the exact dimensions and positions of buildings are unknown, before discussing the applicability of the new method to the 3D case.

We remark that the TDOA methods in this thesis require knowledge simply of the arrival time of a pulse at a receiver, and do not make use of additional information such as the amplitude of the pulse or the arrival direction. The question of how such additional information could be incorporated into the localisation method will not be considered here.

5.2 TDOA localisation in free space

In this section we review the TDOA localisation method in free space. For ease of presentation we begin by considering the 2D problem, before generalising the results to the 3D case in section 5.2.3.

Suppose that at $t = t_0$ a pulse is emitted from the point $\mathbf{x_0} = (x_0, y_0)$, with the medium having been at rest for $t < t_0$. Receivers positioned at the points $\mathbf{x_i} = (x_i, y_i)$, $i = 1, ..., N$, record the respective arrival times t_i of the pulse. For each i the transmission time $t_i - t_0$ is related to the propagation distance $r_i = |\mathbf{x_0} - \mathbf{x_i}|$ by

$$r_i = c_0(t_i - t_0). \tag{5.1}$$

When the emission time t_0 is unknown, a single receiver is unable to provide us with any information at all about the source location. However, for any pair of receivers $\{\mathbf{x_i}, \mathbf{x_j}\}$ the *range difference* D_{ij} from the source to the two receivers is known, being given in terms of the Time Difference Of Arrival (TDOA) $t_i - t_j$ by

$$D_{ij} := r_i - r_j = c_0(t_i - t_j), \tag{5.2}$$

a quantity which is independent of t_0.

The D_{ij} satisfy the following relations:

$$D_{ii} = 0, \quad 1 \leq i \leq N, \tag{5.3}$$

$$D_{ij} = -D_{ji}, \quad 1 \leq i, j \leq N, \tag{5.4}$$

$$D_{ij} = D_{ik} + D_{kj}, \quad 1 \leq i, j, k \leq N. \tag{5.5}$$

Hence, of the N^2 quantities $\{D_{ij}\}_{i,j=1}^{N}$, only $N-1$ are linearly independent as functions of $\mathbf{x_0}$.

Knowledge of D_{ij} places the source on a particular branch of a hyperbola with foci at $\mathbf{x_i}$ and $\mathbf{x_j}$. Indeed, by rewriting equation (5.2) as

$$D_{ij} + r_j = r_i, \quad 1 \leq i, j \leq N, \tag{5.6}$$

we may square both sides and rearrange to obtain the equation

$$2r_j D_{ij} = 2(\mathbf{x_j} - \mathbf{x_i}) \cdot \mathbf{x_0} + |\mathbf{x_i}|^2 - |\mathbf{x_j}|^2 - D_{ij}^2. \tag{5.7}$$

When $D_{ij} \neq 0$ we can write (5.7) as

$$|\mathbf{x_0} - \mathbf{x_j}| = \pm e(\mathbf{x_0} - \mathbf{l}) \cdot \mathbf{n}, \tag{5.8}$$

where

$$e = \frac{|\mathbf{x_j} - \mathbf{x_i}|}{|D_{ij}|}, \qquad \mathbf{n} = \frac{\mathbf{x_j} - \mathbf{x_i}}{|\mathbf{x_j} - \mathbf{x_i}|}, \qquad \mathbf{l} = \frac{1}{2}\left(\mathbf{x_0} + \mathbf{x_j} + \frac{|D_{ij}|}{2e}\mathbf{n}\right), \tag{5.9}$$

and $\pm = \operatorname{sgn} D_{ij}$. Equation (5.8) is the standard form for the equation of one branch of a hyperbola of eccentricity e, focus at $\mathbf{x_j}$ and directrix the line through the point $\mathbf{l}$, perpendicular to $\mathbf{n}$. The sign of D_{ij} determines the particular branch on which the source lies.

Squaring both sides of (5.8) leads to

$$4D_{ij}^2 |\mathbf{x_0} - \mathbf{x_j}|^2 - \left(2(\mathbf{x_j} - \mathbf{x_i}) \cdot \mathbf{x_0} + |\mathbf{x_i}|^2 - |\mathbf{x_j}|^2 - D_{ij}^2\right)^2 = 0, \tag{5.10}$$

which is the Cartesian equation for the hyperbola, including both branches.

With N receivers, there are $\binom{N}{2}$ distinct receiver pairs, and in principle, when N is sufficiently large the source can be located by finding the mutual intersection point of the resulting hyperbola branches. This is basis of Time Difference Of Arrival (TDOA) localisation.

5.2.1 The 2D case with three receivers

When $N = 3$ we have $\binom{3}{2} = 3$ such hyperbola branches, with foci pairs $\{\mathbf{x_1}, \mathbf{x_2}\}$, $\{\mathbf{x_1}, \mathbf{x_3}\}$ and $\{\mathbf{x_2}, \mathbf{x_3}\}$. We call these branches B_{12}, B_{13} and B_{23}, respectively. We first consider pairwise intersections of the B_{ij}. Suppose we fix $\mathbf{x_3}$ as the 'reference receiver', and consider the intersection of B_{13} and B_{23}, which, according to (5.7), are described by the equations

$$2r_3 D_{13} = 2(\mathbf{x_3} - \mathbf{x_1}) \cdot \mathbf{x_0} + |\mathbf{x_1}|^2 - |\mathbf{x_3}|^2 - D_{13}^2, \tag{5.11}$$

$$2r_3 D_{23} = 2(\mathbf{x_3} - \mathbf{x_2}) \cdot \mathbf{x_0} + |\mathbf{x_2}|^2 - |\mathbf{x_3}|^2 - D_{23}^2. \tag{5.12}$$

Eliminating the nonlinear square root term r_3 between (5.11) and (5.12) gives

$$D_{23}\left(2(\mathbf{x_3} - \mathbf{x_1}) \cdot \mathbf{x_0} + |\mathbf{x_1}|^2 - |\mathbf{x_3}|^2 - D_{13}^2\right) = D_{13}\left(2(\mathbf{x_3} - \mathbf{x_2}) \cdot \mathbf{x_0} + |\mathbf{x_2}|^2 - |\mathbf{x_3}|^2 - D_{23}^2\right), \tag{5.13}$$

which is a *linear* equation relating x_0 and y_0. The TDOA problem can therefore be reduced to finding the intersection of a straight line (described by (5.13)) with any one of the three hyperbola branches B_{12}, B_{13} and B_{23}.

The straight line described by (5.13) is, in fact, independent of the choice of $\mathbf{x_3}$ as the reference receiver. Indeed, by use of (5.3)-(5.5), equation (5.13) can be rewritten as

$$ax_0 + by_0 = c, \tag{5.14}$$

where

$$a = 2\left(D_{12}x_3 + D_{23}x_1 + D_{31}x_2\right) = 2\det\begin{pmatrix} r_1 & r_2 & r_3 \\ 1 & 1 & 1 \\ x_1 & x_2 & x_3 \end{pmatrix}, \tag{5.15}$$

$$b = 2\left(D_{12}y_3 + D_{23}y_1 + D_{31}y_2\right) = 2\det\begin{pmatrix} r_1 & r_2 & r_3 \\ 1 & 1 & 1 \\ y_1 & y_2 & y_3 \end{pmatrix}, \tag{5.16}$$

$$\begin{aligned} c &= D_{12}D_{23}D_{31} + D_{12}\left|\mathbf{x_3}\right|^2 + D_{23}\left|\mathbf{x_1}\right|^2 + D_{31}\left|\mathbf{x_2}\right|^2 \\ &= D_{12}D_{23}D_{31} + \det\begin{pmatrix} r_1 & r_2 & r_3 \\ 1 & 1 & 1 \\ \left|\mathbf{x_1}\right|^2 & \left|\mathbf{x_2}\right|^2 & \left|\mathbf{x_3}\right|^2 \end{pmatrix}. \end{aligned} \tag{5.17}$$

The effect of interchanging any two indices in (5.15)-(5.17) is to change the sign of a, b and c. Thus the straight line described by (5.14) is independent of the labeling of the three receivers, and a different choice of reference receiver does not provide us with any new information.

Substituting (5.14) in any one of the three corresponding Cartesian hyperbola equations (5.10) produces a quadratic equation for either x_0 or y_0, which has two real solutions, generally distinct. The linear relation (5.14) then provides the remaining variable (y_0 or x_0, respectively) uniquely for each of these two possible solutions.

If, for some pair $\{i, j\}$, the two solutions lie on *different branches* of the hyperbola described by (5.10), we may discard the incorrect solution and resolve the ambiguity (see Figure 5.1(a) for an example). A sufficient condition for this to occur can be derived by geometrical considerations. Let $0 \leq \theta_{ij} \leq \frac{\pi}{2}$ be the modulus of the acute angle between the line (5.14) and the axis of the hyperbola branch B_{ij}, so that

$$\cos\theta_{ij} = \frac{\left|(\mathbf{x_j} - \mathbf{x_i}) \cdot \mathbf{a}\right|}{\left|\mathbf{x_j} - \mathbf{x_i}\right| \left|\mathbf{a}\right|} = \frac{\left|\mathbf{n} \cdot \mathbf{a}\right|}{\left|\mathbf{a}\right|}, \tag{5.18}$$

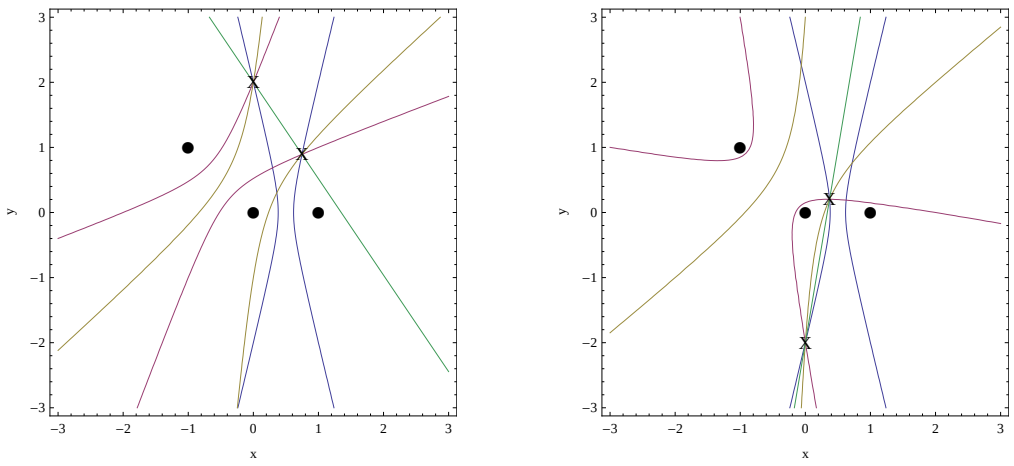


Figure 5.1: Geometry of TDOA localisation in 2D free space with $N = 3$. In (a) the two possible source locations (black crosses) lie on different branches of each of the three hyperbolae, and the correct source location can be determined from the sign of the D_{ij}. In (b) the two possible source locations lie on the same branch of each of the three hyperbolae, and the correct source location cannot be determined from the TDOA data. In both cases the receivers (black points) are at $(0, 0)$, $(1, 0)$ and $(-1, 1)$, and for reference the line (5.14) is drawn in green.

where $\mathbf{a} = (-b, a)$. The semi-angle $0 \leq \gamma_{ij} \leq \frac{\pi}{2}$ of the asymptote cone of B_{ij} satisfies

$$\cos \gamma_{ij} = \frac{|D_{ij}|}{|\mathbf{x_i} - \mathbf{x_j}|} = \frac{1}{e}, \tag{5.19}$$

and a sufficient condition for the line (5.14) to intersect the branch B_{ij} at just one point is[1]

$$\theta_{ij} \leq \gamma_{ij}, \tag{5.20}$$

or, equivalently,

$$\cos \theta_{ij} \geq \cos \gamma_{ij}. \tag{5.21}$$

By (5.18) and (5.19), (5.21) is, in turn, equivalent to the condition

$$|\mathbf{a}| \leq \frac{|(\mathbf{x_j} - \mathbf{x_i}) \cdot \mathbf{a}|}{|D_{ij}|} = e|\mathbf{n} \cdot \mathbf{a}|. \tag{5.22}$$

The dot product on the RHS of (5.22) can be evaluated using (5.15) and (5.16), with the indices $(1, 2, 3)$ replaced by (i, j, k). After some simplification, we find that (5.22)

[1]In fact, (5.19) is also a necessary condition for uniqueness of the intersection point, provided that we exclude the special case where the line (5.14) intersects B_{ij} tangentially.

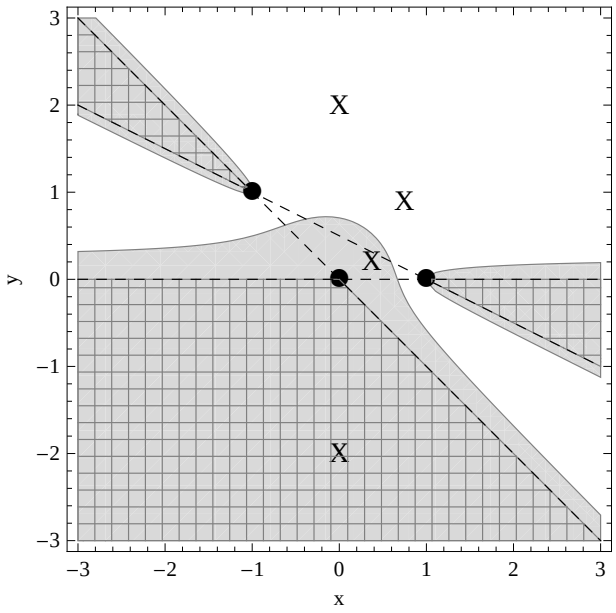


Figure 5.2: Example of the region (shaded) in which the condition (5.23) fails. Sources located in this region cannot, in general, be recovered uniquely from the TDOA data from the three receivers (points), located at $(0,0)$, $(1,0)$ and $(-1,1)$. The two source location pairs of Figure 5.1 are included for reference (crosses). The checked regions, bounded by the lines (dashed) extending the sides of the triangle formed by the three receivers, is entirely contained within the shaded region.

can be written as

$$|\mathbf{a}| \leq 2\,|\det \mathbf{K}|\,, \tag{5.23}$$

where

$$\mathbf{K} = \begin{pmatrix} 1 & 1 & 1 \\ x_i & x_j & x_k \\ y_i & y_j & y_k \end{pmatrix}. \tag{5.24}$$

We note that both sides of the inequality (5.23) are invariant under relabelling of indices, by the properties of the determinant and by the fact that both $|a|$ and $|b|$ are (see the remark after (5.15)-(5.17)). Thus the condition (5.23) is independent of the choice of hyperbola branch B_{ij} used to derive it, and describes a set of source locations that can be recovered uniquely from the TDOA data from the three receivers $\mathbf{x_1}$, $\mathbf{x_2}$ and $\mathbf{x_3}$ (see Figure 5.2 for an example).

We note that the condition (5.23) agrees with that derived by Leva in [57] by a similar method. However, we now give a geometrical interpretation of the result (5.23), which was not pointed out in [57]. Let $\mathbf{X_i} = (x_i, y_i, r_i)$ for each $i = 1, 2, 3$, and

let A be the area of the triangle Δ with vertices $\mathbf{X_i}$. Then we have

$$|a| = 4A_{xr}, \tag{5.25}$$

$$|b| = 4A_{yr}, \tag{5.26}$$

$$|\det \mathbf{K}| = 2A_{xy}, \tag{5.27}$$

where A_{xr}, A_{yr} and A_{xy} are the areas of the projections Δ_{xr}, Δ_{yr} and Δ_{xy} of the triangle Δ onto the xr-, yr- and xy-planes, respectively. Since by de Gua's theorem (see e.g. [5], p. 300)

$$A^2 = A_{xr}^2 + A_{yr}^2 + A_{xy}^2, \tag{5.28}$$

the condition (5.23) is equivalent to requiring that

$$A \leq \sqrt{2} A_{xy}. \tag{5.29}$$

The infinite lines extending the sides of the triangle Δ_{xy} divide the xy-plane into seven regions. Consider the three such regions exterior to Δ_{xy} which meet Δ_{xy} at precisely one vertex only (the checked regions in Figure 5.2). We claim that inside any of these three regions, the condition (5.29) always fails, and we have the possibility of nonuniqueness.

To prove this statement, suppose that $\mathbf{x_0}$ lies inside one of these regions; without loss of generality, the region which meets Δ_{xy} at the vertex $\mathbf{x_1}$ only. Let $\mathbf{p} = (p, q)$ be the point of intersection between the line through $\mathbf{x_0}$ and $\mathbf{x_1}$ and the line through $\mathbf{x_2}$ and $\mathbf{x_3}$. We introduce the function $f(\mathbf{x}) = |\mathbf{x} - \mathbf{x_0}|$, so that $r_i = f(\mathbf{x_i})$. Then, the convexity of the function f implies that the point $(p, q, f(\mathbf{p}))$ lies *below* the line through $\mathbf{X_2}$ and $\mathbf{X_3}$, and since the line from $(x_0, y_0, 0)$ to $(p, q, f(\mathbf{p}))$ contains the point $\mathbf{X_1}$ and makes an angle of $45°$ with the xy-plane, we must have that

$$A > \sqrt{2} A_{xy}, \tag{5.30}$$

so that (5.29) fails.

To end this section we note that in the special case where the three receivers are collinear, the right hand side of (5.23) vanishes. In this case the two possible source locations arising from the solution of the quadratic equation are images of each other under reflection in the line containing the receivers, and only sources lying exactly on this line can be located uniquely from the TDOA data.

5.2.2 The 2D case with four receivers

When (5.23) is not satisfied, it is possible for the two solutions to lie on the same branches of each hyperbola, in which case the correct source location cannot be determined using the TDOA data from the three receivers alone (see Figure 5.1(b) for an example).

To resolve the ambiguity we introduce a fourth receiver at the point $\mathbf{x_4} = (x_4, y_4)$. By carrying out the procedure outlined in the previous section with $\mathbf{x_4}$ rather than $\mathbf{x_3}$ as the reference receiver, we obtain another linear relation between x_0 and y_0, namely

$$a'x_0 + b'y_0 = c', \tag{5.31}$$

where

$$a' = 2\left(D_{12}x_4 + D_{24}x_1 + D_{41}x_2\right), \tag{5.32}$$

$$b' = 2\left(D_{12}y_4 + D_{24}y_1 + D_{41}y_2\right), \tag{5.33}$$

$$c' = D_{12}D_{24}D_{41} + D_{12}\left|\mathbf{x_4}\right|^2 + D_{24}\left|\mathbf{x_1}\right|^2 + D_{41}\left|\mathbf{x_2}\right|^2. \tag{5.34}$$

By combining (5.31) with (5.14), we conclude that the source location must satisfy the linear system

$$\mathbf{A}\mathbf{x_0} = \mathbf{c}, \tag{5.35}$$

where

$$\mathbf{A} = \begin{pmatrix} a & b \\ a' & b' \end{pmatrix}, \qquad \mathbf{c} = \begin{pmatrix} c \\ c' \end{pmatrix}. \tag{5.36}$$

The source location $\mathbf{x_0}$ can then be found uniquely by inverting (5.35), provided that the matrix $\mathbf{A}$ is nonsingular[2].

Using relations such as

$$D_{ij}D_{kl} - D_{ki}D_{lj} = D_{jk}D_{li} \tag{5.37}$$

it can be shown that

$$\begin{aligned} \det\mathbf{A} &= 4D_{12}\left[D_{41}(x_3y_2 - x_2y_3) + D_{32}(x_4y_1 - x_1y_4) + D_{43}(x_2y_1 - x_1y_2)\right. \\ &\qquad \left. + D_{24}(x_3y_1 - x_1y_3) + D_{13}(x_4y_2 - x_2y_4) + D_{21}(x_4y_3 - x_3y_4)\right] \\ &= 4D_{12}\det\mathbf{M}, \end{aligned} \tag{5.38}$$

[2]This condition corresponds to the two lines (5.14) and (5.31) having nonequal gradients.

where

$$\mathbf{M} = \begin{pmatrix} r_1 & r_2 & r_3 & r_4 \\ 1 & 1 & 1 & 1 \\ x_1 & x_2 & x_3 & x_4 \\ y_1 & y_2 & y_3 & y_4 \end{pmatrix}. \tag{5.39}$$

The factor of D_{12} in (5.38) makes $\mathbf{A}$ singular whenever the source is equidistant from the receivers $\mathbf{x_1}$ and $\mathbf{x_2}$ (i.e. along the perpendicular bisector of the line joining $\mathbf{x_1}$ and $\mathbf{x_2}$). This degeneracy can be circumvented by simply choosing a different pair of reference receivers. However, the absolute value of the second factor in (5.38) is clearly invariant under relabeling of the receivers, and source locations for which $\det \mathbf{M}$ vanishes cannot be recovered from the TDOA data using the linear system formulation (5.35).

A necessary and sufficient condition for $\det \mathbf{M}$ to be nonzero for all source locations $\mathbf{x_0}$ is that one of the four receivers lies within the interior of the convex hull of the other three receivers.

To prove this statement we again let $\mathbf{X_i} = (x_i, y_i, r_i)$, and note that

$$\det \mathbf{M} = (\mathbf{X_4} - \mathbf{X_1}) \cdot [(\mathbf{X_2} - \mathbf{X_1}) \wedge (\mathbf{X_3} - \mathbf{X_1})], \tag{5.40}$$

which represents 6 times the 'signed volume' of the tetrahedron with $\mathbf{X_i}$ as vertices. The condition $\det \mathbf{M} = 0$ is therefore equivalent to the points $\mathbf{X_i}$ being coplanar.

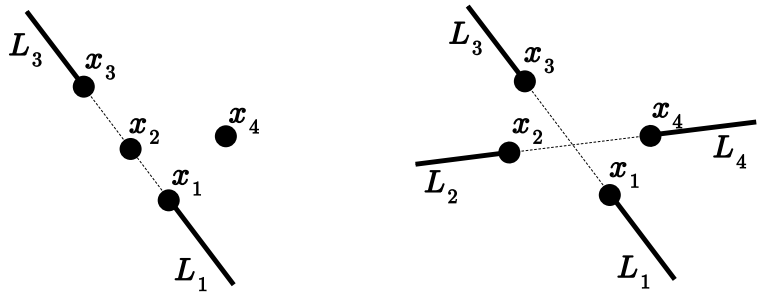
To prove sufficiency, suppose that receiver $\mathbf{x_4}$ lies in the interior of the convex hull of the receivers $\mathbf{x_1}$, $\mathbf{x_2}$ and $\mathbf{x_3}$. With the function f defined as in the previous section, so that $r_i = f(\mathbf{x_i})$, the convexity of f implies that, for any source location $\mathbf{x_0}$, the point $\mathbf{X_4}$ must lie *below* the plane containing $\mathbf{X_1}$, $\mathbf{X_2}$ and $\mathbf{X_3}$, so that $\det \mathbf{M}$ is always strictly non-zero.

To prove necessity we use a contrapositive argument, supposing that none of the four receivers lies within the interior of the convex hull of the other three receivers, and proceeding to show that there exist source locations $\mathbf{x_0}$ for which $\det \mathbf{M}$ vanishes.

One possibility is that three of the receivers, $\mathbf{x_1}$, $\mathbf{x_2}$ and $\mathbf{x_3}$, say, are collinear[3], as in Figure 5.3(a). Then for any source location on the semi-infinite lines L_1 or L_3 the points $\mathbf{X_1}$, $\mathbf{X_2}$ and $\mathbf{X_3}$ are collinear, and hence trivially coplanar with $\mathbf{X_4}$.

The other possibility is that the four receivers define a convex quadrilateral, as in Figure 5.3(b). Then for any source location on the lines L_1 or L_3, the convexity of f

[3]If all four receivers are collinear, $\det \mathbf{M}$ is equal to zero for any source location.



(a) Three receivers collinear (b) Convex quadrilateral

Figure 5.3: Four-receiver configurations not satisfying the convex hull condition.

implies that $\mathbf{X_4}$ must lie *above* the plane containing $\mathbf{X_1}$, $\mathbf{X_2}$ and $\mathbf{X_3}$, so that $\det \mathbf{M}$ has fixed sign $S \in \{-1, 1\}$ on these lines. For any source location on the lines L_2 or L_4, $\mathbf{X_4}$ must lie *below* the plane containing $\mathbf{X_1}$, $\mathbf{X_2}$ and $\mathbf{X_3}$, so that $\det \mathbf{M}$ has fixed sign $-S$ on these lines. Hence by continuity there exists a curve of source locations on which $\det \mathbf{M}$ vanishes, and the proof is complete.

When the 'convex hull condition' is not satisfied, source locations which cannot be recovered from the linear system formulation (5.35) can sometimes still be recovered from the TDOA data, by an application of the three receiver method described in the previous section to a subset of three of the four receivers.

One example of a case in which this approach works is that of a rectangular receiver configuration. Supposing that the receivers are labelled in a clockwise direction, the curves of degeneracy can be shown to satisfy the equation

$$r_1 + r_3 = r_2 + r_4, \tag{5.41}$$

and it is easily shown that (5.41) is satisfied only on the lines $D_{12} = 0$ and $D_{23} = 0$, which are the perpendicular bisectors of $\{\mathbf{x_1}, \mathbf{x_2}\}$ and $\{\mathbf{x_2}, \mathbf{x_3}\}$, respectively. It is easily shown that for any choice of three receivers from the rectangular configuration, the condition (5.23) is always satisfied along these two lines of degeneracy, so that the source location can be recovered uniquely. For example, using receivers $\mathbf{x_1}$, $\mathbf{x_2}$ and $\mathbf{x_3}$, if $D_{12} = 0$ then (5.23) becomes

$$2|D_{23}|\,|\mathbf{x_1} - \mathbf{x_2}| \leq 2\,|\mathbf{x_2} - \mathbf{x_3}|\,|\mathbf{x_1} - \mathbf{x_2}|\,, \tag{5.42}$$

which is true for all source locations.

It should be remarked, however, that there exist four-receiver configurations for which certain source locations cannot be recovered from the TDOA data in this way. An example of this can be found in Figure 5.4.

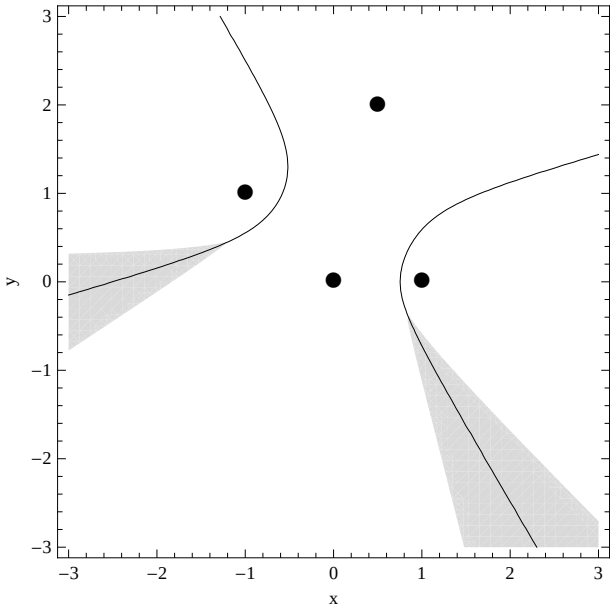


Figure 5.4: Example of a four-receiver configuration for which there exist source locations which cannot be recovered from the TDOA data using either the three-receiver or the four-receiver methods. Here the receivers (black points) are at $(0, 0)$, $(1, 0)$, $(-1, 1)$ and $(0.5, 2)$. The shaded regions represent source locations for which the condition (5.23) fails for any choice of three receivers. The curves represent the source locations for which the determinant of the matrix (5.39) vanishes.

5.2.3 The 3D case

The generalisation of the above analysis to the 3D case is relatively straightforward. Much of the analysis carries over directly, with 2D vectors replaced by 3D vectors, although naturally we find that an extra receiver is needed in the 3D case compared to the 2D case.

The geometrical interpretation of equation (5.7) is now that the source lies on a particular sheet of a hyperboloid of revolution, with the receivers $\mathbf{x_i}$ and $\mathbf{x_j}$ as foci. For any triplet (i, j, k), the pairwise intersection of any two of the resulting hyperboloid sheets constrains the source to lie in a plane described by

$$a_{ijk}x_0 + b_{ijk}y_0 + c_{ijk}z_0 = d_{ijk}, \tag{5.43}$$

where

$$a_{ijk} = 2\left(D_{ij}x_k + D_{jk}x_i + D_{ki}x_j\right), \tag{5.44}$$

$$b_{ijk} = 2\left(D_{ij}y_k + D_{jk}y_i + D_{ki}y_j\right), \tag{5.45}$$

$$c_{ijk} = 2\left(D_{ij}z_k + D_{jk}z_i + D_{ki}z_j\right), \tag{5.46}$$

$$d_{ijk} = D_{ij}D_{jk}D_{ki} + D_{ij}\left|\mathbf{x_k}\right|^2 + D_{jk}\left|\mathbf{x_i}\right|^2 + D_{ki}\left|\mathbf{x_j}\right|^2. \tag{5.47}$$

With $N = 4$, the intersection of the planes arising from two different choices of the triplet (i, j, k) is a line, described by an equation such as

$$\begin{pmatrix} a_{123} & b_{123} & c_{123} \\ a_{124} & b_{124} & c_{124} \end{pmatrix} \begin{pmatrix} x_0 \\ y_0 \\ z_0 \end{pmatrix} = \begin{pmatrix} d_{123} \\ d_{124} \end{pmatrix}. \tag{5.48}$$

This line intersects any of the hyperboloids in at most two points, and with $N = 4$ the source location can therefore be determined up to the solution of a quadratic equation. Under certain conditions, the correct source location can be determined by selecting the point which intersects the correct sheet of the hyperboloid. Geometrical considerations reveal that a sufficient condition for this to be possible is again provided by (5.22), although the vector $\mathbf{a}$ is now any right nullvector of the rank two matrix

$$\begin{pmatrix} a_{123} & b_{123} & c_{123} \\ a_{124} & b_{124} & c_{124} \end{pmatrix}, \tag{5.49}$$

so that $\mathbf{a}$ is a constant multiple of

$$\frac{1}{D_{12}} \begin{pmatrix} b_{123}c_{124} - b_{124}c_{123} \\ c_{123}a_{124} - c_{124}a_{123} \\ a_{123}b_{124} - a_{124}b_{123} \end{pmatrix}. \tag{5.50}$$

The reason for the inclusion of the prefactor $\frac{1}{D_{12}}$ in (5.50) is that each entry of the vector is a 2-by-2 determinant of the form (5.38), the absolute value of which, after dividing by D_{12}, has already been shown to be invariant under relabeling of the receivers.

Evaluation of the RHS of (5.22) then implies that the condition (5.23) should be replaced by[4]

$$|\mathbf{a}| \leq 4 \left| \det \begin{pmatrix} 1 & 1 & 1 & 1 \\ x_1 & x_2 & x_3 & x_4 \\ y_1 & y_2 & y_3 & y_4 \\ z_1 & z_2 & z_3 & z_4 \end{pmatrix} \right|. \tag{5.51}$$

[4]We remark that the RHS of (5.51) represents 24 times the volume of the tetrahedron with vertices $\mathbf{x_1}$, $\mathbf{x_2}$, $\mathbf{x_3}$ and $\mathbf{x_4}$.

We remark that (5.51) is invariant under relabeling of the receivers.

With $N = 5$ the source location can be shown to satisfy the linear system

$$\mathbf{A}\mathbf{x_0} = \mathbf{d}, \tag{5.52}$$

where, for instance,

$$\mathbf{A} = \begin{pmatrix} a_{123} & b_{123} & c_{123} \\ a_{124} & b_{124} & c_{124} \\ a_{125} & b_{125} & c_{125} \end{pmatrix}, \tag{5.53}$$

$$\mathbf{d} = \begin{pmatrix} d_{123} \\ d_{124} \\ d_{125} \end{pmatrix}. \tag{5.54}$$

We find that

$$\det \mathbf{A} = 8D_{12}^2 \det \mathbf{M}, \tag{5.55}$$

where

$$\mathbf{M} = \begin{pmatrix} r_1 & r_2 & r_3 & r_4 & r_5 \\ 1 & 1 & 1 & 1 & 1 \\ x_1 & x_2 & x_3 & x_4 & x_5 \\ y_1 & y_2 & y_3 & y_4 & y_5 \\ z_1 & z_2 & z_3 & z_4 & z_5 \end{pmatrix}. \tag{5.56}$$

The presence of the factor of D_{12}^2 in (5.55) is simply due to our choice of $\mathbf{x_3}, \mathbf{x_4}$ and $\mathbf{x_5}$ as reference receivers. The absolute value of the factor $\det \mathbf{M}$ in (5.55), however, is invariant under relabeling of the receivers, and source locations for which $\det \mathbf{M}$ vanishes cannot be recovered from the TDOA data using the linear system formulation (5.52). A necessary and sufficient condition for $\det \mathbf{M}$ to vanish is that one of the five receivers lies within the interior of the convex hull of the other four receivers. When this convex hull condition is not satisfied, the degenerate source locations form a union of surfaces in 3D space, which is the analogue of the union of curves of degeneracy in the 2D case.

5.2.4 Measurement errors and least-squares solutions

In this section we consider the case where there are errors[5] in the measurement of pulse arrival times t_i and receiver locations $\mathbf{x_i}$. For ease of presentation we consider the 2D case, but the 3D case can be treated similarly.

[5]Another important source of localisation error may be local meteorological variations affecting the sound speed, but this issue will not be discussed here.

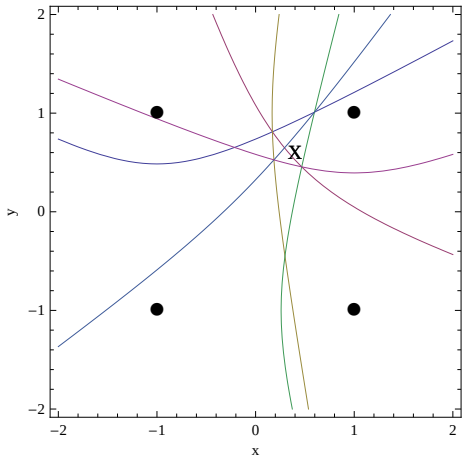


Figure 5.5: TDOA localisation in the presence of measurement errors, $N = 4$. For any choice of three receivers (black points) the three associated hyperbola branches have a point of mutual intersection. However, none of these points coincide with the actual source location (black cross).

Assuming that the measured quantities satisfy

$$|D_{ij}| \leq |\mathbf{x}_i - \mathbf{x}_j| \tag{5.57}$$

for each pair $\{i, j\}$, the TDOA equations (5.2) still describe a collection of hyperbola branches with foci $\mathbf{x}_i$ and $\mathbf{x}_j$ (this is a simple consequence of the triangle inequality).

With $N = 3$ it is easily shown using the relations (5.3)-(5.5), which hold even in the presence of measurement errors, that if two of the hyperbola branches have a point of intersection, then the third must also pass through the same point. The TDOA equations (5.2) are then consistent, and the solution method of section 5.2.1 can be applied. Of course, the resulting solution pair will not, in general, contain the actual source location.

When $N \geq 4$, however, the TDOA equations (5.2) are, in general, inconsistent, and the hyperbolae branches no longer have a point of mutual intersection (see Figure 5.5 for an example with $N = 4$). In this case we may seek an estimate of the source location by solving the TDOA problem in an approximate sense.

The approach taken in [75] and [79] is to consider a least-squares solution of the linear system formulation discussed in section 5.2.2. Each of the $M = \binom{N}{3}$ choices of triplet (i, j, k) gives rise to an equation of the form

$$a_{ijk}x_0 + b_{ijk}y_0 = c_{ijk}, \tag{5.58}$$

where

$$a_{ijk} = 2\left(D_{ij}x_k + D_{jk}x_i + D_{ki}x_j\right), \tag{5.59}$$

$$b_{ijk} = 2\left(D_{ij}y_k + D_{jk}y_i + D_{ki}y_j\right), \tag{5.60}$$

$$c_{ijk} = D_{ij}D_{jk}D_{ki} + D_{ij}\left|\mathbf{x_k}\right|^2 + D_{jk}\left|\mathbf{x_i}\right|^2 + D_{ki}\left|\mathbf{x_j}\right|^2, \tag{5.61}$$

and, after normalising each equation by the factor $\sqrt{a_{ijk}^2 + b_{ijk}^2}$, we may combine (5.59)-(5.61) to form a single matrix equation

$$\tilde{\mathbf{A}}\mathbf{x_0} = \tilde{\mathbf{c}}, \tag{5.62}$$

where $\tilde{\mathbf{A}}$ is an M-by-2 matrix and $\tilde{\mathbf{c}}$ is an M-vector. We then take as our proposed source location $\hat{\mathbf{x}}_\mathbf{0}^\mathbf{l}$ the least-squares solution of the overdetermined[6] linear system (5.62), namely (see e.g. [84], p. 114)

$$\hat{\mathbf{x}}_\mathbf{0}^\mathbf{l} = (\tilde{\mathbf{A}}^\top\tilde{\mathbf{A}})^{-1}\tilde{\mathbf{A}}^\top\tilde{\mathbf{c}}. \tag{5.63}$$

Given a statistical model of the measurement errors, the performance of the estimate (5.63) for a given receiver configuration and source location can be investigated numerically by a Monte Carlo simulation. More precisely, with

$$t_i = t_0^{\text{actual}} + \frac{1}{c_0}\left|\mathbf{x_0}^{\text{actual}} - \mathbf{x_i}^{\text{actual}}\right| + \tau_i, \tag{5.64}$$

$$\mathbf{x_i} = \mathbf{x_i}^{\text{actual}} + \boldsymbol{\xi}_i, \tag{5.65}$$

where the superscript $^{\text{actual}}$ denotes the actual quantities, and the measurement errors τ_i and $\boldsymbol{\xi}_i$ are random variables with known probability distributions, we define the localisation error

$$e^\mathrm{l} := \left|\hat{\mathbf{x}}_\mathbf{0}^\mathbf{l} - \mathbf{x_0}\right|. \tag{5.66}$$

A measure of the performance of the estimate (5.63) may then be obtained by computing the average value $\langle e^\mathrm{l}\rangle$ of (5.66) over a number of realisations of τ_i and $\boldsymbol{\xi}_i$.

As an example, we consider the case where the receiver locations are known exactly ($\boldsymbol{\xi}_i = \mathbf{0}$), and τ_i are assumed to be independent and identically distributed Gaussian random variables with zero mean and known standard deviation σ. Figures 5.6(a)

[6]We remark that when $N = 4$ it can be shown, using the relations (5.3)-(5.5), that the linear system (5.62) is, in general, consistent, even though the original nonlinear system (5.2) is inconsistent. When $N \geq 5$, however, the linear system (5.62) is, in general, inconsistent.

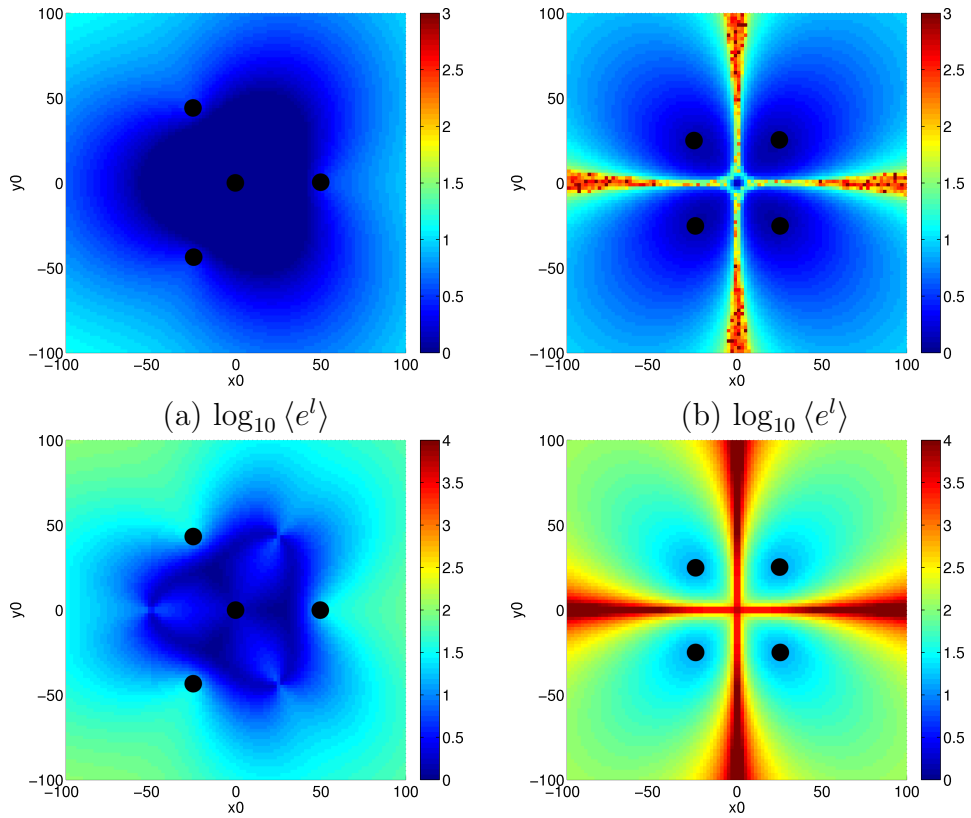


Figure 5.6: TDOA localisation with measurement errors in pulse arrival times; linear minimisation. Plots (a) and (c) correspond to an 'equilateral triangle' four-receiver configuration, and plots (b) and (d) correspond to a 'square' four-receiver configuration. In both configurations the minimum receiver separation is 50m, and the speed of sound $c_0 = 340$m/s. The measurement errors τ_i are taken to be independent and identically distributed Gaussian random variables with zero mean and standard deviation $\sigma = 0.001$s. Localisation errors are averaged over 100 realisations of τ_i.

and 5.6(b) show typical plots of $\langle e^1\rangle$ as a function of $\mathbf{x_0}$ for two particular four-receiver configurations; namely an 'equilateral triangle' configuration, with three of the receivers at the vertices of an equilateral triangle and the fourth at the center of the triangle, and a 'square' configuration, with four receivers at the vertices of a square.

Regions in which the localisation error is large correspond to regions in which the matrix $\tilde{\mathbf{A}}_\mathbf{0}^\top\tilde{\mathbf{A}}_\mathbf{0}$ is ill-conditioned, where $\tilde{\mathbf{A}}_\mathbf{0}$ represents the value of the matrix $\tilde{\mathbf{A}}$ in the absence of measurement errors. This is confirmed by comparing Figures 5.6(a),(b) with Figures 5.6(c),(d). In the case of the square configuration, the localisation error is found to be largest in the vicinity of the x_0 and y_0 axes, where the condition

number of $\tilde{\mathbf{A}}_{\mathbf{0}}^{\top}\tilde{\mathbf{A}}_{\mathbf{0}}$ is infinite[7]. By contrast, since the equilateral triangle configuration satisfies the 'convex hull condition' introduced in section 5.2.2, the matrix (5.39) is not singular anywhere in the plane, and the matrix $\tilde{\mathbf{A}}_{\mathbf{0}}^{\top}\tilde{\mathbf{A}}_{\mathbf{0}}$ does not suffer from the same kind of localised ill-conditioning observed for the square configuration.

The linear least-squares formulation (5.63) is not the only way of estimating the source location in the presence of measurement errors. An alternative approach, taken in [16], is to return to the original nonlinear equations (5.1) and look for an estimated source location which gives rise to arrival times that most closely fit the measured data, by minimising the *nonlinear* function

$$F(\mathbf{x_0}, t_0) := \sum_{i=1}^{N} \left(t_i - t_0 - \frac{|\mathbf{x_0} - \mathbf{x_i}|}{c_0} \right)^2. \tag{5.67}$$

We remark that for the example considered in Figure 5.6 the minimiser of (5.67) represents the *maximum likelihood estimator* of the source location, since it maximises the joint p.d.f. of the measurements t_i, which is given by

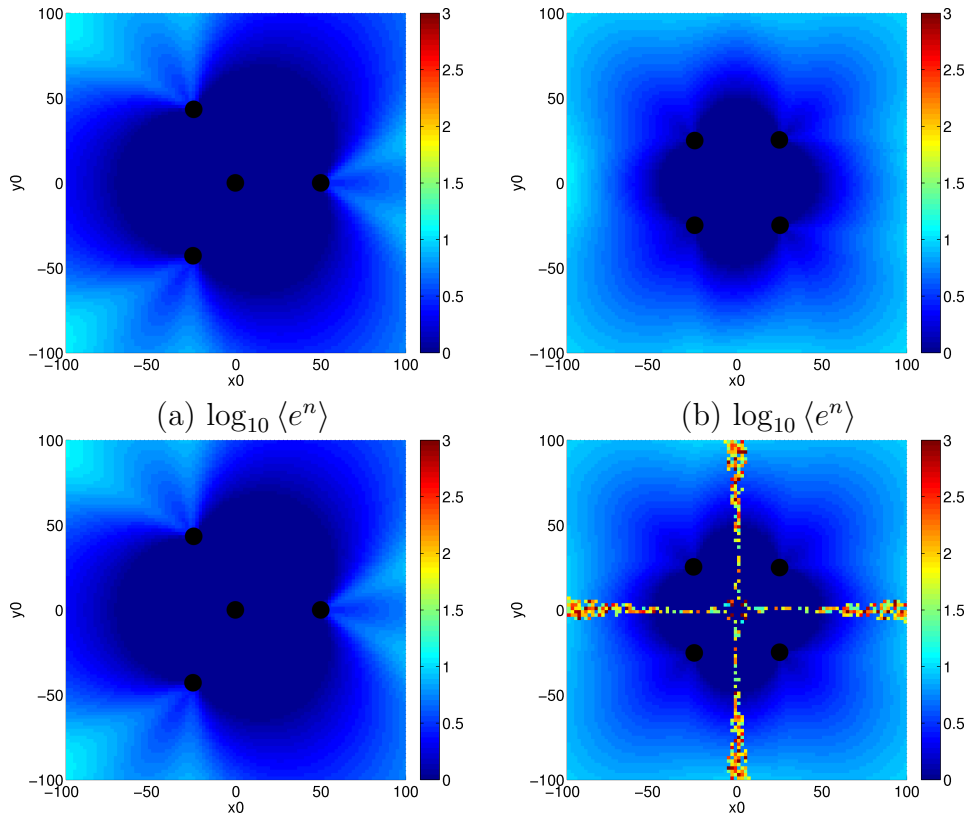
$$\prod_{i=1}^{N} \frac{1}{\sigma\sqrt{2\pi}} \exp\left(-\frac{\left(t_i - t_0 - \dfrac{|\mathbf{x_0} - \mathbf{x_i}|}{c_0} \right)}{2\sigma^2} \right). \tag{5.68}$$

The minimisation over the unknown emission time t_0 in (5.67) can be carried out explicitly, and the problem is therefore equivalent to determining $\hat{\mathbf{x}}_{\mathbf{0}}^{\mathbf{n}}$ minimising

$$G(\mathbf{x_0}) := \sum_{i=1}^{N} \left(\left(t_i - \frac{|\mathbf{x_0} - \mathbf{x_i}|}{c_0} \right) - \frac{1}{N} \sum_{j=1}^{N} \left(t_j - \frac{|\mathbf{x_0} - \mathbf{x_j}|}{c_0} \right) \right)^2. \tag{5.69}$$

As is usually the case with nonlinear minimisations, the solution obtained using a numerical minimisation algorithm may be sensitive to the initial guess supplied to the algorithm, because of the possibility of non-convexity and the existence of local minimisers. An idea of the 'best case' performance of the minimiser of (5.69) is obtained by taking $\mathbf{x_0}^{\text{initial}}$ to be the actual value of $\mathbf{x_0}$. Figures 5.7(a),(b) show typical plots of the average localisation errors $\langle e^{\text{n}} \rangle$ resulting from the nonlinear minimisation, under this choice of initial guess, for the equilateral triangle and square receiver configurations. In both cases the minimisation was carried out in Matlab using the

[7] As was shown in section 5.2.2, these are precisely the curves on which the matrix (5.39) is singular.



(a) $\log_{10}\langle e^n \rangle$ (b) $\log_{10}\langle e^n \rangle$

(c) $\log_{10}\langle e^n \rangle$ (d) $\log_{10}\langle e^n \rangle$

Figure 5.7: TDOA localisation with measurement errors in pulse arrival times; nonlinear minimisation. In (a) and (b) the actual source location $\mathbf{x_0}$ was used as the initial guess for the numerical minimisation. In (c) and (d) $\mathbf{x_0}^{\text{initial}}$ was taken to be the solution (5.63) of the linear minimisation. Other parameter values are as in Figure 5.6.

built-in nonlinear least-squares routine `lsqnonlin`, which is based on an iterative trust-region-reflective algorithm.

The first thing we notice is that, in general, the linear and nonlinear minimisers do not produce the same estimate for the source location. Comparing Figures 5.6(a) and 5.7(a), we observe that for the equilateral triangle configuration, for most source locations the nonlinear minimisation appears to perform as well as, if not better than the linear minimisation. However, for some source locations the linear minimisation performs slightly better (observe the 'streaks' in 5.7(a)). This is rather surprising, given that the nonlinear minimisation represents the maximum likelihood estimator in this case, but we expect the nonlinear minimisation to outperform the linear one as the number of realisations tends to infinity. More importantly, comparing Figures 5.6(b) and 5.7(b), we see that for the square configuration, the nonlinear approach

offers a significant improvement on the linear approach in the regions in which the linear system (5.62) is ill-conditioned.

However, we cannot expect the nonlinear minimisation to achieve the same performance with an arbitrary initial guess. When no *a priori* information about the source location is available, one possible choice of initial guess would be to take $\mathbf{x_0}^{\text{initial}}$ to be the solution (5.63) obtained from the linear formulation. Figures 5.7(c),(d) show typical plots of the average localisation errors $\langle e^{\text{n}} \rangle$ resulting from this choice of initial guess. For the equilateral triangle configuration the result appears unchanged. However, in the case of the square configuration we observe that in the vicinity of the curves of degeneracy of the linear formulation, the nonlinear minimisation cannot overcome the poor initial initial guess resulting from the linear minimisation. Whether this is due to the existence of multiple local minimisers or simply of regions of slow variation in the function G is yet to be determined.

5.3 TDOA localisation in an urban environment: the line-of-sight case

In an urban environment, a single pulse emitted from the source may give rise to multiple pulse arrivals at each receiver, due to the effects of reflection and diffraction from buildings, as described in Chapter 4.

If there is a direct line-of-sight (LOS) between the source and each receiver (for example, if the domain is convex or star-shaped with respect to the source), the free-space localisation method described in the previous section can be applied to the TDOAs obtained from the arrival times of the *first* pulse to arrive at each receiver, which is always the LOS pulse.

In certain special cases, the arrival times of subsequent pulses can be used to reduce the number of receivers required to solve the localisation problem. In the remainder of this section we consider three examples of this.

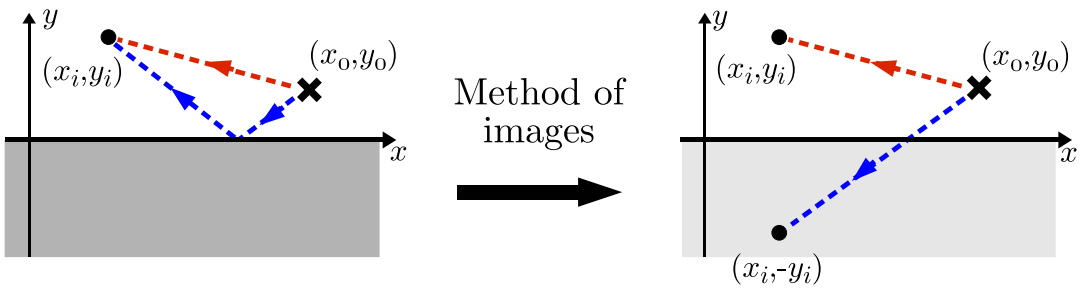


Figure 5.8: Geometry of image receivers for the reflected pulses in a 2D half-plane.

5.3.1 Image receiver method

5.3.1.1 A half space

In the case of a 2D half plane $y > 0$ with a rigid wall at $y = 0$, a single pulse emitted from a source (x_0, y_0) gives rise to two distinct pulses at a receiver (x_1, y_1): a LOS pulse, and a reflected pulse, which can be thought of as having been emitted from an image source at the point $(x_0, -y_0)$. Equivalently, the reflected pulse can be thought of as having been received at an *image receiver* at the point $(x_1, -y_1)$ (see Figure 5.8).

The introduction of a second receiver (x_2, y_2) in the physical domain (distinct from the first), and its corresponding image receiver, provides a total of four receivers in the image domain, with which the localisation problem can be solved by the free-space method described in section 5.2.2. In particular, if $y_1 = y_2$ then the four image domain receivers are in a rectangular configuration, and we have seen that any source location can be uniquely determined in this case. By using the image receivers we have halved the number of physical receivers needed from four (in the free-space case) to just two.

We remark that a similar argument can be used in a 3D half-space (i.e. a 3D urban environment with no buildings) to reduce the number of physical receivers needed from five to three.

5.3.1.2 A 2D corner

Another 2D domain for which this approach works is the quadrant $x > 0$, $y > 0$, with rigid walls at $x = 0, y > 0$ and $y = 0$, $x > 0$. A pulse emitted from the source now results in four pulse arrivals at a physical receiver (x_R, y_R), corresponding to the LOS

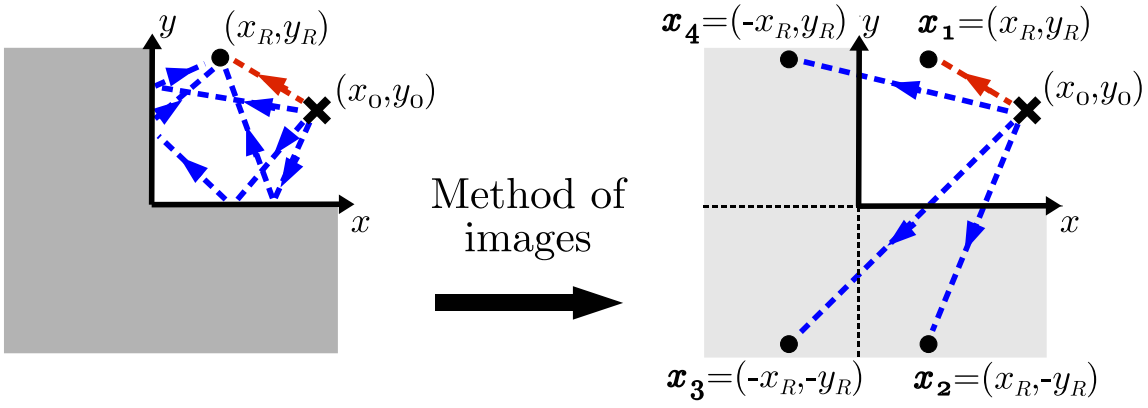


Figure 5.9: Geometry of image receivers for the reflected pulses in a 2D corner.

pulse, a single reflection in the x axis, a double reflection, and a single reflection in the y axis. We associate the three reflected pulses to image receivers $\mathbf{x_2} = (x_R, -y_R)$, $\mathbf{x_3} = (-x_R, -y_R)$ and $\mathbf{x_4} = (-x_R, y_R)$, respectively (see Figure (5.9)).

Since the four receivers $\mathbf{x_1}, \mathbf{x_2}, \mathbf{x_3}, \mathbf{x_4}$ in the image domain are automatically arranged in a rectangular configuration, we would expect to be able to recover the source location uniquely from the TDOA data, having needed just one receiver in the physical domain. However, in order to apply the method of section 5.2.2 we need to know with which image receiver each of the pulses arriving at the physical receiver should be associated.

The first pulse to arrive is always the LOS pulse, and should always be associated with $\mathbf{x_1}$. The last pulse to arrive is always the doubly-reflected pulse, and should always be associated with $\mathbf{x_3}$. The order of arrival of the two singly-reflected pulses depends on the (unknown) source location. When $y_R y_0 - x_R x_0 < 0$ the $\mathbf{x_2}$ pulse arrives before the $\mathbf{x_4}$ pulse, and when $y_R y_0 - x_R x_0 > 0$ the opposite is true. When the source lies on the line $y_R y_0 - x_R x_0 = 0$ the two singly-reflected pulses arrive simultaneously, so that only three distinct pulse arrivals are recorded at the physical receiver. In this special case, the linear system (5.35) can be formed by associating the arrival time of the second of the three pulses to both of the virtual receivers $\mathbf{x_2}$ and $\mathbf{x_4}$. There is no ambiguity to resolve and the source location can be recovered uniquely.

When $y_R y_0 - x_R x_0 \neq 0$ we have to guess which of the two singly-reflected pulses arrived first. If we guess correctly, the solution obtained by solving (5.35) will, of course, be the correct source location. On the other hand, incorrectly assigning the

pulses will lead us to attempt to solve the modified system[8]

$$\tilde{\mathbf{A}}\tilde{\mathbf{x}}_{\mathbf{0}} = \tilde{\mathbf{c}}, \tag{5.70}$$

where

$$\tilde{\mathbf{A}} = -4\begin{pmatrix} D_{14}x_R & D_{34}y_R \\ D_{23}x_R & D_{34}y_R \end{pmatrix}, \qquad \mathbf{c} = \begin{pmatrix} D_{14}D_{43}D_{31} \\ D_{24}D_{43}D_{32} \end{pmatrix}. \tag{5.71}$$

It is easily shown that the degeneracies of $\tilde{\mathbf{A}}$ are the same as those of $\mathbf{A}$, and therefore lie along the lines $x_0 = 0$, $y_0 = 0$. Hence for any source location $x_0 > 0$, $y_0 > 0$, the system (5.70) has a unique solution $\tilde{\mathbf{x}}_{\mathbf{0}} = (\tilde{x}_0, \tilde{y}_0)$, which, after some algebraic manipulation, is found to be

$$\tilde{x}_0 = \frac{y_R}{x_R}y_0, \quad \tilde{y}_0 = \frac{x_R}{y_R}x_0. \tag{5.72}$$

Since $y_R y_0 - x_R x_0 \neq 0$, the proposed solution (5.72) does not provide the correct source location. However, the invalidity of (5.72) can be detected *a posteriori* by a compatibility check against the original data. As previously discussed, we know for certain that D_{13} is the range difference associated with the direct and doubly-reflected pulses. Suppose we calculate this range difference using the proposed solution $\tilde{\mathbf{x}}_{\mathbf{0}}$ and call it $\tilde{D}_{13}$, so that

$$\tilde{D}_{13} = \sqrt{(\tilde{x}_0 - x_1)^2 + (\tilde{y}_0 - y_1)^2} - \sqrt{(\tilde{x}_0 - x_3)^2 + (\tilde{y}_0 - y_3)^2}. \tag{5.73}$$

After repeated squaring and rearrangement we find that a necessary condition for $\tilde{D}_{13}$ to equal D_{13} is given by the sextic equation

$$\frac{256}{x_R^4 y_R^4}(x_R - y_R)(x_R + y_R)(x_0 x_R - y_0 y_R)^2(x_0 x_R + y_0 y_R)^4 = 0, \tag{5.74}$$

and the only way that (5.74) can be satisfied is if $x_R = y_R$. Thus, provided that[9] $x_R \neq y_R$ we can determine whether we have assigned the pulses correctly by checking *a posteriori* that the proposed source location provides the correct value of D_{13}.

[8]This system is obtained from (5.35) by switching the indices 2 and 4 in the TDOA data D_{ij} but not in the receiver locations $\mathbf{x_i}$.

[9]Of course, it is clear from symmetry considerations that unique localisation will not be possible when $x_R = y_R$.

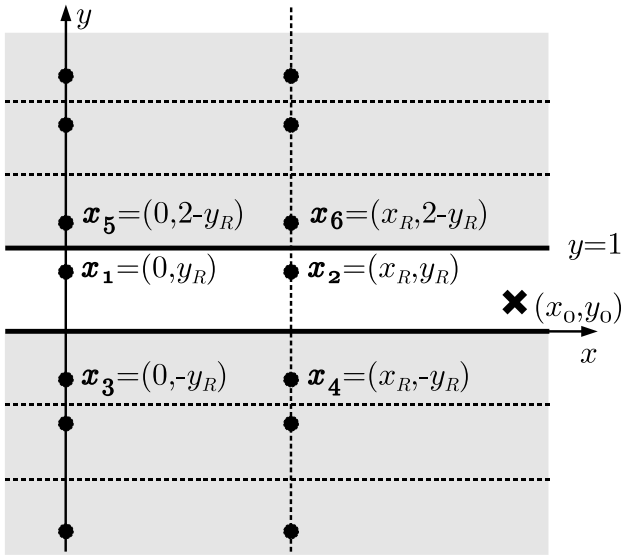


Figure 5.10: Geometry of image receivers for the reflected pulses in a 2D street.

5.3.1.3 A single 2D street

A third domain in which the image receiver method can be applied is an infinite two-dimensional street with rigid walls. In this case a single pulse emitted from the source gives rise to an infinite number of arrivals at each receiver, and, assuming that the walls are at $y = 0$ and $y = 1$, the arrivals at the receiver $\mathbf{x_1} = (0, y_R)$ can be associated with an infinite set of image receivers $(0, 2m \pm y_R)$, $m \in \mathbf{Z}$, as illustrated in Figure 5.10. The first arrival is always due to the LOS pulse, and when $y_0 < 1 - y_R$, the pulse associated with the image receiver $(0, -y_R)$ is the next to arrive, followed by the pulse associated with $(0, 2 - y_R)$. When $y_0 > 1 - y_R$ the two singly-reflected pulses arrive in the opposite order, and when $y_0 = 1 - y_R$ they arrive simultaneously. Similar statements hold for the arrivals of the higher-order reflected pulses.

Since the image receivers are all collinear, the best we can hope to do with a single physical receiver is to determine the source location up to a set of two points which are images of each other in the line $x = 0$, as was remarked at the end of section 5.2.1.

With two physical receivers it is possible to locate the source uniquely. For simplicity we assume that the second receiver has the same y-coordinate as the first, so that $\mathbf{x_2} = (x_R, y_R)$, say (this is the case illustrated in Figure 5.10). Suppose that we record the arrival times of the first two pulses received at each physical receiver. We know that the first pulses should be associated with $\mathbf{x_1}$ and $\mathbf{x_2}$, respectively. We then

make the arbitrary guess that $y_0 \leq 1 - y_R$, and assign the second pulses to $\mathbf{x_3}$ and $\mathbf{x_4}$, respectively. This gives us a rectangular four-receiver configuration, for which a unique solution to the TDOA problem exists. If our guess that $y_0 \leq 1 - y_R$ was false, the resulting solution will not, in general, recover the correct source location, since the second pulses should have been assigned to $\mathbf{x_5}$ and $\mathbf{x_6}$, respectively. However, by a similar analysis to that used in the previous example, it can be shown that, provided $y_R \neq 1/2$ (which is obviously a degenerate case), the ambiguity can be resolved by checking *a posteriori* that the proposed solution produces the correct value of the known range difference D_{12}, although we do not give the details here.

5.4 The non-line-of-sight case

In more complicated domains, in which a direct LOS between the source and each receiver does not always exist, equation (5.1) must be replaced by

$$c_0(t_i - t_0) = L_i, \tag{5.75}$$

where t_i is the arrival time of the *first* pulse to reach the receiver, and L_i is the length of the *shortest* propagation path between the source and receiver, which must be either a LOS path or a (multiply-) diffracted path.

If L_i can be calculated (or appropriately approximated) for any given source location, the natural generalisation of the LOS localisation method is to seek a source location minimising the nonlinear function

$$G(\mathbf{x_0}) = \sum_{i=1}^{N} \left(\left(t_i - \frac{L_i}{c_0} \right) - \frac{1}{N} \sum_{j=1}^{N} \left(t_j - \frac{L_i}{c_0} \right) \right)^2 . \tag{5.76}$$

We remark that in practical applications we need to consider whether the arrival of the weaker multiply-diffracted pulses can be accurately detected against any background noise that may be present, but for the purposes of this thesis we assume that this is always the case.

A simple analytical expression for L_i is not usually available, however, and recovering the source location is therefore more difficult than in the LOS case. In the next section we consider the 2D case, and comment on the more difficult 3D case in section 5.4.3.

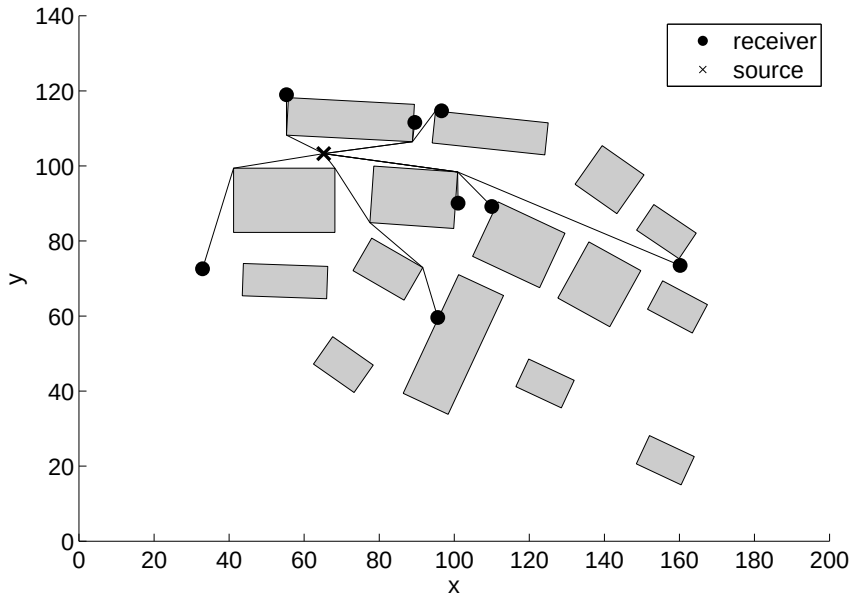


Figure 5.11: Shortest ray paths from source to receivers in a 2D urban environment.

5.4.1 The 2D case - known building distribution

In the 2D case, assuming that the distribution of buildings is known exactly, L_i can be computed using a shortest path algorithm such as Dijkstra's algorithm. We first construct a 'visibility graph' with the building vertices as nodes, and edges weighted according to the distance between vertices, when a LOS exists. An application of the shortest path algorithm then produces a lookup table of the shortest paths between any two building vertices. This permits the rapid calculation of the shortest propagation distances between an arbitrary source and receiver pair for which a direct LOS does not exist by a discrete minimisation over the vertices visible to the source and receiver, respectively.

Figure 5.11 shows the result of applying this algorithm to the 2D environment studied in [4] in the context of time-reversal processing (cf. Figure 1.1 in the Introduction to this thesis). The environment consists of fifteen irregularly-placed buildings, amongst which eight receivers and a source are located. In this case none of the eight receivers have a direct LOS to the source. A plot of the objective function (5.76), computed using the shortest path algorithm, can be found in Figure 5.12(a), and we see that the source location corresponds to a clear global minimum of (5.76) over the propagation domain. Other source locations have also been considered, and the corresponding plots of (5.76) can be found in Figure 5.12(b)-(f).

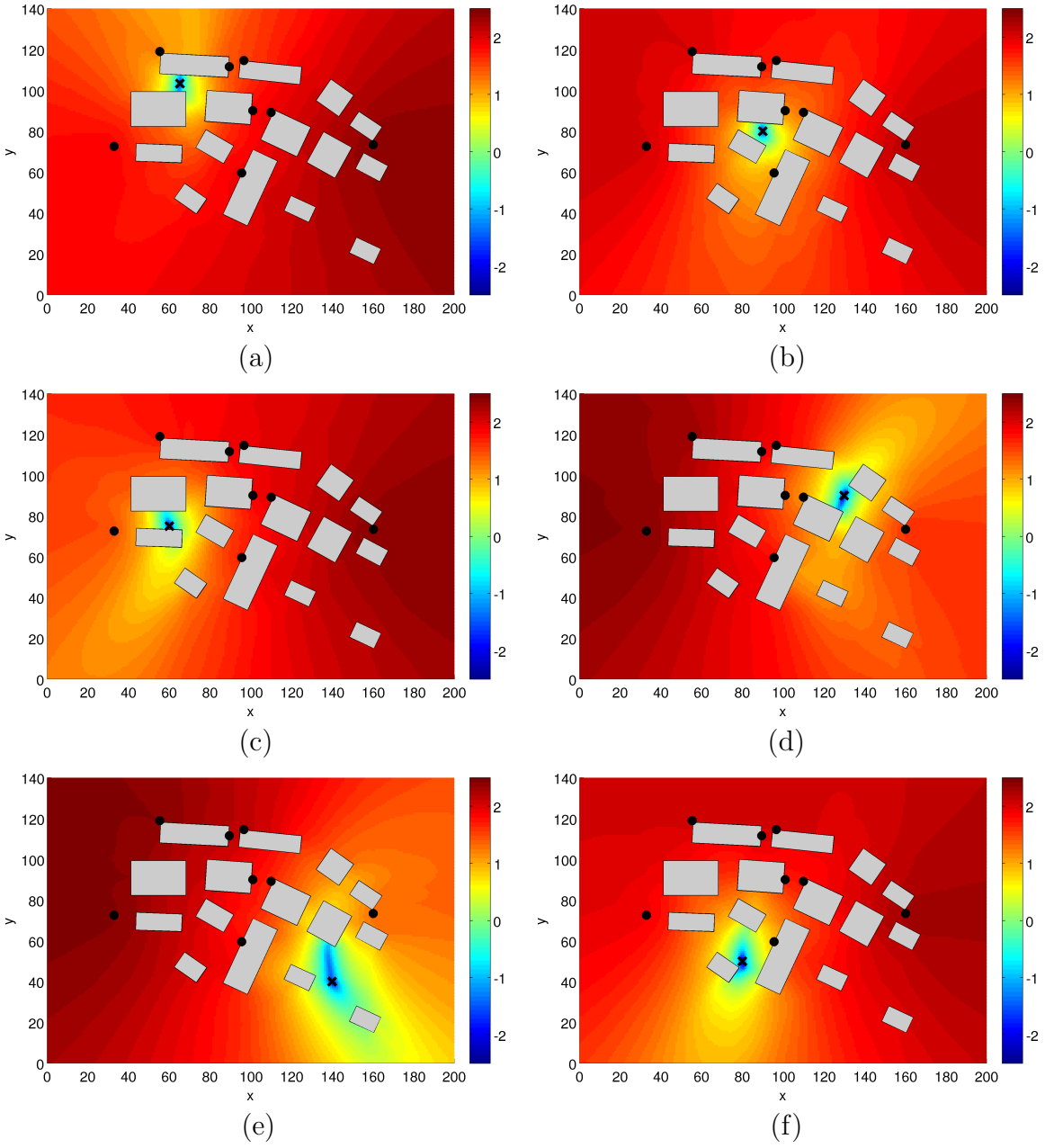


Figure 5.12: TDOA localisation in a 2D urban environment, $N = 8$. Plots (a)-(f) show $\log_{10} G(\mathbf{x_0})$ for six different source locations (crosses). The eight receivers are marked with points.

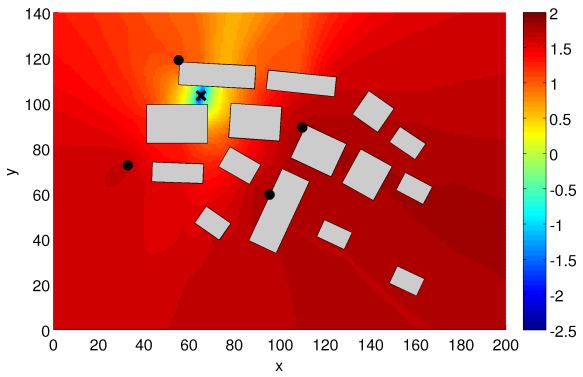


Figure 5.13: TDOA localisation in a 2D urban environment, $N = 4$. The plot shows $\log_{10} G(\mathbf{x_0})$ for the source location considered in Figure 5.12(a).

The numerical minimisation of (5.76) has been implemented in Matlab using the nonlinear least-squares routine `lsqnonlin`. To deal with the geometric constraint that the source location should not lie inside a building, the value of the objective function for a source location inside a building was set to a sufficiently large constant (in this case 1000). For each of the six source locations considered in Figure 5.12, the minimisation converged to the correct source location within five seconds using an initial guess $\mathbf{x_0}^{\text{initial}} = (40, 110)$. This offers a considerable improvement in efficiency over the time-reversal approach adopted in [4]. We expect that the performance of our TDOA method could be improved further using a more sophisticated implementation. We remark that the choice of initial guess was not observed to affect the results dramatically, and similar performance was observed for five other initial guesses.

A detailed investigation into the performance of the minimisation (5.76) for different receiver configurations has not yet been carried out, and this is an important area for future research. However, preliminary investigations suggest that it should be possible to reduce the number of receivers needed. For example, Figure 5.13 shows a plot of the objective function (5.76) when only four of the eight receivers are used.

5.4.2 The 2D case - unknown building distribution

When detailed information about the dimensions and locations of the buildings is unavailable, the localisation method described in the previous section cannot be applied. In this section we consider two particular situations in which assumptions on the distribution of buildings allow the path lengths L_i to be approximated in such a way that reasonable localisation accuracy can still be obtained. Although the results

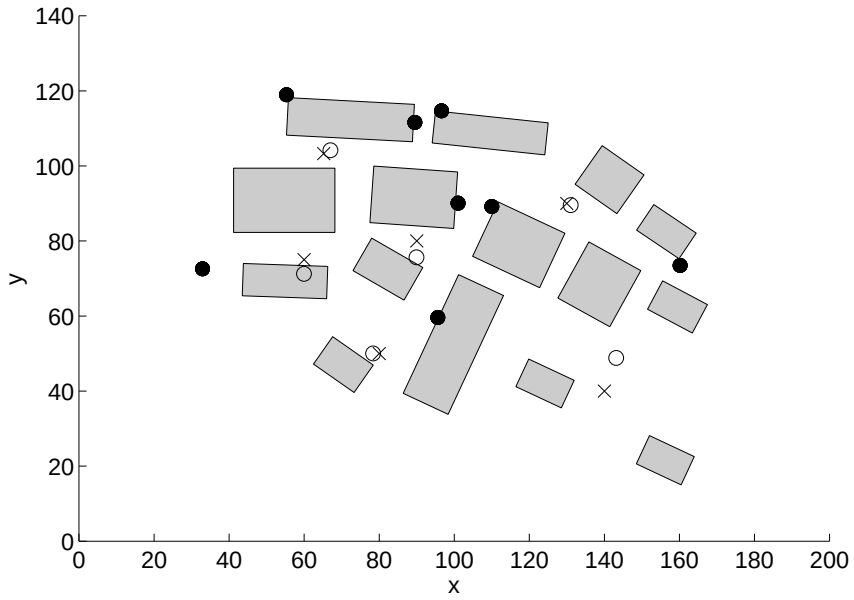


Figure 5.14: TDOA localisation in a 2D urban environment, $N = 8$, using the Euclidean minimisation (5.69).

of this section are rather tentative, they suggest that TDOA methods can still provide a powerful method for source localisation, even when relatively little information about the domain is available.

5.4.2.1 Low building density

First, we consider the case where the buildings are sparsely distributed, so that the shortest ray path between source and receiver does not deviate too much from the free-space path. After nondimensionalising lengths by a typical receiver separation, which we assume is of the order of the typical building separation, we suppose that the typical (nondimensional) building diameter $d \ll 1$. We may then approximate

$$L_i \approx |\mathbf{x_0} - \mathbf{x_i}| \left(1 + O\left(d\right)\right), \qquad d \ll 1, \tag{5.77}$$

provided that $|\mathbf{x_0} - \mathbf{x_i}| \gg d$. Assuming that the relative positions of the receivers are known, an estimate of the source location can then be obtained by an application of the LOS method (i.e. by minimising (5.69)). As an illustration, we have applied this method in the environment considered in the previous section, and the results of the localisation are presented in Figure 5.14. The observed performance is remarkably good given that the environment is not particularly sparse, and that no knowledge

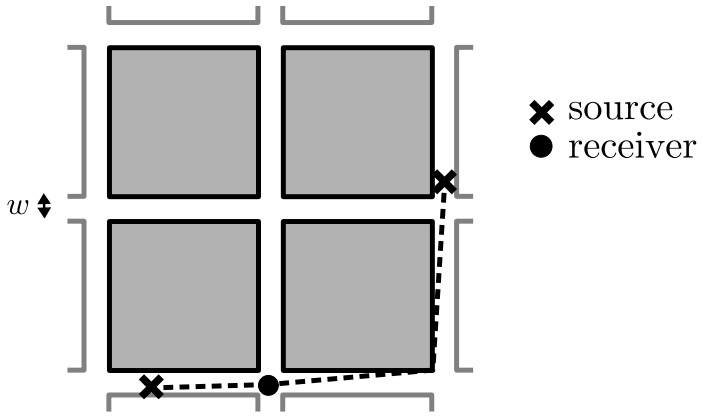


Figure 5.15: A network of 2D streets intersecting at right-angled crossroads.

of the building dimensions or locations was assumed. Another illustration of this method will be presented in section 5.4.2.3.

5.4.2.2 A network of narrow streets

Second, we consider the case of a network of narrow 2D streets intersecting at right-angles, as illustrated in Figure 5.15. After nondimensionalising lengths by a typical receiver separation, which we assume is of the order of the typical street length, we suppose that the (nondimensional) street width $w \ll 1$. We then propose to approximate

$$L_i \approx |\mathbf{x_0} - \mathbf{x_i}|_{\text{sum}} \left(1 - O\left(w\right)\right), \qquad w \ll 1, \tag{5.78}$$

where

$$|\mathbf{x_0} - \mathbf{x_i}|_{\text{sum}} = |x_0 - x_i| + |y_0 - y_i| \tag{5.79}$$

is the 2D sum norm and the minus sign in (5.78) indicates that the approximation is an *overestimate*. The approximation (5.78) is valid provided that $|\mathbf{x_0} - \mathbf{x_i}| \gg w$ and the receiver $\mathbf{x_i}$ is located at a junction.

Under the approximation (5.78), knowledge of the range difference D_{ij} for any pair of receivers $\{\mathbf{x_i}, \mathbf{x_j}\}$ places the source at points in the set

$$B_{ij} := \{\mathbf{x} \,:\, |\mathbf{x} - \mathbf{x_i}|_{\text{sum}} - |\mathbf{x} - \mathbf{x_j}|_{\text{sum}} = D_{ij}\}, \tag{5.80}$$

which represents one branch of the set

$$H_{ij} := \{\mathbf{x} \,:\, |\mathbf{x} - \mathbf{x_i}|_{\text{sum}} - |\mathbf{x} - \mathbf{x_j}|_{\text{sum}} = |D_{ij}|\}, \tag{5.81}$$

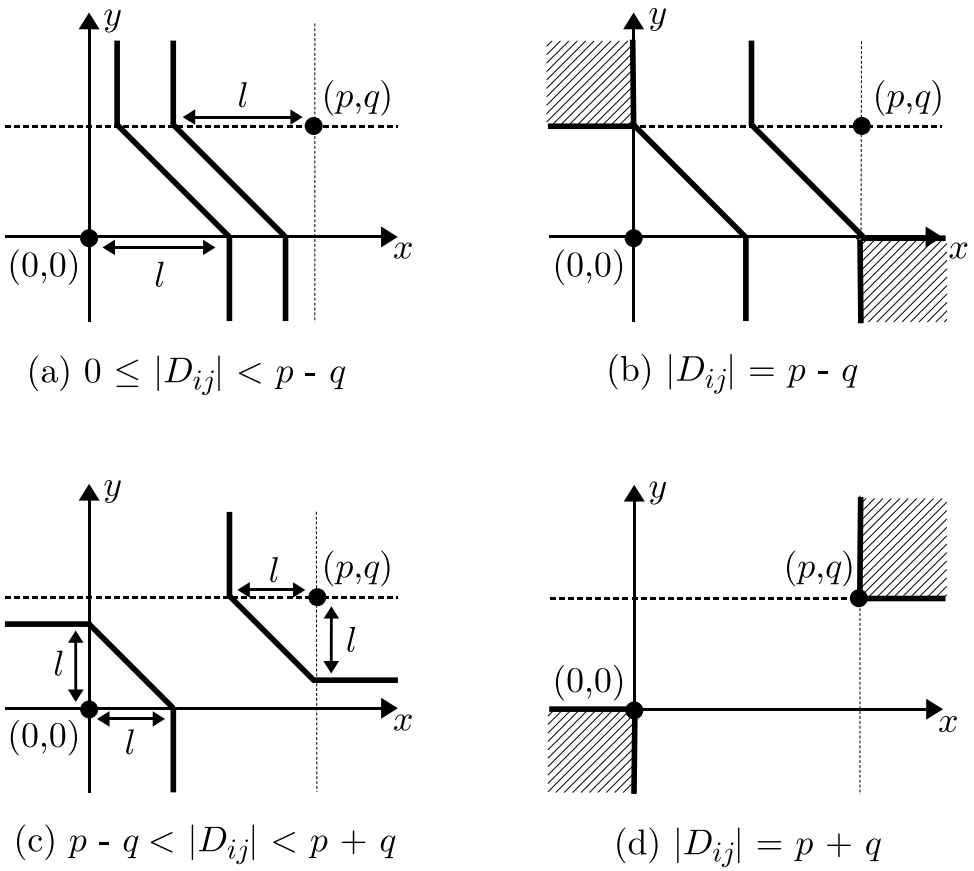


Figure 5.16: The geometrical structure of H_{ij} in the case $(x_i, y_i) = (0, 0)$ and $(x_j, y_j) = (p, q)$, with $0 < q < p$. Here $l = \frac{1}{2}(p + q - |D_{ij}|)$.

analogous to the hyperbolae of the 2D free-space case.

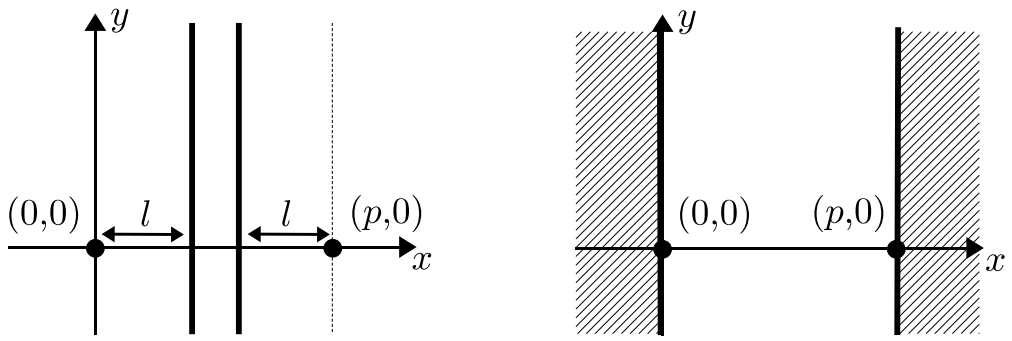
The geometrical structure of H_{ij} varies with the size of the parameter $|D_{ij}|$, as is illustrated in Figure 5.16 in the case where $(x_i, y_i) = (0, 0)$ and $(x_j, y_j) = (p, q)$, with $0 < q < p$ (other cases can be treated similarly). When $0 \leq |D_{ij}| < p - q$ (see Figure 5.16(a)), the positive branch B_{ij}^+ of H_{ij} (i.e. corresponding to $D_{ij} > 0$) is composed of the three straight line segments

$$x = \frac{1}{2}(D_{ij} + (p + q)), \qquad y < 0, \tag{5.82}$$

$$x + y = \frac{1}{2}(D_{ij} + (p + q)), \qquad 0 < y < q, \tag{5.83}$$

$$x = \frac{1}{2}(D_{ij} + (p - q)), \qquad y > q. \tag{5.84}$$

When $|D_{ij}| = p - q$ (see Figure 5.16(b)), B_{ij}^+ is composed of the quadrant $x > p$,



(a) $0 \leq |D_{ij}| < p$ (b) $|D_{ij}| = p$

Figure 5.17: The geometrical structure of H_{ij} when $q = 0$. Here $l = \frac{1}{2}(p - |D_{ij}|)$.

$y < 0$, and the two straight line segments

$$x + y = p, \qquad 0 < y < q, \tag{5.85}$$

$$x = p - q, \qquad y > q. \tag{5.86}$$

When $p - q \leq |D_{ij}| < p + q$ (see Figure 5.16(c)), B_{ij}^{+} is composed of the three straight line segments

$$y = \frac{1}{2}(D_{ij} + (-p + q)), \qquad x > p, \tag{5.87}$$

$$x + y = \frac{1}{2}(D_{ij} + (p + q)), \qquad \frac{1}{2}(D_{ij} - (p - q)) < y < q, \tag{5.88}$$

$$x = \frac{1}{2}(D_{ij} + (p - q)), \qquad y > q. \tag{5.89}$$

Finally, when $|D_{ij}| = p + q$ (see Figure 5.16(d)), B_{ij}^{+} is the quadrant $x > p$, $y > q$. In each of the four cases, the negative branch B_{ij}^{-} is found by rotating the positive branch 180° about the point $(p/2, q/2)$.

In the special case $q = 0$, the geometrical structure of H_{ij} simplifies somewhat (see Figure 5.17). When $0 \leq |D_{ij}| < p$ (see Figure 5.17(a)), B_{ij}^{+} is the straight line

$$x = \frac{1}{2}(D_{ij} + p), \tag{5.90}$$

and when $|D_{ij}| = p$ (see Figure 5.17(b)), B_{ij}^{+} is the half-space $x > p$.

With N receivers, the source location lies within the mutual intersection of the $\binom{N}{2}$ such B_{ij} that result from considering every possible distinct pair of receivers. We immediately notice that if R is defined to be the smallest rectangle containing the N

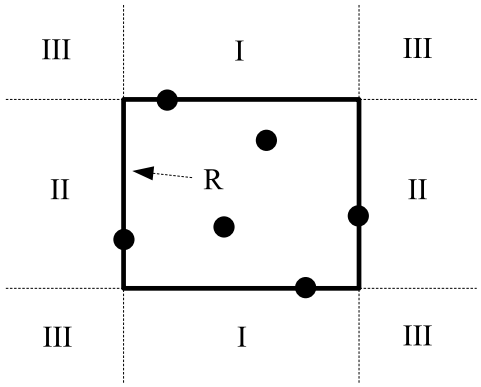


Figure 5.18: Regions (I-III) in which a source cannot be located uniquely in the sum-norm approximation.

receivers, as illustrated in Figure 5.18, then no source location outside of R can be uniquely determined from the TDOA data. For a source located in region I of Figure 5.18, we can at best hope to determine the x coordinate of the source location, and whether the source lies North or South of R. Similarly, for a source located in region II, we can at best hope to determine the y coordinate of the source location, and whether the source lies East or West of R. For a source in region III, we can at best hope to determine in which of the four quarter planes the source lies. Thus, for the purposes of this thesis, we restrict our attention to source locations lying inside R.

If the source is known to lie in a given rectangular subregion R, its precise location

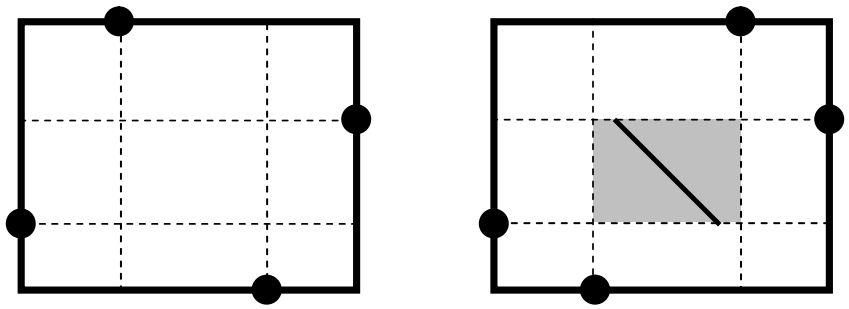


Figure 5.19: TDOA localisation in the sum-norm approximation. The TDOA problem for the four-receiver configuration in (a) admits a unique solution for any source location inside the outer rectangle. In contrast, for the four-receiver configuration in (b), source locations inside the inner (shaded) rectangle cannot be recovered uniquely from the TDOA data. In particular, any source location on the diagonal line segment pictured produces the same TDOA data between the 4 receivers.

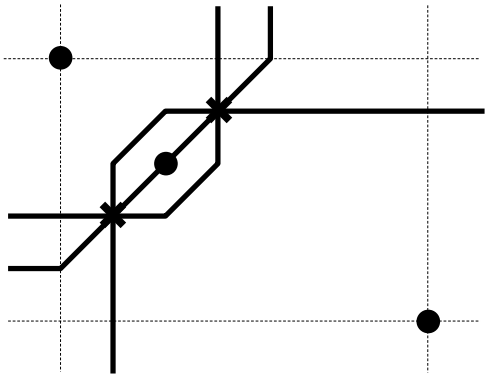


Figure 5.20: TDOA localisation in the sum-norm approximation. The two source locations (crosses) produce the same TDOA data at the three receivers (points). The corresponding 'hyperbola' branches B_{ij} are represented by thick lines.

can be recovered uniquely from the TDOA data from just three receivers, provided that the receivers are placed at vertices of R. The pair of receivers with the same y-coordinate can be used to determine the x-coordinate of the source by formula (5.90), and the pair of receivers with the same x-coordinate can be used to determine the y-coordinate of the source similarly.

However, the general question of which receiver configurations admit a unique solution to the TDOA problem has yet to be resolved. For example, of the two four-receiver configurations illustrated in Figure 5.19, the configuration in Figure 5.19(a) does admit a unique solution to the TDOA problem for all sources inside the rectangle R, whereas that in Figure 5.19(b) does not, since the TDOA data for a source located inside the shaded rectangle is the same as that for any source location on a diagonal line segment passing through the source.

The existence of such a line of source locations which produce the same TDOA data can be avoided by choosing a receiver configuration such that for any source location, at least three of the four quadrants defined by the source location contain a receiver. However, this condition is not sufficient to guarantee global uniqueness, as Figure 5.20 shows. In the three-receiver configuration pictured, both source locations satisfy the condition, but both produce the same TDOA data.

In the case of inconsistent TDOA data and with N receivers, we may seek, following (5.76), an estimated source location $\hat{\mathbf{x}}_\mathbf{0}$ which minimises

$$G_{\mathrm{sum}}(\mathbf{x_0}) := \sum_{i=1}^{N} \left(\left(t_i - \frac{|\mathbf{x_0} - \mathbf{x_i}|_{\mathrm{sum}}}{c_0} \right) - \frac{1}{N} \sum_{j=1}^{N} \left(t_j - \frac{|\mathbf{x_0} - \mathbf{x_j}|_{\mathrm{sum}}}{c_0} \right) \right)^2 . \qquad (5.91)$$

We now present an illustration of this.

5.4.2.3 Results of numerical simulation

The minimisations (5.69) and (5.91) resulting from the approximations (5.77) and (5.78) have been compared in the 2D urban environments illustrated in Figure 5.21. These environments are more general than the network of streets intersecting in crossroads considered in section 5.4.2.2, but the choice of receiver locations ensures that the approximation (5.78) still holds when $w \ll 1$.

In both steps the minimisation was carried out in Matlab using the built-in nonlinear least-squares routine `lsqnonlin`. The initial guess for the iteration was taken to be $\mathbf{x_0}^{\text{initial}} = (1/2, 0)$, but the results were found to agree for five different choices of initial guess.

The results of the calculation are plotted graphically in Figure 5.21, and the maximum and mean localisation errors (measured in terms of Euclidean distance) are displayed in Table 5.1.

The domain in Figure 5.21(a) represents a relatively sparse urban environment. In this domain the Euclidean minimisation (5.69) performs remarkably well, given that many of the source locations considered have no LOS to any of the four receivers. The domain in Figure 5.21(c) represents a relatively dense urban environment, and here the sum-norm minimisation (5.91) provides a more accurate estimate than the Euclidean minimisation. The domain in Figure 5.21(b) represents an intermediate case, in which the performance of the two minimisations is comparable.

We emphasize the fact that for both minimisations, the only information supplied to the algorithm concerning the geometry of the domain was that the source should lie within the rectangle with the receivers as its vertices.

Table 5.1: Results of 2D numerical simulation.

Street width	Euclidean minimisation		Sum-norm minimisation	
	max error	mean error	max error	mean error
(a) $w = 0.2$	0.067	0.027	0.182	0.132
(b) $w = 0.1$	0.127	0.061	0.140	0.089
(c) $w = 0.025$	0.135	0.087	0.043	0.026

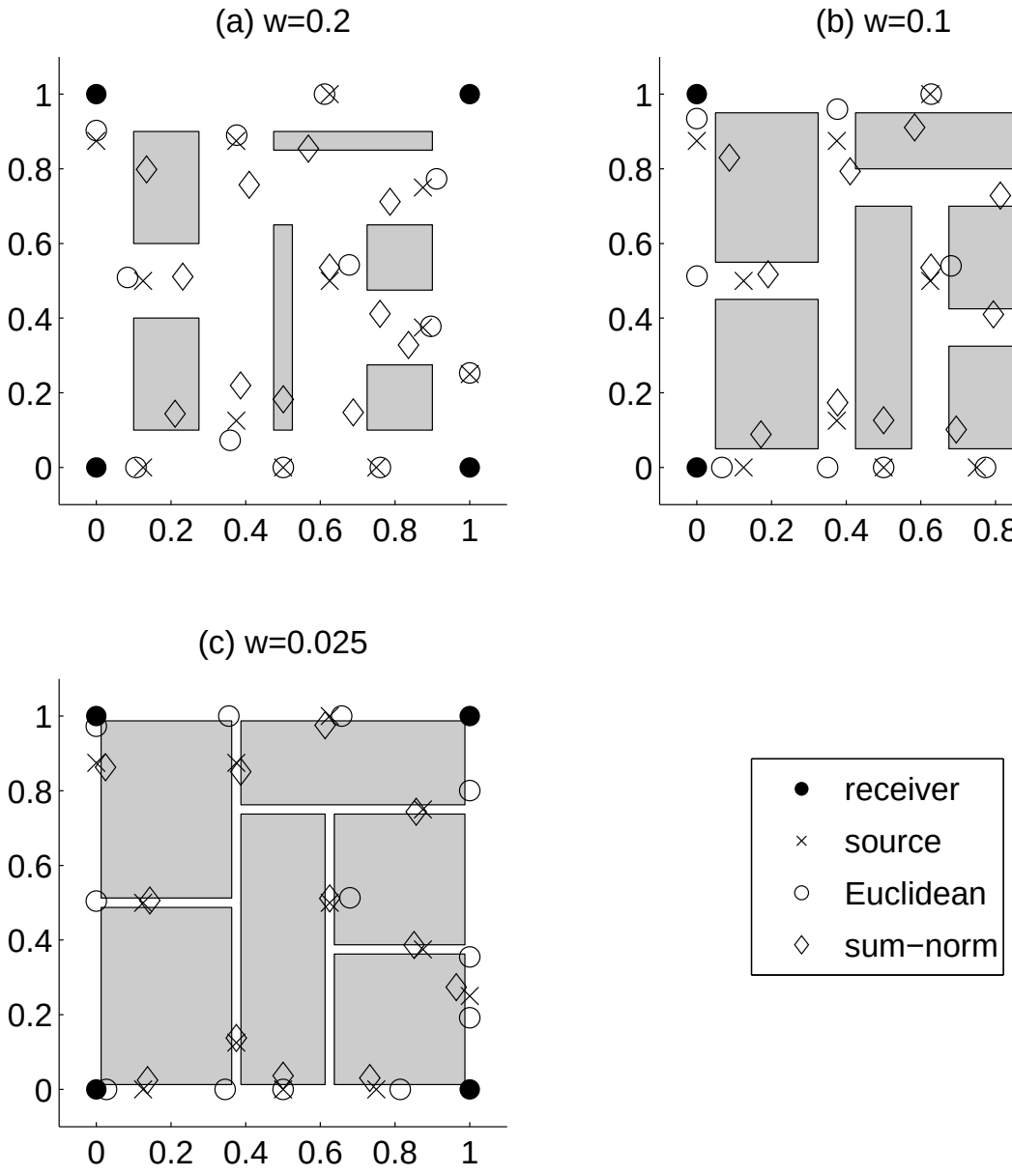
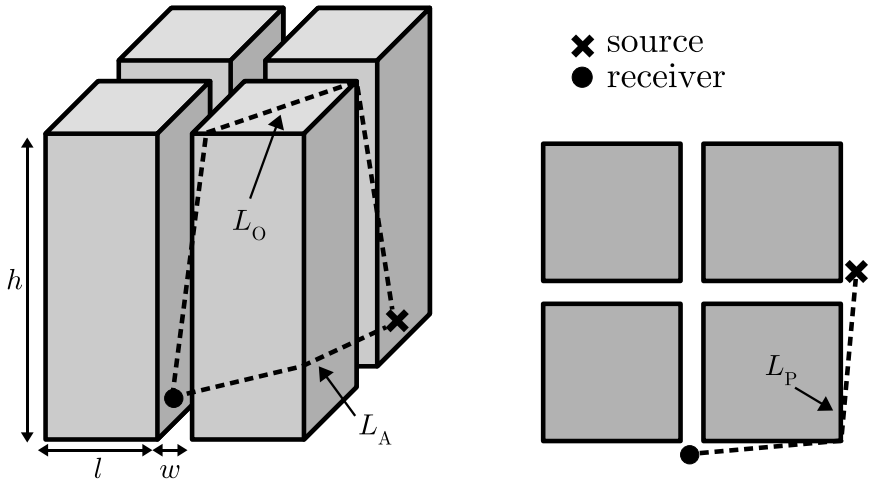


Figure 5.21: Results of 2D numerical simulation.



(a) 3D environment (b) Projection onto xy-plane

Figure 5.22: Diffracted ray paths in a 3D urban environment.

5.4.3 Applicability to the 3D case

In a 3D urban environment, the source localisation problem is complicated by the fact that sound can propagate *over* buildings as well as *around* them (see Figure 5.22(a)). Propagation pathways over buildings may involve diffraction not just at edges, but also at vertices, as discussed in section 4.3.5. Determining the shortest path between the source and a receiver is much more difficult than in the 2D case - even determining the sequence of edges/vertices through which the shortest path passes requires a computation time which grows exponentially in the number of edges (see e.g. [74]), although approximate methods do exist which run in polynomial time (see e.g. [3]). Furthermore, determining the points of contact of the path with these edges then requires the solution of high-degree algebraic equations, which must be accomplished either by numerical approximate methods, or by precise, but very inefficient, symbolic algebraic calculations [76].

A detailed discussion of the 3D shortest path problem would be beyond the scope of this thesis, and in this section we mention only the special case in which shortest paths can be computed exactly in polynomial time, by reduction to the 2D problem discussed in previous sections. Specifically, we make the assumption that the buildings are tall enough to ensure that the shortest ray path between source and receiver involves only diffraction *around* buildings, rather than *over* them.

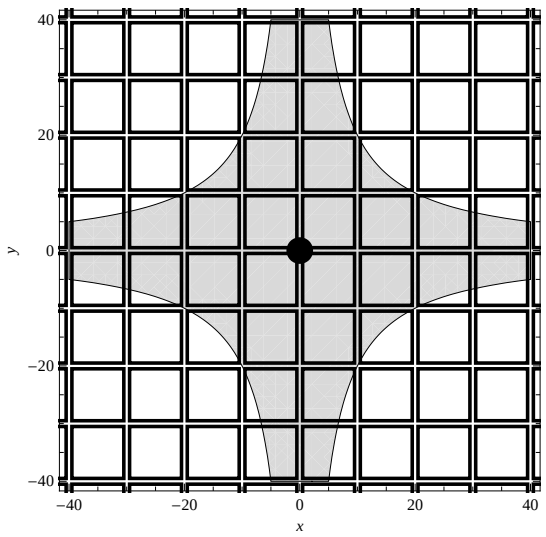


Figure 5.23: Illustration of the region (shaded) in which the condition (5.95) holds. The receiver is located at the origin and the (constant) building height, street length and street width are $h = 10$, $l = 9$, $w = 1$, respectively. Both the source and receiver are assumed to be at ground level. The bounding curves of the shaded region are hyperbolae with centre at the receiver.

Under this assumption, the shortest ray path around buildings is given by

$$L_{\mathrm{A}} = \sqrt{L_{\mathrm{P}}^2 + (z_0 - z_i)^2}, \tag{5.92}$$

where L_{P} is the length of the projection of the ray path onto the xy-plane (see Figure 5.22(b)). When the geometry is known exactly, L_{P} can be computed using the shortest path algorithm described in section 5.4.1. When the geometry is unknown, L_{P} may be approximated by the Euclidean distance (as in section 5.4.2.1) when the building density is low, or by the sum-norm distance (as in section 5.4.2.2) in the case of a network of narrow streets intersecting in right-angled crossroads, with receivers positioned at junctions.

In the latter case we note that the sum-norm approximation provides an upper bound on the length L_{A}, with

$$L_{\mathrm{A}} \leq \sqrt{(|x_0 - x_i| + |y_0 - y_i|)^2 + (z_0 - z_i)^2}. \tag{5.93}$$

Assuming a typical building height h, the length L_{O} of the shortest ray path over buildings can be crudely bounded below by the length of the shortest piecewise-linear curve in 3D free space from the source to the receiver which reaches a height h, i.e.

$$L_{\mathrm{O}} \geq \sqrt{(x_0 - x_i)^2 + (y_0 - y_i)^2 + (h - z_0 + h - z_i)^2}. \tag{5.94}$$

By combining (5.93) and (5.94), we certainly have $L_{\mathrm{A}} \leq L_{\mathrm{O}}$ whenever

$$|x_0 - x_i||y_0 - y_i| \leq 2(h - z_0)(h - z_i). \tag{5.95}$$

An illustration of the region described by (5.95) is given in Figure 5.23. In practice, we expect the region in which $L_{\mathrm{A}} \leq L_{\mathrm{O}}$ to be larger than that described by (5.95), since the lower bound (5.94) is, in general, rather crude. However, a tighter lower bound for L_{O} has not yet been found.

5.5 Summary

In this chapter we have studied the inverse problem for an impulsive source using the method of TDOA localisation. We first considered the free space case, in which the TDOA problem is equivalent to finding the intersection of a collection of hyperbola branches with receivers as foci. With four receivers in 2D (five in 3D) the source location solves a system of linear equations, and we have proved that this system is uniquely solvable for any source location if and only if one of the receivers lies in the interior of the convex hull of the other three (four) receivers.

We have also considered the case where errors in the measurement of pulse arrival times and receiver locations give rise to inconsistent TDOA data, and we have presented two possible approaches by which one may obtain an estimate of the source location in this case. First, we considered the least-squares solution of the linear system formulation. Although this approach provides an explicit solution formula for the estimated source location, it suffers from problems of ill-conditioning, which can give rise to large localisation errors for some source locations. Second, we considered the least-squares solution of the original nonlinear system, which does not suffer from the same ill-conditioning, but requires a numerical solution. The question of how to choose an appropriate initial guess for the nonlinear minimisation is still an open question.

We then addressed the question of how the free-space TDOA methods can be generalised to urban environments. In the simplest case, in which there exists a line of sight (LOS) between the source and each receiver, the free-space methods can be applied to the arrival times of the *first* pulse arrival at each receiver, which is always associated with the LOS. Furthermore, we have shown that in certain simple domains the arrival times of the subsequent reflected pulses can be used to reduce the number of physical receivers needed to locate the source, by an application of the method of images. The success of this method relies crucially upon our ability to assign the reflected pulse arrival times to the correct image receivers, and, as a result, we do not expect it to be feasible in more complicated domains. Having said this, the technique could provide a way of improving the accuracy of location estimates derived by other methods, if the source has been found to lie within a subdomain for which the image method works - a single street, for example.

In the general non-line-of-sight (NLOS) case we have proposed a new TDOA method, which uses the arrival times of diffracted pulses. The method involves the

least-squares minimisation of the nonlinear function (5.76), the evaluation of which requires the calculation of shortest propagation pathways. In the 2D case, this constitutes a discrete optimisation problem, which can be solved exactly and efficiently using Dijkstra's algorithm. We have implemented and tested the method in the 2D domain considered in [4], with very promising results. In particular, the TDOA method offers a significant reduction in computation time over the time-reversal localisation approach taken in [4].

We then considered the case where the exact dimensions and positions of buildings are unknown. In two special 2D cases we have shown, using numerical simulations, that by approximating path lengths appropriately, the inverse problem can be solved with reasonable accuracy, using only limited information about the geometry. The two cases considered were a sparse distribution of buildings, in which a Euclidean approximation was applied, and a network of narrow streets intersecting at right-angles, in which a sum-norm approximation was applied.

Finally, we briefly considered the applicability of the new TDOA method to 3D urban environments. The main difficulty in the 3D case is that the calculation of shortest paths is much more computationally expensive than in the 2D case. However, the problem can be trivially reduced to the 2D case when the buildings are tall enough to ensure that the shortest path involves diffraction only around buildings, rather than over them. We have given an indication of when this assumption holds in the case of a 3D network of narrow streets intersecting at right-angles.

Chapter 6

Conclusions

The principal aim of this thesis has been to investigate the propagation of sound in urban environments. The main new results can be found in Chapters 3-5, and the chapter summaries at the end of these chapters provide an overview of the key results obtained. The purpose of this Conclusion is to draw together these key results and to indicate the common threads running through the thesis. We also suggest some possible areas for future work that have arisen from this investigation.

6.1 Summary of results

Our starting point in Chapter 3 was the study of time-harmonic disturbances in the frequency domain. Focussing on the short wavelength regime, we used geometrical acoustics (ray theory) to develop a model for the propagation of acoustic energy from a time-harmonic point source through a network of interconnecting streets. Our model represents the acoustic power flow from the source along any pathway through the network as the integral of a power density over the launch angle of a ray emanating from the source, and takes into account the key phenomena involved in the propagation, namely energy loss by wall absorption, energy redistribution at junctions, and, in 3D, energy loss to the atmosphere. Interestingly, the model predicts strongly anisotropic decay away from the source, with the power flow decaying exponentially in the number of junctions from the source, except along the axial directions of the network, where the decay is algebraic.

In Chapter 4 we considered sources with arbitrary time dependence. We began by reviewing the general theory concerning the propagation of singularities in the wave

field, another situation in which a geometrical acoustics approximation can be applied. After reviewing a number of exact solutions we stated a general principle concerning the weakening of singularities when they are diffracted by edges and vertices. The correspondence between this principle and the predictions of Keller's Geometrical Theory of Diffraction (GTD) for time-harmonic waves was made explicit via the Fourier transform in section 4.2.4.

We then applied the theory to a situation in which both pulse-like and time-harmonic behaviour is observed, namely the instantaneous switching on of a time-harmonic source. We considered three examples: a point source in 3D and 2D, and the diffraction of a plane wave by a rigid half-line in 2D. In each case we showed how the pulse-like behaviour on the leading wavefront gives way to the time-harmonic behaviour of the corresponding frequency domain solution after a suitable time. Interestingly, we found that the manner in which the source is switched on is of great importance in determining the rate of convergence to the frequency domain solution, with a stronger singularity on the leading wavefront giving rise to a faster rate of convergence.

In section 4.6 we used the theory of pulse diffraction to analyse some real data from an experimental study of the propagation of pulses arising from gunshots in presence of obstacles. Using only a very simple model of the impulse, we were able to predict qualitatively a number of key features of the data, including the arrival times and amplitudes of diffracted pulses.

Finally, in Chapter 5 we applied the pulse propagation theory of Chapter 4 to study the inverse problem of source localisation for an impulsive source. In particular, we generalised to urban environments the existing free-space method of Time Difference Of Arrival (TDOA) localisation, by using the arrival times of reflected and diffracted pulses. The new method offers real-time localisation, and can deal with errors in the measurement of arrival times and receiver locations. Most promising for Dstl is the fact that TDOA methods can still be applied even when the full details of the domain are unknown, as is often the case in practice. We showed that, under certain assumptions, it is possible to localise a source approximately using only general information about the geometry (e.g. typical building diameters or street widths), without needing any detailed information about the exact distribution of buildings.

6.2 Future work

Throughout this thesis we have encountered a number of interesting questions which we have been unable to answer, or which have been beyond the scope of this study. We therefore conclude with some areas for potential future work:

- The model for acoustic energy propagation developed in Chapter 3 is based on a number of simplifying assumptions. One obvious and easily implemented extension of the model would be to make the absorption coefficient angle-dependent. Another relatively easy extension would be to networks involving non-right-angled intersections, and we expect that the probabilistic interpretation of energy redistribution discussed in section 3.6.4 could be of use here. More challenging would be to incorporate diffraction effects, which are neglected in our model (cf. section 3.6.1.1). This would require a significantly more complicated analysis, but could be an excellent test case for next-generation short-wavelength numerical methods (see e.g. [20], [21]). Another important generalisation would be to include the effect of diffuse reflections by inhomogeneous building facades - a brief discussion of this issue, along with some relevant references, was given in the Introduction in section 1.2.1.

- The inverse problem for a time-harmonic source has not been discussed in this thesis. It is feasible that the 'directivity patterns' we obtained in Chapter 3 could form a starting guess for a solution to the source localisation problem in this case; however, further investigation is necessary.

- In section 4.5 we encountered one of the most scientifically interesting problems of the thesis, namely the switching on of a time-harmonic source in the presence of a diffracting edge. The extension of the analysis to the case of wedge diffraction should be fairly easy, since an exact solution to the time-dependent problem exists; however, a more challenging task would be the extension to cases where no exact solution exists, e.g. diffraction by a cone, or problems for which the frequency domain solution possesses caustics.

- In section 5.4 we proposed a new TDOA method for source localisation in an urban environment. One problem of great practical importance that we have not answered concerns the optimal positioning of receivers for a given building configuration. A starting point could be a numerical investigation based on

Monte Carlo simulations similar to those carried out in section 5.2.4 in the free-space case.

- Finally, more work is needed on the application of TDOA methods in unknown geometries. In particular, a numerical investigation based on Monte Carlo simulations in different geometries could provide a starting point for a more extensive comparison of the performance of the two approximate localisation methods (Euclidean and sum-norm) proposed in sections 5.4.2.1 and 5.4.2.2.

Appendix A

Asymptotic analysis of the sums S_1 and S_2

In this Appendix we present details of the analysis of the sums S_1 and S_2 defined in Section 3.5.

Write $S_1(K) = F(K+1) - F(K)$, where

$$F(K) = \sum_{m=0}^{K} f_K(m), \tag{A.1}$$

and

$$f_K(m) = \sqrt{K^2 - m^2}. \tag{A.2}$$

The function $F(K)$ can be approximated for large K by an integral. The Euler summation formula ([9, p315]) gives

$$F(K) = \int_0^K f_K(t)\,dt + \frac{1}{2}\left[f_K(0) + f_K(K)\right] + R(K), \tag{A.3}$$

where

$$R(K) = \int_0^K \left(t - \lfloor t \rfloor - \frac{1}{2}\right) f_K'(t)\,dt. \tag{A.4}$$

The approximating integral can be evaluated explicitly:

$$\int_0^K f_K(t)\,dt = \left[\frac{1}{2}\left(t\sqrt{K^2 - t^2} + K^2 \arctan\left(\frac{t}{\sqrt{K^2 - t^2}}\right)\right)\right]_0^K = \frac{K^2\pi}{4}, \tag{A.5}$$

as can the endpoint contribution:

$$\frac{1}{2}\left[f_K(0) + f_K(K)\right] = \frac{K}{2}. \tag{A.6}$$

Then, noting that

$$f'_K(t) = -\frac{t}{\sqrt{K^2 - t^2}} < 0 \quad \text{for all } 0 < t < K, \tag{A.7}$$

the remainder term can be estimated as follows:

$$\begin{aligned}
|R(K)| &\le \sum_{m=1}^{K-1} \left| \int_{m-1}^{m} \left(t - \lfloor t \rfloor - \frac{1}{2} \right) f'_K(t)\, dt \right| + \left| \int_{K-1}^{K} \left(t - \lfloor t \rfloor - \frac{1}{2} \right) f'_K(t)\, dt \right| \\
&\le \sum_{m=1}^{K-1} \left| \int_{m-1}^{m-1/2} \left(t - m + \frac{1}{2} \right) f'_K(t)\, dt + \int_{m-1/2}^{m} \left(t - m + \frac{1}{2} \right) f'_K(t)\, dt \right| - \frac{1}{2} \int_{K-1}^{K} f'_K(t)\, dt \\
&\le \sum_{m=1}^{K-1} \frac{1}{4} \left| f'_K(m-1) - f'_K(m) \right| + \sqrt{2K-1} \\
&= \sum_{m=1}^{K-1} \frac{1}{4} \left(f'_K(m-1) - f'_K(m) \right) + \sqrt{2K-1} \\
&= -\frac{1}{4} f'_K(K-1) + \sqrt{2K-1} \\
&= \frac{K-1}{4\sqrt{2K-1}} + \sqrt{2K-1} \\
&= O(\sqrt{K}).
\end{aligned} \tag{A.8}$$

Thus we have that

$$\begin{aligned}
S_1(K) &= F(K+1) - F(K) \\
&\sim \frac{(K+1)^2 \pi}{4} + \frac{K+1}{2} - \frac{K^2 \pi}{4} - \frac{K}{2} + O(\sqrt{K}) \\
&\sim \frac{K\pi}{2} + O(\sqrt{K}).
\end{aligned} \tag{A.9}$$

To estimate $S_2(K)$ we first write

$$S_2(K) = \operatorname{Re} \left[\sum_{m=0}^{K} a_m b_m \right], \tag{A.10}$$

where

$$\begin{aligned}
a_m &= \sqrt{(K+1)^2 - m^2} - \sqrt{K^2 - m^2}, \\
b_m &= z^m, \\
z &= e^{2i\pi y_0}.
\end{aligned} \tag{A.11}$$

Note that the a_m form a monotonically increasing sequence. Now set $B_m = \sum_{r=0}^{m} b_r = \frac{1-z^{m+1}}{1-z}$ and note that $|B_m| \leq \frac{2}{1-z}$ for all $m = 0, 1, ..., K$. We can then use partial summation to estimate the sum in (A.10):

$$\begin{aligned}
\left|\sum_{m=0}^{K} a_m b_m\right| &= \left|a_K B_K + \sum_{m=0}^{K-1}(a_m - a_{m+1})B_m\right| \\
&\leq \frac{2}{|1-z|}\left(a_K + \sum_{m=0}^{K-1}(a_{m+1} - a_m)\right) \\
&= \frac{2}{|1-z|}(2a_K - a_0) \\
&= \frac{2}{|1-z|}(2\sqrt{2K+1} - 1) \\
&= O\left(\frac{\sqrt{K}}{|1-z|}\right).
\end{aligned} \tag{A.12}$$

Hence

$$S_2(K) = O\left(\frac{\sqrt{K}}{|1-z|}\right), \tag{A.13}$$

and this is lower order than $S_1(K)$ provided $\frac{\sqrt{K}}{|1-z|} \ll K$. The only problem could be when $z = e^{2i\pi y_0}$ is close to 1, which corresponds to the source being close to one of the walls. Without loss of generality we assume that $0 < y_0 \leq 1/2$. Then for $y_0 \ll 1$ we expand

$$\frac{1}{|1-z|} = \frac{1}{|1-e^{2i\pi y_0}|} \sim \frac{1}{2\pi y_0} + \frac{\pi y_0}{12} + \ldots, \tag{A.14}$$

to see that the validity condition on y_0 is that $y_0 \gg 1/\sqrt{K}$. The same result holds for $1/2 \leq y_0 < 1$, with y_0 replaced by $1 - y_0$. Thus we conclude that $S_2(K) \ll S_1(K)$ provided $y_* \gg 1/\sqrt{K}$, where $y_* = \min\{y_0, 1 - y_0\}$.

Appendix B

Paths through a network of streets

Consider an infinite lattice of crossroads indexed by $(x, y) \in \mathbf{Z} \times \mathbf{Z}$ and joined by straight streets, with a point source located in the street between junctions $(0, 0)$ and $(1, 0)$.

Question 1: How many paths of minimal length exist between the source and junction (X, Y) when $X \geq 1$ and $Y \geq 0$?

Answer 1: By definition, a path of minimal length encounters exactly $X + Y$ junctions, and any such path must therefore consist of exactly X moves to the East and Y moves to the North. Since the first move must be to the East (from the source to the junction $(1, 0)$) the number of paths of minimal length is equal to the number of distinct orderings of a set of $X - 1$ objects of one type (representing the remaining $X - 1$ moves to the East) and Y objects of another type (representing the Y moves to the North), which is $\binom{X+Y-1}{X-1}$.

Question 2: In the special case of a regular network of streets where the street widths are all equal, how many of these paths of minimal length make a non-zero contribution to the power flow $P^E_{X,Y}$ out of the East exit of the junction (X, Y)?

Answer 2: As was remarked in section 3.7.3, there is no propagation along any path that crosses junctions in both the West-East and South-North directions.

When $X \geq Y$, any path of minimal length that crosses a junction in the South-North direction must also cross at least one junction in the West-East direction, and hence makes no contribution to the power flow. The total number of contributing

paths is therefore equal to the number of ways of assigning the Y Northerly moves to the X positions $x = 1, \ldots, X$ *without repetition*, which is equal to $\binom{X}{Y}$.

When $X < Y$, any path of minimal length that crosses a junction in the West-East direction must also cross at least one junction in the South-North direction, and hence makes no contribution to the power flow. Furthermore we note that an Easterly move at $y = 0$ or $y = Y$ would automatically force the path to cross a junction in the West-East direction since the source and the receiver are both in West-East streets. As remarked in Answer 1, the first move must be an Easterly one, and the total number of contributing paths is therefore equal to the number of ways of assigning the remaining $X - 1$ Easterly moves to the $Y - 1$ positions $y = 1, \ldots, Y - 1$ *without repetition*, which is equal to $\binom{Y-1}{X-1}$.

Appendix C

Evaluation of a useful sum and integral

In this appendix we explicitly evaluate a sum and an integral encountered in section 3.8.

First, we consider the sum

$$S = \sum_{n=0}^{\infty} \rho^n \cos \xi(x \pm n), \tag{C.1}$$

with $0 < \rho < 1$. By writing the cosine term as the sum of exponentials, and using the formula for the sum of a geometric progression, we obtain

$$\begin{aligned} S &= \frac{1}{2}\left(\frac{e^{\pm i\xi x}}{1-\rho e^{i\xi}} + \frac{e^{\mp i\xi x}}{1-\rho e^{-i\xi}}\right) \\ &= \frac{\cos \xi x - \rho \cos \xi(x \mp 1)}{1 + \rho^2 - 2\rho \cos \xi}. \end{aligned} \tag{C.2}$$

Second, we consider the integral

$$I = \int_0^{\pi} \frac{\cos \eta y}{a \cos \eta + b}\, d\eta, \tag{C.3}$$

where y is a positive integer and $a, b \in \mathbf{R}$ with $|b| > |a|$. We note that

$$I = \frac{1}{2}\mathrm{Re}\left[\int_{-\pi}^{\pi} \frac{e^{i\eta y}}{a \cos \eta + b}\right] d\eta, \tag{C.4}$$

and by substituting $z = e^{i\eta}$ we see that I is a parametrisation of the contour integral

$$I = \mathrm{Re}\left[-i \oint_C \frac{z^y}{q(z)}\right] dz, \tag{C.5}$$

where the contour C is the unit circle (traversed in the anti-clockwise direction) and

$$q(z) = a(z^2 + 1) + 2bz, \tag{C.6}$$

after using the fact that $\cos\eta = \frac{1}{2}(z + 1/z)$. By factoring the function $q(z)$ into

$$q(z) = a(z - z_+)(z - z_-), \tag{C.7}$$

we see that the two roots $z_\pm$ must satisfy $z_+ z_- = 1$, so that one of the roots must lie inside the unit circle (assuming that they do not both lie on the unit circle). Indeed, solving (C.6) using the quadratic formula gives

$$z_\pm = \frac{-b \pm \sqrt{b^2 - a^2}}{a}, \tag{C.8}$$

and since $|b| > |a|$, both roots are real. When $b < 0$, the root inside the unit circle is z_-, and when $b > 0$, the root inside the unit circle is z_+. By the Residue Theorem we can then evaluate I in either case as

$$\begin{aligned} I &= \mathrm{Re}\left[2\pi i \ \mathrm{res}_{z=z_\pm}\left(-i\frac{z^y}{q(z)}\right)\right] \\ &= \mathrm{Re}\left[2\pi\frac{z_\pm^y}{q'(z_\pm)}\right] \\ &= \pi\frac{z_\pm^y}{az_\pm + b} \\ &= \pm\pi\frac{z_\pm^y}{\sqrt{b^2 - a^2}}. \end{aligned} \tag{C.9}$$

Appendix D

A useful integral identity

In this Appendix we prove the integral identity

$$\int_{\sqrt{\eta}}^{\infty} e^{is^2}\,ds = \frac{e^{i(\eta+\pi/4)}}{2\sqrt{\pi}}\sqrt{\eta}\int_0^{\infty}\frac{e^{is}}{\sqrt{s}(s+\eta)}\,ds, \qquad \eta > 0, \tag{D.1}$$

used in section 4.5.4.2 (equation (4.178)).

We begin by writing

$$I = \int_0^{\infty}\frac{e^{is}}{\sqrt{s}(s+\eta)}\,ds = \int_0^{\infty}\frac{e^{is}}{\sqrt{s}}\left(\int_0^{\infty} e^{-(s+\eta)u}\,du\right)ds. \tag{D.2}$$

Then, defining

$$f(s,u) = e^{-(s+\eta)u}\frac{e^{is}}{\sqrt{s}}, \tag{D.3}$$

we note that

$$\begin{aligned}\int_0^{\infty}\int_0^{\infty}|f(s,u)|\,du\,ds &= \int_0^{\infty}\frac{1}{\sqrt{s}}\left(\int_0^{\infty} e^{-(s+\eta)u}\,du\right)ds \\ &= \int_0^{\infty}\frac{1}{\sqrt{s}(s+\eta)}\,ds = \frac{\pi}{\sqrt{\eta}} < \infty.\end{aligned} \tag{D.4}$$

By Tonelli's theorem (see e.g. [50, p206]) we conclude that $f(x,y)$ is absolutely integrable on $(0,\infty)\times(0,\infty)$, and hence that Fubini's theorem applies[1]. Swapping the order of integration in (D.2) then gives

$$I = \int_0^{\infty} e^{-\eta u}\left(\int_0^{\infty}\frac{e^{is(1+iu)}}{\sqrt{s}}\,ds\right)du. \tag{D.5}$$

[1]Here we interpret the integrals in the Lebesgue sense. We note, however, that the integral on the LHS of (D.1) is not convergent in the Lebesgue sense, and must be interpreted as an improper Riemann integral, as is the case for other related integrals in the main body of the text.

The inner integral in (D.5) can be evaluated by changing variable to $\tilde{s} = s(1+iu)$ (which can be justified by a contour integration) to give

$$\begin{aligned}\int_0^\infty \frac{e^{is(1+iu)}}{\sqrt{s}}\,ds &= \frac{1}{\sqrt{1+iu}}\int_0^\infty \frac{e^{i\tilde{s}}}{\sqrt{\tilde{s}}}\,d\tilde{s} \\ &= \frac{2}{\sqrt{1+iu}}\int_0^\infty e^{is^2}\,ds = \frac{\sqrt{\pi}e^{i\pi/4}}{\sqrt{1+iu}},\end{aligned} \tag{D.6}$$

with the result that

$$I = \sqrt{\pi}e^{i\pi/4}\int_0^\infty \frac{e^{-\eta u}}{\sqrt{(1+iu)}}\,du. \tag{D.7}$$

We then change variable to $s^2 = \eta(1+iu)$ (justified by another contour integration) to give

$$I = \frac{2\sqrt{\pi}e^{-i(\eta+\pi/4)}}{\sqrt{\eta}}\int_{\sqrt{\eta}}^\infty e^{is^2}\,ds, \tag{D.8}$$

which proves (D.1).

Bibliography

[1] 01db metravib. http://www.01db-metravib.com/, 2007.

[2] M. Abramowitz and I. A. Stegun. *Handbook of Mathematical Functions*. United States Department of Commerce, 1964.

[3] P. K. Agarwal, R. Sharathkumar, and H. Yu. Approximate Euclidean shortest paths amid convex obstacles. *Proceedings of the Nineteenth Annual ACM -SIAM Symposium on Discrete Algorithms*, pages 283–292, 2009.

[4] D. G. Albert, L. Liu, and M. L. Moran. Time-reversal processing for source location in an urban environment. *J. Acoust. Soc. Am.*, **118**(2):616–619, August 2005.

[5] N. Altshiller-Court. *Modern Pure Solid Geometry*. Chelsea, New York, 1979.

[6] K. Attenborough, K. M. Li, and K. Horoshenkov. *Predicting outdoor sound*. Taylor and Francis, 2006.

[7] V. Babich, D. Dement'ev, and B. Samokish. On the diffraction of high-frequency waves by a cone of arbitrary shape. *Wave Motion*, **21**:203–207, 1995.

[8] S. Bancroft. An algebraic solution of the GPS equations. *IEEE Transactions on Aerospace and Electronic Systems*, **21**:56–59, 1985.

[9] C. M. Bender and S. A. Orszag. *Advanced mathematical methods for scientists and engineers*. McGraw-Hill, 1978.

[10] J. Billingham and A.C. King. *Wave motion*. Cambridge University Press, 2000.

[11] B. D. Bonner, I. G. Graham, and V. P. Smyshlyaev. The computation of conical diffraction coefficients in high-frequency acoustic wave scattering. *SIAM J. Numer. Anal.*, **43**(3):1202–1230, 2005.

[12] V. A. Borovikov and B. Ye. Kinber. *Geometrical theory of diffraction.* The Institution of Electrical Engineers, 1994.

[13] R. N. Buchal. The approach to steady state of solutions of exterior boundary value problems for the wave equation. *Journal of Mathematics and Mechanics*, **12**(2):225–234, 1963.

[14] R. Bullen and F. Fricke. Sound propagation in a street. *Journal of Sound and Vibration*, **46**(1):33–42, 1976.

[15] R. Bullen and F. Fricke. Sound propagation at a street intersection in an urban environment. *Journal of Sound and Vibration*, **54**(1):123–129, 1977.

[16] J. J. Caffrey and G. L. Stüber. Radio location in urban CDMA microcells. *Proceedings of the IEEE International Symposium on Personal, Indoor and Mobile Radio Communications 1995*, pages 858–862, 1995.

[17] H. S. Carslaw. Multiform solutions of certain partial differential equations. *Proceedings of the London Mathematical Society*, **30**:121–165, 1898.

[18] H. S. Carslaw. Diffraction of waves by a wedge of any angle. *Proceedings of the London Mathematical Society*, **s2-18(1)**:291–306, 1920.

[19] K. Chan and L. B. Felsen. Transient and time-harmonic diffraction by a semi-infinite cone. *IEEE Transactions on Antennas and Propagation*, **AP-25**(6):802–806, November 1977.

[20] S. N. Chandler-Wilde and I. G. Graham. Boundary integral methods in high frequency scattering. *Highly Oscillatory Problems, Cambridge University Press. B Engquist, T Fokas, E Hairer, A Iserles (editors)*, pages 154–193, 2009.

[21] S. N. Chandler-Wilde and S. Langdon. A galerkin boundary element method for high frequency scattering by convex polygons. *SIAM Journal on Numerical Analysis*, **43**:610–640, 2007.

[22] E. T. Copson. *An introduction to the theory of functions of a complex variable.* OUP, 1935.

[23] R. Courant and D. Hilbert. *Methods of Mathematical Physics, Vol.I.* Interscience Publishers, 1953.

[24] R. Courant and D. Hilbert. *Methods of Mathematical Physics, Vol.II.* Interscience Publishers, 1962.

[25] M. Crocker. *Handbook of Noise and Vibration Control.* John Wiley and Sons, 2007.

[26] H. G. Davies. Noise propagation in corridors. *J. Acoust. Soc. Am.*, **53**(5):1253–1262, 1973.

[27] H. G. Davies. Multiple-reflection diffuse-scattering model for noise propagation in streets. *J. Acoust. Soc. Am.*, **64**(2):517–521, August 1978.

[28] M. E. Delany and E. N. Bazley. Monopole radiation in the presence of an absorbing plane. *J. Sound Vib.*, **13**(3):269–279, 1970.

[29] G. F. Duff and D. Naylor. *Differential Equations of Applied Mathematics.* John Wiley and Sons, 1966.

[30] J. C. Engineer, J. R. King, and R. H. Tew. Diffraction by slender bodies. *Euro. Jnl of Applied Mathematics*, **9**:129–158, April 1998.

[31] F. Fahy. *Sound intensity.* Taylor and Francis, 1995.

[32] B. T. Fang. Simple solutions for hyperbolic and related position fixes. *IEEE Transactions on Aerospace and Electronic Systems*, **26**(5):748–753, September 1990.

[33] L. B. Felsen and N. Marcuvitz. *Radiation and Scattering of Waves.* Prentice-Hall, 1973.

[34] F. G. Friedlander. *Sound pulses.* Cambridge University Press, 1958.

[35] A. G. Galitsis and W. N. Patterson. Prediction of noise distribution in various enclosures from free-field measurements. *J. Acoust. Soc. Am.*, **60**(4):848–856, October 1976.

[36] M. Gensane and F. Santon. Prediction of sound fields in rooms of arbitrary shape: validity of the image sources method. *J. Sound Vib.*, **63**(1):97–108, 1979.

[37] I. S. Gradshteyn and I. M. Ryzhik. *Table of Integrals, Series and Products.* Academic Press Inc, 1993.

[38] D. P. Hewett, J. R. Ockendon, and D. J. Allwright. Switching on a two-dimensional scalar wave in the presence of a diffracting edge. *Wave Motion*, to appear.

[39] E. J. Hinch. *Perturbation methods*. Cambridge University Press, 1994.

[40] C. H. Hodges and J. Woodhouse. Theories of noise and vibration transmission in complex structures. *Rep. Prog. Phys.*, **49**:107–170, 1986.

[41] W. Hope-Jones. The sound-ranging problem. *The Mathematical Gazette*, **10**(153):306–307, 1921.

[42] W. Hope-Jones. The sound-ranging problem. *The Mathematical Gazette*, **14**(195):173–186, 1928.

[43] U Ingard. On the reflection of a spherical sound wave from an infinite plane. *J. Acoust. Soc. Am.*, **23**(3):329–335, May 1951.

[44] K. K. Iu and K. M. Li. The propagation of sound in narrow street canyons. *J. Acoust. Soc. Am.*, **112**(2):537–550, August 2002.

[45] D. S. Jones. *Acoustic and Electromagnetic Waves*. Oxford University Press, USA, 1989.

[46] J. Kang. Sound propagation in street canyons: comparison between diffusely and geometrically reflecting boundaries. *J. Acoust. Soc. Am.*, **107**:1394–1404, March 2000.

[47] J. Kang. *Urban sound environment*. Taylor and Francis, 2006.

[48] J. B. Keller. Geometrical theory of diffraction. *Journal of the Optical Society of America*, **52**(2):116–130, February 1962.

[49] J. B. Keller and A. Blank. Diffraction and reflection of pulses by wedges and corners. *Comm. Pure and App. Math.*, **4**(1):75–94, 1951.

[50] H. Kestelman. *Modern theories of integration*. Dover Publications, Inc., 1960.

[51] W. A. Kinney, A. D. Pierce, and Rickley E. J. Helicopter noise experiments in an urban environment. *J. Acoust. Soc. Am.*, **56**(2):332–337, August 1974.

[52] D. E. Knuth. Big omicron and big omega and big theta. *ACM SIGACT News*, **8**:18–24, Apr-June 1976.

[53] L. Kraus and L. M. Levine. Diffraction by an elliptic cone. *Comm. Pure Appl. Math.*, **14**(1):49–68, 1961.

[54] H. Lamb. On Sommerfeld's diffraction problem; and on reflection by a parabolic mirror. *Proceedings of the London Mathematical Society*, **s2-4(1)**:190–203, 1907.

[55] H. Lamb. On the diffraction of a solitary wave. *Proceedings of the London Mathematical Society*, **8**:422–437, 1910.

[56] T. Le Pollès, J. Picaut, M. Bérengier, and C. Bardos. Sound field modeling in a street canyon with partially diffusely reflecting boundaries by the transport theory. *J. Acoust. Soc. Am.*, **116**(5):2969–2983, November 2004.

[57] J. L. Leva. An alternative closed-form solution to the GPS pseudo-range equations. *IEEE Transactions on Aerospace and Electronic Systems*, **32**(4):1430–1439, October 1996.

[58] M. J. Lighthill. *Waves in Fluids*. Cambridge University Press, 2003.

[59] L. Liu, D. G. Albert, and D. K. Wilson. The effect of changing scatterer positions on acoustic time-reversal refocusing in a 2D urban environment at low frequencies. *Journal of Geophysics and Engineering*, **4**(2):276–284, November 2007.

[60] R. H. Lyon. Propagation of environmental noise. *Science*, **179**:1083–1090, March 1973.

[61] R. H. Lyon. Role of multiple reflections and reverberation in urban noise propagation. *J. Acoust. Soc. Am.*, **55**(3):493–503, March 1974.

[62] R. H. Lyon and R. G. DeJong. *Theory and application of statistical energy analysis*. Butterworth-Heinemann, 1995.

[63] J. Meixner. The behavior of electromagnetic fields at edges. *IEEE transactions on antennas and propagation*, **20**:442–446, 1972.

[64] J. W. Miles. On the diffraction of an acoustic pulse by a wedge. *Proc. Roy. Soc. Lon. Series A, Math. and Phys. Sci.*, **212**:543–547, 1952.

[65] C. S. Morawetz. The limiting amplitude principle. *Comm. Pure and App. Math.*, **15**(3):349–361, 1962.

[66] C. S. Morawetz. The limiting amplitude principle for arbitrary finite bodies. *Comm. Pure and App. Math.*, **18**(1-2):183–189, 1965.

[67] B. G. Nikolaev. Diffraction of field of a point source by circular cone (nonaxisymmetric case). *J. Sov. Math.*, **9**(4):598–612, 1978.

[68] M. A. Nobile and S. I. Hayek. Acoustic propagation over an impedance plane. *J. Acoust. Soc. Am.*, **78**(4):1325–1336, October 1985.

[69] F. Oberhettinger. On the diffraction and reflection of waves and pulses by wedges and corners. *Journal of Research of the National Bureau of Standards*, **61**:343–364, 1958.

[70] H. Ockendon and J. Ockendon. *Waves and Compressible Flow*. Springer, 2004.

[71] J. Ockendon, S. Howison, A. Lacey, and A. Movchan. *Applied partial differential equations*. Oxford University Press, 2006.

[72] J. Picaut, J. Hardy, and L. Simon. Sound propagation in urban areas: a periodic disposition of buildings. *Physical Review E*, **60**(4):4851–4859, October 1999.

[73] J. Picaut, L. Simon, and J. Hardy. Sound field modelling in streets with a diffusion equation. *J. Acoust. Soc. Am.*, **106**(5):2638–2645, November 1999.

[74] J. H. Reif and J. A. Storer. A single-exponential upper bound for finding shortest paths in three dimensions. *Journal of the Association for Computing Machinery*, **41**(5):1013–1019, 1994.

[75] R. O. Schmidt. A new approach to the geometry of range difference location. *IEEE Transactions on Aerospace and Electronic Systems*, **8**(6):821–835, 1972.

[76] M. Sharir and A. Schorr. On shortest paths in polyhedral spaces. *SIAM J. Comput.*, **15**(1):193–215, 1986.

[77] H. Shirai and L. B. Felsen. Rays, modes and beams for plane wave coupling into a wide open-ended parallel-plane waveguide. *Wave motion*, **9**(2):301–317, 1987.

[78] ShotSpotter. http://www.shotspotter.com, 2007.

[79] J. O. Smith and J. S. Abel. Closed-form least-squares source location estimation from range-difference measurements. *IEEE Transactions on Acoustics, Speech and Signal Processing*, **35**(12):1661–1669, 1987.

[80] V. P. Smyshlyaev. Diffraction by conical surfaces at high frequencies. *Wave Motion*, **12**:329–339, 1990.

[81] A. Sommerfeld. Mathematische Theorie der Diffraktion. *Math. Ann.*, **47**:317–74, 1896.

[82] A. Sommerfeld. *Partial differential equations in physics*. Academic Press, 1949.

[83] R. Stoughton. Measurements of small-caliber ballistic shock waves in air. *J. Acoust. Soc. Am.*, **102**(2):781–787, August 1997.

[84] G. Strang. *Linear algebra and its applications*. Acadamic Press, Inc., 1980.

[85] R. H. Tew, S. J. Chapman, J. R. King, J. R. Ockendon, B. J. Smith, and I. Zafarullah. Scalar wave diffraction by tangent rays. *Wave Motion*, **32**:363–380, October 2000.

[86] J. Thompson. Closed solutions for wedge diffraction. *SIAM Journal of Applied Mathematics*, **22**:300–306, 1972.

[87] B. van der Pol and H. Bremmer. *Operational calculus based on the two-sided Laplace integral*. Cambridge University Press, 1950.

[88] M. Van Dyke. *Perturbation methods in fluid mechanics*. Academic Press, 1964.

[89] E. J. Watson. Infinite regular electrical networks. *European Journal of Applied Mathematics*, **16**(5):555–567, October 2005.

[90] G. B. Whitham. *Linear and Nonlinear waves*. John Wiley and Sons, 1974.

[91] F. M. Wiener, C. I. Malme, and C. M. Gogos. Sound propagation in urban areas. *J. Acoust. Soc. Am.*, **37**(4):638–747, April 1965.

[92] H. Y. Yee, L. B. Felsen, and J. B. Keller. Ray theory of reflection from the open end of a waveguide. *SIAM J. App. Math.*, **16**(2):268–300, 1968.

[93] S. H. Zemell. New derivation of the exact solution for the diffraction of a cylindrical or spherical pulse by a wedge. *Int. J. Engng. Sci.*, **14**:845–851, 1976.